Photoinitiators in 3D laser printing: a quantum-mechanical investigation

Zur Erlangung des akademischen Grades einer

DOKTORIN DER NATURWISSENSCHAFTEN

(Dr. rer. nat.)

von der KIT-Fakultät für Chemie und Biowissenschaften

des Karlsruher Instituts für Technologie (KIT)

genehmigte

DISSERTATION

von

M.Sc. Anna Mauri

1. Referent: PD Dr. Sebastian Höfener
2. Referent: Prof. Dr. Wolfgang Wenzel

Tag der mündlichen Prüfung: 18.04.2024

Aknowledgments

I would like to express my sincere gratitude to everyone who contributed to the completion of this work. This journey would not have been possible without the support, guidance, and encouragement from various individuals and institutions.

Firstly, I express my gratitude to Prof. Dr. Wolfgang Wenzel, for the possibility to conduct my PhD at KIT in his group and under his supervision. His expertise and insights have significantly shaped the development of this project. Thank you for your constant scientific help and support.

I extend my gratitude to my fist supervisor PD Dr. Sebastian Höfener, for his great supervision and continuous suggestions during our meetings about my projects. His insights have been of great importance for the project.

I am grateful to my research supervisor Dr. Mariana Kozlowska, for being next to me in good and bad times, for supporting, helping, coordinating, guiding and teaching me how to do research. Without her this entire project would have not been possible.

I would like to acknowledge the assistance and collaboration of several PhD students and Professors from the experimental side, who shared their knowledge and expertise. Especially AG Wegener, AG Bräse, AG Unterreiner and AG Barner-Kowollik, their input has enriched the depth of this project.

I am grateful for the financial support to my PhD provided by the Excellence Cluster "3D Matter Made to Order" funded by the Carl Zeiss Foundation Program.

Further, I want to thank my colleagues for sharing this journey with me, especially Helmy, Srdjan, Niklas and Saientan.

Thanks to Lele and Dalila and to all my new friends for being there. Special thanks go to my family, Mum, Dad and Sara, for their constant encouragement, understanding and infinite love. I could not ask for more. Last but not least I want to express my gratitude to Deniz, for his tremendous help and support in every aspect of life.

Abstract

Employing quantum mechanical calculations, including density functional theory and time-dependent density functional theory, the investigation focuses on two-photon absorption and two-step absorption active photoinitiators that, upon exposure to light, initiate free radical polymerization. The photochemical and photophysical properties of these initiators are thoroughly explored, providing theoretical insights into their polymerization reaction mechanisms, which have yet to be fully comprehended by the scientific community. Key photoinitiators for two-photon absorption include 2,2-dimethoxy-2-phenylacetophenone (Irgacure 651) and 2-benzyl-2-N,N-dimethyl- amino-1-(4-morpholinophenyl)-1-butanone (Irgacure 369), classified as Norrish type I, diethylamino-3-thenoylcoumarin (DETC) and (2E,6E)-2,6-bis(4-(dimethylamino)benzylidene)-4-methylcyclohexanone (BBK), classified as Norrish type II. For the two-step absorption process, benzil, biacetyl, and tetramethylbenzil were chosen as candidates. Norrish type I initiators generate radicals upon bond cleavage in the first triplet states, while Norrish type II initiators do so through a bimolecular reaction with a co-initiator, which triggers a hydrogen atom transfer reaction with the photoinitiator, generating reactive radicals. However, DETC and BBK stand out as unique Norrish type II photoresists. When combined with the monomer pentaerythritol triacrylate, they undergo a mysterious radical generation mechanism in the absence of a co-initiator, based on a three-photon process instead of the expected two-photon initiated pathway. On the other hand, the two-step absorption photoinitiators generate radicals similarly to Norrish type I but from high triplet states. Since their use is connected with less complex laser setup than the one used for two-photon based processes, they have recently become popular in the field of 3D laser printing. Therefore the objective of the research reported in the thesis is to reveal the distinctions and similarities in terms of efficiency and radical formation mechanisms triggered by both one-photon and multiphoton absorption of these photoinitiators, aligning theoretical findings with experimental data. Conducting a benchmark of potential functionals and an in-depth analysis of the one-photon and multiphoton properties of the mentioned photoinitiators, the study aims to pinpoint the optimal methodology to apply for the study. The computational exploration encompasses crucial photophysical channels originating from excited states shedding light on the pathways leading to radical generation. In addition, detailed insights are provided into the cleavage reaction mechanism of Norrish type I and two-step two-photon absorption initiators. For DETC and BBK, investigations extend to intermolecular-hydrogen atom transfer with co-initiator for the N=2 (where N is the number of photon) process alongside with intermolecular-hydrogen atom transfer with the monomer and various hypothetical radical generation pathways for

the third order behaviour, such as photolysis, intermolecular-, and intramolecular-hydrogen atom transfer which are thoroughly explored. Given the limitations of existing quantum-mechanical methods in precisely replicating the real conditions where the initiators operate, this contribution is positioned as important in rationalizing experimental observations that have remained for many years poorly understood, thereby enhancing our comprehension of designing principles for new photoinitiators used in 3D laser nanoprinting. Moreover, this study emphasizes the need for improved molecular-based structure-activity relationships to better interpret experimental dependencies and facilitate the virtual design of novel photoinitiators, with the ultimate goal of enhancing 3D laser nanoprinting sensitivity, resolution, and speed.

Kurzfassung

Mit Hilfe quantenmechanischer Berechnungen, einschließlich der Dichtefunktionaltheorie und der zeitabhängigen Dichtefunktionaltheorie, liegt der Fokus der Untersuchung auf Zweiphotonenabsorption und Zweischritt-Absorption aktivierter Photoinitiatoren, die bei Lichteinwirkung die Polymerisation durch freie Radikale initiieren. Die photochemischen und photophysikalischen Eigenschaften dieser Initiatorsubstanzen werden umfassend erforscht und bieten theoretische Einblicke in ihre Polymerisationsreaktionsmechanismen, die von der wissenschaftlichen Gemeinschaft noch nicht vollständig verstanden wurden. Schlüssel-Photoinitiatoren für die Zweiphotonenabsorption sind Irgacure 651 und Irgacure 369, klassifiziert als Norrish Typ I, DETC und BBK, klassifiziert als Norrish Typ II. Für den Zweischritt-Absorptionsprozess wurden Benzil, Biacetyl und Tetramethylbenzil als Kandidaten ausgewählt. Norrish Typ I-Initiatoren erzeugen Radikale durch Bindungsspaltung in den ersten Triplettzuständen, während Norrish Typ II-Initiatoren dies durch eine bimolekulare Reaktion mit einem Co-Initiator tun, der eine Wasserstoffatomübertragungsreaktion mit dem Photoinitiator auslöst und reaktive Radikale erzeugt. DETC und BBK hingegen zeichnen sich als einzigartige Norrish Typ II-Photosensibilisatoren aus. In Kombination mit dem Monomer Pentaerythrittriacrylat unterliegen sie einem mysteriösen Mechanismus zur Radikalerzeugung in Abwesenheit eines Co-Initiators, basierend auf einem Dreiphotonenprozess anstelle des erwarteten zweiphotoneninitiierten Pfads. Andererseits erzeugen Zweischritt-Absorptions-Photoinitiatoren Radikale ähnlich wie Norrish Typ I, jedoch aus hohen Triplettzuständen. Da ihr Einsatz mit einer weniger komplexen Lasereinrichtung verbunden ist als bei den zweiphotonenbasierten Prozessen, sind sie in letzter Zeit im Bereich des 3D-Laserdrucks populär geworden. Das Ziel der in der Arbeit vorgestellten Forschung besteht daher darin, die Unterschiede und Gemeinsamkeiten in Bezug auf Effizienz und Mechanismen zur Radikalerzeugung, ausgelöst durch ein- und mehrphotonische Absorption dieser Photoinitiatoren, aufzudecken und theoretische Erkenntnisse mit experimentellen Daten abzugleichen. Durchführung eines Benchmarks potenzieller Funktionaler und einer eingehenden Analyse der ein- und mehrphotonischen Eigenschaften der genannten Photoinitiatoren zielt die Studie darauf ab, die optimale Methodik für die Untersuchung zu identifizieren. Die Berechnungen umfassen entscheidende photophysikalische Kanäle, die von angeregten Zuständen ausgehen und Einblicke in die Wege zur Radikalerzeugung bieten. Darüber hinaus werden detaillierte Einblicke in den Spaltungsreaktionsmechanismus von Norrish Typ I- und Zweischritt-Zweiphotonenabsorptions-Initiatoren gegeben. Bei DETC und BBK erstrecken sich die Untersuchungen auf die intermolekulare Wasserstoffatomübertragung mit dem Co-Initiator für den N=2-Prozess (wobei N die Anzahl der Photonen ist)

sowie auf die intermolekulare Wasserstoffatomübertragung mit dem Monomer und verschiedene hypothetische Mechanismen zur Radikalerzeugung für das Verhalten dritter Ordnung, wie Photolyse, intermolekulare und intramolekulare Wasserstoffatomübertragung, die gründlich erforscht werden. Angesichts der Einschränkungen bestehender quantenmechanischer Methoden bei der genauen Reproduktion der realen Bedingungen, unter denen die Initiatoren arbeiten, stellt dieser Beitrag eine wichtige Positionierung dar, um experimentelle Beobachtungen zu rationalisieren, die seit vielen Jahren schlecht verstanden blieben, und damit unser Verständnis der Entwurfsprinzipien für neue Photoinitiatoren, die im 3D-Lasernanodruck verwendet werden, zu verbessern. Darüber hinaus betont diese Studie die Notwendigkeit verbesserter molekularbasierter Struktur-Aktivitäts-Beziehungen, um experimentelle Abhängigkeiten besser zu interpretieren und die virtuelle Gestaltung neuartiger Photoinitiatoren zu erleichtern, mit dem ultimativen Ziel, die Empfindlichkeit, Auflösung und Geschwindigkeit des 3D-Lasernanodrucks zu verbessern.

Publications and conference contribution

Results presented in the thesis based on publications

Results presented in the thesis are reported in the following publications:

- **A. Mauri**, P. Kiefer, P. Neidinger et al. Two- and three-photon processes during photopolymerization in 3D laser printing. Chem. Sci., 2024,15, 12695-12709
  DOI:10.1039/D4SC03527E
- Planned submission before publication of the thesis, first author - **A. Mauri**, P. Kiefer, et al. Initiation of free radical polymerization in 3D laser printing using Norrish type I and Norrish type II photoinitiators. Macromol. Rapid Commun. (2024-2025 planned).

Additional publications

List of publications conducted during PhD whose results are not presented in the thesis:

- Published, first author from theory - Y. Xiu, **A. Mauri**, S. Dinda et al. Angew. Chem. Int. Ed. 2023, 62, e202212339; Angew. Chem. 2023, 135, e202212339.
  DOI: 10.1002/anie.202212339
- Published, first author from theory - S. Begum, K. Kutonova, **A. Mauri**, M. Koenig et al. Disulfide-Bridged Dynamic Covalent Triazine Polymer Thin Films by Interface Polymerization: High Refractive Index with Excellent Optical Transparency. Adv. Funct. Mater. 2023, 2303929.
  DOI:10.1002/adfm.202303929
- Published, first author from theory - L. Vaghi, F. Rizzo, J. Pedrini, **A. Mauri** et al. Bypassing the statistical limit of singlet generation in sensitized upconversion using fluorinated conjugated systems. Photochem. Photobiol. Sci. 2022, 21, 913–921.
  DOI:10.1007/s43630-022-00225-z
- Published, shared first authorship - C. Leonhardt, I. Garin, **A. Mauri** et al. Tetrazole and oxadiazole derivatives as thermally activated delayed fluorescence emitters. Chem. Eur. J. 2024, e202401682
  DOI:10.1002/chem.202401682

- Planned submission before publication of the thesis, first author from theory - Z. Xu, A. Chandresh, **A. Mauri** et al. Tuning Charge Transfer and Transport in Oriented Donor-Acceptor Metal-Organic Frameworks for Highly-Sensitive Photodetectors. Chemistry - a European Journal
- Planned submission before publication of the thesis, first author from theory - C. R. Adam, D. Marhöfer, **A. Mauri** et al. Introducing TADF Copper (I) Complexes with Dual Bridging Ligands and Excitation-Dependent Emission (2024 planned)

Results presented in conferences

Internal conferences

Data reported in the thesis were presented at the internal conferences and seminars organized by the Excellence cluster 3D Matter Made to Order (3DMM2O):

- 23 February 2021 (Neustadt an der Weinstraße, Germany): 3DMM2O Winter Cluster Meeting 2021 - poster presentation with the title "Multiphoton processes for direct laser writing"
- 3-8 April 2022 (Kloster Schöntal, Germany): Future 3D Additive Manufacturing, The 3DMM2O Conference 2022- flash oral presentation and poster presentation with the tile "Quantum-mechanical study of photoinitiators for 3D laser nanoprinting".

  Best Poster Award at Future 3D Additive Manufacturing - The 3DMM2O Conference 2022. The awards were presented by Conference chair Christine Selhuber-Unkel, Principal Investigator in 3DMM2O Cluster of Excellence.
- 19-20 April 2022 (Neustadt an der Weinstraße, Germany): 3DMM2O Winter Cluster Meeting - poster presentation with the tile "Quantum-mechanical study of photoinitiators for 3D laser nanoprinting"
- 10-11 October 2022 (Heidelberg, Germany) : 3DMM2O Summer Cluster Meeting - oral presentation with the tile "Quantum-mechanical study of photoinitiators for 3D laser nanoprinting" and two poster presentations with the title "Quantum mechanical study of photoinitiators for 3D laser nanoprinting" and "Quantum-mechanical study of organic molecules showing Thermally-Activated Delayed Fluorescence (TADF) properties"
- 12-16 March 2023 (Kloster Schöntal, Germany): Future 3D Additive Manufacturing, The 3DMM2O Conference 2023 - poster presentation with the title "In-depth investigation of the polymerization mechanisms for high resolution 3D printing"
- 18 April 2023 (online): Invitation for the oral presentation at the 3DMM2O "Challenges and Opportunities" - "Quantum-mechanical study of photoinitiators for 3D laser nanoprinting"

External conferences

Data reported in the thesis were presented at the following external conferences and seminars:

- 5 May 2021 (online): Virtual Center for Multiscale Theory and Computation (CMTC) Minisymposium "Quantum Embedding Methods" - poster presentation with the title "Multiphoton processes for direct laser writing"
- 19-23 September 2021 (online): 57th Symposium on Theoretical Chemistry, Würzburg, Germany - poster presentation with the title "Multiphoton processes for direct laser writing"
- 22-25 August 2022 (EPFL Lausanne, Switzerland): Psi-k-International Conference, SwissTech Convention Center - poster presentation with the title "Quantum-mechanical study of photoinitiators for 3D laser nanoprinting"

List of Figures

List of Tables

Acronyms

1PA one-photon absorption 2

2PA two-photon absorption 2

3D three-dimensional 1

3PA three-photon absorption 5

ACN acetonitrile 48

AH adiabatic Hessian 56

AO atomic orbital 14

AS adiabatic shift 58

BAPO phenylbis(2,4,6-trimethylbenzoyl)phosphine oxide 74

BBK (2E,6E)-2,6-bis(4-(dimethylamino)benzylidene)-4-methylcyclohexanone ii

BDE bond dissociation energy 53

BO Born-Oppenheimer 19

BPADA ethoxylated bisphenol A diacrylate 7

BSE Bethe-Salpeter equation 43

CC2 coupled cluster 50

CD contour deformation 50

cLR corrected linear response 50

COSMO conductor-like screening model 48

CPCM conductor-like polarizable continuum model 56

CT charge transfer 42

cw continuous wavelength 3

D3(BJ) Grimme's D3-dispersion correction with Becke-Johnson damping 49

DBA dibutylamine 6

DCM dichloromethane 49

DETC diethylamino-3-thenoylcoumarin ii

DFT density functional theory 30

DLW direct laser writing 1

DMSO dimethylsulfoxide 49

DPIHFP diphenyliodonium hexafluorophosphate 6

EA electron affinity 43

ECP effective core potential 39

EI external Iteration 51

ET electron transfer 5

evGW eigenvalue-only self-consistent GW 50

FC Franck-Condon 16

FGR Fermi golden rule 54

FOM figure-of-merit 7

FRP free radical polymerization 1

fs femtosecond 2

GGA generalized gradient approximation 37

GM Göppert-Mayer 23

GTOs Gaussian type orbitals 39

HAT hydrogen atom transfer 6

HF Hartree-Fock 30

HK Hohenberg-Kohn 31

HWHM half-width at half-maximum 49

IC Internal conversion 15

ICT intramolecular charge transfer 68

inter-HAT intermolecular hydrogen atom transfer 5

intra-HAT intramolecular hydrogen atom transfer 122

IP ionization potential 43

IRC intrinsic reaction coordinate 54

Irgacure 369 2-benzyl-2-N,N-dimethyl- amino-1-(4-morpholinophenyl)-1-butanone ii

Irgacure 651 2,2-dimethoxy-2-phenylacetophenone ii

ISC intersystem crossing 5

ITX isopropylthioxanthone 112

KS Kohn-Sham 31

LCAO linear combination of atomic orbitals 14

LCM linear coupling model 53

LDA local density approximation 37

LE local exciton 67

LR linear response 41

MNPT many-body perturbation theory 43

MO molecular orbital 14

MOMAP molecular materials property prediction package 54

MPA multiphoton absorption polymerization 2

NACME nonadiabatic coupling matrix elements 56

NLT nonlinear transmission 23

P product 78

PCM polarizable-continuum model 48

PES potential energy surface 12

PETA pentaerythritol triacrylate 5

PI photoinitiator 2

PIs photoinitiators 50

PMMA polymethyl methacrilate 5

QM quantum-mechanical 8

R reagent 78

RI resolution of identity 50

RISC reverse intersystem crossing 10

RPA random phase approximation 46

SCF self-consistent field 50

SCS spin-component scaled 96

SCS-ADC2 second order algebraic diagrammatic construction with spin-component scaled variant 50

SCS-CC2 spin-component scaled coupled cluster 50

SOC spin-orbit coupling 18

SOS scaled-opposite-spin 96

SOS-CC2 scaled-opposite-spin couple cluster 50

SS state-specific 51

STED stimulated emission depletion 3

STOs Slater type orbitals 38

TA triplet absorption 6

TD time-dependent 49

TD-DFT time-dependent density functional theory 39

TDA Tamm-Dancoff approximation 49

TI time independent 53

TICT twisted intramolecular charge transfer 93

TM transition moment 17

TPEF two-photon excited fluorescence 23

TPP two-photon polymerization 3

TS transition state 54

TTA triplet-triplet annhilation 10

TVCF thermal vibration correlation function 55

ZPVE zero-point energy correction 54

Contents

1 Introduction

1.1 3D direct laser writing based on two-photon polymerization

Beyond its conventional role as energy source, light plays a central role in advanced manufacturing through the groundbreaking technique of 3D printing [1, 2]. Here light is used as a sophisticated tool for manipulating the formation and properties of polymeric materials [3, 4]. In recent years, the global application and popularity of 3D printing technology have experienced significant growth. Among the various 3D printing techniques, three-dimensional (3D)-direct laser writing (DLW) based on two-photon free radical polymerization (FRP) has emerged as a leading contender, providing high resolution at the nano- and micro-scale with remarkable ease [5, 6, 7, 8, 9, 10, 11, 12].

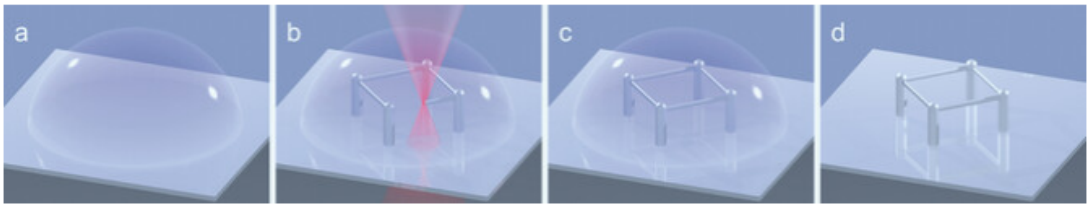

Figure 1.1: Key principle of 3D direct laser writing (DLW)in additive manufacturing: **a** Apply a liquid photoresist by dropcasting it onto a glass coverslip. **b** Focus a femtosecond pulsed laser into the liquid resist, inducing 2PA only in the focal volume, leading to spatially controlled cross-linking. **c** Move the laser focus through the photoresist to fabricate arbitrary 3D microstructures. **d** Rinse the solvent to remove non-cross-linked liquid resist. Scale of the graph is in meters. Readapted with permission from Ref.[5]. Copyright 2017 Springer Nature.

In two-photon FRP DLW a femtosecond (fs) laser beam is precisely focused into a photosensitive liquid material containing a mixture of monomeric matrix molecules and a photoinitiator (PI) (Figure 1.1**a**). By moving the laser focus through the liquid material in the three dimensions, this process enables the continuous, arbitrary formation of 3D materials (Fig. 1.1**b-c**) with a "pen of light". The remaining liquid is washed out using a solvent such as acetone (Fig. 1.1**d**). Thus, multiphoton absorption polymerization (MPA) i.e. two-photon absorption (2PA) is used to excite a tiny focal spot known as a voxel, 3D analogous of the 2D pixel, that is the only region with enough photon density to enable the simultaneous absorption of two-photon, achieving exceptional resolution. This distinguishes it from one-photon absorption (1PA) processes, which exhibit lower performance and resolution, as depicted in Figure 1.2. At the same time, the two-photon probability outside of the focus is low, suppressing accumulation effects in the periphery. The extent of local cross-linking is contingent on the accumulated absorbed dose. In the case of 1PA, the tails of the laser focus can aggregate across multiple exposures, significantly distorting the intended pattern (see Figure 1.2). For instance, a tail with 1% intensity relative to the focus maximum will accumulate to 100% when summed over 100 exposures. In stark contrast, 2PA results in an absorbed dose proportional to the square of the local intensity. Consequently, a 1% tail contribution will have a strength of $(0.01)^2 = 0.0001$ relative to the focus maximum. Summing this over the same 100 exposures results in an effective exposure for the tail area of a negligible 1%. Within the focus, the 2PA process initiates the photochemical cross-linking process, leading to the locally defined cross-linking of the matrix molecules.

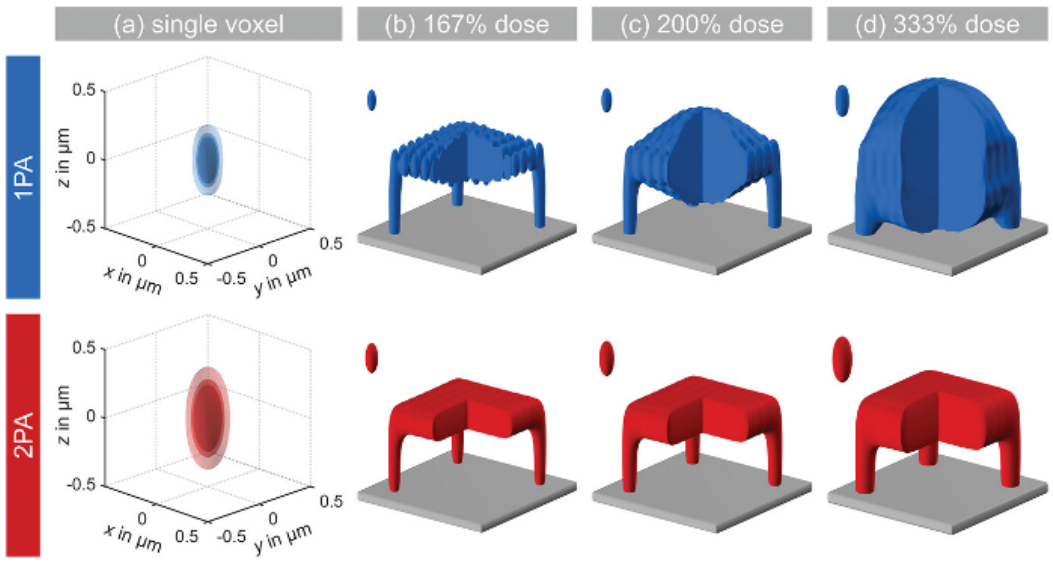

Figure 1.2: Illustration of 3D laser nanoprinting with a numerical aperture of NA = 1.4. In the first row, we consider one-photon absorption (1PA) at wavelength $\lambda 0/2$ = 400 nm with an exposure dose proportional to the intensity of light, Dexp $\propto$ I. In the second row, we consider two-photon absorption (2PA) at fundamental wavelength $\lambda 0$ = 800 nm with an exposure dose proportional to the squared intensity, Dexp $\propto$ I2. In column (a), we assume the photoresist threshold model and show resulting structures for single-voxel exposure doses of 167%, 200%, and 333%, displayed by three isosurfaces. At a single-voxel exposure dose defined by 100%, the peak of the dose profile of a single voxel is at the threshold and, hence, only a singular point results. In columns (b–d), we additionally assume the photoresist accumulation model and sum up sequential exposure doses as shown in column (a), aiming at 3D printing a table, composed of a plate and four legs. The in-plane voxel spacing used for the plate is 0.2 µm. The used single-voxel exposure doses are indicated at the top. Note the huge proximity effect for 1PA despite the smaller voxel size for 1PA. Copyright 2020 Springer Nature.

Although the notable advancements of two-photon polymerization (TPP) in the field of 3D laser nanoprinting, yet challenges persist, particularly concerning resolution and speed, addressed by several works [13, 14, 15, 16, 17]. One crucial limiting factor is the Abbe's diffraction limit of light [6, 18, 19, 20], according to which the smallest features distinguishable in an image are approximately half the wavelength of the light used. Consequently, the spatial resolution is restricted by diffraction, affecting the performance of the fabricated system. While the current smallest voxel size achieved is around 45 nm [20, 5, 21], more than ten times smaller than the wavelength of the laser used, it remains insufficient for manufacturing components such as the ones found in modern mobile phones [5]. Hence, there is a need to develop techniques that allow for further enhancement of the resolution of DLW [5]. One promising improvement is the concept of stimulated emission depletion (STED), introduced by Stefan Hell in 2014 [22, 23, 24]. STED relies on a straightforward concept where electrons are excited by a pulsed fs red laser source to a singlet excited state. Subsequently, a second continuous wavelength (cw) green laser source

with a characteristic "donut" shape, resulting in zero depletion in the center, deactivates the system back to the ground state through the stimulated emission of light [20, 5, 21, 25]. The superposition of these two laser wavelengths is crucial for achieving super-resolution, as the regions that are two-photon excited but not adequately depleted by the cw laser are the only ones leading to polymerization [5]. Therefore, STED enables the switching on and off of the radical generation mechanism using the depletion laser beam. However, it is important to note that, so far, only DETC has been reported to support photoinitiation at 810 nm and stimulated emission at 532 nm [26]. Additionally, absorption of the depletion laser starts to occur at large depletion laser powers, placing constraints on the accessible resolution [20]. Clearly, STED-inspired 3D laser printing is still in an early development stage, and further research is warranted.

Additional challenges for TPP lie in achieving finer features or smaller voxel sizes for enhanced spatial resolution, increasing manufacturing speed in terms of printed voxels per second, and exploring diverse materials and intricate multimaterial architectures. Today, printing rates are around 10^6 voxels s^{-1} [27]. Addressing this challenge involves grappling with the intricate dependence of photochemical properties on TPP printing sensitivity, as highlighted by Kiefer et al[28]. Boosting the printing rate signifies either utilizing higher laser power for the same photoresist or employing more sensitive photoresists [28]. Given the fact that lasers with very high optical power (i.e. higher than 3 W) cannot be sent through high-numerical-aperture microscope objective lenses without risking damage, having highly sensitive photoresists becomes imperative. Unfortunately, deciphering the photoinduced properties of common photoresists proves challenging based solely on their chemical composition and electronic structure in the ground state or the triplet state[29], from where radicals are supposed to be formed.

Another prominent issue for two-photon FRP is the occurrence of micro-explosions, initiated by observed increases in laser power beyond the polymer crosslinking threshold. These micro-explosions result in the undesired population of high-energy states [30] and are attributed to three- and four-photon absorption processes, as outlined in a pertinent study [31]. Typically, the laser power level at which micro-explosions occur is only slightly above the writing point [6]. However, the presence of small pollutants or microparticles in the photoresist can lead to micro-explosions even at the writing point. This can result in ineffective and time-consuming printing. Moreover, the cost and size of fs laser oscillators required for 2PA have prompted the exploration of alternative techniques that maintain the achieved resolution but with more cost-effective instruments. Despite progress in 3D laser nanoprinting and the emergence of new two-photon and two-step absorption photoresists (as explained below), a comprehensive understanding of the photophysical and photochemical processes, coupled with the characteristics of PIs during multiphoton polymerization, remains limited.

1.1.1 Two-photon absorption photoinitiators

Multiphoton photoinitiation involves intricate photophysical processes between the excited states of the PI that extend beyond conventional studies of the reactivity of photoactive molecules. In the standard process, PI molecules are excited through MPA from the ground state (S_0) to the first singlet excited state

(S_1). Subsequently, the first highly reactive triplet state (T_1) is reached via intersystem crossing (ISC)[32]. This excited state then should activate the radicals responsible for initiating the polymerization process, ultimately leading to the formation of a stable, cross-linked polymer network. The performance of PIs used in 3D laser nanoprinting depends on the radical generation mechanism, the reactivity of the formed radical, and the effectiveness of the $S_0 \rightarrow S_1$ transition, controlling the light absorbance characteristics of the PI molecules. Norrish type I and Norrish type II initiators, discovered by Norrish and colleagues in 1932 [33, 34], are commonly used in 3D printing [20, 18, 6, 35]. While both types of PIs exhibit light absorption, their radical generation mechanisms differ significantly, influencing their reactivity and selectivity. The former generates reactive radicals through a bond dissociation mechanism, specifically α or β-cleavage, depending on the breakable bond relative to the carbonyl [36, 37, 38]. On the other hand, the latter is known to generate reactive radicals through a "bimolecular" reaction. This reaction involves the T_1 state of the PI and another molecule, termed a co-initiator, triggering an intermolecular hydrogen atom transfer (inter-HAT) [39, 40] or electron transfer (ET) [39, 41] reaction with the preceding PI. This process generates radicals on both the PI and the co-initiator, where only the latter initiates polymerization. For a comprehensive description of PIs properties, refer to Section 2.3.3.

Among the highly effective PIs within the Norrish type I group, successfully employed in MPA, are Irgacure 369 and Irgacure 651 [6, 42]. Irgacure 369, when coupled with the free radical cross-linked pentaerythritol triacrylate (PETA) monomer (2 wt%), exhibits a distinctive fragmentation mechanism where the α-cleavage reaction occurs upon the absorption of two photons at ~800 nm wavelength. This process leads to the formation of benzoyl and alkylamino radicals via the first triplet state [43]. A parallel mechanism is observed for Irgacure 651 combined with polymethyl methacrilate (PMMA) (5 wt%), resulting in the α-cleavage of the carbonyl compound and the generation of benzoyl and dimethoxybenzyl radicals at shorter wavelengths [44].

Among the most responsive photoresists ever utilized in 3D laser nanoprinting are those combining the PETA monomer with DETC and BBK as Norrish type II PIs[28, 45, 6]. DETC demonstrates noteworthy printing efficiency, even in formulations with 0.25 and 0.50 wt% of the initiator, while BBK, discovered later, surpasses DETC in terms of printing sensitivity, likely owing to its higher solubility in PETA (0.70 wt%)[28]. Other PIs, specifically Norrish type I, may exhibit similar efficiency in 3D laser nanoprinting as DETC and BBK, but at significantly higher concentrations, for example, Irgacure 369 at 2%[18, 28, 26]. Achieving higher concentrations of DETC is challenging due to its limited solubility in PETA. As members of the ketocoumarines class, DETC and BBK behave as Norrish Type II PIs and, for photoresists with co-initiators, exhibit N=2 photon absorption dependence (where N is the number of photon) using 800 nm fs laser pulses, meaning that two-photon are needed to activate the radical formation reaction. Additionally, the initiation of polymerization in 3D laser nanoprinting for photoresists characterized by DETC and BBK with PETA monomer has been reported to occur in the absence of a co-initiator. In such cases, a remarkably effective nonlinear behavior of a third-order process is observed for both PIs in combination with the same monomer, meaning that three-photon, instead of the commonly reported two, are needed to start the polymerization. The unique three-photon absorption (3PA) exhibited by DETC was detected firstly by Yang et al.[46] using the "reciprocity law" for N-photon

absorption, where radicals form upon the simultaneous absorption of three photons. Norrish type I PIs (e.g. Irgacure 369) consistently exhibit the expected N = 2 non-linearity for two-photon PIs. The three-photon-based mechanism is reported to be characterized by a singlet-singlet transition to S_1 induced by 2PA, followed by triplet absorption (TA) of the third photon from the T_1 state to reach high triplet states [20]. Experimental measurements on various DETC combinations with co-initiators, namely dibutylamine (DBA) and diphenyliodonium hexafluorophosphate (DPIHFP), reveal that the anticipated N=2 photon dependence is observed when DETC is combined with DPIHFP (Fig.1.3**a**). However, in the case of pure DETC and the resist system incorporating DETC and DBA, the scaling factor remains at N=3 (Fig.1.3**b**).

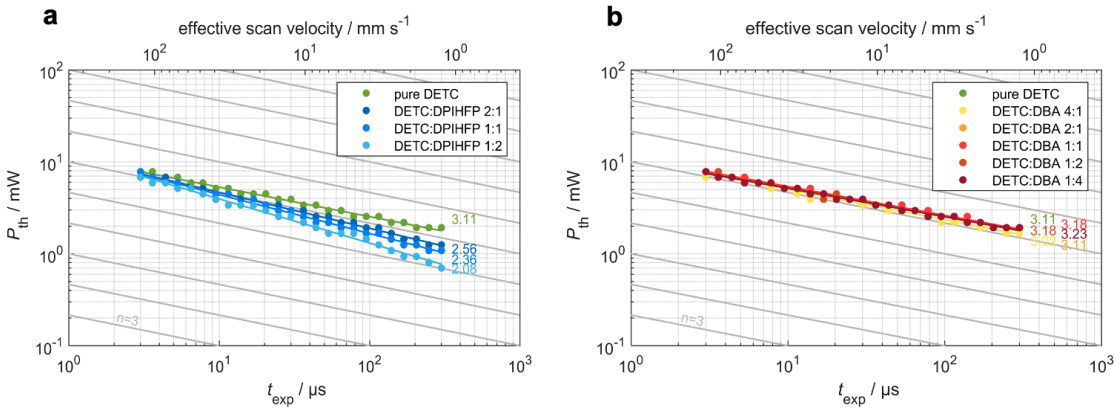

Figure 1.3: Measured threshold laser power versus exposure time on a double-logarithmic scale for resist systems with only DETC as initiator as well as resist systems with DETC and additionally **a** onium salt DPIHFP and **b** amine-based DBA co-initiators in varying ratios. The slopes of the fits indicate the nonlinearity of the resist system. The gray lines are guides to the eye with a slope of N=3 as expected for the DETC system. **a** With increasing concentration of DPIHFP, the nonlinearity changes from N=3 to N=2. **b** Independently on the concentration of DBA, the nonlinearity stays at N=3.

Remarkably, variations in the concentration of DBA as a co-initiator do not result in changes in the scaling behavior. The mechanism governing radical generation between DETC and DPIHFP is characterized by an ET process, initiating 2PA-induced polymerization. This mechanism implies that the formation of the diaryliodine radical occurs from the interaction between the photoexcited sensitizer and the iodonium cation, initiating in the lowest triplet state. In this context, two photons are adequate to activate radical formation. Conversely, the radical generation mechanism involving the hydrogen atom transfer (HAT) reaction between DBA and DETC proceeds through an inter-HAT reaction. Since the scaling factor remains at N∼3 in this case, it suggests that the radical generation channel, involving 2PA followed by TA from T_1 and resulting in highly reactive DETC triplet states, is more likely to occur. The mechanism starting from the first triplet state, which would require a deviation in the scaling behavior from N∼3 to N∼2, is impeded and does not manifest in the DETC-DBA resist system. This could be attributed to the influence of diffusion-modulated reactions, particularly prominent in high-viscosity resins. A similar scenario characterizes the polymerization activation mechanism in pure PETA, where

a third-order scaling behavior is also observed. In this instance, the TA process starting from T_1, leading to high triplet states, is responsible for generating reactive radicals that cannot be formed in the T_1 state.

The three-photon-based mechanism of BBK was first reported by Kiefer et al. [28] (see Fig. 1.4). The authors plotted the threshold laser power P_{th} (logarithmic scale) for various multiphoton photoresist systems versus the focus scanning velocity v (logarithmic scale), revealing that the effective nonlinear behavior of BBK in ethoxylated bisphenol A diacrylate (BPADA), akin to DETC in PETA, is not a second-order process.

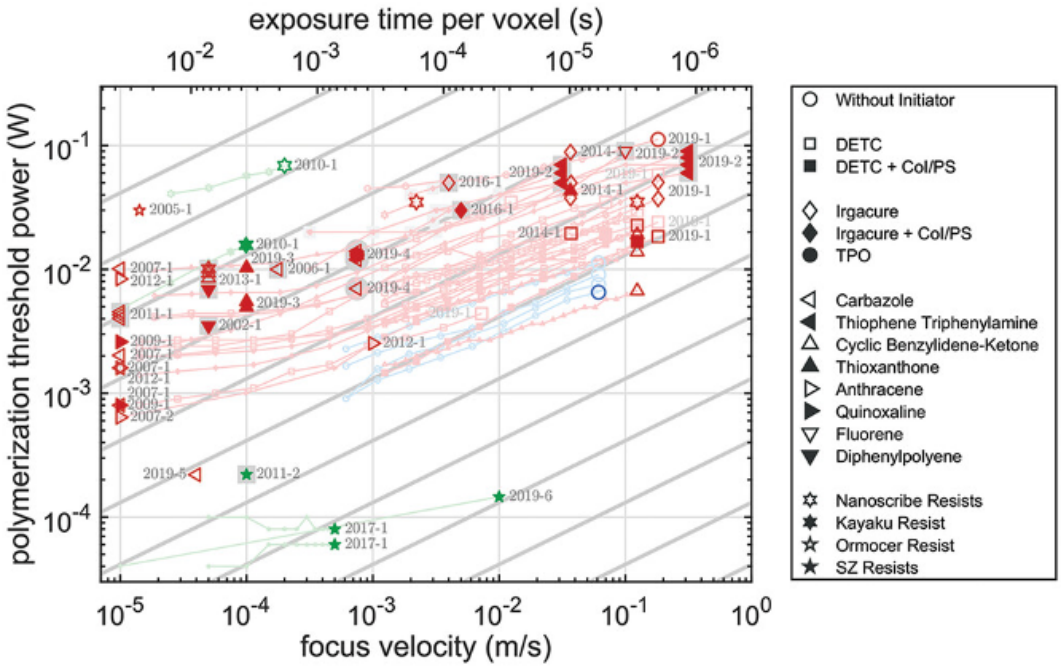

Figure 1.4: The threshold laser power P_{th} (logarithmic scale) for various multiphoton photoresist systems is plotted versus the focus scanning velocity v (logarithmic scale). The upper horizontal scale provides the effective exposure time texp (for a voxel size of 364 nm, corresponding to λ_0= 800 nm exposure wavelength) that is equivalent to v. The color of the symbols roughly indicates the exposure wavelength. The various symbol types are explained in the legend. For simplicity, only the photoinitator classes have been indicated except for last group (star symbols) where the names of the commercially available photoresist are given. For the data points indicated by the gray background, no threshold power is available and we have instead taken a typical 3D printing power. Hence, these points have to be taken with some caution. Data points with bright colors indicate measurements of the same photoinitiator but different monomer. Small data points connected by lines indicate measurements of the same photoresist but varying focus velocity. Measurements without labels have been performed by us. The parallel gray straight lines with a slope of 1/2 correspond to the scaling $P_{th} \propto v$. Adapted with permission from Ref. [28].

In their analysis of more than 70 different photoresists, they employed the dimensionless quantity called the figure-of-merit (FOM) for effective multiphoton sensitivity comparison. The larger the FOM,

the more sensitive the photoresist system. While the FOM of Norrish type I PIs, such as Irgacure 369 in PETA (2.00 wt%), is 56.1 at the focus velocity $v = 18.2$ cm s^{-1}, it increases to 229 and 905 at effective focus velocities of $v = 18.2$ and 12.4 cm s^{-1} for DETC (0.25 wt%) and BBK (0.70 wt%) in PETA, respectively. The latter represents the largest FOM reported at large focus velocities to date.

Moreover, both DETC and BBK exhibited depletion at the absorption wavelength when a cw laser was introduced alongside the fs laser[45]. Specifically, in the case of BBK, various studies using a 400 nm cw laser in combination with a second cw laser at either 640 nm or 532 nm revealed a decrease in the printing threshold[45]. In the former scenario, BBK behaves as a two-step-two-colors PI, while in the latter, it becomes evident that the 532 nm second laser does not leverage the STED mechanism, contrary to what was reported for DETC[5, 20, 18, 26].

Despite numerous studies conducted over the years, particularly on DETC, which was discovered earlier than BBK, the comprehension of the distinct N-photon absorption and radical formation mechanisms with the utilization of these and similar PIs (i.e., BBK) has remained elusive. This lack of understanding has constrained further optimization and the design of initiators for efficient 3D laser nanoprinting. Therefore, the primary focus of the current dissertation is to conduct detailed investigations, employing quantum-mechanical (QM) calculations, into the photophysical properties and electronic structure of these PIs, alongside their radical formation reaction mechanisms and subsequent polymerization. The aim is to provide a more complete understanding of their exceptional efficiency and unique mechanisms. Additionally, a comprehensive analysis of Norrish type I PIs, such as Irgacure 651 and Irgacure 369, is presented to highlight similarities and differences. This information serves as a foundational knowledge base for the further development of PIs for high-efficient and high-speed 3D laser printing techniques.

1.2 Two-step absorption photoinitiators

The two-step absorption technique for 3D laser nanoprinting, stands out as one of the best alternatives to 2PA [31]. The fundamental concept of two-step absorption involves replacing the virtual state of 2PA with a real state possessing a much longer lifetime, as depicted in Figure 1.5. This substitution allows the 2PA process to be replaced by two subsequent 1PA processes. The advantages of employing two-step absorption over 2PA include an increase in the efficiency of populating the excited state, determined by the ratio of real state lifetime to virtual state lifetime [31]. This ratio is higher with two-step absorption. Additionally, under suitable conditions, two-step absorption exhibits the same quadratic optical nonlinearity as 2PA but only requires inexpensive compact low-power CW blue laser diodes instead of fs laser systems in the red spectral region [31]. However, in the two-step absorption process, there is a risk that the polymerization reaction could initiate from the intermediate state. It is crucial to suppress such initiation because this process would correspond to polymerization by ordinary one-photon absorption.

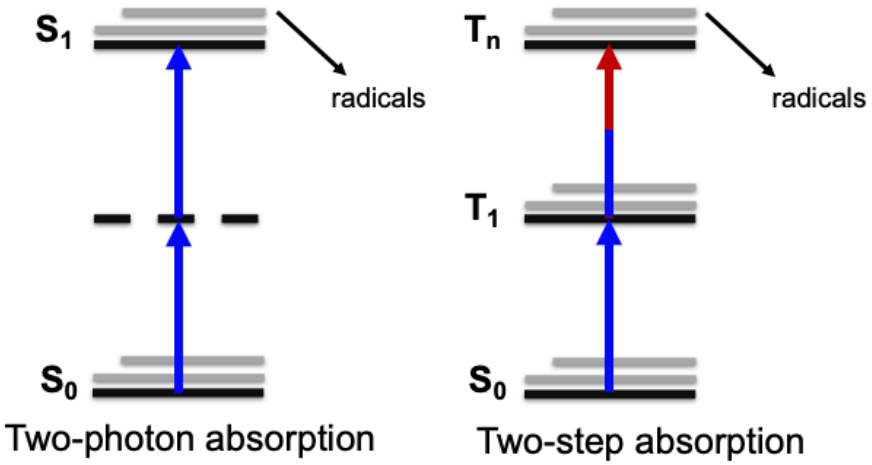

Figure 1.5: Schematic representation of a two-photon absorption (2PA) process (left) where the excitation from the ground state S_0 to the first singlet excited state S_1 pass through a virtual state (dashed line) and, upon intersystem crossing (ISC) to the triplet manifold, leads to the radical formation and a two-step absorption process (right) where the virtual state is substituted with a real state, specifically T_1. Upon absorption from S_0 to a higher singlet state and ISC to the triplet, the second absorption happens which leads to the formation of radicals. The second step can be characterized by a different wavelength that the first one (red-blue arrow).

The mechanism of radical formation for an effective two-step absorption PI, as illustrated in Figure 1.6, involves the absorption from S_0 to a higher singlet state in the first step. Subsequent ISC leads to the formation of T_1. In the second step, the molecules are excited to from the latter to higher triplet states through a second 1PA step, where bond dissociation and radical formation occur. Notably, the real state of T_1 replaces the virtual state of 2PA[31]. Hence, it is crucial to employ PIs with excellent singlet and triplet one-photon absorption characteristics. Additionally, the radicals should not be generated in T_1, as this would initiate polymerization through a standard 1PA process, making Norrish type I class of PIs unsuitable. PIs capable of generating radicals in high triplet states are essential.

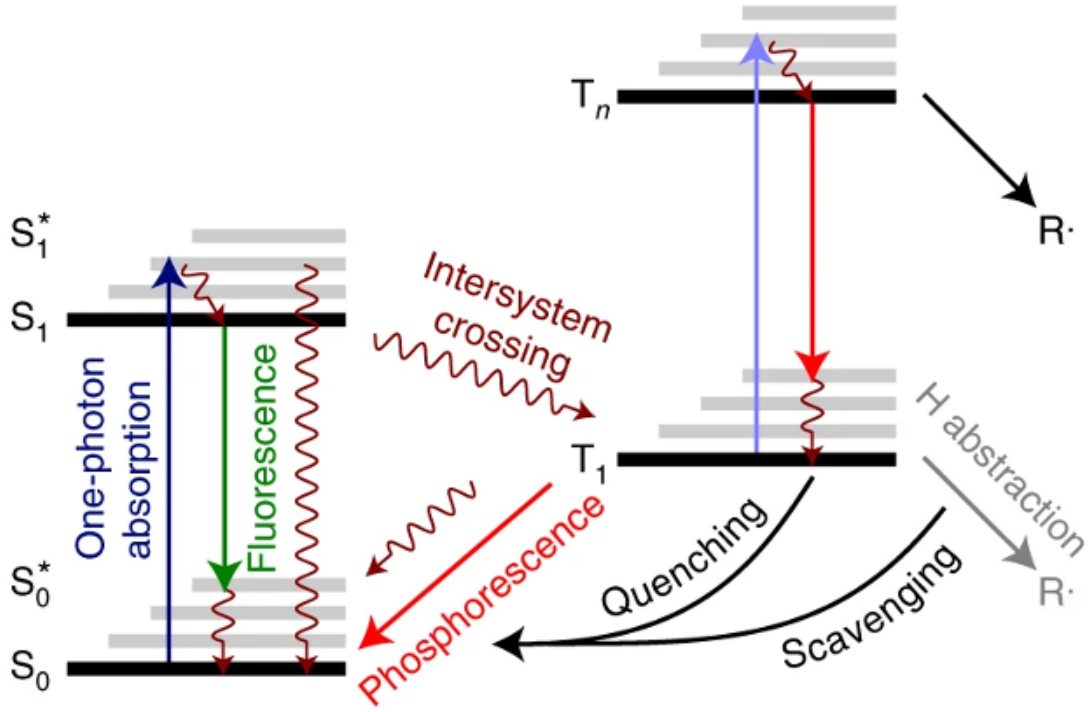

Figure 1.6: The Jablonski diagram for two-step absorption PIs, as outlined in the research by Flamigni et al.[47], unveils a sequential process. PIs undergo optical excitation, for example, by blue light, transitioning from the ground-state S_0 to higher singlet states. These higher singlet states rapidly decay to the lowest singlet state, S_1, due to their inherent high instability. Subsequently, molecules undergo ISC to the triplet manifold with an almost complete quantum yield [48]. In the triplet-state T_1 thus obtained, further excitation to higher triplet-states T_n [49] occurs with a second step of light absorption. In this state, the energy barrier for reaction cleavage becomes sufficiently low, allowing for bond dissociation and the formation of radicals. However, several reactions can also take place from T_1, such as triplet-triplet annhilation (TTA), reverse intersystem crossing (RISC), quenching, phosphorescence, or hydrogen abstraction. The latter, in particular, could lead to polymerization activated by one-photon absorption [50, 31]. Therefore, it is imperative to actively inhibit this reaction. Readapted with permission from Ref. [27]. Copyright 2022 Springer Nature.

In Bojanowski et al. [51], 22 potential candidates for 3D laser printing based on two-step absorption were investigated (see Figure 1.7). Generally, the PIs employed in two-step absorption are derivatives of ketones containing a carbonyl group [31, 51]. While the S_1 and T_1 states of ketones and derivatives have $n\pi^*$-character, excited triplet state can have $\pi\pi^*$ or mixed $n\pi^*$–$\pi\pi^*$ character [52]. The reaction cleavage of these PIs involve mostly the breaking of the C-C bond next to the C=O bonds and , on the contrary to Norrish type I PIs, where the dissociation happens in T_1 [32], here it takes place in higher triplet states [53, 54, 55]. For this reason, these PIs are called "reluctant" Norrish type I and specifically, their triplet ground-state energy is too low compared to the bond dissociation energy [53] and therefore the cleavage does not occur in T_1 [53, 31]. Interestingly, similarly to Norrish type II initiators, a common

and well-known reaction of ketones [32, 50] is to trigger the polymerization reaction from the first long living triplet-state abstracting hydrogen atoms from nearby susceptible groups [53, 55]. As reported above, it is of primary importance to suppress such a possible trigger, generally through the involvement of scavengers like TEMPO [31, 56, 57], that can shorten the lifetime of T_1 of the PI [58, 59].

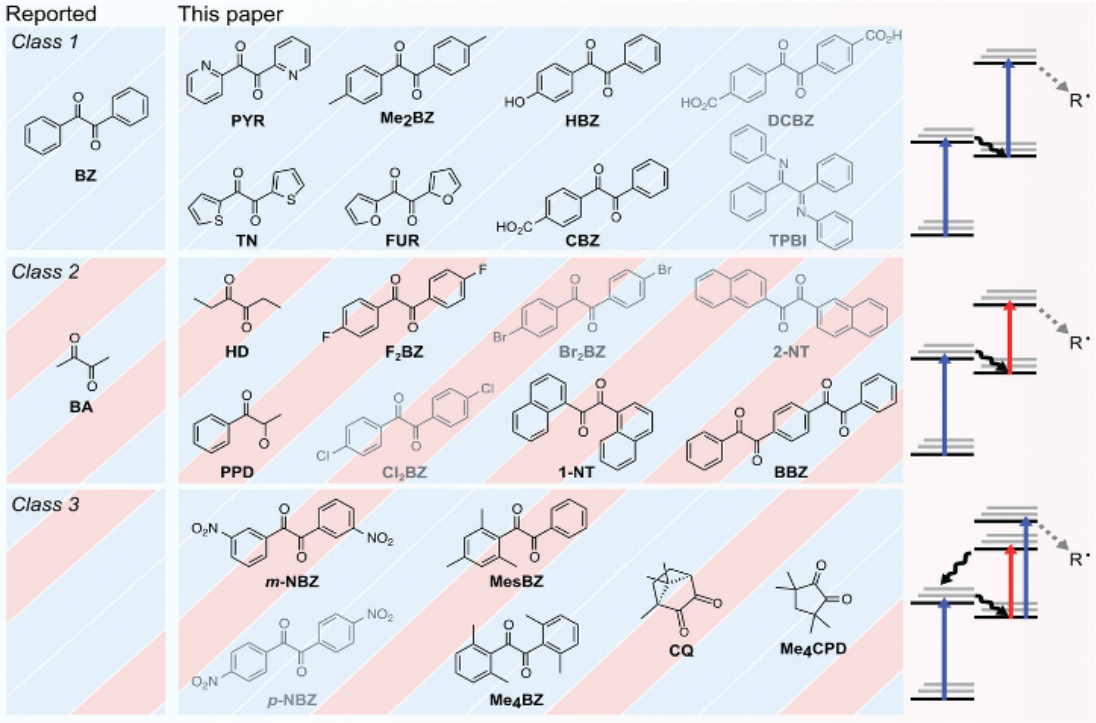

Figure 1.7: Diketone compounds serving as two-step absorption PIs scrutinized in Ref.[51]. These compounds were categorized into three classes: one-color two-step absorption, two-color two-step absorption, and one-color two-step absorption combined with a depletion process. The characterization experiments utilized laser wavelengths, with blue denoting 405 nm and red representing 640 nm. Energy-level diagrams were employed to illustrate one-color two-step absorption, two-color two-step absorption, and one-color two-step absorption combined with a depletion mechanism. Initiators marked in grey either exhibited insolubility or demonstrated no reaction to light at 405 nm. This adaptation is done with permission from Ref.[51], Copyright 2022 Springer Nature.

In their exploration of potential candidates for two-step absorption, Bojanowski et al. [51] employed two different laser wavelengths, specifically at 405 nm and 640 nm. The two-step absorption PIs were categorized into three classes based on the wavelength of the laser used for the first-step absorption, transitioning from the ground state to the first singlet excited state, and for the second-step absorption from T_1 to high triplet states (see Figure 1.7. In the first class, referred to as one-color two-step absorption PIs, a laser with a wavelength of 405 nm was utilized for both steps. For the second class, known as two-color two-step absorption PIs, the first step involved the same 405 nm laser as in the first class, while the second step employed a 640 nm laser. The third class represents a combination of the previous

two. In the second step of this class, the 405 nm laser brings the molecule to a high triplet state, leading to radical generation, while the 640 nm laser transitions the system from the high triplet state back to the singlet manifold, resulting in the depletion of the printing process.

Drawing upon this robust experimental knowledge and aiming for a deeper understanding of the chemistry and physics underlying radical generation mechanisms, several PIs were selected from the candidates and further analyzed through QM calculations. Specifically, benzil (**BZ** in Figure 1.7) for the first class, biacetyl (**BA** in Figure 1.7) for the second, and tetramethylbenzil (**Me4BZ** in Figure 1.7) for the third. The calculations, detailed in Chapter 7, aimed to unveil the mechanisms of radical generation and enhance the design of more efficient PIs for two-step absorption.

Outline of the thesis

The doctoral dissertation comprises eight Chapters, each dedicated to a specific aspect of the conducted research. Chapter 1 serves as an introduction to the research topic, providing an overview of the systems under analysis and establishing foundational concepts essential for understanding the subject. In Chapter 2, the fundamentals of light-induced processes are explored, with a particular focus on photochemical electronic transitions, potential energy surface (PES)s and on the (multi)photon absorption properties of PIs in FRP for 3D laser nanoprinting. A comprehensive theoretical and mathematical description of the applied computational methods is detailed in Chapter 3, while Chapter 4 outlines the computational details employed in achieving the results reported in the subsequent parts of the thesis. Chapters 5 and Chapter 6 delve into the results and discussions of the investigation of 2PA PIs, specifically Irgacure 651 and Irgacure 369 as Norrish type I and DETC and BBK as Norrish type II, reported in Chapter 5 and Chapter 6, respectively. Chapter 7 presents the quntum-mechanical analysis of benzil, biacetyl and tetramethylbenzil as candidates for two-step absorption, thoroughly explaining the conducted calculations and their subsequent outcomes. The conclusive findings and outlook of the research are summarized in Chapter 8. Additionally, the preface sections provide information on published scientific articles related to the work presented in the dissertation as well as articles published or submitted but nor related to the thesis. The participation in conferences, where the results reported in the thesis were presented, is also reported.

2

Theory and background

The current chapter presents a comprehensive review of the theoretical background necessary to furnish the reader with the essential information that serves as the foundation for the scientific output presented in the thesis. The central focus is the examination of theoretical principles underpinning light-activated FRP.

2.1 The essence of light

Light is a form of electromagnetic radiation, and a fundamental component of the electromagnetic spectrum visible to the human eye [60]. It consists of packets of energy called photons, elementary massless particles which travel in wave-like patterns exhibiting both particle- and wave-like properties, defined as wave-particle duality [61]. From a wave perspective, electromagnetic radiation is characterized by wavelength (λ), frequency (ν) and velocity (c) related by the relationship:

$$\lambda \nu = c \tag{2.1}$$

where λ represents the wavelength of light, ν represents its frequency, and c denotes the speed of light in vacuum. This is a fundamental constant with an approximate value of 299792458 meters per second (ms). The wavelength of light determines its color or frequency. Visible light encompasses wavelengths ranging from about 400 nm to 700 nm, with shorter wavelengths corresponding to violet and longer wavelengths corresponding to red. However, the electromagnetic spectrum extends beyond the visible

range, encompassing shorter wavelengths (such as ultraviolet and X-rays) and longer wavelengths (such as infrared, microwaves, and radiowaves). From a foundational perspective, light provides humanity with the ability to visually perceive and comprehend the world granting the power to distinguish colors, shapes, and objects. Beyond its role in vision, light plays a fundamental part in numerous biological processes, such as photosynthesis, and light based technologies (i.e. optical fibres). Among all, the interaction between light and matter, along with the remarkable process of photoactivation, has had a profound impact on scientific exploration and technological breakthroughs. This thesis focuses on the photoactivated processes wherein light serves as a catalyst to initiate polymerization. This process involves the absorption of light by molecules which can induce the generation of highly reactive radicals responsible to activate the monomer through cross-linking reactions that lead to the formation of a 3D network structure.

2.2 Light induced processes

2.2.1 Electronic transitions

The movement of an electron between energy levels of an atom, molecule, or solid material is known as electronic transition [60]. These transitions occur when the electron absorbs or emits energy in the form of electromagnetic radiation, typically in the form of photons. In a molecule, electrons occupy specific energy levels associated with a distinct amount of energy, where electrons can transit by gaining or losing energy. When an electron absorbs energy upon the interaction of the molecule with photons of specific energies, it moves to a higher energy level, also defined as excited state. Conversely, when an electron in an excited state returns to a lower energy level, it can emit energy in the form of photons. This emission corresponds to the release of electromagnetic radiation, falling within the visible, ultraviolet, or infrared regions of the electromagnetic spectrum, depending on the specific electronic transition involved.

The electronic structure of molecules or solids is frequently described using the linear combination of atomic orbitals (LCAO)s approach. LCAOs involves combining the wavefunctions of atomic orbital (AO)s from individual atoms, which represent regions of space where the probability of finding an electron is high, to form molecular orbital (MO)s. These molecular orbitals represent the electronic states of the overall system, allowing for the determination of their spatial distribution and energy levels. The linear combination of atomic orbitals facilitates the description of bonding and antibonding interactions between atoms, providing valuable insights into the electronic structure and properties of the molecule [60, 36, 62]. This approach also enables predictions regarding the stability, reactivity, and spectroscopic properties of the molecule. A depiction of all possible electronic transitions for organic molecules can be found in Figure 2.1[60, 36, 63].

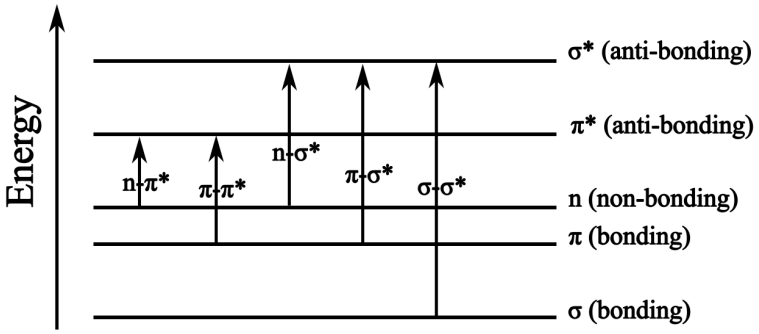

Figure 2.1: Schematic representation of the electronic transitions involving σ,π and n electrons

$\sigma \rightarrow \sigma^*$ **transition** The $\sigma \rightarrow \sigma^*$ transition consists in an excitation of an electron from a σ bonding orbital to a σ^* antibonding orbital along the internuclear axis. This transition requires high energy due to the strong σ bonds involved.

$\pi \rightarrow \pi^*$ **transition** Similarly, the $\pi \rightarrow \pi^*$ transition involves the excitation of an electron from a π orbital, generally belonging to conjugated compounds, such as those containing double bonds or aromatic rings, to an antibonding π^* orbital. This transition is exhibited by many organic chromophores and requires less energy than the $\sigma \rightarrow \sigma^*$ transition.

n $\rightarrow \sigma^*$ **transition and n** $\rightarrow \pi^*$ **transition** The n $\rightarrow \sigma^*$ and n $\rightarrow \pi^*$ transition involves the excitation of an electron from a non-bonding (n) orbital to a σ^* or π^* antibonding orbital, respectively. They commonly occur in compounds with lone pairs electrons (e.g. oxygen atom), such as amines and carbonyl compounds. The n $\rightarrow \pi^*$ transition requires less energy than n $\rightarrow \sigma^*$.

In this thesis, the most important transitions upon absorption of photon by the various PIs, will be thoroughly explained and characterized, in order to define the associated initiators properties.

2.2.2 Jablonski diagram

The deactivation process consequent to the absorption of a photon to a high-energy excited state, can lead, within a short period of time, to the ground state of the original molecule (photophysical process) or to the formation of other species (photochemical process) [60]. The positions of the electronic states as well as the activation and deactivation processes are molecule dependent and can be represented in a so-called Jablonski diagram (Figure 2.2). Such a diagram, named after the Polish physicist Aleksander Jabłoński, who introduced the concept in the 1930s, is characterized by thick horizontal lines that represent the electronic states of a molecule, with the ground state at the lowest level, while the excited states are depicted above the ground state [64, 65]. The vibrational states of each electronic state are depicted with thin lines, with the lowest one indicating the $\nu = 0$ level, while the rotational levels are not depicted. Moreover, processes such as absorption, fluorescence, phosphorescence, Internal conver-

sion (IC), ISC and RISC are represented by vertical arrows whose direction follows the direction of the process [60].

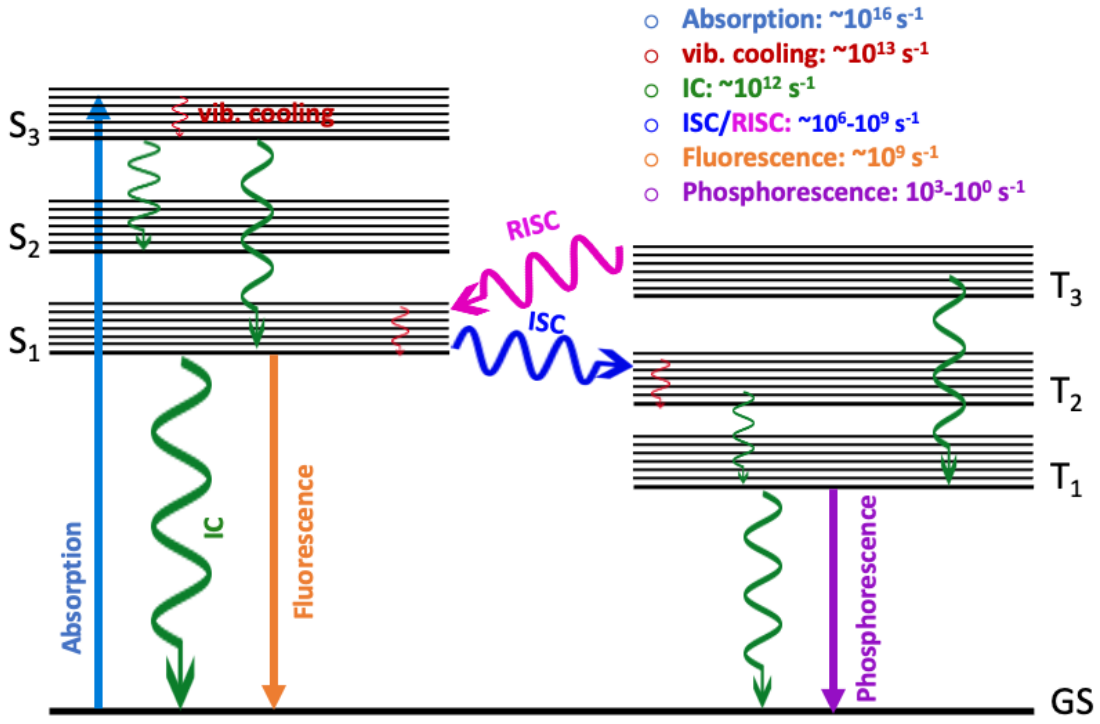

Figure 2.2: Jablonski diagram: the energies of the electronic states of a molecule such as ground state S_0 , excited singlets S_n, and triplets T_n are depicted by horizontal lines. The most important radiative (fluorescence and phosphorescence) and non-radiative (internal conversion (IC) and (reverse)intersystem crossing (R)ISC) processes are depicted by arrows.

The processes depicted in the Jablonski diagram that leads from the absorption to the final emission back to the ground state are:

- Absorption: upon absorption of a photon of light, the molecule is promoted from the vibrational ground state ($v = 0$) of the electronic ground state (S_0) to a certain vibrational level of an electronic excited state (S_n, $n \geq 1$). The transition takes place on the order of $\sim 10^{16}$ s^{-1}. The probability and intensity of the transition is determined by the overlap of the wavefunctions of the involved vibrational states, as showed by the Franck-Condon (FC) principle[66, 67], reported in Section 2.2.4).

- Fluorescence: relaxation process that involves the emission of light from an excited singlet state (usually S_1) back to the ground state. It is a radiative process on the order of $\sim 10^{9}$ s^{-1}. Thereby, as for most of the systems where the Kasha rule[68] is applied (see Section 2.2.3), the transition takes place from the vibrational ground state ($v = 0$) of the first excited singlet electronic state S_1 to one of the vibrational levels of the ground state S_0. However there are some exceptions, such as azulene and its derivatives, which possess an exceptionally large S_2-S_1 energy gap (14

000 cm^{-1} for azulene [69]) that leads to a very low S_2-S_1 IC rate (7x10^8 s^{-1} [60]) and therefore the S_2-S_0 fluorescence can be observed. Again, the most probable transition occur between electronic states with the highest overlap of the vibrational wavefunction (see Section 2.2.4).

- Phosphorescence: radiative relaxation process which occurs from the vibrational ground state ν=0 of the first electronic triplet state T_1 to one of the vibrational level of the S_0. Due to the spin forbidden transition (Section 2.2.3), the lifetime of the triplet state is generally much longer than the one of a singlet state and subsequently the rate of the process lies generally in the range $\sim10^3$-10^0 s^{-1}.

- IC: non-radiative process where the molecule undergoes a transition between different vibrational (or rotational) levels within the same electronic state. Therefore this is a very fast process that takes place between $\sim10^{12}$ s^{-1}. Furthermore, due to the spin selection rules (section 2.2.3) internal conversion takes place only between electronic level of the same spin multiplicity.

- ISC: spin forbidden (refer to Section 2.2.3) transition that occurs between different electronic states, such as from a singlet state to a triplet state or vice versa (RISC). The time scale of the process is $\sim10^6$-10^9 s^{-1}.

- Vibrational relaxation: vibrational cooling resulting in the emission of photons. When a molecule undergoes a radiative transition from an excited vibrational state to a lower vibrational state, it emits a photon, carrying away the excess energy. It is a very fast process that takes place in the order of $\sim10^{13}$ s^{-1}.

2.2.3 Selection rules in photochemistry

The study of chemical reactions initiated by light relies on the selection rules that govern the pathways and outcomes of light-induced processes and serve as fundamental principles for investigating the likelihood and nature of electronic excitation. The selection rules in photochemistry stem from the principles of quantum mechanics and symmetry considerations, outlining the criteria that determine the probability of electronic transitions between different energy levels of molecules upon absorption of photons [70, 71]. These rules apply to the separated integrals that contribute to the transition moment (TM), whose squared value is proportional to the probability of a given transition, appearing in the following:

$$TM = \int \phi_i \hat{\mu} \phi_f d\tau_r \int S_i S_f d\tau_S \int \theta_i \theta_f d\tau_N \tag{2.2}$$

The first term is called "the electronic transition moment", whose value depends on the symmetry and amount of spatial overlap of initial (ϕ_i) and final (ϕ_f) orbitals. The second term is called "the spin overlap integral" whose value depends on the initial (S_i) and final (S_f) spin states of the promoted electron. The third term is called the "integral overlap of the initial (θ_i) and final (θ_f) wavefunction for nuclear vibrations" and it is the quantum-mechanical basis of the FC principle (see Section 2.2.4). The

transition is said to be forbidden when the TM is zero, whereas when TM is not zero then the transition is said to be allowed [72]. In practice, since the TM is zero if any of the term is zero, forbidden transition can often be observed although with much less intensity than the allowed ones.

The symmetry selection rule

The symmetry selection rule, also called Laporte selection rule or orbital selection rule, is related to the first term of equation 2.2 and applies to molecules that have a center of symmetry (aka center of inversion, centrosymmetric). This rule forbids transitions between states with the same parity (symmetry) with respect to an inversion center (i). Parity is indicated on molecular orbitals and on term symbols with subscripts g (gerade, or even) and u (ungerade, or uneven). Transitions between u and g terms are allowed but those between two g or two u terms are forbidden. It forbids transitions within one type of orbital subshell. For example, p orbitals are antisymmetric with respect to i, while both s and d orbitals are symmetric with respect to i. This rule forbids s $\rightarrow$ s, p $\rightarrow$ p, d $\rightarrow$ d, and d $\rightarrow$ s transitions, but allows transition between d $\rightarrow$ p and d $\rightarrow$ s orbitals.

The spin selection rule

The spin selection rule states that transitions between electronic states with different spin multiplicities (such as singlet and triplet states) are forbidden or less likely to occur due to the orthogonality of the spin wavefunctions that leads to the vanishing of $\int S_i S_f d\tau_S$[60], the second term of equation 2.2. For instance, when a molecule is in a singlet (or triplet) electronic state the total spin S is 0 (or 1), and it undergoes a photochemical transition to another singlet (or triplet) state, the total spin S remains 0 (or 1). In a singlet-triplet transition this does not occur. Therefore, singlet $\rightarrow$ singlet and triplet $\rightarrow$ triplet transitions are spin allowed ($\int S_i S_f d\tau_S = 1$) whereas singlet $\rightarrow$ triplet or triplet $\rightarrow$ singlet transitions are spin forbidden ($\int S_i S_f d\tau_S = 0$). However spin-orbit coupling (SOC), which describes the interaction between the spin of an electron and its orbital motion around the nucleus, enables spin-forbidden transitions to occur. The strength of this coupling determines the rate at which the system can transition between singlet and triplet states. This perturbation increases as the fourth power of the atomic number of the atoms involved and consequently, stronger SOC are especially present in systems characterized by heavy atoms, leads to more efficient ISC [73]. In this scenario operates the El-Sayed rule [74, 75] (see Equation 2.3), which provides insights into the factors that influence the rate of ISC and predicts the probability of these transitions. This rule states that the rate of ISC, e.g. from the lowest singlet state to the triplet manifold, is relatively large if the radiationless transition involves a change of molecular orbital type because the SOC between the electronic states involved is allowed [60, 74, 76]. For example, a (π,π^*) singlet could transition to a (n,π^*) triplet state, but not to a (π,π^*) triplet state and vice versa.

$$^1(n,\pi^*) \longleftrightarrow {}^3(\pi,\pi^*) \text{ and } {}^3(n,\pi^*) \longleftrightarrow {}^1(\pi,\pi^*) \text{ allowed}$$
$$^1(n,\pi^*) \longleftrightarrow {}^3(n,\pi^*) \text{ and } {}^3(\pi,\pi^*) \longleftrightarrow {}^1(\pi,\pi^*) \text{ forbidden}$$

Even the forbidden process, however, can occur due to vibronic coupling. In fact, when the orbital matrix element in the Fermi golden rule is zero, the vibronic matrix element will be small but not zero. Molecular symmetry plays a role in the El-Sayed rule as well [76]: transitions with different symmetry between the singlet and triplet states are more likely to exhibit efficient ISC, according to Laporte's rule. The Kasha rule, named after its proposer Michael Kasha [68], is another important principle in photochemistry that describes the outcome of electronic transitions in molecules within the spin selection rule. Specifically, the Kasha rule states that upon absorption of light energy, a molecule undergoing an electronic transition will predominantly emit fluorescence from the lowest excited singlet state (S_1) rather than from higher excited singlet states. However, exception of this rule exist and are already studied [69]: azulene whose fluorescence emission from the S_2 state occurs at longer wavelengths than the absorption, contrary to the behavior expected based on the Kasha rule. It is important to note that selection rules are not absolute prohibitions but provide guidelines for the likelihood of electronic transitions. In some cases, other factors such as vibronic coupling, solvent effects, SOC or non-adiabatic processes can influence the occurrence of transitions that would be otherwise forbidden.

2.2.4 The Franck-Condon principle

The FC principle, named after the physicists James Franck and Edward Condon, who formulated it in the 1920, is a fundamental concept in molecular spectroscopy that describes the electronic transitions of molecules [66, 77, 78]. The principle states that during an electronic transition in a molecule, such as absorption or emission of light, the nuclear configuration changes much more slowly compared to the electronic transition itself [79, 80]. In other words, the positions of the atomic nuclei remain almost unchanged during the electronic transition since the latter happens on a much faster timescale than the nuclear motion (electronic transitions occur on the order of fs (10^{-15} s), while the nuclear motion occurs on the order of ps (10^{-12} s) or longer). This approximation is more restrictive than the Born-Oppenheimer (BO) approximation, according to which nuclear and electronic motions can be separated (as further discussed in Section 3.1.3). Vibronic transitions where the energy spacing decreases with increasing vibrational energy. Electronic transitions to and from the lowest vibrational states are often referred to as 0–0 (zero-zero) transitions (ν_{0-0}) and have the same energy in both absorption and fluorescence. The overlap between the wavefunctions of the initial and final electronic states affects the intensity of the spectral lines in the resulting spectrum: the stronger the overlap, the higher the intensity of the spectral line.

The intensity of a vibrational transition is quantified by the square of the overlap integral of the vibrational wavefunctions associated with two electronic states. This set of electronic transitions, along with their respective probabilities (intensity), constitutes a spectrum.

In practical terms, the FC principle helps explain the shape and intensity distribution of electronic absorption and emission spectra of molecules. It provides insights into the vibrational and rotational structures observed in these spectra, allowing the interpretation and analysis of data related to molecular electronic transitions.

2.2.5 Photochemical reactions on potential energy surfaces

The PES is used to represent the electronic state of a molecule, where the energy of the system varies as the nuclear coordinates change. In the framework of the BO approximation, these surfaces are known as adiabatic potential energy surfaces, indicated by the blue and red curves in Figure 2.3, where no crossing of the boundaries is observed. The PESs typically exhibit minima and maxima at different nuclear coordinates for various excited states and, as a result, the surfaces of two distinct electronic states can be widely separated or come close together, even intersecting at specific nuclear coordinates[60]. However, crossings can only occur between states that do not interact, such as those with different multiplicity, otherwise, the crossing is avoided. A surface in which actual intersections are present instead of avoided crossings is defined *diabatic* surface. If the nuclei move slowly, they tend to follow a single adiabatic energy surface, even in the region of an avoided crossing, while, if they have sufficient velocity, the BO approximation breaks down, and the nuclei may effectively disregard the gap in the avoided crossing, transitioning directly to the other adiabatic surface. The breakdown of the BO approximation near an avoided crossing, caused by the so called Jahn-Teller distortion, gives rise to a *conical intersection*. At this point, the wavefunction becomes degenerate, allowing for a rapid transition between surfaces, a highly non-adiabatic process characterized by swift movement between PESs.

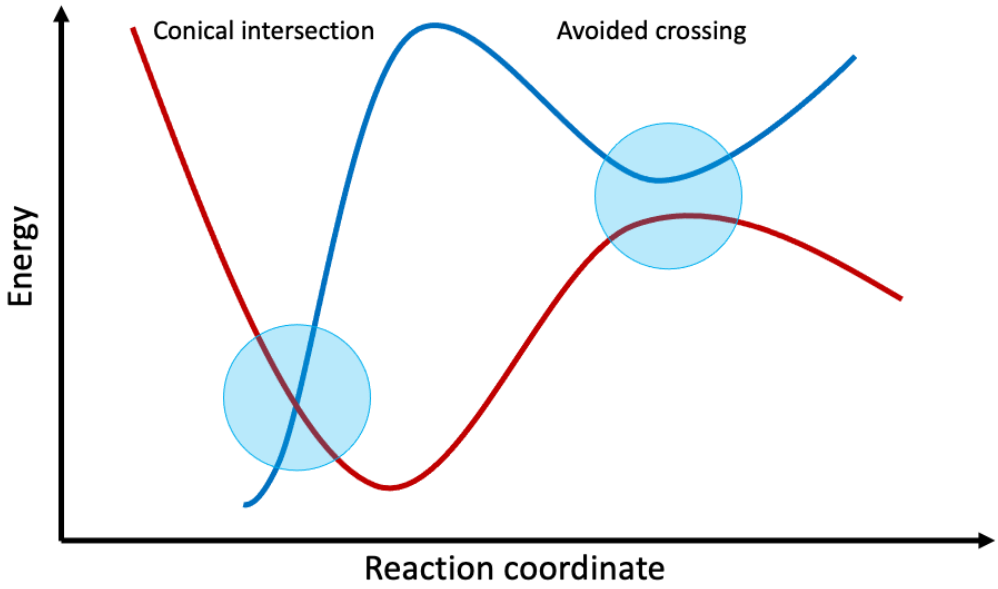

Figure 2.3: Example of conical intersection and avoided crossing. The horizontal plane represents the multi-dimensional configuration space of the molecule, while the vertical axis shows the electronic energy for each configuration. The two potential energy surfaces, drawn in blue and red, undergo a conical intersection (left side) and an avoided crossing (right side) when viewed along a molecular coordinate.

2.3 Multiphoton processes in 3D laser printing

In the realm of typical photochemical processes, a molecule undergoes the absorption of a single photon, leading to the emergence of an electronic excited state. However, when exposed to high light intensities, such as laser excitation, multiphoton processes can happen. Among these processes, 2PA assumes particular significance, especially in the context of achieving high resolution in 3D printing, as thoroughly explained in Chapter 1. The inception of the concept of 2PA was discovered by Maria Göppert-Mayer in 1931 during her doctoral dissertation[81, 82]. Three decades after Kaiser and Garret[83, 84] proved the existence of 2PA from the experimental point of view. 2PA represents a nonlinear phenomenon in which a molecule simultaneously absorbs two photons, either of the same or different frequencies, and is excited from the ground state to a higher energy electronic state. The energy difference between the two states involved in this process equals the sum of the energies of the two absorbed photons:

$$h\nu_1 + h\nu_2 = E \tag{2.3}$$

where h is the Planck constant, ν represents the frequency of the i-th absorbed photon, and E represents the transition energy. Diverging from single-photon absorption, the process of 2PA exhibits several significant distinctions (see Figure 2.4). 2PA is a nonlinear process, where the magnitude is directly proportional to the square of the light intensity, in stark contrast to 1PA, which follows a linear process closely tied to light intensity. In 2PA, two photons, each with half the energy and twice the wavelength, combine to provide the energy necessary for the transition. Unlike single-photon absorption, there is no requirement for an intermediate state to be populated prior to reaching the final state. Instead, the electron is excited to a virtual state enabled by the principles of quantum mechanics, diverging from two-step absorption where real intermediate levels come into play and are populated. In 2PA the virtual state becomes directly accessible once the molecules absorb the first photon.

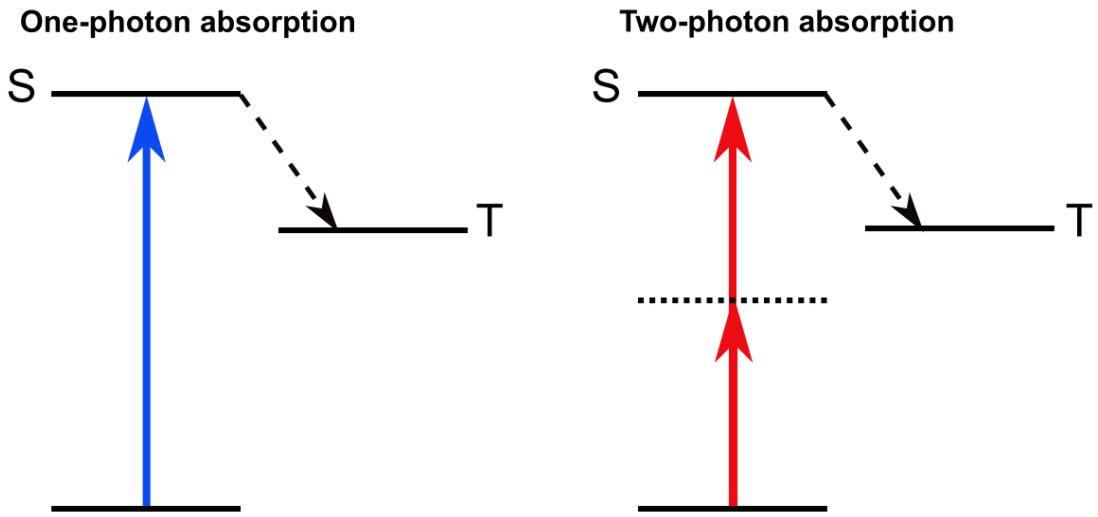

Figure 2.4: Schematic representation of two distinct processes: on the left, a one-photon absorption (1PA) process, where the transition from the ground state to the first excited state requires a single photon, followed by intersystem crossing (ISC) leading to the triplet manifold. On the right, a two-photon absorption (2PA) process is depicted, in which the excitation from the ground state to the first excited state necessitates two photons of the same energy. These photons traverse a virtual state (illustrated by a dashed line) and, upon intersystem crossing (ISC), result in the triplet manifold.

Moreover, as a third-order non-parametric process, the selection rules governing 2PA differ from those associated with 1PA, especially in centrosymmetric molecules. Single-photon transitions are exclusively allowed between states of different parity (ungerade ↔ gerade), whereas two-photon transitions can occur between states of the same parity (gerade ↔ gerade and ungerade ↔ ungerade). Since the ground level typically exhibits gerade parity, 2PA simplifies the exploration of excited gerade parity levels, which would pose challenges in conventional linear absorption spectroscopy. However, for non-centrosymmetric molecules, there is no formal mutual exclusion between the selection rules for 1PA and 2PA.

2.3.1 Methods for measuring two-photon absorption

For 2PA involving an incident plane wave of radiation, the correlation between light intensity and distance can be expressed by the equation:

$$I(x) = \frac{I_0}{1 + \beta x I_0} \tag{2.4}$$

Here, $I(x)$ represents the light intensity concerning the path length or cross-section x, where I_0 is the initial light intensity, and β serves as the 2PA coefficient or two-photon cross-section (often denoted as σ_{2PA}). This coefficient quantifies the likelihood of a 2PA event, indicating the probability of two photons being simultaneously absorbed within a specific volume or material. The molecular 2PA

cross-section is commonly denominated in units of Göppert-Mayer (GM), where 1 GM is equivalent to 10^{-50} $cm^4 s photon^{-1}$. These units result from the multiplication of two areas (each for one photon, both in cm^2) and a time (within which the two photons must arrive to act simultaneously).

Multiple techniques can be employed to measure two-photon absorption, including two-photon excited fluorescence (TPEF), z-scan, self-diffraction, and nonlinear transmission (NLT). TPEF involves detecting the emitted fluorescence resulting from 2PA events. Self-diffraction assesses changes in the diffraction pattern of a laser beam passing through a nonlinear medium, providing insights into 2PA. NLT involves measuring changes in transmitted intensity as a function of input intensity, offering valuable information about the nonlinear optical properties, including two-photon absorption, in a material. These techniques collectively contribute to a comprehensive understanding of the 2PA characteristics in various substances. The z-scan technique, the one will be mention in the thesis can measure the 2PA cross-section. This technique entails scanning a sample through the focus of a tightly focused laser beam while measuring the intensity of the transmitted or reflected light. In the z-scan setup, a pulsed laser beam is tightly focused onto the sample using a lens. The sample is then moved along the z-axis, which corresponds to the direction of laser beam propagation and, as the sample is scanned through the laser's focal spot, the intensity of the transmitted or reflected light is measured. By analyzing the measured light intensity as a function of the sample position, a z-scan curve is obtained. Typically, the curve is fitted to a theoretical model to determine the relevant 2PA-related parameters. The z-scan technique furnishes quantitative information about the 2PA properties of a material and can also offer insights into other nonlinear optical processes. However, it necessitates careful experimental setup, including precise control of the sample position and laser parameters, as well as accurate calibration of the detector. Finally, the analysis of z-scan data often entails numerical simulations or fitting to theoretical models to precisely determine the desired parameters.

2.3.2 Free radical polymerization in 3D printing

Light serves as an incredibly potent tool for manipulating the formation, structure, and properties of polymeric materials, providing unprecedented control and opening up a realm of possibilities. Light-activated FRP[85] is a chain-growth process that harnesses the energy of light and holds the remarkable capability to convert liquid monomers into solid polymers. The key element at the heart of these reactions is the PI, a critical player that, upon exposure to light, sets in motion a chain of events leading to the formation of highly reactive radicals species responsible in activating the monomer molecules, initiating the polymerization process, and ultimately yielding the desired polymer structure (see Figure 2.5).

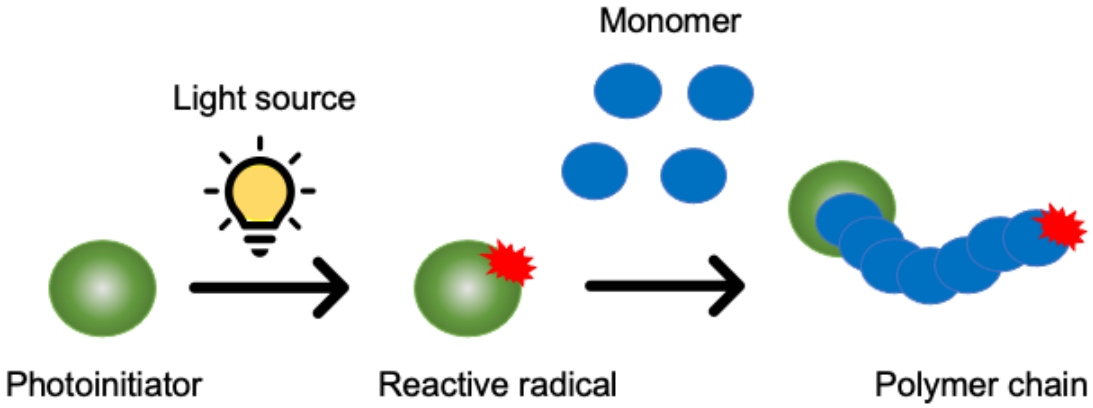

Figure 2.5: Schematic representation of the polymerization process upon light absorption operated by the PI with subsequent formation of reactive species. Newly generated radicals or ions are therefore responsible to activate the monomer and form the final polymer chains.

The core processes of FRP are constituted by four fundamental steps, each contributing to the creation of diverse polymer structures with tailored properties: initiation, propagation, termination and chain transfer, reported in Figure 2.6. The first stage is the absorption from the incident radiation[38] by the initiator i.e. PI with subsequent transfer of the energy of the photon to the electronic structure of the PI-molecule. The PI molecule generates highly reactive species i.e. radicals or ions that can either initiate the polymerization process[20, 18, 86, 87] or be quenched e.g. by oxygen[46]. The propagation step involves the reaction of the free radicals with the monomer molecules, activating them through the abstraction of a hydrogen atom. This results in the formation of a new radical at the monomer's active site. The monomer, now with an active radical, engages in successive reactions, binding to additional monomers and elongating the polymer chain. This process continues, leading to a growing chain with an increasing number of monomer units until the termination step. Polymerization may terminate through the combination of two active radicals, forming a stable, non-radical species (coupling or recombination)[88].

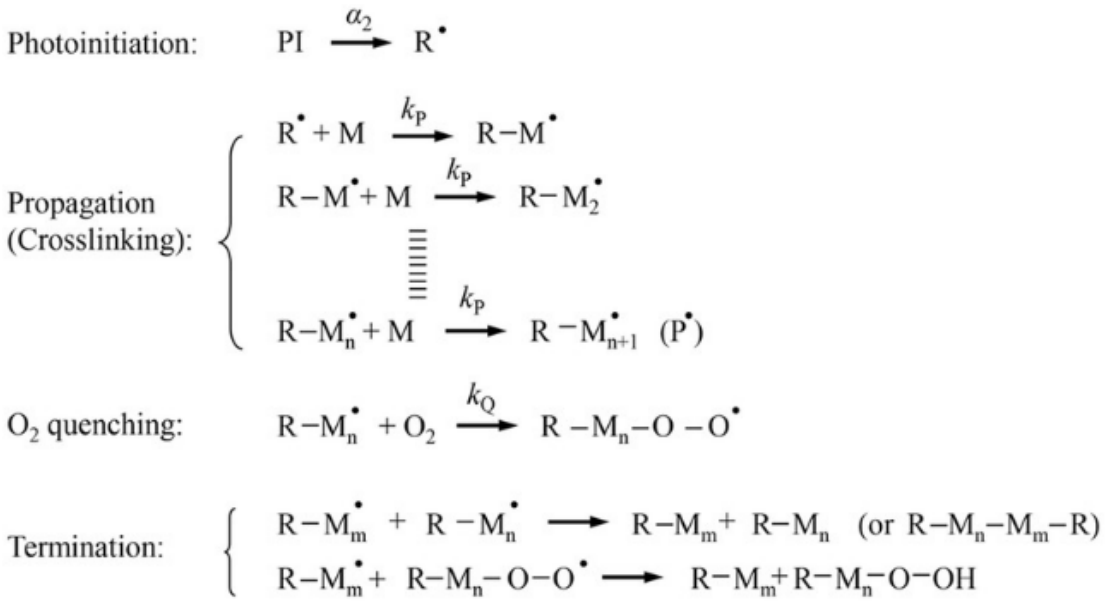

Figure 2.6: Illustration of the underlying polymerization steps including photoinitiation, propagation, oxygen quenching, and the most common termination processes. Adapted with permission from Ref. [46]. Copyright 2019 Springer Nature.

In the realm of light-activated FRP for 3D printing, factors such as intensity, wavelength, and exposure duration enable fine control over the polymerization reaction with the goal to achieve efficient and high-resolution manufacturing processes. The spatial control of light exposure permits the creation of intricate 3D structures endowed with exceptional precision at the micron and sub-micron scale. In this process, a focused laser beam is carefully employed to selectively solidify or ablate a photosensitive material at the nanoscale level, with the laser beam being tightly controlled and scanned across the material's surface to build up the structure layer by layer. (Meth)acrylate monomers/oligomers are frequently used for 3D photopolymerization processes which proceed via a radical system [89]. (Meth)acrylate-based resins are compatible with different types of commercially available 3D printers as well as custom-made 3D printers [90]. Most common (meth)acrylate monomer/oligomers used in 3D printing are PEGDA [91], UDMA [92], triethylene glycol dimethacrylate (TEGDMA) [93], bisphenol A-glycidyl methacrylate (Bis-GMA) [93], trimethylolpropane triacrylate (TTA) [94], and bisphenol A ethoxylate diacrylate (Bis-EDA) [95] (see Figure 2.7).

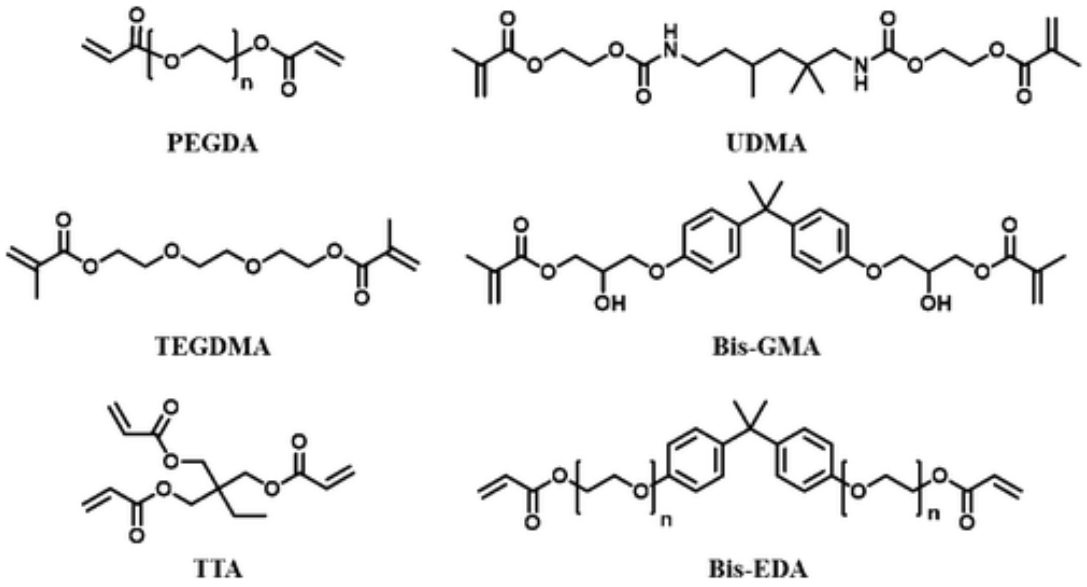

Figure 2.7: Examples of meth(acrylate) monomer/oligomer typically used in 3D photopolymerization. Adapted with permission from Ref. [89].

3D laser printing holds immense potential for advanced manufacturing, nanotechnology research, and a wide array of applications that demand high-resolution. With ongoing advancements in laser technology, materials, and process optimization, 3D laser nanoprinting continues to evolve as a powerful tool for pushing the boundaries of precision manufacturing at the nanoscale.

2.3.3 Radical of photoinitiators

When incorporated into the monomeric liquid matrix, PIs play a crucial role in the field of FRP by initiating the polymerization process upon absorbing light. These compounds possess the ability to transform light energy into reactive species, such as radicals or ions, which then interact with the monomer, triggering the formation of the polymer network. The absorption of light transitions the system from the ground state (S_0) to the singlet excited state (S_1), achieved, for example, through 2PA in TPP, where subsequent ISC results in the creation of a triplet excited state (often T_1), leading to the generation of radicals[6, 18, 26]. PIs for FRP are commonly classified into two groups based on their radical generation mechanisms: Norrish type I and Norrish type II.

Norrish type I PIs generate highly reactive radicals upon light absorption through a bond dissociation mechanism, as illustrated in Figure 2.8. These PIs typically contain a carbonyl group, such as a ketone or an aldehyde, capable of undergoing homolytic cleavage upon irradiation [36]. Examples of such PIs include indole, pyrrole, (thio)phenol, and aniline [39, 96, 97]. The cleavage mechanisms observed are commonly known as α- and β-fragmentation, depending on the position of the broken bond relative to the carbonyl group of the initiator. Specifically, α-cleavage occurs adjacent to the carbonyl group, while β-cleavage occurs in the β position concerning the carbonyl. In these cases, the

presence of heteroatoms is generally responsible for weakening the bonds adjacent to carbon (C-Cl, C-S, or C-N), allowing for possible β-cleavage and the generation of various radicals [37, 38]. Norrish type I PIs constitute a family of commercial compounds, well known as efficient initiators of polymerization of various kinds of monomers i.e PMMA and PETA [18, 26, 44, 98]. Such PIs as benzyl ketals ,-dialkoxyacetophenones and -hydroxyalkylphenones contain chromophoric groups that absorb radiation in ultraviolet or visible range and undergo photolysis with formation of free radicals [99]. The radical initiation mechanism of Irgacure 369, as Norrish type I PI, in combination with PETA monomer (2 wt%) [28], is characterized by two possible fragmentation mechanisms which are formed via the first triplet state: the α-cleavage takes place upon the absorption of two photon at $\sim$ 800 nm wavelength and leads to the formation of a benzoyl radical and alkylamino radical while the β-cleavage generates, at the same wavelength, α-alkyl and α-alkylamino radicals. However, the former remains the more significant dissociation mechanism [6, 26, 100, 43, 101]. Similar mechanism was observed for Irgacure 651, known MPA PI [102, 42] in the Norrish type I group combined with PMMA (5 wt%) [44], where the cleavage of the carbonyl compound leads to the generation of the benzoyl and dimethoxybenzyl radicals (α-cleavage)[44]. No other molecules are involved in these processes i.e., unimolecular reactions (see Figure 2.8).

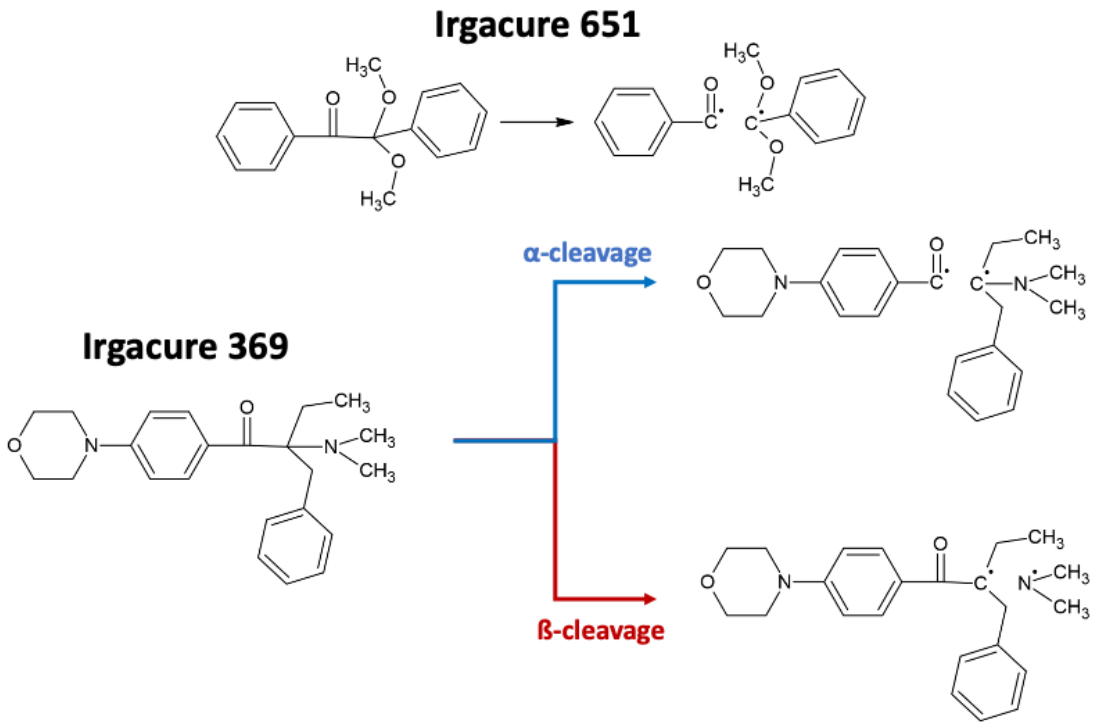

Figure 2.8: α-cleavage reaction mechanism of Irgacure 651 generating benzoyl and dimethoxybenzyl radicals (up); α- and β-cleavage reaction of Irgacure 369 with subsequent formation of benzoyl and α-aminoalkyl radicals for the former, α-alkyl and α-aminoalkyl radicals for the latter (down).

Norrish type II PIs, exemplified by benzophenone, thioxanthone, or ketocoumarins [39, 96, 97, 103, 104], absorb light and generate radicals through a bimolecular process involving either HAT[39, 40] or ET [39, 41] with a co-initiator molecule. Co-initiators encompass amines, thiols, alcohols, silanes, and various other species. HAT reactions involve the transfer of a hydrogen atom from a suitable hydrogen donor (co-initiator) to the carbonyl group of the PI, resulting in the formation of a ketyl radical on the PI and an alkyl radical on the co-initiator [105, 106, 103]. Tertiary amines, among various co-initiators, exhibit the highest efficiency as hydrogen donors and are commonly utilized [105]. It is crucial to note that, generally, only the radical originating from the co-initiator starts the initiation process due to resonance stabilization and steric hindrance associated with the formed ketyl radical on the PI [107, 39]. In the ET reaction, the PI, while in its triplet state, acts as an electron donor or acceptor in conjunction with the co-initiator, depending on the nature of both species [39, 41]. One important example is characterized by DETC combined with DPIHFP salt where the ET from the photoexcited sensitizer to the iodonium cation is followed by the rapid decomposition of the resulting unstable diaryliodine radical that prevents back ET and renders the overall process irreversible [41]. The detailed mechanisms are depicted in Figure 2.9.

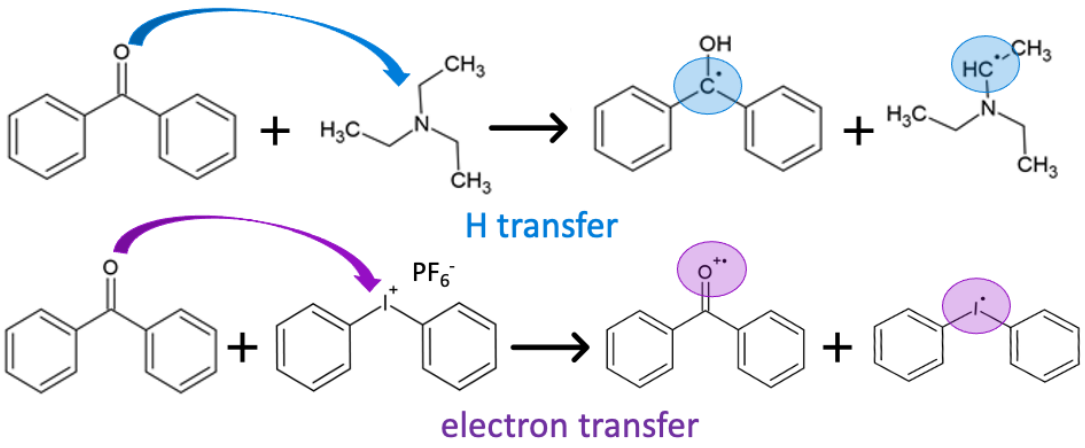

Figure 2.9: H-abstraction reaction with an amine and ET reaction with iodonium salt operated by Norrish type II initiators.

2.3.4 Norrish type I and Norrish type II photoinitiators for two-photon absorption

Norrish type I and Norrish type II PIs not only differ in their radical generation mechanisms but also showcase distinctive characteristics concerning reactivity, quantum yields, and sensitizing capabilities. Norrish type I PIs are often preferred for polymerization reactions requiring rapid initiation and high reactivity. However, they tend to be less selective in multiphoton polymerization due to the generation of a mixture of free radicals that can activate multiple sites simultaneously. In contrast, Norrish type II PIs are favored for polymerization reactions demanding more controlled initiation and slower polymer-

ization rates, as a bimolecular process is necessary for radical formation. Experimentally, Norrish Type I PIs have been reported to exhibit weaker emission (approximately 100 L $mol^{-1}cm^{-1}$) [26] compared to the green-emitting fluorescence observed in Norrish type II PIs (approximately 54,000 L $mol^{-1}cm^{-1}$)[26]. The distinction in their reactivity profiles is notable, as type I PIs demonstrate efficient radical generation, making them suitable for reactions requiring a significant quantity of reactive species. Conversely, type II PIs exhibit a more selective reactivity, engaging primarily in hydrogen or electron transfer reactions. This selectivity makes them valuable in applications where controlled reactivity and lower radical concentrations are desired, despite generally having lower quantum yields compared to type I PIs.

2.3.5 "Reluctant" Norrish type I photoinitiators for two-step absorption

The term "reluctant" Norrish type I initiators, reported starting from the 1980's in several works[31, 108, 109], describes systems for which, although the chemical structures would make them classify as typical Norrish type I initiators, the radical formation reaction is very inefficient in the first triplet state under conditions of one—photon excitation. The efficiency can be significantly enhanced when the triplet state absorbs a second photon, generating radicals in high triplet states. The most common example of "reluctant" Norrish type I initiator is benzil, depicted in Figure 1.7 [109, 31]. For common Norrish type I PIs, radicals are generated by the cleavage of chemical bonds, with typical bond energies above 3 eV (69 kcal mol^{-1})[108] and T_1 energy above that energy: for efficient bond scission from the triplet state, the triplet energy must be higher than the bond energy [108, 31]. Since the triplet energy of benzil, ~2.3 eV (54 kcal mol^{-1}), is well below that energy it has been referred to as a "reluctant" Norrish type I initiator and for this reason investigated as a candidate for two-step absorption mechanism, explained below [31].

3
Quantum-mechanical methods

The emergence of computers has brought about a profound transformation in theoretical chemistry. The availability of powerful computers and advanced algorithms has revolutionized the field, enabling the execution of complex calculations and simulations that were previously inconceivable. This computational power has opened up new avenues for exploring chemical systems, understanding their behavior, and making accurate predictions about their properties. Quantum chemistry plays a vital role in theoretical chemistry, providing the theoretical foundations for various computational methods, including density functional theory (DFT) and ab initio calculations, which have become indispensable for predicting and interpreting chemical phenomena.

DFT, as a computational quantum mechanical modeling approach, is employed to investigate the electronic structure and properties of systems composed of multiple particles, such as atoms, molecules, and solids. This method is based on the assumption that these systems' properties can be determined using the electron density, which is a function of position in space. By employing functionals, i.e., functions of another function, DFT bypasses the complexities associated with explicitly solving the Schrödinger equation for each electron in a many-electron system, as this equation is analytically solvable only for systems containing a single electron. In DFT, properties like the total energy of a system can be expressed as functionals of the electron density, encompassing the kinetic energy of the electrons, electron-electron repulsion, and electron-nucleus attraction.

The development of DFT can be traced back to the 1960s and 1970s when quantum chemists were exploring alternative methods for solving the electronic structure problem. Prior to the advent of DFT, calculations primarily relied on wave function methods, such as Hartree-Fock (HF) theory and post-HF

methods. While these methods provided valuable insights, they were computationally intensive and often limited in their applicability to small systems. In 1964, Walter Kohn and Pierre Hohenberg independently formulated the Hohenberg-Kohn (HK) theorems, which laid the theoretical groundwork for DFT. These theorems demonstrated that the ground state properties of a many-electron system can be uniquely determined by the electron density. However, it was not until 1965, when Kohn and his colleague Lu Jeu Sham introduced the Kohn-Sham (KS) equations, a set of self-consistent equations based on the HK theorems, that DFT became a practical method. The KS equations introduced a fictitious non-interacting system of electrons that yielded the same electron density as the true interacting system. Solving these equations allowed for the determination of the ground state electronic structure and properties. The success of DFT was further enhanced in the 1980s with the development of exchange-correlation functionals that accounted for electron-electron interactions beyond the mean-field approximation.

3.1 Ab initio methods

3.1.1 Molecular Schrödinger equation

In classical mechanics, the dynamics of particles is given by Newton's second law, or equation of motion:

$$\vec{F} = m\vec{a} \tag{3.1}$$

where $\vec{F}$ is the force, $\vec{a}$ the acceleration, and m is the mass of the particle. However, since electrons are very light particles that exhibit both a corpuscular and undulatory nature, the best way to describe their behavior is through the wave function Ψ. The tool available to search for this wave function is the Schrödinger equation, which represents the equivalent in quantum mechanical terms of Newton's second law. The Schrödinger equation, formulated by the Austrian physicist Erwin Schrödinger in 1925, describes how the quantum state of a physical system evolves over time. Mathematically, the Schrödinger equation is a partial differential equation that relates the wave function of a quantum system to its energy. The wave function represents the probability amplitude of finding the system in a particular state.
The time-independent Schrödinger equation is written as:

$$\hat{H}(\vec{r})\Psi(\vec{r}) = E\Psi(\vec{r}) \tag{3.2}$$

In this equation, Ψ is the wave function of the system, and $\hat{H}$ is the Hamiltonian operator, which represents the total energy E of the system. The Schrödinger equation essentially describes how the wave function evolves under the influence of the Hamiltonian operator providing a mathematical framework to calculate and predict the behavior of quantum systems, such as electrons in an atom or particles in a potential well. As originally formulated the equation does not account for relativistic effects such as time dilation and length contraction.

The wave function is a fundamental concept that describes the quantum state of a particle or system and provides information about the probability distribution of finding the particle in different states. The square of the wave function gives the probability density of finding the particle at a particular position $\vec{r}$. Since all particles must be found somewhere in space, the wave function must be normalized:

$$\int |\Psi(\vec{r}_1, \vec{r}_2, \dots, \vec{r}_N)|^2 \, d\vec{r}_1 \dots d\vec{r}_N = 1 \tag{3.3}$$

3.1.2 The molecular Hamiltonian

The Schrödinger equation can be solved analytically up to one electron system due to the complexity of realistic systems, such as molecules with multiple atoms or interacting particles for which the Hamiltonian operator is (in atomic units) [110, 111, 112]:

$$\hat{H} = -\frac{1}{2}\sum_{i=1} \vec{\nabla}_i^2 - \frac{1}{2M_A}\sum_{A=1} \vec{\nabla}_A^2 - \sum_{A=1}\sum_{i=1} \frac{Z_A}{|R_A - r_i|} + \sum_{i=1}\sum_{j>i} \frac{1}{|r_i - r_j|} + \sum_{A=1}\sum_{B>A} \frac{Z_A Z_B}{|R_A - R_B|} \tag{3.4}$$

Where M_A is mass of nuclei, Z_A and Z_B represent the atomic numbers of nuclei, $|\vec{R}_A - \vec{r}_i|$, $|\vec{r}_i - \vec{r}_j| = r_{ij}$, and $|\vec{R}_A - \vec{R}_B|$ represent the distances between nucleus-electron, electron-electron and nucleus-nucleus respectively. The first two terms in 3.4 correspond to the kinetic energies of the electrons and nuclei, respectively while the remaining three terms represent the potential operators of the Hamiltonian, accounting for nucleus-electron, electron-electron and nucleus-nucleus interactions between particles. The negative sign in front of the term involving the sum over A and i signifies an attractive potential between electrons and nuclei, while the positive signs in the last two terms denote repulsive potentials between electrons and electrons, as well as between nuclei.

3.1.3 Born-Oppenheimer approximation

In order to further simplify the Hamiltonian operator, the BO approximation is now introduced [113]. This approximation allows for the separation of nuclear and electronic motions, treating them as independent, since the motion of the nuclei is much slower than the one of electrons. Experimental evidence supports this decoupling of motions: for instance, the timescale for electron excitation from the fundamental electronic state to the first excited electronic state (a lower energy transition in the absorption spectrum) is on the order of 10^{-16} s, whereas appreciable atomic displacements during molecular vibrations require times on the order of 10^{-13} s. Hence, it can be assumed that the molecular geometry does not significantly change during electronic transitions i.e. the kinetic term of the nuclei is assumed to be constant or, in other words, electrons see constant configuration of the nuclei.

Consequently, the molecular Hamiltonian in equation 3.4 can be written as an electronic Hamiltonian which focuses on the terms associated with the electronic structure of the molecule, which primarily involve the kinetic energy of electrons and the interactions between electrons and nuclei as well as between electrons .

$$\hat{H}_{el} = \hat{T}_e + \hat{V}_{Ne} + \hat{V}_{ee} + \hat{V}_{NN} \tag{3.5}$$

where $\hat{T}_e$ is the electronic kinetic energy operator, $\hat{V}_{Ne}$ is the nuclear-electron interaction operator, $\hat{V}_{ee}$ is the electron-electron interaction operator and $\hat{V}_{NN}$ is the nuclear-nuclear interaction operator. The first term represents the kinetic energy of the electrons in the molecular system and accounts for the quantum mechanical motion of electrons. The second term accounts for the interaction between electrons and nuclei including the attractive Coulombic interaction between electrons and nuclei (the $\hat{V}_{Ne}$ is defined also as external potential and accounts for the interactions of particles with the external perturbations). The third term represents the repulsive Coulombic interaction between electrons, which, being negatively charged, repel each other. The last term represents the repulsive interaction between nuclei. Nuclei, being positively charged, repel each other due to the Coulombic repulsion. The nuclear-nuclear interaction, is included for completeness and to account for the nuclear repulsion. While it involves the nuclei, it does not depend on the electronic coordinates and is considered a constant energy offset. In the Born-Oppenheimer approximation, the nuclear motion is treated classically, and the nuclei are considered fixed during electronic calculations, therefore $\hat{V}_{NN}$ is assumed to be constant for a specific molecular conformation. The electronic Hamiltonian combines these terms to describe the interplay between kinetic energy, potential energy from the external potential, and the electron-electron interactions in the system. By solving the electronic Schrödinger equation with this Hamiltonian, the electronic wave functions and energies that characterize the electronic structure of the molecular system can be obtained.

However, as mentioned above, the Schrödinger equation is exactly solvable only for one electron system where there is no electron-electron interaction to consider and the potential energy term simplifies to the external potential experienced by the electron. For example, in the case of a hydrogen atom, the potential energy term corresponds to the electrostatic attraction between the electron and the proton. On the contrary, there is no general analytical solution for the Schrödinger equation that includes the electron-electron interaction for systems with more than one electron. This is known as the "many-body problem" [114]. The inclusion of the electron-electron interaction account for the repulsive interaction between electrons due to their Coulombic charges. As the number of electrons increases, the mathematical complexity of the electron-electron interaction term grows significantly. To study such systems, various approximation methods and numerical techniques are employed. These approximations include mean-field approximations like HF theory [115] and post-HF methods, as well as DFT [112] and quantum Monte Carlo methods that provide approximate solutions to the electronic structure of multi-electron systems, allowing for the investigation of their properties and behavior.

The methodology employed in the thesis involves mostly the utilization of DFT, which is introduced in section 3.2

3.2 Density functional theory

The central object in DFT is the electron density [116]. DFT is based on the idea that the properties of a many-electron system can be determined entirely by the electron density rather than the complicated many-body wave function. The electron density is the key quantity that is used to calculate various properties of the system, such as total energy, electronic structure, and response properties. The electron density is defined as the probability density of finding an electron at a particular position in space.

In order to find the electron density that minimizes the total energy of the system under consideration it is necessary to solve the KS equations, which are a set of self-consistent equations derived from the variational principle [112]. The KS equations involve an effective potential, known as the exchange-correlation potential, which takes into account the electron-electron interactions beyond the classical electrostatics. By obtaining the electron density and solving the KS equations, DFT allows for the calculation of a wide range of properties and phenomena in atoms, molecules, and solids.

3.2.1 Energy in terms of density

As mentioned, the central object of DFT is the electron density which for a N-electron system and a normalized wave function is defined as:

$$\rho(\vec{r}) = N \int |\Psi(\vec{r}_1 \dots \vec{r}_N)^2| \, d\vec{r}_1 \dots d\vec{r}_N \tag{3.6}$$

The density as an observable can be calculated with the many-electron wave function $\Psi_n(\vec{r}_1, \dots, \vec{r}_N)$, where n denotes the state of the system. In equation 3.6 the spin coordinates are neglected and the elctron density is expressed as an observable only dependent on spatial coordinates.

All terms in the electronic Hamiltonian (equation 3.5) have to be expressed in terms of the density.

Electron-nuclei term: The electron-nuclei interaction term reads as:

$$\langle \Psi | \hat{V}_{\text{Ne}} | \Psi \rangle = -\sum_{A}^{N} \int \frac{Z_A \rho(r)}{|R_A - r|} \, d\vec{r}_1 \dots d\vec{r}_N = \int \rho(\vec{r}) V_{\text{ext}}(\vec{r}) \, d\vec{r} \tag{3.7}$$

Electron-electron term: The term is expressed in terms of the pair-density $\rho(\vec{r}_i, \vec{r}_j)$:

$$\langle \Psi | \hat{V}_{\text{ee}} | \Psi \rangle = \int d\vec{r}_i \, d\vec{r}_j \frac{\rho(\vec{r}_i, \vec{r}_j)}{|\vec{r}_i - \vec{r}_j|} \, . \tag{3.8}$$

The pair-density can be decomposed in uncorrelated (single electron) and strictly correlated contributions:

$$\rho(\vec{r}_i, \vec{r}_j) = \frac{\rho(\vec{r}_i)\rho(\vec{r}_j)}{2} + \Delta\rho(\vec{r}_i, \vec{r}_j) \tag{3.9}$$

The expectation-value of the electron-electron term therefore reads:

$$\langle \Psi | \hat{V}_{ee} | \Psi \rangle = \frac{1}{2} \int d\vec{r}_i \, d\vec{r}_j \frac{\rho(\vec{r}_i)\rho(\vec{r}_j)}{|\vec{r}_i - \vec{r}_j|} + \int d\vec{r}_i \, d\vec{r}_j \frac{\Delta\rho(\vec{r}_i, \vec{r}_j)}{|\vec{r}_i - \vec{r}_j|} = E_C[\rho(\vec{r})] + \Delta E_{ee}[\rho(\vec{r})] \tag{3.10}$$

where E_C stands for mean field Coulomb energy interaction.

Kinetic term: The expectation-value of the kinetic energy operator can be decomposed in uncorrelated (single electron) and correlated terms because it is hard to express it in term of the density:

$$\langle \Psi | \hat{T} | \Psi \rangle = T_0 + \Delta T[\rho(\vec{r})] \tag{3.11}$$

where T_0 is the uncorrelated kinetic term. Finally, the expression for the energy as a function of the density can be written as:

$$E[\rho(\vec{r})] = T_0 + E_H[\rho(\vec{r})] + \int d\vec{r} \, \rho(\vec{r}) V_{ext}(\vec{r}) + \Delta T[\rho(\vec{r}] + \Delta E_{ee}[\rho(\vec{r}] \tag{3.12}$$

where ΔT and ΔE_{ee} are the unknown terms.

3.2.2 Hohenberg-Kohn theorems

The HK theorems provide a solid theoretical foundation for the DFT method [117, 118]. These theorems were formulated by P. Hohenberg and W. Kohn in 1964:

- First HK theorem: the external potential of a system uniquely determines its ground-state electron density. This theorem establishes a one-to-one correspondence between the external potential and the ground-state electron density. It implies that the ground-state properties of a many-electron system can be determined entirely by the electron density.
- Second HK theorem: there exists a universal energy functional, known as the HK functional, that depends only on the electron density and is minimized by the true ground-state density. This theorem states that there is a functional relationship between the electron density and the total energy of the system. The HK functional is a universal functional that is the same for all systems and depends solely on the electron density. The true ground-state electron density minimizes this functional, meaning that the actual ground-state properties of the system can be obtained by finding the density that minimizes the functional.

The mathematical representation of the first HK theorem starts with the assumption that the ground state properties of a system can be determined uniquely by its electron density ρ_0. The total energy of the system can be expressed as:

$$E_0[\rho_0] = T[\rho_0] + E_{ee}[\rho_0] + E_{Ne}[\rho_0] \tag{3.13}$$

The kinetic and electron-electron repulsion terms can be grouped inside the so called HF functional as:

$$E_{\mathrm{HK}}[\rho(\vec{r})] = E_{\mathrm{Ne}}[\rho_0] + F_{\mathrm{HK}}[\rho_0] = \int \rho(\vec{r}) V_{\mathrm{Ne}} d\vec{r} + F_{\mathrm{HK}}[\rho(\vec{r})] \tag{3.14}$$

According to the second theorem, the density that minimize the total energy of the system is the ground state density:

$$E_0 \leqslant E_{\mathrm{HK}}[\rho(\vec{r})] \tag{3.15}$$

3.2.3 Kohn-Sham equations

In the previous section the energy functional of the density (equation 3.12) has been conceived for a real system of interacting electrons, where $V_{\mathrm{ext}}(\vec{r}) \leftrightarrow \rho(\vec{r})$.
The KS idea is based on the KS theorem, which states that the ground-state electron density of a system determines the external potential in which the electrons move [112]. According to this idea, the complex problem of interacting electrons in a many-electron system can be mapped onto a system of non-interacting electrons moving in an effective potential. In this approach, the system is described by a set of one-electron wavefunctions called KS orbitals; each orbital represents the motion of a non-interacting electron in the effective potential For a system of independent particles the Schrödinger equation looks like:

$$\left[-\frac{1}{2}\vec{\nabla}_i^2 + V_{\mathrm{eff}}^{\mathrm{KS}}(\vec{r})\right] \psi_i^{\mathrm{KS}}(\vec{r}) = \epsilon_i \psi_i^{\mathrm{KS}}(\vec{r}) \ , \tag{3.16}$$

where the equation for each particle contains a kinetic and a potential term, defined as the effective potential and $\psi_i^K S$ are the KS orbitals.
The electron density can be written as:

$$\rho(\vec{r}) = \sum_i^N |\psi_i^{\mathrm{KS}}(\vec{r})|^2 \tag{3.17}$$

From HK theorem, knowing that there is a unique correspondence between the density and the external potential, which now correspond to the effective potential V_{eff} it can be stated:

$$\rho(\vec{r}) \leftrightarrow V_{\mathrm{eff}}^{\mathrm{KS}} \tag{3.18}$$

Moreover, the energy, as a unique functional of the density is:

$$E_s[\rho] = T_s + E_{\mathrm{C}}[\rho] + \int d\vec{r}\ \rho(\vec{r}) V_{\mathrm{eff}}^{\mathrm{KS}}(\vec{r}) \tag{3.19}$$

where s stands for and the electron-electron interaction term is absent due to the fact that the electrons are supposed to be independent.

The definition of the effective potential is:

$$V_{\text{eff}}^{\text{KS}}(\vec{r}) = V_{\text{ext}}(\vec{r}) + \int d^3\vec{r}' \frac{\rho(\vec{r}')}{|\vec{r} - \vec{r}'|} + \frac{\delta E_{\text{XC}}[\rho(\vec{r})]}{\delta\rho(\vec{r})} \,. \tag{3.20}$$

The last term of equation 3.20 is the functional for exchange and correlation potential and it is not known except for free electron gas. For this reason DFT functionals are here incorporated in order to approximate the E_{XC}.

3.2.4 Functionals in density functional theory

Before being able to solve the mono-electronic equations of KS it is necessary to specify the mathematical form of the exchange-correlation functional $E_{\text{XC}}[\rho]$, calculate its functional derivative and insert it in the operator. Once the mathematical form of $E_{\text{XC}}[\rho]$ has been fixed, the KS-SCF method is variational in the sense that the KS orbitals generate the electron density which minimizes the value of E_0. The mathematical forms proposed for $E_{\text{XC}}[\rho]$ are now numerous and represent the attempt to "guess" its true expression. Since the universal functional is not known we use approximate functionals that can be of three types:

- local density approximation (LDA) or local functionals
- generalized gradient approximation (GGA) or non-local functionals
- hybrid functionals

The choice of the approximate functional is of fundamental importance for the DFT calculation, since it is the factor that introduces the deviation from the exact resolution. In general, the functional is divided into two contributions: the exchange functional E_x, which refers to the exact exchange contribution obtained with the HF method, and the correlation functional E_c. The first generation of correlation and exchange functionals, defined as local functionals, used the LDA, for which only the value of the electron density at a given point in space determines the contribution of this point in the energy E_{xc}; all non-local effects are neglected.

$$E_{\text{XC}}^{\text{LDA}} = E_{\text{xc}}[\rho(r)] \tag{3.21}$$

That is, it integrates with the variable r, limiting itself to considering the value that the density assumes only in r, without giving importance to the trend of $\rho(r)$ in the neighborhood of the point. This approximation treats the molecules as if they contained a homogeneous electron gas in a uniformly distributed positive charge field. This is an unrealistic representation, however the functional LDA provides a relatively accurate structure, even if it underestimates the exchange energy and overestimates the correlation energy. The GGA of non-local functionals adds a term that takes into account the trend of $\rho(r)$ around r and not only of its value at the point r.

$$E_{\text{XC}}^{\text{GGA}} = E_{\text{xc}}[\rho(r), \nabla\rho(r), \dots] \tag{3.22}$$

Besides these pure density functionals, LDA and GGA, there are functional hybrids, which combine the DFT correlation and exchange functional, usually approximated by the GGA, and the exact HF exchange. These hybrids functionals are the most used and, among them, are B3LYP and CAM-B3LYP, thoroughly discussed in the thesis. The former mixes the HF exchange with the GGA type correlation and exchange contribution while the latter contains three parameters that specify the contributions of the exact HF exchange, the local exchange, the exchange contribution and correlation corrected for the gradient. More specifically B3LYP combines three different components: Becke's three-parameter exchange functional (B3), Lee-Yang-Parr correlation functional (LYP), and the Vosko-Wilk-Nusair (VWN) correlation functional. The formulation of this functional can be expressed as:

$$E_{\mathrm{XC}} = 0.80E_{\mathrm{X}}^{\mathrm{LSDA}} + 0.20E_{\mathrm{X}}^{\mathrm{HF}} + 0.72\Delta E_{\mathrm{X}}^{\mathrm{B}} + 0.19E_{\mathrm{C}}^{\mathrm{LSDA}} + 0.81E_{\mathrm{C}}^{\mathrm{LYP}}E_{\mathrm{X}}^{\mathrm{B}} \tag{3.23}$$

The CAM-B3LYP functional has similar structure ad B3LYP but it is characterized by a short and long range differentiation. These functionals will be discussed further in the next chapters of the thesis, comparing their ability to guarantee accuracy in the prediction of geometries and charge transfer properties of excited states.

Dispersion corrections

Dispersion corrections in the context of DFT are introduced to account for the limitations of traditional DFT functionals in describing dispersion forces or van der Waals interactions. Dispersion interactions arise from the attractive forces between temporary fluctuations in electron distributions in neighboring molecules, and they are crucial for the accurate description of molecular and material properties, especially in systems with weak interactions. Standard DFT functionals do not inherently include an accurate description of dispersion interactions. As a result, dispersion corrections, also known as van der Waals corrections, are added to the DFT calculations to improve the description of long-range dispersion interactions. The Stefan Grimme dispersion correction approach [119], often referred to as the Grimme-D2 or Grimme-D3 correction, is based on the idea of adding an attractive potential to account for dispersion forces, and it is designed to be compatible with various DFT functionals. The Grimme-D2 and Grimme-D3 corrections differ in the damping functions used. Grimme-D3 typically employs a more sophisticated damping function to provide better accuracy over a wide range of molecular systems. The D3BJ method (Becke-Johnson damping) has a damping function that helps to prevent unphysical long-range contributions in the dispersion correction and it is the method chosen in this work.

3.2.5 Basis set

Basis sets are used to approximate the wavefunction of the system by expanding it in terms of basis functions. The basis set represents the wavefunction as a linear combination of these functions, which are typically referred to as basis functions or basis orbitals. These basis functions can be atomic orbitals, such as the well-known hydrogen-like orbitals (s, p, d, etc.), or more complex mathematical functions. There are generally two types of basic functions that are used in molecular calculations: the Slater type

orbitals (STOs) and the Gaussian type orbitals (GTOs). STOs are a type of Slater-type radial functions multiplied by a spherical harmonic. The radial part is expressed as a power series of exponentials and polynomials. STOs have more accurate overlap integrals than GTOs, making them suitable for describing electron-electron interactions at short distances. However, they are computationally expensive due to their slower convergence rate, which may limit their usage. GTOs are mathematically represented by Gaussian functions, and although they have less accurate overlap integrals than STOs, they are computationally convenient and provide good results for many molecular properties. They can indeed describe both the core and valence regions of molecules and exhibit exponential decay for describing long-range interactions. Because of the good compromise between accuracy and computational cost, GTOs are widely used in DFT. Having decided the type of function for atomic orbitals it is important to define its number. Theoretically it would be possible to use only one function for each atomic orbital (minimum base set): these basis functions capture the basic shape and behavior of the electrons within the atom or molecule but, although a minimal basis set is relatively simple, it can not accurately capture electron correlation effects and may not be sufficient for describing systems with strong electron-electron interactions. As a result, more elaborate basis sets, such as double zeta (DZ), triple zeta (TZ), or quadruple zeta (QZ) basis sets, are often employed to improve the accuracy of calculations. These higher-level basis sets include additional basis functions per atomic orbital, allowing for a more detailed description of the electronic structure and improved accuracy in predicting molecular properties. It is important to note that the choice of basis set, including the type and number of basis functions, depends on the specific requirements of the calculation and the level of accuracy desired. For the elements from the third period onwards, further problems arise. These atoms have a greater number of core electrons, which must be described by a sufficient number of basic functions and in which the relativistic effects, or the dependence of mass on velocity, are manifested in a way that is no longer negligible. An effective core potential (ECP) is therefore used, commonly called pseudopotential, which represents the core electrons as a single function and only valence electrons are explicitly treated in the calculation.

3.3 Time-dependent density functional theory

Time-dependent density functional theory (TD-DFT) allows the calculation of electronic excited states and their properties. It extends the DFT framework, which is primarily used for ground-state calculations, to describe the dynamics and properties of excited states in molecules and solids.

The starting point is the Schrödinger equation, which, considering the presence of a time-dependent scalar field in equation 3.2, reads:

$$i\hbar\frac{\partial}{\partial t}\Psi(\vec{r},t) = H\Psi(\vec{r},t) \tag{3.24}$$

The Runge–Gross theorem [120], the analogous of the first HK theorem, establishes the existence of a time-dependent exchange-correlation potential that depends solely on the time-dependent electron density $\rho(\vec{r},t)$. This time-dependent exchange-correlation potential can be used to solve the time-dependent

KS equations and obtain the time-dependent electronic wave function and properties.
The time-dependent density in TD-DFT is given by:

$$\rho(\vec{r},t) \leftrightarrow V_{\text{ext}}(\vec{r},t) \tag{3.25}$$

where

$$\rho(\vec{r},t) = \sum_{i}^{N} |\psi_i^{\text{KS}}(\vec{r},t)|^2 \tag{3.26}$$

These KS orbitals are solution of the time-dependent Schrödinger equation:

$$i\hbar\frac{\partial}{\partial t}\Psi(\vec{r},t) = \left[-\frac{\hbar^2}{2m}\vec{\nabla}^2 + V_{\text{eff}}(\vec{r},t)\right]\Psi(\vec{r},t) \tag{3.27}$$

where

$$V_{\text{eff}}^{\text{KS}}(\vec{r},t) = V_{\text{ext}}(\vec{r},t) + \int d^3\vec{r}'\frac{\rho(\vec{r}')}{|\vec{r}-\vec{r}'|} + \frac{\delta E_{\text{XC}}[n(\vec{r})]}{\delta n(\vec{r}),t}\,. \tag{3.28}$$

As it was for equation 3.28, the last term of equation 3.28 is the functional for exchange and correlation potential, typically approximated using various functionals. Commonly used approximation include the adiabatic local density approximation, where the exchange-correlation potential is assumed to be instantaneous and depends only on the instantaneous electron density [121]. The adiabatic local density approximation considers the density at each time t as the ground-state density of the system and therefore this approximation is valid if the time-dependent potential changes very slowly. In order to reduce the computational cost of TD-DFT calculations, they are carried out by perturbation theory, in a weak perturbation regime. The weak perturbation corresponds to the situation in which the external electric field is significantly smaller than the one generated by the nuclear charge. In this situation, the perturbation is generally an oscillating electric field, written as:

$$V_{\text{ext}}(t) = \mu F\ \cos(\omega t) \tag{3.29}$$

Where ω is the frequency, F is the strength of electric field and μ is the dipole moment.

In order to calculate the wavefunction or the density response, a vector $[Y,Z]^{\intercal}$ can be used. It represents the real and the imaginary part of the first order answer and can be obtained by solving a set of linear equations as:

$$\left(\begin{bmatrix} A & B \\ B^* & A^* \end{bmatrix} - \omega\begin{bmatrix} 1 & 0 \\ 0 & -1 \end{bmatrix}\right)\begin{bmatrix} Y \\ Z \end{bmatrix} = -\begin{bmatrix} P \\ P^* \end{bmatrix} \tag{3.30}$$

Where A matrix is that of the differences in the orbitals energies, while matrix B is that of the differences

in the electron-electron interactions. The elements of these two matrices can be expressed as follow:

$$A_{ij}^{ab} = \langle \psi_i^a | \hat{H}_0 | \psi_j^b \rangle - E_0 \delta_{ij} \delta ab = \delta_{ij} \delta ab(\epsilon_a - \epsilon_i) + \langle ij | ab \rangle - \langle ia | jb \rangle \tag{3.31}$$

$$B_{ij}^{ab} = \langle \psi_0 | \hat{H}_0 | \psi_{ij}^{ab} \rangle = \langle ij | ab \rangle - \langle ij | ba \rangle \tag{3.32}$$

$$P_i^a = \langle i | \vec{r} | a \rangle \tag{3.33}$$

Where ij and ab are occupied and virtual orbitals respectively. If

$$\begin{bmatrix} P \\ P^* \end{bmatrix} = 0$$

an eigenvalue equation can be obtained:

$$\begin{bmatrix} A & B \\ B^* & A^* \end{bmatrix} \begin{bmatrix} Y \\ Z \end{bmatrix} = \omega \begin{bmatrix} 1 & 0 \\ 0 & -1 \end{bmatrix} \begin{bmatrix} Y \\ Z \end{bmatrix} \tag{3.34}$$

where ω is the eigenvalue.

3.3.1 Linear response approach

Linear response (LR)-TD-DFT is an extension of TD-DFT that allows for the calculation of electronic excitations and response properties in a linear regime. LR-TD-DFT is particularly useful for studying optical and spectroscopic properties, such as absorption spectra, excitation energies, and oscillator strengths.

In LR-TD-DFT, the system is assumed to be perturbed by an external time-dependent potential $V_{\text{ext}}(\vec{r}, t)$. The response of the electron density and other properties is then The interacting system with a partitioned Hamiltonian is expressed as:

$$H = H_0 + V_{\text{ext}}(\vec{r}, t) \tag{3.35}$$

Where H_0 is time-independent unperturbed system, and V_{ext} is the time-dependent Hamiltonian describing the field potential. The key quantity in LR-TD-DFT is the linear response function, often denoted as $\chi(r, r', \omega)$, which describes the change in the electron density at position r due to the perturbation at position r' and frequency ω. The linear response function can be expressed in terms of the time-dependent perturbed electron density $\rho(r, t)$ and the perturbing potential $V_{\text{ext}}\vec{r}, t)$. In the frequency domain, it can be written as:

$$\chi(r, r', \omega) = \lim_{\epsilon \to 0} \int_{-\infty}^{\infty} dt\, e^{i(\omega + i\epsilon)t} \langle \delta\rho(r, t) | \delta V_{\text{ext}}(r', 0) \rangle \tag{3.36}$$

where $\delta\rho(r, t) = \rho(r, t) - \rho_0(r)$ is the change in electron density from the unperturbed ground-state density $\rho_0(r)$, and $\delta V_{\text{ext}}(r', t) = V_{\text{ext}}(r', t) - V_{\text{ext}}(0, r')$ is the change in the external potential from the

unperturbed potential $V_{\text{ext}}(0, r')$.

The linear response function $\chi(r, r', \omega)$ is related to the frequency-dependent polarizability $\alpha(r, r', \omega)$ through the equation:

$$\alpha(r, r', \omega) = \int d^3r_1 d^3r_2 \, \chi(r, r_1, \omega) v(r_1, r_2, \omega) \chi^*(r_2, r', \omega) \tag{3.37}$$

where $v(r, r', \omega)$ is the dynamically screened Coulomb interaction, also known as the density-density response kernel. Once the linear response function is obtained, it can be used to calculate various properties, such as the absorption spectrum. The absorption spectrum is typically obtained by evaluating the imaginary part of the frequency-dependent polarizability and relates to the excitation energies and oscillator strengths of the system.

$$\text{Absorption spectrum} = \text{Im}[\alpha(r, r', \omega)] \tag{3.38}$$

Advantages and disadvantages of density functional theory

The adoption of DFT in this thesis for optimizing the ground state of the studied singular molecules is driven by several considerations. A key advantage of DFT is its ability to strike a balance between accuracy and computational cost. By approximating electronic interactions within a system, DFT provides a practical and reliable approach for predicting molecular electronic structures, making it well-suited for examining stable molecular conformations.

The decision to employ TD-DFT for investigating the electronic structure and excited state properties of the presented photoactive molecules is carefully considered. Since DFT relies on approximations for the exchange-correlation functional, the choice of functional is crucial for accurately representing system properties [122]. Selecting the appropriate functional can be challenging, as different functionals may be more suitable for specific systems. Therefore, careful calibration of the functional choice based on the properties of interest is imperative, and discussions about the selection of the DFT functional are provided at the beginning of each thesis chapter.

The choice of the exchange-correlation functional significantly influences the description of charge transfer (CT) excited states with large spatial separation of electron and hole densities [123]. TD-DFT tends to underestimate excitation energies for such systems, leading to deviations from experimental outcomes. Additionally, TD-DFT struggles with predicting correct geometries for optimized CT states, a challenge mitigated by employing a range-separated functional (CAM-B3LYP) [124] designed to address long-range and short-range electron-electron correlation effects effectively.

Accurate description of open-shell states, such as triplets, is another critical aspect. Traditional DFT functionals often suffer from self-interaction errors, particularly pronounced for triplet states. While methods beyond standard DFT can help address these issues, accurately capturing triplet states remains challenging in TD-DFT. Hybrid functionals like CAM-B3LYP, incorporating exact exchange, aim to overcome limitations of pure DFT, especially concerning electronic excitations and open-shell states [125].

The choice of TD-DFT for this study is strategic, considering its computational efficiency compared

to more demanding wavefunction-based methods. This efficiency is essential for systems with a high number of atoms, highly excited states, and the exploration of photochemical rates and bimolecular reactions. The selection of the functional follows a detailed benchmark analysis, validating the appropriateness of TD-DFT for the precise PIs investigated in the thesis. Thus, TD-DFT proves to be a suitable approach for studying the outlined photochemical and photophysical processes in the dissertation.

3.4 The GW approximation and Bethe-Salpeter equation

In the framework of many-body perturbation theory (MNPT), the GW method plays a pivotal role, utilizing the single-particle Green's function to predict precise ionization potential (IP) and electron affinity (EA) [126, 127]. To simulate optical properties e.g., absorption spectra, the Bethe-Salpeter equation (BSE) formalism is added. The GW-BSE approach exhibits excellent agreement with experimental data [128], especially for CT-type excitations [128]. Through GW-BSE, one can calculate approximate excitation energies for a many-electron system described by the many-body Schrödinger equation. Notably, the central quantity in this approach is the single-particle Green's function, distinguishing it from DFT where the focus is on electronic density. The computational cost scales with N^4 where N is the number of electrons in the system [129]. This makes GW calculations computationally expensive, especially for larger systems, but still a valuable alternative to wavefunction-based methods [130, 131].

3.4.1 The single-particle Green's function

The single-particle Green's function describes propagation of an electron from (r1,t1) to (r2,t2):

$$G(\mathbf{r}_1, \mathbf{r}_2; t_1 - t_2) = -i\langle \Psi_0^N | \hat{T}[\hat{\psi}(\mathbf{r}_1, t_1)\hat{\psi}^\dagger(\mathbf{r}_2, t_2)] | \Psi_0^N \rangle \tag{3.39}$$

where Ψ_0^N is the many-electron ground state, $\psi^\dagger$ is the field operator that creates an electron at point $\mathbf{r}$ and T is the time-ordering operator. It is a function that depends on two points in space ($\mathbf{r}_1$ and $\mathbf{r}_2$) and time (t_1 and t_2). The single-particle Green's function is the probability amplitude for a propagation process of a particle (electron or hole) from a point $\mathbf{1} = (\mathbf{r}_1, t_1)$ to a point $\mathbf{2} = (\mathbf{r}_2, t_2)$. Specifically, when $t_1 > t_2$ the single-particle Green's function gives the probability amplitude that a hole created at $\mathbf{1}$ will propagate to $\mathbf{2}$, while when $t_2 > t_1$ gives the probability amplitude of an electron injected in $\mathbf{2}$ propagating to $\mathbf{1}$. Applying the Fourier transformation to Equation 3.39 the time domain is transformed into the frequency domain ω obtaining the so called Lehmann (or spectra) expression [132]:

$$G(\mathbf{r}_1, \mathbf{r}_2, \omega) = \sum_n \frac{\psi_n^{N+1}(\mathbf{r}_1)\psi_n^{N+1*}(\mathbf{r}_2)}{\omega - (E_n^{N+1} - E_0^N) + i\eta} + \sum_n \frac{\psi_n^{N-1}(\mathbf{r}_1)\psi_n^{N-1*}(\mathbf{r}_2)}{\omega - (E_n^N - E_0^{N-1}) - i\eta} \tag{3.40}$$

where n represents the collection of electron and hole, η is an infinitely small positive regularization parameter which is necessary to perform the Fourier transformation since the Lehman representation has singularities for $\omega = \mathrm{E}_n^{(N+1)} - \mathrm{E}_0^N$. The frequency dependent function contains in the denominators the eigenvalues of the many-body Schrödinger equation, $(E_n^N - E_0^{N-1})$ and $(E_n^{N+1} - E_0^N)$ that are the

single-particle excitation energies measured in photoemission spectroscopy, where an electron is either removed (direct photoemission) or added (inverse photoemission) in the system [133, 134]. These quantities correspond to the negative of the EA and IP, respectively.

Computing the Green's function of an interacting system is as complicated as solving the Schrödinger equation directly. The point is that one can express the full Green's function describing propagation in an interacting system in terms of Green's functions of non-interacting particles G_0 by using the Dyson equation:

$$G = G_0 + G_0 \Sigma G \tag{3.41}$$

where G_0 is the Green's function that define the probability of a non-interacting reference system to undergo a certain process from one point to another point. In practice the G_0 is computed not for entirely free particle but for free quasi-particles in an effective potential just as described by the KS equation. G_0 can be obtained from KS DFT, using functionals. The Σ is called electronic self-energy and takes into account the sum overall scattering processes i.e. electronic exchange and electronic screening of all orders that the particle can undertake (scattering potential).

The Dyson equation is not solved directly in most GW codes but instead it is reformulated into an effective single- particle equation of motion defines quasi-particle equation:

$$\hat{h}_0(\mathbf{r})\psi_n(\mathbf{r}) + \int \Sigma(\mathbf{r},\mathbf{r'}; E_n)\psi_n(\mathbf{r'})d^3r' = E_n\psi_n(\mathbf{r}) \tag{3.42}$$

The Hamiltonian in the initial term of equation 3.42 includes the kinetic energy, external potential, and Hartree potential, reminiscent of the KS Hamiltonian in absence of the exchange-correlation potential in DFT. The second term ($\int \Sigma(\mathbf{r},\mathbf{r'}; E_n)\psi_n(\mathbf{r'})d^3r'$) includes all electron-electron interactions and plays the role of the "exchange-correlation functional". Notably, the self-energy is both non-local and energy-dependent. Intriguingly, the eigenvalues E_n that require determination also appear in the operator as an argument of the self-energy, rendering the quasi-particle equation nonlinear. The self-energy contribution to the eigenvalues are complex where the real part resembles the excitation energies and the imaginary part the excitation lifetimes. The most common approximation is the GW self-energy.

The expansion of the self-energy in the bare Coulomb potential v taking into account only linear terms, gives the HF approximation of the self-energy, which is however a poor approach for extended electronic systems:

$$\Sigma^{HF} = iG_0 v \tag{3.43}$$

where v is the bare Coulomb potential. An improved approximation arises when, instead of dealing with strongly interacting electrons, quasi-particles are taken into consideration. Envision placing an electron within a many-electron system; this electron induces repulsion among the surrounding electrons, leading to the formation of a Coulomb hole around it. Quasi-particles are defined as single electrons (or holes) accompanied by the virtual cloud generated by the Coulomb repulsion with other

electrons in the system. These quasi-particles serve as solutions to effective single-particle equations, encompassing the influences of interactions involving the surrounding electron-hole pairs, electron-electron interactions, and hole-hole interactions. The interaction between quasi-particles is denoted as W and is smaller than v due to the screening effect, resulting in a reduced charge for a quasi-particle compared to an electron.

The screened Coulomb interaction can be expressed with a Dyson equation:

$$W = v_0 + v_0 P W \tag{3.44}$$

where v_0 is the bare Coulomb interaction, P is the polarizability and W is the screened Coulomb interaction. Expanding the self-energy in terms of the screened interaction, created by the charge of a quasi-particle, will give:

$$\Sigma^{GW} = iG_0 W \tag{3.45}$$

Equation 3.45 is called GW approximation and corresponds to the HF approximation with the inclusion of the dynamically screened Coulomb interaction.

The expansion of the Green's function and self-energy in terms of the screened Coulomb interaction potential W is given by the Hedin's equation (formulated by Lars Hedin in 1965) also known as Hedin's GW equations, a set of integral differential equations of the Green's function G, the self-energy Σ, the screened interaction W, the polarization function P and and the vertex function Γ.

$$G(\mathbf{1},\mathbf{2}) = G_0(\mathbf{1},\mathbf{2}) + \int G_0(\mathbf{1},\mathbf{3})\Sigma(\mathbf{3},\mathbf{4})G(\mathbf{4},\mathbf{2})d\mathbf{3}d\mathbf{4}) \tag{3.46}$$

$$\Sigma(\mathbf{1},\mathbf{2}) = i\int G(\mathbf{1},\mathbf{3})W(\mathbf{1},\mathbf{4})\Gamma(\mathbf{3},\mathbf{2},\mathbf{4})d\mathbf{3}d\mathbf{4}) \tag{3.47}$$

$$W(\mathbf{1},\mathbf{2}) = v(\mathbf{1},\mathbf{2})\int v(\mathbf{1},\mathbf{3})P(\mathbf{3},\mathbf{4})W(\mathbf{4},\mathbf{2})d\mathbf{3}d\mathbf{4}) \tag{3.48}$$

$$P(\mathbf{1},\mathbf{2}) = -i\int G(\mathbf{1},\mathbf{3})\Gamma(\mathbf{3},\mathbf{4},\mathbf{2})G(\mathbf{4},\mathbf{1})d\mathbf{3}d\mathbf{4}) \tag{3.49}$$

$$\Gamma(\mathbf{1},\mathbf{2},\mathbf{3}) = \delta(\mathbf{1},\mathbf{2})\delta(\mathbf{1},\mathbf{3}) + \int \frac{\delta\Sigma(\mathbf{1},\mathbf{2})}{\delta G(\mathbf{4},\mathbf{5})}G(\mathbf{4},\mathbf{6})G(\mathbf{7},\mathbf{5})\Gamma(\mathbf{6},\mathbf{7},\mathbf{3})d\mathbf{4}d\mathbf{5}d\mathbf{6}d\mathbf{7} \tag{3.50}$$

The notation $\mathbf{1} = (\mathbf{r}_1, t_1)$ is used. The set of equation can be solved self-consistently but some simplifications have to be introduced. The first approximation is the vertex approximation where the self-energy is zero yielding to first-order: Γ (**1**,**2**,**3**) = δ(**1**,**2**)δ(**1**,**3**) keeping only diagonal contribution. Subsequently, the GW approximation for the self-energy is expressed by:

$$\Sigma(\mathbf{1},\mathbf{2}) = iG(\mathbf{2},\mathbf{1})W(\mathbf{1},\mathbf{2}) \tag{3.51}$$

The second approximation introduced is related to the polarization function which is approximated by the product of two Green's functions, meaning that the electron-hole pair interaction is neglected

(random phase approximation (RPA)).

$$P_0(\mathbf{1},\mathbf{2}) = iG(\mathbf{2},\mathbf{1})G(\mathbf{1},\mathbf{2}) \tag{3.52}$$

These simplifications allow to calculate the Green's function of an interacting many-electron system using the Green's function G_0 of a non-interacting reference system with an effective screened potential [135].

3.4.2 The Bethe-Salpeter equation

GW serves as an approximation for the self-energy term, used for the computation of the one-particle Green's function and while it allows for the calculation of processes involving the addition and removal of an electron in a many-body system, such as photoemission, it falls short in addressing the excitation of an electron. The latter process involves considering the electron-hole interaction and necessitates the use of a two-particle Green's function. In the case of non-interacting electron-hole pairs, the two-particle correlation function L_0 can be described by the product of two single-particle Green's functions that describes the propagation of one particle from **3** to **1** and of another particle from 4 to **2**:

$$L_0(\mathbf{1234}) = -iG(\mathbf{1,3})G(\mathbf{4,2}) \tag{3.53}$$

The two particle correlation function L(**1234**) takes into account the electron-hole interaction, the so called excitonic effects. It is a four points quantity that describes the interaction between the excited electron and the hole left behind connected with L_0 through the following Dyson equation:

$$L(\mathbf{1234}) = L_0(\mathbf{1234}) + \int d5678 L_0(\mathbf{1256}) K L(\mathbf{7834}) \tag{3.54}$$

K in equation 3.54 is defined as BSE kernel:

$$K = v(\mathbf{57})\delta(\mathbf{56})\delta(\mathbf{78}) + i\frac{\delta\Sigma(\mathbf{56})}{\delta G(\mathbf{78})} \tag{3.55}$$

where v is the bare Coulomb potential and Σ is the self-energy of Equation 3.41
The BSE can be therefore expressed as:

$$L = L_0 + L_0(v + i\frac{\delta\Sigma}{\delta G})L \tag{3.56}$$

To calculate the derivative of equation 3.56, an approximation to the self-energy Σ must be employed, with the GW approximation being the most commonly utilized one. While theoretically, other approximations could be chosen, GW is the predominant choice. The self-energy is expressed as follows:

$$\Sigma \sim iGW \tag{3.57}$$

where G is the one-particle Green's function and W is the screened Coulomb interaction. Applying this approximation to L_0 and Σ the following expression is obtained:

$$L = L_0 + L_0(\nu - \frac{\delta GW}{\delta G})L \tag{3.58}$$

where

$$-\frac{\delta GW}{\delta G} = W + G\frac{\delta W}{\delta G} \tag{3.59}$$

The approximation made in equation 3.59 is possible since $\frac{\delta W}{\delta G}$ is of higher order in W and describes the variation of the screened interaction for the perturbation that can be neglected.

Thus, the BSE in the GW approximation is:

$$L(\mathbf{1234}) = L_0(\mathbf{1234}) + L_0(\mathbf{1256}) + G\frac{\delta W}{\delta G} \tag{3.60}$$

Another approximation is then further introduced, considering the static approximation of the Coulomb interaction of the screened interaction W, similar to the adiabatic approximation in TD-DFT. This means to neglect the time needed to build the polarization cloud:

$$W(\mathbf{r}_1, \mathbf{r}_2; t_1 - t_2) \rightarrow W(\mathbf{r}_1, \mathbf{r}_2, \omega = 0)\delta(t_1 - t_2) \tag{3.61}$$

These approximations are introduced into the Dyson equation for two-particle correlation function. The final result is BSE in GW approximation, expressed as:

$$L(\mathbf{1234}) = L_0(\mathbf{1234}) + L_0(\mathbf{1256})[\nu(\mathbf{57})\delta(\mathbf{56})\delta(\mathbf{78}) - W(\mathbf{56})\delta(\mathbf{57})\delta(68)]L(7834) \tag{3.62}$$

This equation connects L_0 to L plus a correction given by the BSE-kernel of the Dyson equation where ν is the bare Coulomb interaction (as in TD-DFT) and W is the screened Coulomb interaction.

4 Computational details

This chapter offers a comprehensive overview of all the calculations performed outlining and elucidating the computational methods and specific details employed for the investigation of Irgacure 651, Irgacure 369 (Chapter 5), DETC and BBK (Chapter 6), benzil, biacetyl and tetramethylbenzil (Chapter 7).

Considerations on the methodology applied It is important to mention that, for the complete analysis of the photochemical and photophysical properties of the PIs, covering the computation of the multiphoton absorption and emission properties, optimization of the excited states, computation of the photophysical rates and investigation of the radicals formed and subsequent polymerization process, several programs had to be employed due to the impossibility to analyze and simulate all the properties with the usage of one program. Specifically: Gaussian16 Rev.C.01, Dalton 2020.0, ADF 2020.1, Turbomole V7.4-V7.5, MOMAP 2022A (version 2.3.3), ORCA Version 4.2.1 and Dynavib were employed.

4.1 Computation of absorption properties

The 1PA spectra [136], emission spectra and subsequent multiphoton (two-[137, 82] and three-photon [82, 138]) absorption spectra were investigated using TD-DFT starting from the previously optimized ground state geometry. For all PIs spectra were computed in implicit acetonitrile (ACN), for DETC they were also performed in the gas phase, PETA, DMSO and DCM. The solvent was treated implicitly employing polarizable-continuum model (PCM) (if performed in Gaussian 16 and Dalton) and conductor-like screening model (COSMO) (when performed in Turbomole) [139, 140]. For the computation of

the 1PA spectra the time-dependent (TD)-CAM-B3LYP [124]-Grimme's D3-dispersion correction with Becke-Johnson damping (D3(BJ))[119]/def2-TZVP [141, 142, 143] method was employed; in the case of BBK the Tamm-Dancoff approximation (TDA)-CAM-B3LYP-D3(BJ)/def2-TZVP method was used. Norrish type II PIs i.e. DETC and BBK, the TD-B3LYP [144]-D3(BJ)/def2-TZVP and TDA [145]-B3LYP-D3(BJ)/def2-TZVP level of theory were added, respectively. 1PA spectra were performed in Gaussian16 Rev.C.01 [146] for all PIs. 2PA spectra were computed in Dalton 2020.0 [147] with PCM model employing TD-CAM-B3LYP-D3(BJ)/def2-TZVP for DETC, Irgacure 651 and Irgacure 369 (TD-B3LYP-D3(BJ)/def2-TZVP only for DETC) while TDA-B3LYP-D3(BJ)/def2-TZVP and TDA-CAM-B3LYP-D3(BJ)/def2-TZVP were used for BBK. Spectra computed in dichloromethane (DCM) and dimethylsulfoxide (DMSO) for DETC were computed in Dalton 2020.0 with TD-B3LYP-D3(BJ)/def2-TZVP while spectrum in PETA in TD-B3LYP-D3(BJ)/def2-TZVP was computed in Turbomole V7.5 employing the COSMO [140] solvation model due to the absence of PETA model in Dalton 2020.0. 3PA spectra [143] for DETC and BBK were computed in Dalton 2020.0 with TD-CAM-B3LYP-D3(BJ)/def2-TZVP and TD-B3LYP-D3(BJ)/def2-TZVP for DETC and TD-CAM-B3LYP-D3(BJ)/def2-SVP and TD-B3LYP-D3(BJ)/def2-SVP in the gas phase, due to lack of TDA and solvation model implementation in the software. The def2-SVP basis set was used for BBK to reach convergence. 2PA and 3PA absorption spectra were calculated simulating the experimental setup with a double laser beam, linearly polarized light, and parallel polarization[137]. Transition moments were defined for two and three photons of the same frequency, respectively. The spectra were plotted with half-width at half-maximum (HWHM) of 0.1 eV and Lorentzian-type broadening function. The 2PA and 3PA cross sections (σ_{2PA} and σ_{3PA}) were calculated using the following equations implemented in the Dalton program. The references for the equations are [82] and [138], respectively:

$$\langle \sigma_{2PA} \rangle = \frac{N\pi^2 \alpha a_0^5 \omega^2}{c} \langle \delta^{2PA} \rangle g(2\omega, \omega_0, \Gamma) \tag{4.1}$$

$$\langle \sigma_{3PA} \rangle = \frac{N\pi^3 \alpha a_0^8 \omega^3}{3c^2} \langle \delta^{3PA} \rangle g(2\omega, \omega_0, \Gamma) \tag{4.2}$$

where N is an integer value, α is the fine structure constant, a_0 is the Bohr radius, ω is the photon energy in atomic units, c is the speed of light, δ^{2PA} and δ^{3PA} are the rotationally averaged 2PA and 3PA strength, respectively. The lineshape function representing spectral broadening effects is denoted as $g(2\omega, \omega_0, \Gamma)$. The rotationally averaged 2PA and 3PA strengths (in atomic units) were obtained from the 2PA and 3PA transition moments S for linearly polarized light with parallel polarization[148, 149, 150] and two photons of the same energy, calculated as follows[137, 82]:

$$\langle \delta^{2PA} \rangle = \frac{1}{15} 2 \sum_{a,b} S_{ab} S^{ab} + \sum_{a,a} S_{aa} S^{bb} \tag{4.3}$$

$$\langle \delta^{3PA} \rangle = \frac{1}{35} 2 \sum_{a,b} S_{ab} S^{ab} + 3 \sum_{a,a} S_{aa} S^{bb} \tag{4.4}$$

The TA spectra were calculated for Norrish type I, Norrish type II and two-step absorption photoinitiators (PIs) in ACN using the TD-(U)CAM-B3LYP-D3(BJ)/def2-TZVP (for Irgacure 651, Irgacure 3609, DETC, benzil, biacetyl and tetramethylbenzil) and TDA-(U)CAM-B3LYP-D3(BJ)/def2-TZVP (for BBK) approach, respectively employing the optimized geometry of T_1 as the starting point. In the case of DETC, BBK and biacetyl the TA spectra were calculated also employing TD-(U)B3LYP-D3(BJ)/def2-TZVP and TDA-(U)B3LYP-D3(BJ)/def2-TZVP (only BBK). Spectra were performed with Gaussian16 Rev.C.01.

In the case of DETC and two-step absorption PIs, to assess the reliability of the TD-DFT approach in predicting singlet and triplet vertical excitation energies, the GW-BSE[129, 151] method was also utilized. The GW-BSE calculations were carried out in Turbomole V7.4, considering the optimized ground state and first triplet state geometries for singlets and triplets, respectively. Vertical excitation energies were corrected by eigenvalue-only self-consistent GW (evGW) calculations, employing the contour deformation (CD) variant[152], where the Green's function G0 was computed from the DFT wavefunction and the quasi particle eigenvalues were updated iteratively in the calculation of G and W (evGW). The scheme reported in Ref.[153] was adopted, where firstly the electron self-energy operator within the GW approximation is constructed and the one-particle Green's function is calculated, yielding the quasi-particle energies that correspond to single-electron ionization energy and electron affinity[154]. In a second step, the two-particle interaction is constructed, and the BSE for the two-particle Green's function is solved, resulting in the neutral excitation energies[154, 126]. For these calculations, the def2-TZVP basis set, def2-TZVP auxiliary basis set[143, 155], and the resolution of identity (RI) approximation[156, 157] were employed. Calculation were performed in the gas phase and ACN (COSMO) using CAM-B3LYP and B3LYP. The convergence criterion for self-consistent field (SCF) energies was set to 10^{-8}.

In addition, for DETC, the comparison between the TD-DFT (CAM-B3LYP) method was calibrated with wavefunction-based methods like coupled cluster (CC2), spin-component scaled coupled cluster (SCS-CC2), second order algebraic diagrammatic construction with spin-component scaled variant (SCS-ADC2), and scaled-opposite-spin couple cluster (SOS-CC2) methods [158, 159, 137, 130, 160, 161]. All methods mentioned were applied in combination with the def2-TZVP basis set in implicit ACN. The excitation energies were computed using both the optimized S_0 and S_1 geometry computed with TD-DFT-CAM-B3LYP in ACN. The solvation effects were included by employing the COSMO model. In the case of SCS-ADC2, corrected linear response (cLR) correction[162] was also applied. The latter were not computed for the other wavefunction-based methods, because they are not yet implemented in Turbomole (up to V.7.7)[163]. To be consistent, the singlet and triplet vertical excitation energies with the inclusion of the cLR effects with TD-DFT CAM-B3LYP starting from both S_0 and S_1 previously optimized geometries were computed in Gaussian16 Rev.C.01.

4.2 Geometry optimization

The ground state geometry of the Norrish type I, Norrish type II and two-step absorption PIs investigated in the thesis was optimized and used as the starting point for subsequent calculations involving the excited states. As for excited states of Irgacure 651, TD-CAM-B3LYP-D3(BJ)/def2-TZVP in ACN were used to optimize the lowest singlet and triplet excited states geometries (S_1 and T_1), respectively. The S_1 state of Irgacure 369 was optimized with TD-CAM-B3LYP-D3(BJ)/def2-TZVP in ACN and gas-phase and T_1 state was optimized with TD-CAM-B3LYP-D3(BJ)/def2-TZVP in ACN and gas-phase. For DETC and BBK, the optimization of the excited states was performed with both TD-CAM-B3LYP-D3(BJ)/def2-TZVP and TD-B3LYP-D3(BJ)/def2-TZVP in ACN (including TDA approximation for BBK). The excited states of two-step absorption PIs were optimized with TD-CAM-B3LYP-D3(BJ)/def2-TZVP in ACN. The optimization of ground and excited states for all PIs investigated was performed using Gaussian16 Rev. C.01, employing a default ultra-fine grid for numerical integrations and an energy convergence criterion of $10^{-}8$. The solvent (ACN) was employed through the PCM model. A non-equilibrium solvation method was used for single-point calculations, while an equilibrium PCM procedure was employed for the optimization of excited state geometries. The optimized geometries obtained were confirmed through vibrational analysis. In the case of excited states, additional confirmation was obtained through analysis of MOs. The computational scheme employed in this study was optimized based on available experimental data and calculations of the 0-0 transition energy (ν_{00})[164, 165] between the the first excited singlet state and the ground state, using different DFT functionals. For completeness, the energy of the optimized T_1 state for each investigated PI was compared to the optimized T_1 energy with unrestricted DFT approach and the deviations was less than 0.01 eV in the case of B3LYP and *sim* 0.1 eV in the case of CAM-B3LYP.

4.2.1 Beyond the linear response approach

When performing excited state calculations in solution, it is crucial to distinguish between equilibrium and non-equilibrium scenarios. The solvent responds differently to changes in the solute state, involving rapid polarization of its electron distribution and slower molecular reorientation, such as rotation. Equilibrium calculations depict situations where the solvent has ample time to fully respond to the solute in both ways, such as during geometry optimization, which occurs on a timescale similar to molecular motion in the solvent. On the other hand, non-equilibrium calculations are suitable for processes too swift for the solvent to respond fully, such as vertical electronic excitations. Equilibrium solvation is the default for TD-DFT excited state geometry optimizations, where the solvent response is considered in both polarization and molecular reorientation. Non-equilibrium is the default for TD-DFT energies, particularly when using the default PCM procedure. In regular TD SCF calculations, the LR approach is employed, treating the ground state reference and solvent reaction field as self-consistent. Conversely, the state-specific (SS)[166, 167] approach calculates energy in solution by ensuring the electrostatic potential aligns with the solvent reaction field (external Iteration (EI)[166, 167]), achieving equilibrium with the excited state density. For excitations involving significant density rearrangement,

the LR scheme is insufficient as it neglects the density-dependent relaxation of solvent polarization and therefore, to bridge the gap between LR and SS computed vertical excitation energies, maintaining computational feasibility, the cLR approach was developed. This method employs a linear response approach to describe the formation and relaxation of an electronically excited solute in the presence of a time-dependent solvent reaction field. Essentially, the cLR approach modifies the self-consistent reaction field in equilibrium with the ground SCF electron density, incorporating additional solvation terms to approximate the EI approach, which is computationally more demanding.

To broaden the analysis of the properties of all investigated PIs, absorption and emission energies were computed using LR, cLR, and EI (SS) methods. The dynamic behavior of the solvent played a crucial role in selecting the appropriate functional to accurately reproduce the photophysical properties of the PIs. Choosing the right functional in TD-DFT is a critical aspect influencing the accuracy of predictions for electronic excitations and spectroscopic properties. Given the absence of a universally secure choice for a specific functional, the decision often relies on the system's specific properties, the nature of the system under investigation, and the available computational resources. It is customary to benchmark and validate the selected functional against experimental data and/or higher-level QM methods when possible to assess its reliability. Generally, for large systems where higher-level methods are not feasible, functionals are chosen based on the comparison of vertical excitation energies (absorption spectra) and the zero-point energy obtained as the difference between the optimized ground state and the first singlet state (ν_{00} energy) with available experimental data. However, as extensively detailed in Chapter 5 and 6, even though the B3LYP functional could reproduce absorption spectra and ν_{00} energy close to the experiment, it exhibited catastrophic values for emission properties, particularly when the CT upon excitation is not negligible, leading to an incorrect interpretation of the characteristics of the PIs. Therefore, the validation of the functional used should not be limited to the default LR approach, computing vertical excitation energies and E_{00} energies and comparing them to experiment. It should be extended to include the SS method and cLR approaches.

4.2.2 Analysis of charge transfer character

The analysis of the CT character associated to each singlet and triplet excitation from the ground state for Norish type I and Norrish type II PIs presented in the thesis was conducted through the investigation of the so called CT indices [168]. Data are reported in Tables 5.7,6.14 and 6.15 where H is the average distribution of electron and hole, H_{CT} is the average degree of spatial extension of hole and electron distribution in CT direction, t is the separation degree of electron and hole in the charge transfer direction (t = D - HCT), D is the total magnitude of CT length and Sr is the overlap of electrons and holes. Data were computed using Multiwfn (version 3.6) analyzer. The density transition upon excitation (electron and hole) for all PIs reported in the thesis was analyzed using Multiwfn (version 3.6)[169] while the analysis of MOs was conducted via Gaussian 16 Rev.C.01 and Turbomole V7.4.

The analysis of the CT associated to each transition (from ground state to singlets and triples) was also validated through the SCS-CC2 approach for DETC and Irgacure 369, which is known to deliver more accurate data than DFT in terms of capturing electron correlation effects[158]. In particular the

S1 state of DETC and Irgacure 369 presented high CT character with conformation problems during the optimization (see Chapter 5 and 6). Data were computed in Turbomole V7.5 employing COSMO solvation model for ACN starting from the S_0 geometry previously optimized with CAM-B3LYP-D3(BJ)/def2-TZVP in ACN (PCM model).

4.3 Vibrationally resolved singlet and triplet spectra

The TD-DFT calculations were utilized to obtain vibronically resolved singlet and triplet spectra. For Norrish type II PIs the FC[170, 171, 172] approximation was employed, and the linear coupling model (LCM)[173, 174]-G16 served as the PES model, neglecting Duschinsky rotation[175]. For biacetly the spectrum was computed within the FC-time independent (TI) approximation including Duschinsky rotation. All spectra were generated at a temperature of 100K. A Lorentzian-type broadening function was applied, and the spectra were plotted with HWHM of 80 cm^{-1} (equivalent to 0.01 eV) and the convergence factor of $1.0x10^{-4}$ was utilized. The transitions considered were from the vibrational levels of the initial state (ground state or first triplet state) to the vibrational levels of the final excited state (singlet or triplet). The strength of each transition was determined based on the population of the corresponding state and the overlap between the initial and final vibrational wavefunction. The calculations were performed using the Dynavib program[176, 177] inputting the optimized geometries performed in Gaussian 16 in implicit ACN. The vibronic absorption from both ground state and T_1 and emission spectra from S_1 of DETC were performed with TD-CAM-B3LYP-D3(BJ)/def2-TZVP and TD-B3LYP-D3(BJ)/def2-TZVP. The TA spectra of BBK were performed with both TDA-CAM-B3LYP-D3(BJ)/def2-TZVP and TDA-B3LYP-D3(BJ)/def2-TZVP. The TA spectrum of biacetyl was performed with TD-CAM-B3LYP-D3(BJ)/def2-TZVP.

4.4 Thermodynamic properties of photoinitiators

All thermodynamic quantities were computed after vibrational analysis. Spin-unrestricted approach was used for the optimization of species with unpaired electrons i.e. radicals and biradicals considered. For the simulation of the homolytic cleavage of the broken bonds (e.g. C-H,C-N) of DETC and BBK at different electronic states (ground, singlet and triplet excited) bond dissociation energy (BDE)[178], as well as the Gibbs free energy were employed. Both (U)CAM-B3LYP-D3(BJ)/def2-TZVP and (U)B3LYP-D3(BJ)/def2-TZVP level of theory were used, reported to be valuable approaches (with the mean absolute error of 2.4 kcal mol^{-1}) in good agreement with experimental values [178, 179]. Similarly, the approach for the computation of the C-C bond cleavage of Norrish type I using (U)CAM-B3LYP-D3(BJ)/def2-TZVP and (U)B3LYP-D3(BJ)/def2-TZVP and two-step absorption PIs using (U)CAM-B3LYP-D3(BJ)/def2-TZVP was computed according to:

$$BDE_{(\text{A-B})} = \Delta H_{\text{AB}} - (\Delta H_{\text{A}} + \Delta H_{\text{B}}) \tag{4.5}$$

where AB is the bond broken and formed in the chemical reaction, H_A and H_B are enthalpy values of respective optimized radicals. The Gibbs free energy can be defined as:

$$\Delta G = (\Delta G_{\mathrm{P}} - \Delta G_{\mathrm{R}}) \tag{4.6}$$

where ΔG_{P} and ΔG_{R} refer to the Gibbs free energy for products and reagents obtained as a sum of electronic and thermal free energy, respectively. The Norrish Type II reaction mechanism of DETC with DBA and the cleavage reactions of Irgacure 651, Irgacure 369 and biacetyl were calculated using the approach based on transition state (TS) and intrinsic reaction coordinate (IRC)[180], as implemented in Gaussian16 Rev.C.01. The energy profiles of forward and reverse directions both in the ground (only DETC) and first triplet excited states were explored. The transition state geometry was verified by vibrational analysis, and the final activation energy barrier was used in the Eyring[181] equation to determine the rate constant of the HAT reaction:

$$k = \frac{k_{\mathrm{B}}T}{h} e^{-\frac{\Delta G^{\ddagger}}{RT}} \tag{4.7}$$

where where k is the rate constant, $\Delta G^{\ddagger}$ is the Gibbs energy of activation, κ is the transmission coefficient, k_{B} is the Boltzmann constant, T is the temperature, and h is the Planck constant. Temperature of 298 K and pressure of 1 atm were considered. Both (U)CAM-B3LYP-D3(BJ)/def2-TZVP and (U)B3LYP-D3(BJ)/def2-TZVP level of theory were employed in Gaussian16 for DETC and Irgacure 651 while only (U)B3LYP-D3(BJ)/def2-TZVP was used for Irgacure 369 due to convergence issue of the transition state when employing the CAM-B3LYP functional. For two-step absorption (U)CAM-B3LYP-D3(BJ)/def2-TZVP approach was employed. The reaction between DETC and BBK with PETA monomer could not be performed via the transition state method due to the large number of atoms considered and subsequent convergence issue in Gaussian16.

4.5 Photophysical properties of photoinitiators

The determination of nonradiative and radiative rates, specifically IC, ISC, RISC and fluorescence involved the utilization of molecular materials property prediction package (MOMAP) 2022A (version 2.3.3) [182, 183, 184, 185, 186, 187], employing the FC approximation [170], Fermi golden rule (FGR) and second-order perturbation theory[188]. The optimized geometries in Gaussian16 at the CAM-B3LYP-D3(BJ)/def2-TZVP level of theory in ACN were given as input in MOMAP software with the respective adiabatic energies (including zero-point energy correction (ZPVE)) and electric dipole moments for all PIs investigated in the thesis. In addition, for BBK, rates were computed employing B3LYP-D3(BJ)/def2-TZVP level of theory.

The non-radiative decay rate constant can be defined as:

$$k_{\mathrm{nr}} = \frac{2\pi}{\hbar} \sum_{\nu_i,\nu_f} \hat{P}_{i\nu_i}(T) \left| \hat{H}'_{\nu_f,\nu_i} + \sum_{\nu_f} \frac{\hat{H}'_{\nu_f,\nu_j} \hat{H}'_{\nu_j,\nu_i}}{E_{i\nu_i} - E_{f\nu_f}} \right|^2 \delta \times (E_{i\nu_i} - E_{f\nu_f}) \tag{4.8}$$

where $\hbar$ is the reduced Planck's constant, ν_i, ν_f, and ν_j are the vibrational quanta of the initial, final, and intermediate states, $\hat{P}_{i\nu_i}(T)$ is the Boltzmann distribution of the vibrational manifolds in the initial state, and $\hat{H}'$ is the sum of the non-adiabatic coupling $\hat{H}^{\mathrm{BO}}$ and spin-orbit coupling $\hat{H}^{\mathrm{SO}}$ operators. When the two states are in the same spin manifold, only the first-order perturbation is considered, and the spin-orbit coupling can be neglected. The IC rate constant, after applying the Fourier transformation, reads:

$$k_{\mathrm{IC}} = \frac{1}{2} \int dt e^{(i\omega_{if}t)} \sum_{k,l} Z_i^{-1} \langle \Theta_f \hat{P}_k \Theta_i \rangle \langle \Phi_i \hat{P}_f \Phi_f \rangle \times \mathrm{Tr}\left[\hat{P}_k e^{(-i\tau_f \hat{H}_f)} \hat{P}_l e^{(-i\tau_i \hat{H}_i)} \right] \tag{4.9}$$

where $\hat{P}_k$ is the nuclear momentum operator for the k_{th} mode, and Φ and Θ are the electronic and vibrational state vectors, respectively. Z_i^{-1} is the partition function of the initial state, $\tau_i = -i\beta - t/\hbar$, $\tau_f = t/\hbar$, and $\hat{H}_i$ and $\hat{H}_f$ are the harmonic oscillator Hamiltonian of the initial and final states, respectively. The DFT/TDDFT approach can be used for solving the thermal vibration correlation function (TVCF)[189] in eq. 4.9. Similarly, the ISC rate constant is computed as:

$$k_{\mathrm{ISC}} = \frac{2\pi}{\hbar}^2 \int dt\, e^{(i\omega_{if}t)} Z_i^{-1} \rho_{\mathrm{ISC}}(t,T) \langle \Phi_f \hat{H}^{\mathrm{SO}} \Phi_i \rangle^2 \tag{4.10}$$

Each term can be written as a time integration of vibrational correlation functions such as:

$$\left(e^{-i\tau_f \hat{H}_f} e^{-i\tau_i \hat{H}_i} \right)^T, \left(e^{-i\tau_f \hat{P}_k} e^{-i\tau_i \hat{H}_i} \right)^T \; or \left(e^{-i\tau_f \hat{P}_k} e^{-i\tau_i \hat{P}_l} \right)^T \tag{4.11}$$

multiplied by the appropriate prefactors from the corresponding electronic couplings[185]. For radiative processes (fluorescence and phosphorescence) analogous vibrational correlation function formalisms, as in equation 4.9 were applied. In this case, the electronic coupling term becomes the electric dipole moment μ. For the emission spectrum as an example, FGR gives:

$$\sigma_{\mathrm{em}} = \frac{4\omega^3}{3c^3\hbar} \sum_{\nu_i,\nu_f} \hat{P}_{i\nu_i}(T) \langle \Theta_{f\nu_f} | \hat{\mu_{fi}} | \Theta_{i\nu_i} \rangle^2 \delta(\omega_{i\nu_i,f\nu_f} - \omega) \tag{4.12}$$

where ω is the frequency, c is the speed of light, i and f are the vibrational quanta of the initial and final state, Θ is the vibrational state vector associated to initial and final state, f_i is the transition dipole moment between initial and final state. Equation 4.12 can easily be expressed as the transition dipole multiplied by a time integration over the correlation function. The radiative decay rate constant is

therefore the integration over the emission spectrum

$$k_r = \int \sigma_{em}(\omega) d\omega \tag{4.13}$$

Rates for IC, ISC and RISC were calculated employing the FC approximation using MOMAP 2022A (version 2.3.3), considering the integral interval of the correlation function i.e. tmax of 1000 fs combined with the integration timestep of the correlation function i.e. dt of 0.01 fs neglecting the Duschinsky rotation. For Irgacure 651 the ISC and RISC and rates were computed including the Dushinsky rotation. Nonadiabatic coupling matrix elements (NACME) [190, 191, 192] for IC and SOC for ISC were calculated using Gaussian16 Rev.C.01 and ADF 2020.1 [193], utilizing the respective optimized structures. SOC was calculated at the Scalar level within ZORA formalism [194, 195, 175], where relativistic effects are included, adding the so-called non-equilibrium properties (as implemented in ADF 2020.1). SOC[196] was calculated in ACN and TZP basis set with CAM-B3LYP (and B3LYP for BBK) functional for all PIs. In the case of BBK, SOC included TDA. SOC in CAM-B3LYP for two-step absorption PIs were computed in ACN without the inclusion of non-equilibrium effects. SOC for the S_0-T_1 coupling were computed in ORCA Version 4.2.1[197, 198] employing the conductor-like polarizable continuum model (CPCM) [199] model for ACN using quasi-degenerate perturbation theory and CAM-B3LYP (also B3LYP for BBK) functional. In the case of BBK TDA was included. The radiative rate constants, i.e. fluorescence and phosphorescence, were calculated using the respective optimized singlet and triplet state structures at CAM-B3LYP in ACN and with MOMAP. The electric dipole moments of absorption and emission used in MOMAP for the computation of the phosphorescence rate were computed in Dalton 2020.0 with the respective functional. Adiabatic Hessian (AH) PES model within TD-DFT was used for the computation of all the radiative rates.

Validation of the photophysical rates

In order to assess the quality of the IC and fluorescence rates computed for DETC with CAM-B3LYP functional, the integration time step and the Duschinsky rotation (see Table 4.1) were tested and the respective graphs with IC rate constant (k_{ic}, s^{-1}) in Y in logarithmic scale versus adiabatic energy (in Hartree) in X in linear scale were reported in Figure 4.1. The distribution of time (time in fs) vs real part ($TVCF_{RE}$) of correlation function for all cases of Table 4.1 is reported in Figure 4.2. Data for B3LYP was not generated.

Table 4.1: Rates of internal conversion (IC, s^{-1}) and fluorescence (Fluorescence, s^{-1}) obtained in MOMAP 2022.0 with different values of integration time step (dt) combined with consideration/neglect of Duschinsky rotation (t is true or f is false). The f-scale refers to a scaling factor added to the integral time to reach the convergence of the correlated function.

	IC	Fluorescence	dt	Duschinsky
1	$6.13x10^{11}$	$6.38x10^{8}$	1	t
2	$1.35x10^{6}$	$4.59x10^{8}$	1	f
3	$3.02x10^{11}$	$1.23x10^{8}$	0.01	t
4	$0.43x10^{3}$	$4.44x10^{8}$	0.01	f
5*	$1.60x10^{8}$	$4.30x10^{8}$	0.01	f
AS	$2.22x10^{8}$	$4.86x10^{8}$	0.01	f

*as reported in Ref. [200]

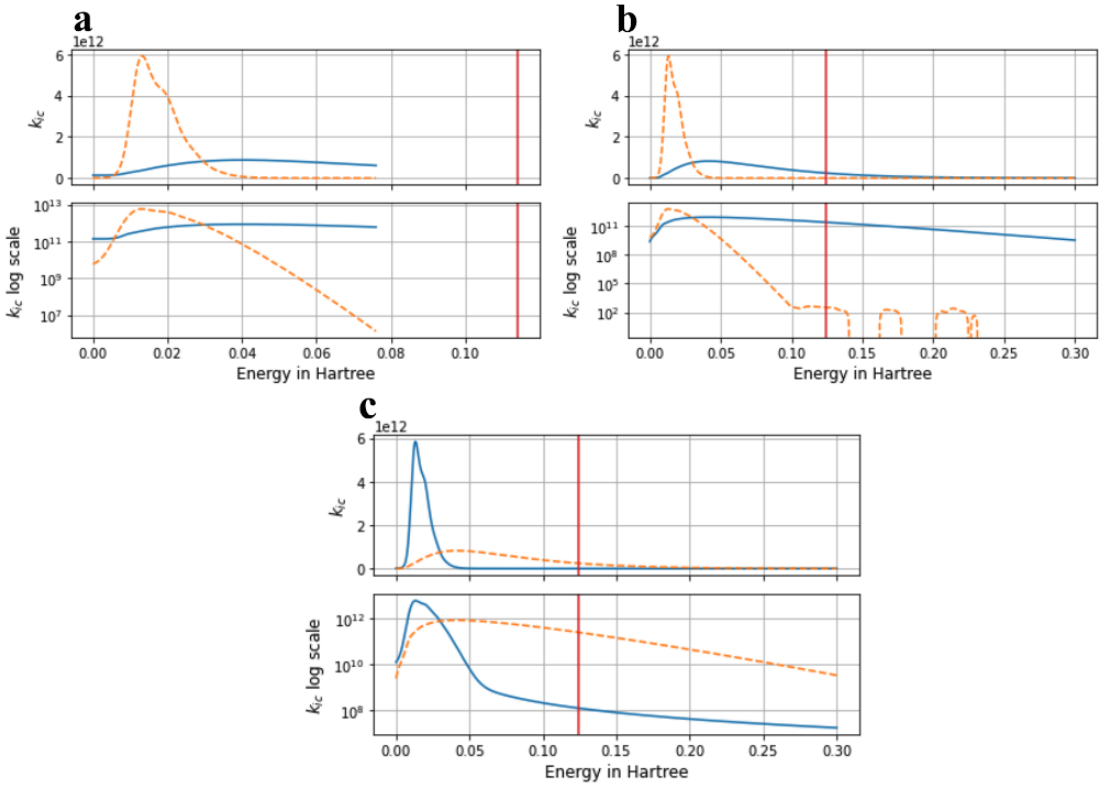

Figure 4.1: Comparison of the evolution of the IC rates as a function of the adiabatic energies, i.e. IC rate constant (k_{ic}, s^{-1}) in Y in log scale versus adiabatic energy (energy in Hartree) in X in linear scale. a) comparison of the case 1 (blue solid line) with 2 (orange dashed line); b) comparison of 3 (blue solid line) with 4 (orange dashed line); c) comparison of 3 (orange dashed line) with 5 (blue solid line). Adiabatic energy for S_1-S_0 (0.1118 Hartree, CAM-B3LYP) is shown as a red straight line.

Data reported in Figure 4.1 shows the crossing point of the IC rate with the adiabatic energy (depicted as a red straight line) only for cases 3 and 5. Due to the fact that the IC rate cannot be three orders of

magnitude faster than fluorescence for DETC since this dye emits the light, as discussed in the previous revision of the paper, and the lifetime of S_1 in experiment is 1 ns and 0.25-0.44 ns in toluene and methanol [20, 103], the setup, used in the calculation of case 5, was chosen for the IC rate. In addition, since there are no differences between AH and adiabatic shift (AS) (see Table 4.3), AH was kept as a model for all calculations.

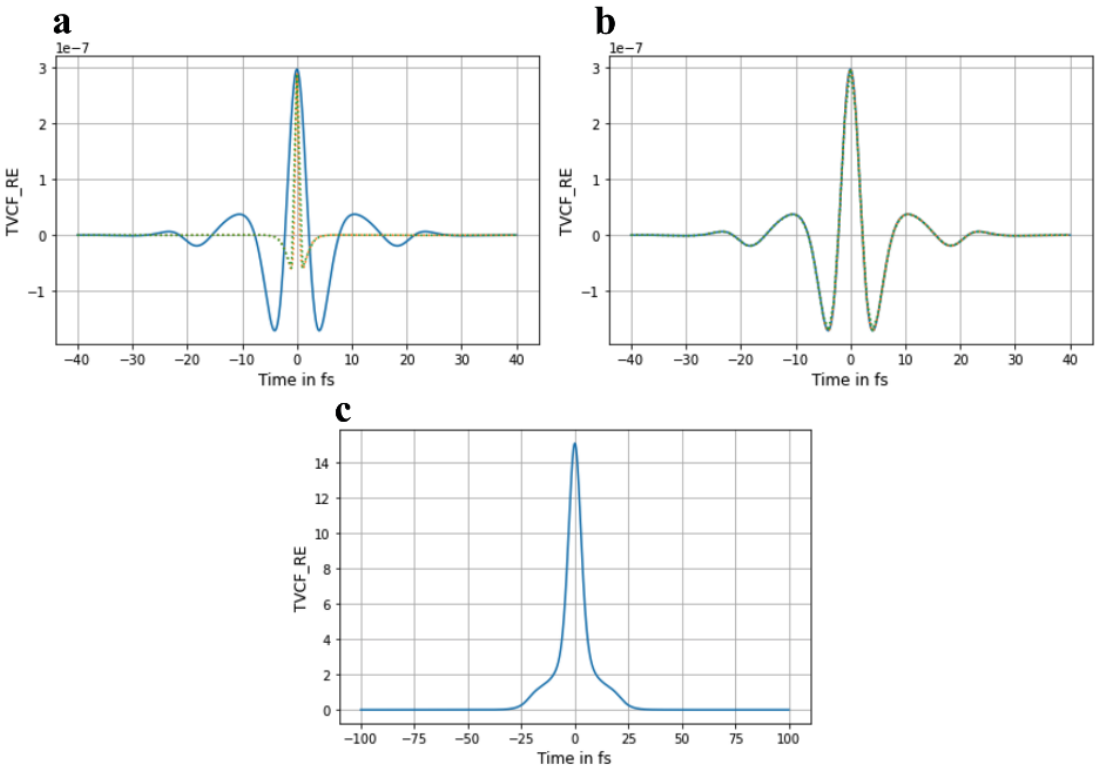

Figure 4.2: Comparison of the evolution of the IC rates as a function of the adiabatic energies, i.e. the distribution of time (Time in fs) vs real part (

Table 4.2: Calculated rates of internal conversion (IC) and fluorescence (fluorescence) of DETC in ACN (in s^{-1}). Rates were computed with MOMAP using t of 1000 fs, dt of 0.01 fs and neglecting Duschinsky rotation. The respective lifetimes (in ns) are given for clarity. The lifetime of S_1 in experiment is $\sim$ 1 ns [20] and 0.25-0.44 ns [103] in toluene and methanol.

	IC	Fluorescence	IC lifetime	Fluorescence lifetime
B3LYP	1.00×10^7	1.10×10^6	99.44	908.17
CAM-B3LYP	1.60×10^8	4.30×10^8	6.25	2.33

The AH approach adopted for the computation of fluorescence and S_1-S_0 internal conversion rates, normally, is the most accurate but, if the change of geometry from S_0 to S_1 is large, vertical models do perform better (again ample literature by Cerezo others on this). AH will work only in a very harmonic

potential when one can hamonically project the Hessians of the two states on one another. In case of significant reorganization, it will fail. The comparison between AS defined as ground state Hessian on S_1 geometry and AH is reported in Figure 4.3 and Table 4.3. Data shows no significant differences between two approaches. Considering the fact that the structural differences between geometries of S_0 and S_1 in the case of the CAM-B3LYP functional are minor (see Chapter 6, Figure 6.6), we have used the AH model in the present study.

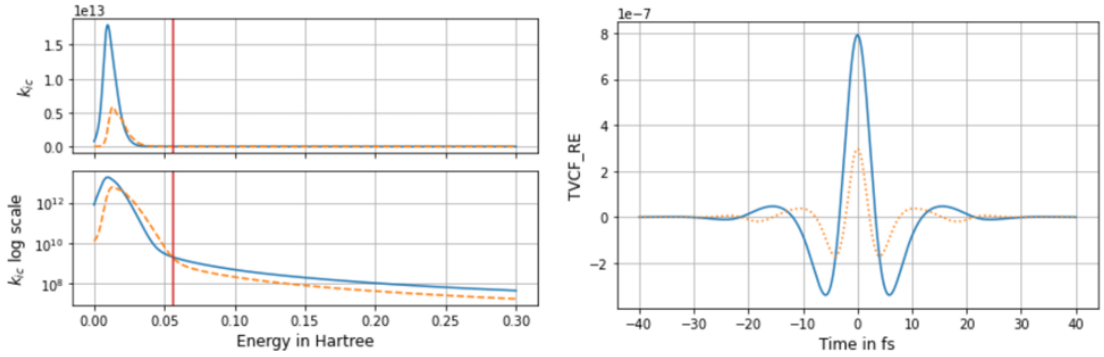

Figure 4.3: Comparison of the evolution of the internal conversion (IC) rates as a function of the adiabatic energies, i.e. IC rate (k_{ic}) in Y in log scale versus adiabatic energy (energy in Hartree) in X in linear scale (left) and the distribution of time (Time in fs) vs real part ($TVCF_{\mathrm{RE}}$) of correlation function (right) for AH corresponding to case 5 in Table 4.1 (orange,dashed line) and AS (blue solid line).

Table 4.3: Internal conversion and fluorescence rates using AH and AS models considering the same setup as reported in Table 4.1 for CAM-B3LYP in ACN.

	IC rate	Fluorescence rate
AH	$1.60\text{x}10^{8}$	$4.30\text{x}10^{8}$
AS	$2.22\text{x}10^{8}$	$4.86\text{x}10^{8}$

Every rate presented in the thesis underwent validation by examining the convergence of the correlation function, unless explicitly stated otherwise.

4.6 Experimental measurements

Note: Experimental measurements were conducted by Pascal Kiefer and Tobias Messer (Institute of Applied Physics (APH), Karlsruhe Institute of Technology (KIT), Germany) and are added for clarity.

In Ref.[29], to investigate the polymerization laser threshold of various DETC-containing resists, the previously reported setup [28] was applied. For that a mode-locked fs laser oscillator (Mai Tai HP, Spectra-Physics), working at RP=80 MHz repetition rate and λ=820 nm center wavelength, a microscope lens (Leica HCX PL APO 100x/1.4-0.7 Oil CS) for beam focussing in oil-immersion mode, and an

acousto-optic modulator (AA MT80-A1.5-IR) were utilized. The resists were prepared by adding DETC (30 µmol), DBA (7.5 µmol, 15 µmol, 30 µmol, 60 µmol, and 120 µmol), or DPIHFP (15.6 µmol, 31.2 µmol, and 62.4 µmol), respectively, to PETA (2 g) in a vial under constant stirring. DETC was purchased from Exciton. DPIHFP (>97.5% purity) was purchased from TCI. PETA (technical grade) and DBA (99.5% purity) were purchased from Sigma-Aldrich. To measure the laser polymerization threshold for a given exposure time texp, separated points of the photoresist were illuminated with different laser powers P. The lowest laser power, which still forms a visible polymer dot[46] after development with acetone is then defined as the laser polymerization threshold power P_{th}.

5

Norrish type I photoinitiators

This section of the thesis delves into the study of Norrish type I PIs specifically focusing on their radical generation pathway known for producing radicals from the T_1 state upon bond cleavage. The investigated compounds in the Chapter are the commercial PIs Irgacure 651 and Irgacure 369, whose chemical structure is illustrated in Figure 5.1. The comprehensive theoretical investigation encompasses an exploration of their chemical properties and reactivities, including the meticulous analysis of absorption and emission characteristics, excited states (singlets and triplets), photophysical rates and bond cleavage reaction contributing to FRP. This marks the first instance where such a detailed analysis has been conducted through QM calculations.

Data presented in this Chapter will be reported in the following paper (planned submission before publication of the thesis): A. Mauri, P. Kiefer, P. Somers et al. Polymerization mechanisms of Norrish type I and type II photoinitiators in 3D laser nanoprinting: the case of Irgacure 651, Irgacure 369 and BBK. Chemistry-A European Journal (2024 planned).

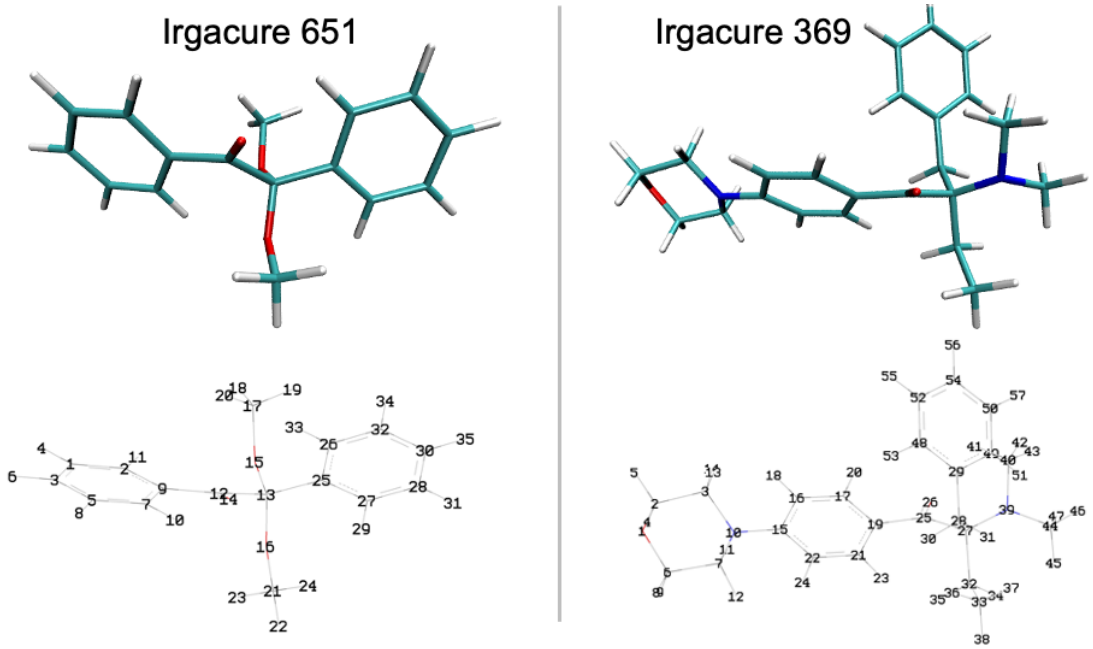

Figure 5.1: Ground state structure of Irgacure 651 and Irgacure 369 optimized using CAM-B3LYP-D3(BJ)/def2-TZVP in implicit ACN (PCM model) with respective atom labels.

5.1 One-photon absorption and emission properties

In order to reproduce the experimental available data on the photochemical properties and reactivity of Irgacure 651 and Irgacure 369, depicted in Figure 5.1, absorption and emission spectra were computed (see Figure 5.2). The functional employed was chosen not only on the good agreement between calculated multiphoton absorption spectra (i.e., 1PA and 2PA spectra) and available experimental data, as commonly reported in the community [99, 201], but also on the validation of the CT properties of the lowest singlet and triplet transitions and on the investigation of cLR [162] and SS (EI [166, 167]) approaches, as discussed in Section 4.2.1. The computed absorption spectra of Irgacure 651 and Irgacure 369, depicted in Figure 5.2, exhibit bathochromic shift of $\sim$ 14 nm and $\sim$ 17 nm, respectively, compared to experimental data listed in Table 5.1 i.e. 328.45 nm and 303.50 nm (in theory) versus 342 nm and 320 nm (in experiment), respectively [44]. Upon absorption and according to the experimental values, the most probable transition was identified as $S_0 \rightarrow S_1$ with oscillator strength of 0.0022 and 0.0278 for Irgacure 651 and Irgacure 369, respectively (see Tables 5.2 and 5.3).

Table 5.1: Experimental absorption maxima for Irgacure 651 and Irgacure 369 in ACN.

	Irgacure 651	**Irgacure 369**
eV	3.63	3.87
nm	342	320

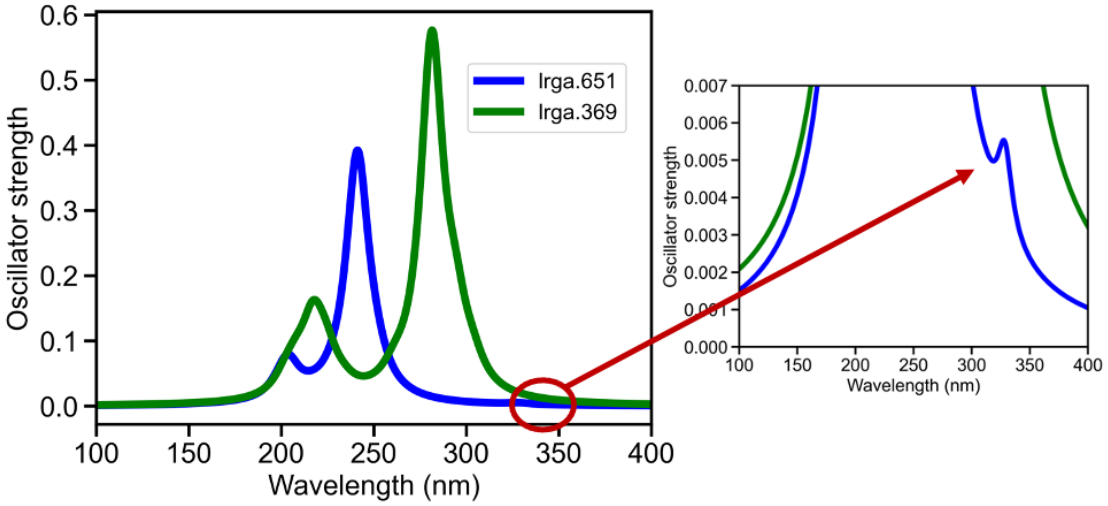

Figure 5.2: Computed one-photon absorption spectra (1PA) of Irgacure 651 (Irga.651) and Irgacure 369 (Irga.369) using TD-CAM-B3LYP-D3(BJ)/def2-TZVP in implicit ACN. Spectra were plotted as reported in Chapter 4. Experimental values are 342 nm and 320 nm for Irgacure 651 and Irgacure 369 respectively.

Table 5.2: Vertical excitation energies (energy in eV and wavelength in nm) for singletexcitations of Irgacure 651 in ACN calculated using TD-CAM-B3LYP-D3(BJ)/def2-TZVP method, starting from the optimized ground state geometry (S_0).

Excited State	Energy	Wavelength	Osc. str.
1	3.78	328.45	0.0022
2	4.94	250.76	0.0267
3	5.14	241.09	0.0378
4	5.46	226.92	0.0067
5	5.69	218.03	0.0020
6	5.76	215.32	0.0022
7	6.05	204.87	0.0019
8	6.09	203.51	0.0549
9	6.22	199.44	0.0076
10	6.29	197.00	0.0007

Table 5.3: Vertical excitation energies (energy in eV and wavelength in nm) for singlet excitations of Irgacure 369 in ACN calculated using TD-CAM-B3LYP-D3(BJ)/def2-TZVP method, starting from the optimized ground state geometry (S_0).

Excited State	Energy	Wavelength	Osc. str.
1	4.09	303.50	0.0278
2	4.22	294.04	0.0895
3	4.41	281.35	0.5447
4	4.75	261.15	0.0210
5	5.31	233.61	0.0099
6	5.53	224.25	0.0487
7	5.70	217.36	0.1058
8	5.89	210.60	0.0102
9	5.98	207.37	0.0285
10	6.13	202.12	0.0217

This $S_0 \rightarrow S_1$ transition mainly corresponds to HOMO → LUMO with contribution of 51.0% (see Table 5.4) for Irgacure 651 while for Irgacure 369 it corresponds to HOMO-3 → LUMO 20.8%, HOMO-4 → LUMO 34.1%, HOMO-5 → LUMO 12% and HOMO-1 → LUMO 11%, see Table 5.5.

Table 5.4: Transition molecular orbitals (MOs) and contributions for Irgacure 651 in ACN with CAM-B3LYP-D3(BJ)/def2-TZVP level of theory.

Transition	Molecular Orbitals	Contribution (%)
$S_0 \rightarrow S_1$	HOMO → LUMO	51.0
$S_0 \rightarrow T_1$	HOMO → LUMO	46.8

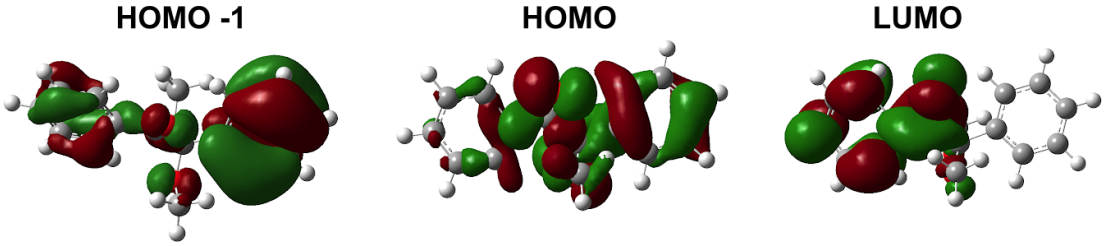

Figure 5.3: Visualization of molecular orbitals (MOs) of Irgacure 651 in ACN obtained using CAM-B3LYP-D3(BJ)/def2-TZVP level of theory. HOMO and LUMO correspond to the highest occupied molecular orbital and lowest unoccupied molecular orbital, respectively. Isovalue of 0.002 a.u. was used for visualization.

Table 5.5: Transition molecular orbitals (MOs) and contributions for Irgacure 369 in ACN with CAM-B3LYP-D3(BJ)/def2-TZVP level of theory.

Transition	Molecular Orbitals	Contribution (%)
$S_0 \rightarrow S_1$	HOMO -1 → LUMO	11.4
	HOMO -2 → LUMO	7.6
	HOMO -3 → LUMO	20.8
	HOMO -4 → LUMO	34.1
	HOMO -5 → LUMO	12.3
$S_0 \rightarrow T_1$	HOMO → LUMO	38.0
	HOMO -1 → LUMO	38.7

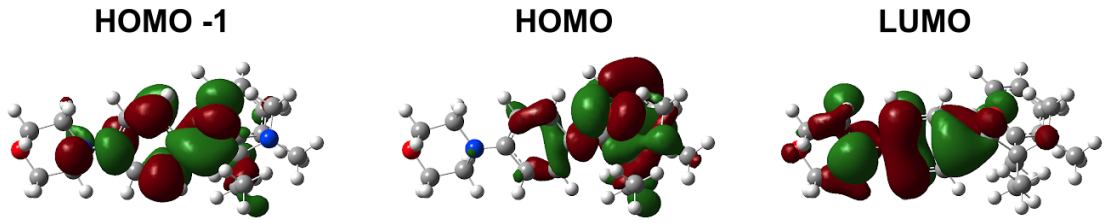

Figure 5.4: Visualization of molecular orbitals of Irgacure 369 in ACN obtained using CAM-B3LYP-D3(BJ)/def2-TZVP level of theory. HOMO and LUMO correspond to the highest occupied molecular orbital and lowest unoccupied molecular orbital, respectively. Isovalue of 0.002 a.u. was used for visualization.

The hole and electron analysis, computed in order to identify the movement of electrons upon excitation, reveals that the $S_0 \rightarrow S_1$ transition, for both Irgacure 651 and Irgacure 369, has $n\pi^*$ character (see Figure 5.5), involving the excitation from the non-bonding (n) to the anti-bonding (π^*) orbital localized on the carbonyl group of the initiators. The T_1 state of Irgacure 651 is mainly characterized by similar $n\pi^*$ character to S_1, localized on the carbonyl bond, while for Irgacure 369 it is evident a more mixed character with $\pi\pi^*$ contribution involving the carbonyl bond of the initiator. The nature of the transitions to the first singlet excited state of Irgacure 651 and Irgacure 369 is in agreement with previously reported studies on similar systems which show $n\pi^*$ character of the first singlet state [51, 99].

The analysis of the MOs contributing to the S_0-S_1 transition of Irgacure 369 was further performed employing the SCS-CC2 method (see Chapter 4), which is known to deliver more accurate data with respect to DFT, especially when CT is involved [158, 159, 137, 130, 160, 161]. Data reported in Table 5.6 and Figure 5.6 show that the S_1 state is characterized by a mix of HOMO → LUMO, HOMO-5 → LUMO and HOMO-6 → LUMO transitions with contribution of 27.1%, 23.4% and 20.5%, respectively. The T_1 state is mainly characterized by HOMO → LUMO with contribution of 83.5%. The the S_1 state investigated employing TD-DFT (see Table 5.5) is mainly characterized by HOMO-3 → LUMO , HOMO-4 → LUMO, HOMO-5 → LUMO, and HOMO-1 → LUMO transitions with contribution of 20.8%, 34.1%, 12% and 11%, respectively. The hole-electron analysis computed for this state with SCS-CC2 shows a larger hole delocalization on the morpholino part with respect to the one computed via TD-DFT (see Figure 5.4) while the presence of the same nπ^* orbital on the carbonyl group is evident for both. The

hole-electron distribution computed for T_1 with SCS-CC2 and TD-DFT share also high similarities. In addition, while the energy of S_1 computed with TD-DFT and SCS-CC2 slightly differ (4.08 eV and 4.04 eV, respectively see Table 5.3), higher is the difference for the energy of T_1 (2.98 eV and 3.59 eV, respectively see Table A.2). These observations might influence the correct representation of, especially, S_1 state via TD-DFT, leading to high distortion of the molecule during the optimization, as further discussed below.

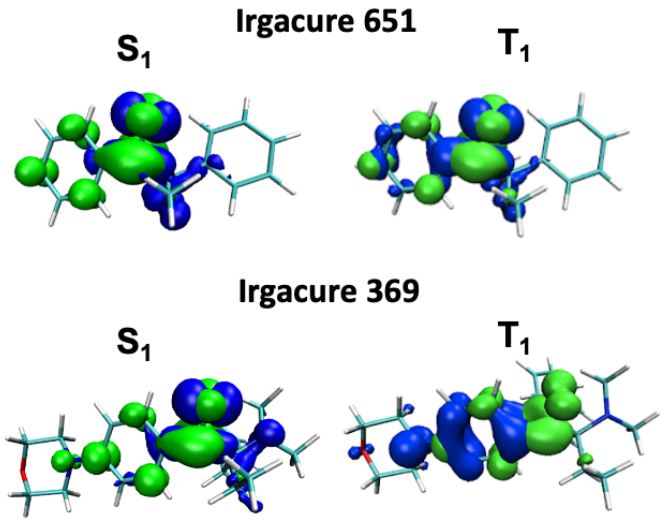

Figure 5.5: Visualization of electron donating (hole, in blue) and electron accepting (electron, in green) density transfer upon excitation of Irgacure 651 and Irgacure 369 from the ground state to first singlet and triplet state with CAM-B3LYP-D3(BJ)/def2-TZVP in ACN (PCM model) level of theory. Isovalue of 0.002 a.u. was used for visualization.

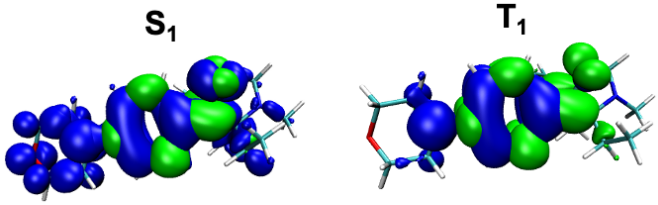

Figure 5.6: Visualization of electron donating (hole, in blue) and electron accepting (electron, in green) density transfer upon excitation of Irgacure 369 from the ground state to first singlet and triplet state with SCS-CC2 in ACN (COSMO model) level of theory. Isovalue of 0.03 a.u. was used for visualization.

Table 5.6: Transition molecular orbitals (MOs) and contributions of Irgacure 369 in SCS-CC2 ACN (COSMO model).

Transition	Molecular Orbitals	Contribution (%)
	HOMO → LUMO	27.1
$S_0 \rightarrow S_1$	HOMO -5 → LUMO	23.4
	HOMO -6 → LUMO	20.5
$S_0 \rightarrow T_1$	HOMO → LUMO	83.5

The CT characteristics of the examined PIs, assessed through diverse parameters, as explained in details in Chapter 4, are listed in Table 5.7.

Table 5.7: For the excited states of Irgacure 651 and Irgacure 369 the charge transfer (CT) data were computed in CAM-B3LYP-D3(BJ)/def2-TZVP. H represents the average distribution of electron and hole, t indicates the degree of separation between the electron and hole in the charge transfer direction (t = D - HCT), where D represents the total magnitude of the CT length, and Sr represents the overlap of electron and hole.

State	H (Å)	t (Å)	D (Å)	Sr (a.u.)
		Irgacure 651		
S_1	2.110	-0.213	1.232	0.495
T_1	2.317	-1.392	0.348	0.608
		Irgacure 369		
S_1	2.346	-0.210	1.495	0.479
T_1	2.613	-0.116	1.977	0.583

A notable D index suggests a substantial distance between the regions of the hole and electron. Based on the D values, the $S_0 \rightarrow S_1$ transition of Irgacure 651, the $S_0 \rightarrow S_1$ and $S_0 \rightarrow T_1$ transitions of Irgacure 369 exhibit values greater than 1.2, indicating a significant CT character. In contrast, the $S_0 \rightarrow T_1$ transition of Irgacure 651 shows much lower D index, suggesting a diminished CT character. The separation of the hole and electron distribution visualized in Figure 5.5 show indeed that the electron and hole for the $S_0 \rightarrow S_1$ transitions of Irgacure 651 and Irgacure 369 are predominantly localized on the carbonyl bond. Although the $S_0 \rightarrow T_1$ transition of Irgacure 651 follows a similar trend, a more mixed distribution of electron and hole is observed on the phenyl ring. The $S_0 \rightarrow T_1$ transition of Irgacure 369 is characterized by a low degree of localization of the electron and hole with a higher degree of separation, resulting in a more prominent CT. The Sr indices, reflecting the overlap between the hole and electron distribution, for $S_0 \rightarrow S_1$ of Irgacure 651, $S_0 \rightarrow S_1$ and $S_0 \rightarrow T_1$ transitions of Irgacure 369 are approximately 0.5, signifying that half of the hole and electron distribution overlaps. The Sr value for the $S_0 \rightarrow T_1$ transition of Irgacure 651 is slightly higher at 0.61, indicating that more than half of the electron and hole distribution overlaps. Additionally, the H indices, which reflect the breadth of the average distribution of the hole and electron, indicate that the distribution of the hole and electron for all transitions of Irgacure 651 and Irgacure 369 is localized. The highest H index is for the $S_0 \rightarrow T_1$ transition of Irgacure 369, which has less local exciton (LE) character. The t index corresponding to the excitations $S_0 \rightarrow S_1$ of Irgacure 651 and $S_0 \rightarrow S_1$ and $S_0 \rightarrow T_1$ of Irgacure 369 is less negative than the

$S_0 \rightarrow T_1$ transition of Irgacure 651, indicating a slightly higher separation of the hole and electron.

The computed emission peaks (see Table 5.8) at 379.65 nm and 606.99 nm displayed an increase of the Stoke shift[164, 165] from Irgacure 651 (∼50 nm) to Irgacure 369 (∼300 nm), which might be attributed to a significant relaxation occurring after absorption for the latter.

Table 5.8: Fluorescence peaks of Irgacure 651 and Irgacure 369 in ACN (in nm and eV) and oscillator strength (f) computed with CAM-B3LYP-D3-(BJ)/def2-TZVP in implicit ACN. Emission spectra in the experiment are not available and therefore not reported in the Table.

	Irgacure 651	**Irgacure 369**
Emission (nm)	379.65	606.99
Emission (eV)	3.27	2.04
Oscillator strength (f)	0.0014	0.0014

As previously reported by Cao et al. [202], such mega Stoke shift (210 nm in the cited work) was attributed to a substantial intramolecular charge transfer (ICT) character of the first singlet excited state accompanied by significant molecular geometry relaxation involving the rotation of one functional group. However, as previously shown the $S_0 \rightarrow S_1$ transition of Irgacure 369 shows a mixed LE-CT character rather than only CT. Figure 5.7 illustrates the alterations introduced during the optimization of the S_1 state in comparison to the ground state of the investigated PIs. The optimized S_1 geometry of Irgacure 651 exhibits marked similarities to the S_0 state (Figure 5.7**a**). However, when employing both the S_1 state of Irgacure 369 in ACN and gas phase, distinct behaviors are observed in the optimized S_0 and S_1 geometries (Figure 5.7**c**). While the gas-phase S_1 geometry closely resembles the ground state structure, substantial divergences are evident in the S_1 geometry obtained with the inclusion of the solvent (Figure 5.7**b**). For the latter a notable relaxation is observed compared to the S_0 geometry, resulting in a significant twist of the side group to -6.62° concerning (C16C15N10C3, Figure 5.7**d**). In contrast, the twist in the S_0 geometry is 32.10°. Conversely, the S_1 geometry optimized in the gas phase exhibits a twist of 57.55° (47.3° in S_0), as depicted in Figure 5.7**c**. The considerable relaxation observed in the S_1 ACN optimized geometry, similarly to what was reported by Cao et al. [202], can be attributed to the combination of the ICT character of S_1 and the polarization effects induced by the implicit solvent, which can explain the large Stoke shift for this PI. The lack of emission experimental data do not allow to further compare the theoretical calculations conducted.

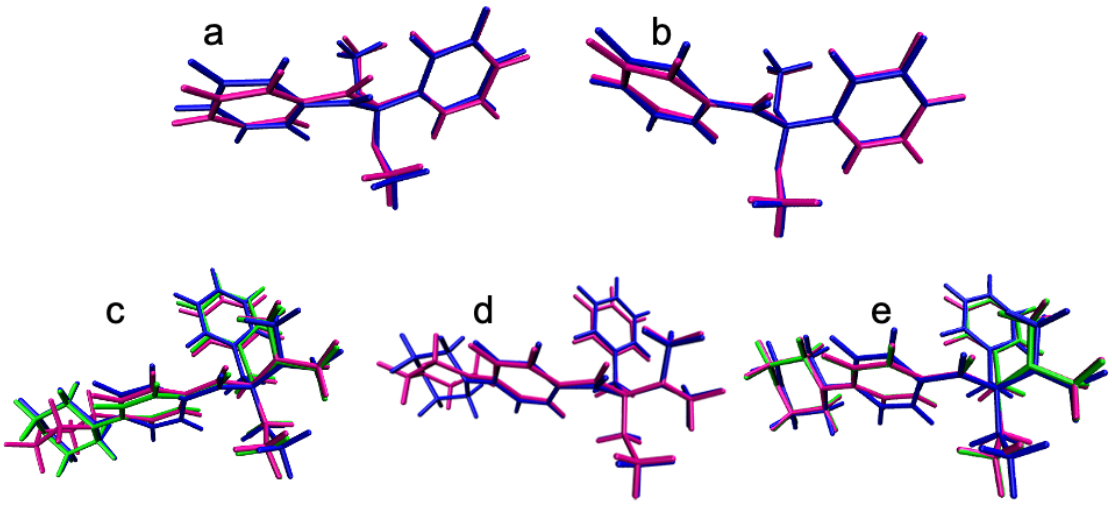

Figure 5.7: Graphical comparison of S_0, S_1 and T_1 optimized geometries of Irgacure 651 (**a**,**b**) and Irgacure 369 (**c**,**d**) with CAM-B3LYP: **a** ground state in ACN (in blue) to S_1 in ACN (in magenta), **b** ground state in ACN (in blue) to T_1 in ACN (in magenta), **c** ground state in ACN (in blue) to S_1 in ACN (in magenta) and to S_1 in gas phase (in green), **d** ground state in ACN (in blue) to T_1 in ACN (in magenta), **e** ground state in gas (blue) with S_1 (magenta) and T_1 (green) in gas phase.

In addition, as explained in Section 4.2.1 the absorption and emission properties of Irgacure 651 and Irgacure 369 were further analyzed through the employment of cLR method with CAM-B3LYP and B3LYP, for comparison purposes. Table 5.9 demonstrates that employing the cLR for the solvent dynamic utilizing CAM-B3LYP for Irgacure 651 and Irgacure 369 yield consistent values. On the other hand, data computed with B3LYP, especially for Irgacure 369, are not reliable: the emission energies drops down to very low values with respect to experimental data. This phenomenon is connected to the important relaxation of the S_1 state in ACN with respect to S_0 and it is generally sign of the presence of a significant CT character, which cannot be correctly reproduced employing B3LYP, due to the lack of correct asymptotic behavior for the exchange-correlation potential of this hybrid functional [144]. In addition, the contribution of several MOs to the S_1 state of Irgacure 369, as reported in Table 5.5, might further affects the poor performance of TD-DFT in handling such cases, causing the emission energies to reach such low values [128]. Additionally, the influence of solvation on MOs could contribute to this discrepancy.

Table 5.9: Comparison of the absorption and emission energy computed with CAM-B3LYP and B3LYP functional for Irgacure 651 and Irgacure 369 with linear response (LR) and corrected LR (cLR) approaches. The absorption (abs.) and emission (emiss.) were computed as a single point on the S_0 minimum geometry for absorption (abs. S_1 cLR) and S_1 minimum geometry for emission (emiss. S_1 cLR). E_{0-0} LR is computed as the adiabatic energy difference between optimized S_0 and S_1 excited states energies including zero point energy correction (ZPVE). All values listed are in eV.

	Irgacure 651		**Irgacure 369**	
	CAM-B3LYP	B3LYP	CAM-B3LYP	B3LYP
abs. exp.	3.63		3.87	
abs. S_1 cLR	3.77	3.44	4.07	3.00
abs. S_1 LR	3.78	3.47	4.09	3.22
E_{0-0} LR	3.43	3.02	3.27	2.44
emiss. S_1 cLR eq*	3.16	2.25	1.59	0.96
emiss. S_1 cLR noneq.**	3.20	2.34	1.74	1.27
Corrected Tot.E. + ZPVE	3.36	2.85	2.97	1.86
Corrected Tot.E.*	3.46	2.96	3.01	1.92

*Emission state-specific solvation corrected linear-response approach equilibrium solvation based: the state-specific equilibrium solvation of the excited state S_1 at its equilibrium geometry.
**Emission state-specific solvation corrected linear-response approach non-equilibrium solvation based

5.2 Two-photon absorption

Irgacure 651 and Irgacure 369 are used for 2PA polymerization; Irgacure 369 is experimentally reported to be 2PA active in the range of ∼ 800 nm [141, 18, 6] while Irgacure 651 is active at lower wavelength [102]. The multiphoton absorption character of the PIs, was investigated through the computation of 2PA spectra which are depicted in Figure 5.8 and reported in Tables 5.10 and 5.11. They show distinct bands peaked at 502.98 nm and 609.26 nm for Irgacure 651 and Irgacure 369 respectively, with the respective intensity of 28.40 GM and 2.89 GM. It is worth noting that 2PA cross sections for Norrish type I PIs, like Irgacure 651 and Irgacure 369, typically do not exceed 30 GM [141, 18, 6], i.e., 28 GM for Irgacure 651 at ∼ 500 nm (only experimental data available) and 7 GM and 0.27 GM for Irgacure 369 at ∼ 650 nm and ∼ 800 nm, respectively [141, 6]. For Norrish type II initiators as BBK and DETC the expected 2PA cross-sections are in the range of 191 GM [203, 204] for the former and ∼ 80-40 GM [201, 11] for the latter at ∼ 800 nm. The 2PA spectrum of Irgacure 651 matches experimental data with absorption in the range 484-503 nm with GM values of 8-0.5 GM while the blue shift of the 2PA spectrum of Irgacure 369 with respect to the experimental reported data at ∼ 800 nm [141, 18, 6] can be attributed to the choice of the functional employed, which shows ∼ 20 nm blue-shift even for 1PA. For comparison, the B3LYP spectra were computed and reported in Tables A.3 and A.4; they show 2PA first peak at 713 nm and 782 nm with G.M. values of 0.06 GM and 3.07 GM for Irgacure 651 and Irgacure 369 respectively, reducing for the latter, with respect to CAM-B3LYP, the blue shift with respect to experimental data. However, the primary focus in this study is on accurately representing experimental data from a photophysical perspective. This includes parameters such as CT, adiabatic energies (E_{00}), and emission properties, as

detailed in Tables 5.9 and 5.7. The emphasis is placed on capturing the essential photophysical features rather than achieving an exact match with experimental spectra.

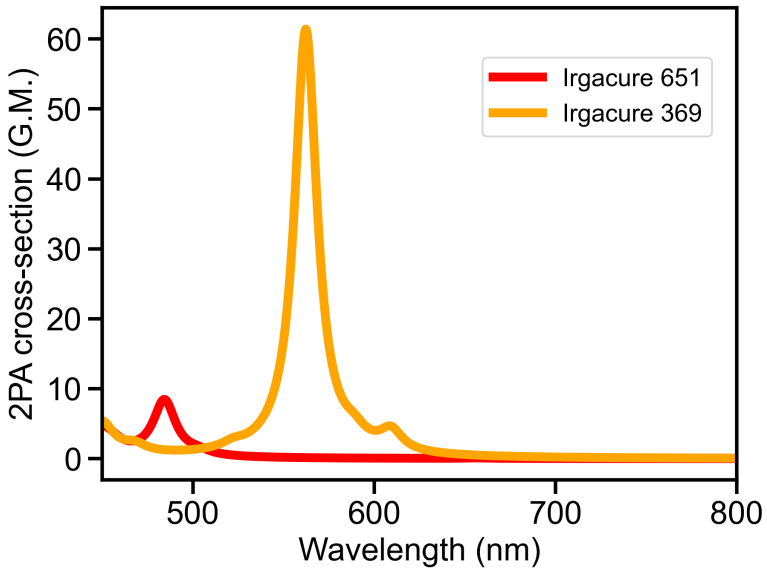

Figure 5.8: Computed two-photon absorption spectra (2PA) of Irgacure 651 (Irga.651) and Irgacure 369 (Irga.369) using TD-CAM-B3LYP-D3(BJ)/def2-TZVP in implicit ACN. Spectra were plotted as reported in Chapter 4. Experimental values are ~ 500 nm and ~ 650-800 nm for Irgacure 651 and Irgacure 369 respectively.

Table 5.10: Values for one-photon absorption (1PA) as excitation energy (E, eV), wavelength (λ1PA, nm), oscillator strength (Osc.str.), and two-photon absorption (2PA) as wavelength (λ2PA, nm), 2PA strength (δ2PA, a.u.), cross section (σ2PA, GM) of Irgacure 651 in ACN (PCM model) computed as reported in chapter 4. Data obtained using TD-CAM-B3LYP/def2-TZVP level of theory starting from the optimized ground state geometry. No rescaling with regard to experimental data was applied. 1GM corresponds to 1×10^{-50} cm^4 s photon^{-1} molecule^{-1}. The spectrum is depicted in Figure 5.8.

Excitation	Energy	λ_{1PA}	Osc.str.	λ_{2PA}	δ_{2PA}	σ_{2PA}
1	3.78	328.45	0.0022	656.00	7.03	0.07
2	4.94	250.76	0.0267	502.98	28.40	0.51
3	5.14	241.09	0.0378	484.31	412.00	7.93
4	5.46	226.92	0.0067	454.15	64.30	1.41
5	5.69	218.03	0.0020	437.33	0.44	10.40
6	5.76	215.32	0.0022	431.25	0.26	6.19
7	6.05	204.87	0.0019	410.54	18.70	0.50
8	6.09	203.51	0.0549	407.17	20.00	0.54
9	6.22	199.44	0.0076	399.95	19.40	0.55
10	6.29	197.00	0.0007	392.98	8.22	0.24

Table 5.11: Values for one-photon absorption (1PA) as excitation energy (E, eV), wavelength (λ1PA, nm), oscillator strength (Osc.str.), and two-photon absorption (2PA) as wavelength (λ2PA, nm), 2PA strength (δ2PA, a.u.), cross section (σ2PA, GM) of Irgacure 369 in ACN (PCM model) computed as reported in chapter 4. Data obtained using TD-CAM-B3LYP/def2-TZVP level of theory starting from the optimized ground state geometry. No rescaling with regard to experimental data was applied. 1GM corresponds to 1×10^{-50} cm^4 s photon^{-1} molecule^{-1}. The spectrum is depicted in Figure 5.8.

Excitation	Energy	λ_{1PA}	Osc.str.	λ_{2PA}	δ_{2PA}	σ_{2PA}
1	4.09	303.50	0.0278	609.26	238.00	2.89
2	4.22	294.04	0.0895	589.00	124.00	1.61
3	4.41	281.35	0.5447	562.29	4280.00	61.10
4	4.75	261.15	0.0210	522.04	44.00	0.73
5	5.31	233.61	0.0099	467.86	52.40	1.08
6	5.53	224.25	0.0487	450.03	177.00	3.94
7	5.7	217.36	0.1058	434.27	6.41	0.15
8	5.89	210.60	0.0102	422.43	90.10	2.28
9	5.98	207.37	0.0285	414.66	62.00	1.62
10	6.13	202.12	0.0217	405.18	1050.00	28.80

5.3 Photophysical rates

The Jablonski diagram in Figure 5.9 illustrates the optimization of the first singlet and triplet excited states with TD-CAM-B3LYP-D3(BJ)/def2-TZVP in implicit ACN and relative adiabatic energies, including ZPVE. Table 5.12 provides information on SOC, reorganization energies, radiative and non-radiative rates for the investigated PIs.

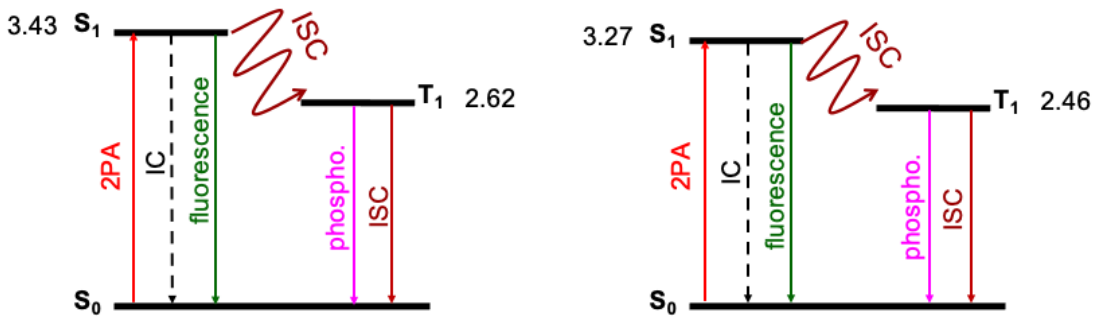

Figure 5.9: Jablonski diagram of Irgacure 651 (left) and Irgacure 369 (right). Excited states are optimized with TD-CAM-B3LYP-D3(BJ)/def2-TZVP in implicit ACN. Adiabatic energy values are expressed in eV and include the zero point energy correction (ZPVE).

The generation of the initial singlet excited state occurs through the absorption of two photon, resulting in energy levels of 3.43 eV and 3.27 eV for Irgacure 651 and Irgacure 369, respectively. Both PIs share a radical formation mechanism involving transitions between states of different multiplicity, notably the spin-forbidden S_1–T_1 transitions, which are typically less likely than symmetry and spin-allowed transitions. However, the presence of atoms such as O and N promotes the SOC between singlet

and triplet wavefunctions, facilitating ISC. In accordance with El Sayed rule[60, 75, 205], the S_1 $n\pi^*$ state of Irgacure 651 and Irgacure 369 couples respectively with the $n\pi^*$ and $\pi\pi^*$ T_1 states (see Figure 5.5), exhibiting 46% and 70% of allowed ISC. ISC rates are 4.54x10^7 s^{-1} and 7.92x10^7 s^{-1} (considering S_1 and T_1 in ACN), with SOC values of 1.64 cm^{-1} and 1.20 cm^{-1}, respectively (see Table 5.12). The RISC process back to the singlet manifold is characterized by rates of 1.02x10^8 s^{-1} and 4.17x10^5 for Irgacure 651 and Irgacure 369, respectively. The significant difference of the RISC rate between Irgacure 651 and Irgacure 369 is due to the notable difference in the SOC of T_1-S_1 which counts 33.96 cm^{-1} and 4.31 cm^{-1}, respectively, and in reorganization energies (0.375 eV and 1.149 eV respectively). Notably, the ISC rates are competitive with IC $S_1 \rightarrow S_0$ rates of 1.35x10^7 s^{-1} and 1.37x10^7 s^{-1}, respectively (see Table 5.12). The weak fluorescence observed in Irgacure 651 and Irgacure 369, with rates of 4.53x10^5 s^{-1} and 4.21x10^2 s^{-1} reported in Table 5.12, aligns with previously reported experimental findings showing weak fluorescence for Norrish type I PIs i.e. ($\sim$ 100 L mol^{-1}cm^{-1} compared to green-emitting fluorescence type II PIs like DETC $\sim$ 54000 Lmol^{-1}cm^{-1}) [26]. Being typical Norrish type I PIs exhibiting N=2 photon dependency[28, 18, 98, 45, 102, 206] and relying on the reactive T_1 state for generating radicals, higher triplet excited states for both Irgacure 651 and Irgacure 369 were not explored. Additionally, the non-radiative decay of the T_1 state in the order of 10^5 s^{-1} results in lifetimes of 1.53-8.03 μs for both PIs. As expected, the phosphorescence rate is much slower i.e., in the order of 10^{-1} s^{-1} with lifetime of 1.3-2.5 s for Irgacure 651 and Irgacure 369, respectively. The fluorescence and IC rates for Irgacure 369 were determined using the S_1 state optimized in the gas phase due to convergence issues in the correlation function computed with MOMAP when calculating rates with S_1 in ACN (refer to Chapter 4). This observation, similar to what was noted for DETC (refer to Chapter 6), may be linked to the substantial structural differences of the S_1 state with respect to the ground state (see Figure 5.7).

Table 5.12: For Irgacure 651[a] and Irgacure 369[b] the photophysical rates such as internal conversion (IC), intersystem crossing (ISC) and reverse ISC (RISC) were computed as reported in Section 4.5 in implicit ACN with TD-CAM-B3LYP-D3(BJ)/def2-TZVP level of theory. For the IC and ISC rates (in s^{-1}) the non-adiabatic coupling matrix elements (NACME, in a.u.), spin-orbit coupling (SOC, in cm^{-1}) and reorganization energy (λ, in eV) were also calculating as described in Section 4.5. For the radiative rates such as fluorescence and phosphorescence, the level of theory reported in Section 4.5 was employed.

Non-radiative rates			
	Rate (s^{-1})	NACME (au)	λ (eV)
[a]IC $S_1 \rightarrow S_0$	$1.35x10^{7}$	0.003	0.547
[b◦]IC $S_1 \rightarrow S_0$	$1.37x10^{7}$	0.003	1.222
	Rate (s^{-1})	SOC (cm^{-1})	λ (eV)
[a*]ISC $S_1 \rightarrow T_1$	$4.54x10^{7}$	1.64	0.478
[b]ISC $S_1 \rightarrow T_1$	$7.92x10^{7}$	1.20	1.232
[a*]RISC $T_1 \rightarrow S_1$	$1.02x10^{8}$	33.96	0.375
[b]RISC $T_1 \rightarrow S_1$	$4.17x10^{5}$	4.31	1.149
[**a]ISC $T_1 \rightarrow S_0$	$6.56x10^{5}$	5.87	0.763
[**b]ISC $T_1 \rightarrow S_0$	$1.24x10^{5}$	2.40	0.621
Radiative rates			
	Rate (s^{-1})	ΔE (eV)	lifetime (s)
[a]Fluorescence	$4.53x10^{5}$	3.43	$2.21x10^{-6}$
[b◦]Fluorescence	$4.21x10^{2}$	3.27	0.0024
[a]Phosphorescence	$7.93x10^{-1}$	2.62	1.26
[b]Phosphorescence	$3.96x10^{-1}$	2.46	2.53

*Dushinsky rotation include
◦S_1 in gas and S_0 in ACN combined with ΔE in ACN
** T_1 state lifetime is $1.53x10^{-6}$ s (Irgacure 651) and $8.03x10^{-6}$ s (Irgacure 369).

5.4 Triplet absorption

Norrish type I PIs are recognized for generating radicals exclusively from the T_1 state, independently and without the involvement of additional processes [36]. Conversely, Norrish type II PIs, exemplified by DETC and BBK, exhibit a distinct TA process originating from the T_1 state, occurring at approximately 800 nm wavelength [45, 20, 206], as explained in Chpater 6. To confirm the absence of the TA mechanism in Irgacure 651 and Irgacure 369 [6, 18, 206], the TA spectrum was conducted with the anticipation of negligible triplet state absorption at the 2PA wavelength i.e., 500 nm and 650-800 nm range for Irgacure 651 and Irgacure 369, respectively. As illustrated in Table 5.13 the PIs display peaks in those range with oscillator strength of 0.04-0.02 at 483-529 nm for Irgacure 651 and 0.01 for Irgacure 369 at 622-803 nm, comparable to the previously reported Norrish I PI phenylbis(2,4,6-trimethylbenzoyl)phosphine oxide (BAPO) [206] and smaller when compared to the TA spectrum for DETC (i.e oscillator strength of 0.18 at $\sim$ 800 nm). The triplet energies computed employing GW approach show similar results in terms of wavelength but different oscillator strength i.e. 0.010-0.043 at 477-532 nm for Irgacure 651 and 0.009-0.008 in the range 609-810 nm for Irgacure 369.

Table 5.13: Triplet vertical excitation energies (energy in eV and wavelength in nm) of Irgacure 651 and Irgacure 369 computed using (U)CAM-B3LYP-D3(BJ)/def2-TZVP in ACN starting from the optimized first triplet state. To note that the transitions reported in the Table are not directly related to triplet excited states numbering used in Tables 5.2 and 5.3.

	Irgacure 651			**Irgacure 369**		
Excitation	Energy	Wavelength	Osc.str.	Energy	Wavelength	Osc.str.
1	0.44	2789.35	0.0048	1.54	803.02	0.0013
2	2.13	581.27	0.0071	1.67	741.70	0.0105
3	2.15	576.13	0.0066	1.99	622.00	0.0112
4	2.34	528.81	0.0158	2.10	589.81	0.0043
5	2.57	483.37	0.0447	2.36	526.36	0.1158
6	2.91	426.18	0.0102	2.81	440.59	0.5979
7	3.01	411.53	0.0113	3.45	359.56	0.0038
8	3.26	380.68	0.0235	3.56	348.48	0.0089
9	3.40	364.35	0.0047	3.60	344.70	0.0074
10	3.65	339.87	0.0003	3.72	333.08	0.0046

Table 5.14: GW-BSE triplet vertical excitation energies (in eV and nm) of Irgacure 651 and Irgacure 369 in ACN starting from optimized T_1 geometry. Excitations were computed using evGW calculations, employing CD variant with CAM-B3LYP functional, def2-TZVP basis set and def2-TZVP auxiliary basis set. RI approximation for the Coulomb term in molecular and periodic systems was also included. Transitions labeled "1" to "10" are not directly related to triplet excited states numbering used in Tables 5.2 and 5.3

.

	Irgacure 651			**Irgacure 369**		
Excitation	Energy	Wavelength	Osc.str.	Energy	Wavelength	Osc.str.
1	0.16	7751.78	0.0017	1.51	821.95	0.0023
2	1.48	835.91	0.0013	1.53	810.60	0.0076
3	1.94	639.70	0.0059	1.96	632.48	0.0070
4	2.02	613.20	0.0142	2.03	609.98	0.0089
5	2.33	532.45	0.0426	2.27	547.27	0.0665
6	2.60	477.00	0.0097	2.73	453.43	0.5651
7	2.66	466.97	0.0055	3.32	373.53	0.0008
8	2.99	415.17	0.0028	3.53	351.31	0.0064
9	3.02	409.99	0.0092	3.58	346.24	0.0135
10	3.33	372.64	0.0013	3.70	334.76	0.0027

5.5 Radical formation upon reaction cleavage

In order to investigate the dissociation of Norrish type I PIs in the T_1 state and define the weakest bond in the possible type of homolytic reaction cleavage, the Gibbs free energies and BDEs, related to the fragmentation of the possible bonds in the α- and β-cleavage for the PIs were computed.

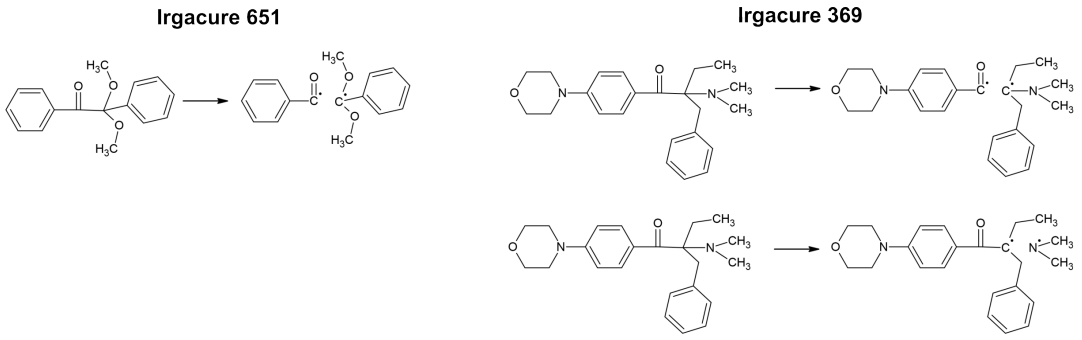

Figure 5.10: Fragmentation mechanisms for Irgacure 651 (α-cleavage) and Irgacure 369 (α- up and β-cleavage down). Bond dissociation energies (BDEs) starting from S_0 and T_1 with involved atoms are reported in Table 5.15

As previously reported in Section 2.3.3, in the case of Irgacure 651, the α-cleavage is the mainly reported fragmentation mechanism [44, 207], which generates benzoyl and α,α-dimethoxybenzyl radicals upon light impact. Meanwhile, although both α- and β-cleavage mechanisms were reported as possible fragmentation pathways for Irgacure 369 [43] that lead to the generation of benzoyl and alkyl radicals for the former and α-alkyl and α-alkylamino radicals for the latter (see Figure 5.10), the primary reaction for this PI remains the α-cleavage from the triplet and the β-cleavage is less significant [43, 101]. The involved bonds are C12-C13 (see Figure 5.1) for Irgacure 651, C25-C27 (α cleavage) and C27-N39 (see Figure 5.1) (β cleavage) for Irgacure 369, which are listed in Table 5.15 and reported in Figure 5.10.

Table 5.15: BDEs computed in CAM-B3LYP-D3(BJ)/def2-TZVP and B3LYP-D3(BJ)/def2-TZVPin ACN related to all the possible fragmentation reactions of Irgacure 651 and Irgacure 369. Values listed are in kcal mol^{-1}.

	Irgacure 651			**Irgacure 369**		
Type of cleavage	bond	S_0	T_1	atoms	S_0	T_1
			CAM-B3LYP			
α-	C12-C13	55.20	-4.59	C25-C27	57.46	0.64
β-	-	-	-	C27-N39	47.85	-8.97
			B3LYP			
α-	C12-C13	57.39	-3.28	C25-C27	56.03	0.18
β-	-	-	-	C27-N39	46.25	-9.60

The calculated BDEs related to the dissociation reaction for both initiators were computed with both CAM-B3LYP and B3LYP functional, for comparison purposes. Data suggest that the α-cleavage is energetically more favorable when the respective PI is in T_1, with values of -4.59 kcal mol^{-1} and 0.64 kcal mol^{-1} for Irgacure 651 and Irgacure 369, respectively (CAM-B3LYP). Such fragmentation reaction cannot take place when the initiators are in the ground state, where the BDEs are 55.20 kcal mol^{-1}

and 57.46 kcal mol^{-1} for Irgacure 651 and Irgacure 369, respectively (CAM-B3LYP). The calculated spin density values of the atoms involved in the cleavage reaction from the T_1 state are reported in Table 5.16 and Figure 5.11.

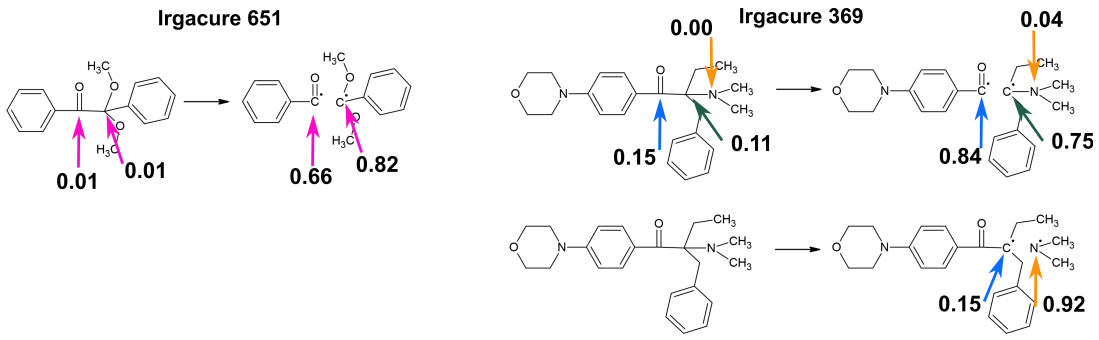

Figure 5.11: Fragmentation reaction mechanism with spin densities values on atoms for Irgacure 651 (α-cleavage) and Irgacure 369 (α- on top and β-cleavage on the bottom). Results are reported in Table 5.16.

A higher spin density on certain atoms suggests a higher likelihood of radical character. Data confirms that the homolytic cleavage of the C-C bonds (α-cleavage for Irgacure 651 and Irgacure 369) and C-N (β-cleavage of Irgacure 369) produces free radicals. Spin density moves, upon cleavage, from values of 0.54 au on C12 0.14 au on C13 (in T_1) to 0.66 au and 0.82 au, respectively for the α-cleavage of Irgacure 651. In the case of Irgacure 369 C25, C27 and N36 are characterized by the initial spin density values (in T_1) of 0.15 a.u., 0.01 a.u. and 0.00 a.u. respectively and, upon the cleavage reaction, values become 0.84 a.u., 0.75 a.u. and 0.04 a.u. for the α-cleavage and 0.00 au, 0.92 au and 0.92 au for the β-cleavage.

Table 5.16: Electronic spin density values on the radical fragments (in a.u.) related to the α- and β-cleavage of Irgacure 651 and Irgacure 369 computed with CAM-B3LYP-D3(BJ)/def2-TZVP and B3LYP-D3(BJ)/def2-TZVP in ACN

Photoinitiator	cleavage	atoms	spin density
CAM-B3LYP			
Irgacure 651	α-cleavage	C12	0.66
		C13	0.82
Irgacure 369	α-cleavage	C27	0.84
		C25	0.75
	β-cleavage	N39	0.92
		C27	0.92
B3LYP			
Irgacure 651	α-cleavage	C12	0.65
		C13	0.79
Irgacure 369	α-cleavage	C27	0.82
		C25	0.66
	β-cleavage	N39	0.91
		C27	0.92

Going in line with the experimental data, in the next considerations we have focused mainly on the α-cleavage of both PIs. In order to further investigate this dissociation mechanism, the more accurate scan of the PES i.e. IRC approach, as explained in detail in Chapter 4 was employed. The α-cleavage reaction of Irgacure 369 could not be performed with the CAM-B3LYP-D3(BJ)/def2TZVP level of theory due to the lack of convergence of the transition state and therefore data in B3LYP are reported. Considering that Tables 5.15 and 5.16 reveal minor variations in BDEs and spin values based on the chosen functional, owing to its superior convergence in this specific case, the B3LYP-D3(BJ)/def2TZVP level of theory was employed for computing TS energy and conducting IRC simulation of Irgacure 369.

For consistency, results for Irgacure 651 are reported with both approaches (see Figure 5.12). The energy profile along the IRC for this PI computed with both CAM-B3LYP and B3LYP is shown in Figure 5.12. This profile can be decomposed into three stages: elongation of the C12-C13 bond starting from the optimized T_1 geometry (R), cleavage of the bond with subsequent formation of radical fragments (TS) and conformational rearrangements involving rotations of the generated fragments (P). The activation energy related to the fragmentation event is 4.20 kcal mol^{-1} (2.63 kcal mol^{-1} B3LYP) considering implicit ACN. It results in the reaction rate of 5.19x10^9 s^{-1} (7.24x10^{10} s^{-1} B3LYP), overcoming by more than four order of magnitude the non-radiative decay T_1-S_0 in the order of 10^5 s^{-1}. This clearly indicates the radical formation in the T_1 state of this Norrish type 1 PI. The C-C bond elongation at which the cleavage occurs is estimated to be 0.48 Å (0.45 Å B3LYP), computed as the difference between the bond in the TS (2.05 Å for both, Figure 5.12) and in T_1 (1.57 Å and 1.60 Å respectively). The α-cleavage reaction of Irgacure 369 is depicted in Figure 5.12 with the IRC profile describing the fragmentation mechanism of C25-C27 bond upon excitation. The activation energy reported in Figure 5.12 is 2.20 kcal mol^{-1} starting from the first triplet excited state geometry. The TS geometry exhibits stretching of the C25-C27 bond about 0.48 Å (from 1.56 Å in T_1), similarly to previously reported Irgacure 651. Similarly to Irgacure 651, the computed bond breaking rate is extremely fast in implicit ACN, i.e. 2.50x10^{11} s^{-1}, overcoming by six order of magnitude the non-radiative T_1-S_0 decay reported in Table 5.12 (CAM-B3LYP). The lower energy of the product (P) with respect to the reagent (R) for the dissociation reaction of both PIs studied defines the exothermicity of the reaction. As further confirmation of the generation of reactive radicals upon the α-cleavage reaction, results reported in Figures 5.14 and 5.13 show the change of the spin density on T_1 upon dissociation, involving the computed TS for both Irgacure 651 and Irgacure 369. For the former, it is mostly localized on the carbonyl group and, upon cleavage, the spin density moves towards the formed radical centers on the two carbon atoms C12 and C13. For Irgacure 369 the spin density on T_1 is more delocalized all over the molecule, being still the highest in the part involving the carbonyl group. Upon cleavage, the spin moves towards the two radicals formed on the carbon atoms.

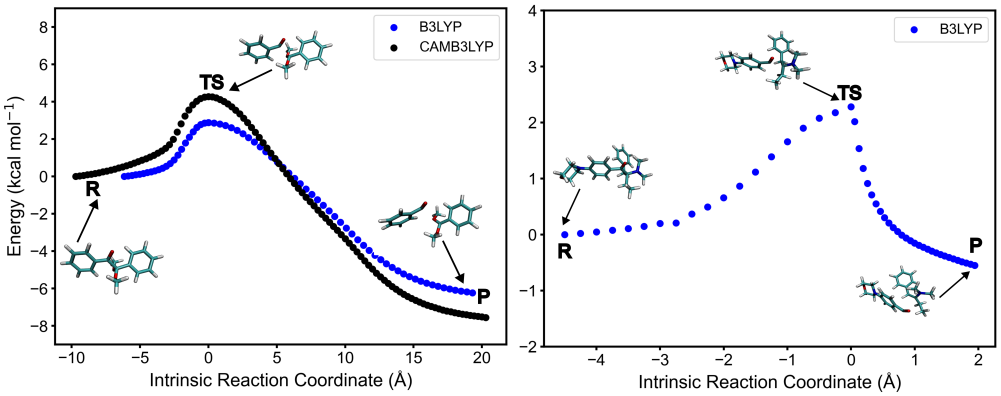

Figure 5.12: Norrish type-I fragmentation reaction mechanism of Irgacure 651 (α-cleavage) computed with (U)CAM-B3LYP-D3(BJ)/def2TZVP (ACN) and (U)B3LYP-D3(BJ)/def2TZVP in implicit ACN respectively (left) and Irgacure 369 (α-cleavage) in (U)B3LYP-D3(BJ)/def2TZVP in implicit ACN (right). The IRC profile was computed starting from the T_1 optimized geometry (R) of Irgacure 651 and Irgacure 369 and moving through the TS where the actual cleavage occurs, for reaching the formation of the products (P) upon relaxation and rearrangement.

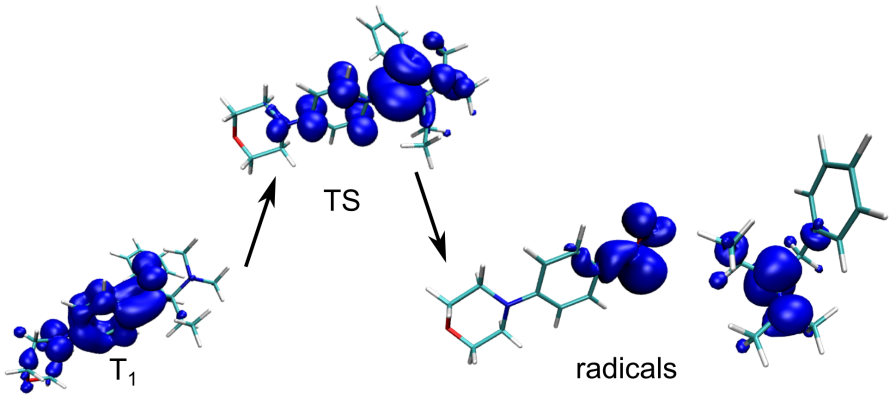

Figure 5.13: Spin density visualization upon α-cleavage of Irgacure 369 computed in B3LYP-D3(BJ)/def2-TZVP in ACN. The spin density for optimized T_1, TS and radicals is reported. Isovalue used for visualization is 0.002.

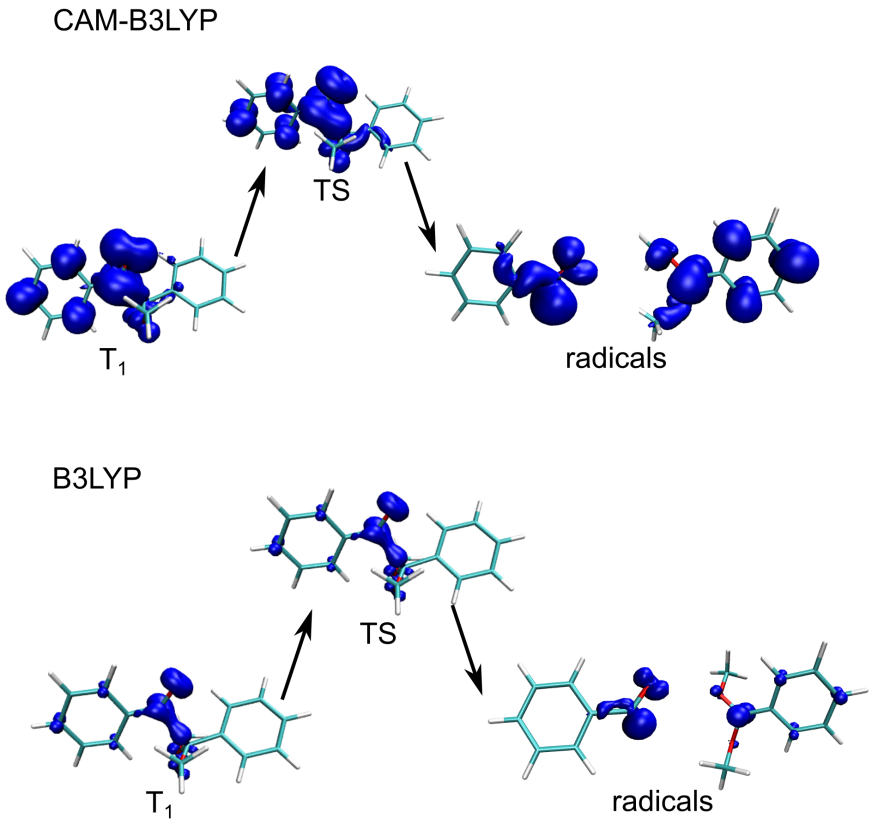

Figure 5.14: Spin density visualization upon α-cleavage of Irgacure 651 computed in CAM-B3LYP-D3(BJ)def2-TZVP and B3LYP-D3(BJ)-def2-TZVP in ACN. The spin density for the optimized T_1, TS and radicals is reported. Isovalue used for visualization is 0.002.

As reported in [109, 108, 31], the cleavage of the PIs in the T_1 state can occur if the BDE is lower than the energy of the optimized T_1. In order to further prove the Norrish type I behaviour of Irgacure 651 and Irgacure 369, the BDEs for breaking the bond in the ground state (E_{BOND}) were compared with the energy of the optimized T_1 state. Results listed in Table 5.17 show indeed that in the case of Irgacure 651, the energy of T_1 is higher than the BDE in the ground state for both α- and β-cleavage with both functionals, while for Irgacure 369 the T_1 energy is higher than the bond energy in the case of β-cleavage (with both functionals) but not in the case of α-cleavage with CAM-B3LYP. However, due to the almost negligible difference between the T_1 energy and the bond energy in the latter case (only 0.04 eV) and considering that the T_1 energy is slightly higher than the bond energy considering B3LYP, it is possible to state that the reaction will occur.

Table 5.17: Comparison of bond dissociation energy (BDE) as (E_{BOND}) and first triplet excited state energy ($E_{\mathrm{T_1}}$) for Irgacure 651 and Irgacure 369.

		$E_{\mathbf{BOND}}$		$E_{\mathbf{T_1}}$		$E_{\mathbf{T_1}}$>$E_{\mathbf{BOND}}$
	cleavage	eV	kcal mol^{-1}	eV	kcal mol^{-1}	eV
			CAM-B3LYP			
Irgacure 651	α-	2.48	55.20	2.62	60.30	2.62 > 2.48
Irgacure 369	α-	2.49	57.46	2.42	56.56	2.42 < 2.49
	β-	2.08	47.85			2.42 > 2.08
			B3LYP			
Irgacure 651	α-	2.48	57.39	2.62	60.34	2.62 > 2.48
Irgacure 369	α-	2.42	56.02	2.46	55.68	2.46 > 2.42
	β-	2.00	46.12			2.46 > 2.00

Similar approach and methodology used for the calculations reported in this Chapter were employed for the characterization of Norrish type II and two-step two-photon PIs in order to understand their properties and reactivity, as further discussed in Chapters 6 and 7.

6

Two- and three-photon based photoinitiators

This chapter delves into a comprehensive exploration of the photochemical and photophysical properties exhibited by DETC and BBK, belonging to the class of Norrish type II initiators (see Figure 6.1) and classified, when combined to PETA monomer, among the most efficient used photoresists in 3D laser printing. Their chemical structure is depicted in Figure 6.2. Through the utilization and combination of QM calculations and experiments a thorough investigation of the mechanisms that bring DETC and BBK, upon multiphoton activation, to FRP is provided. This is the first time where such a comprehensive analysis of the reactions and possible pathways that would lead to the radical formation is conducted, elucidating the properties of the unique and mysterious three-photon based behavior shown by these PIs. The three-photon based mechanism is hypothesize to be characterized by two-subsequent steps: 2PA that excited the PI from S_0 to S_1, ISC to the triplets with formation of T_1 (step 1) which is characterized by a second absorption that leads to the formation of high triplet states (step 2) from where radicals are generated.

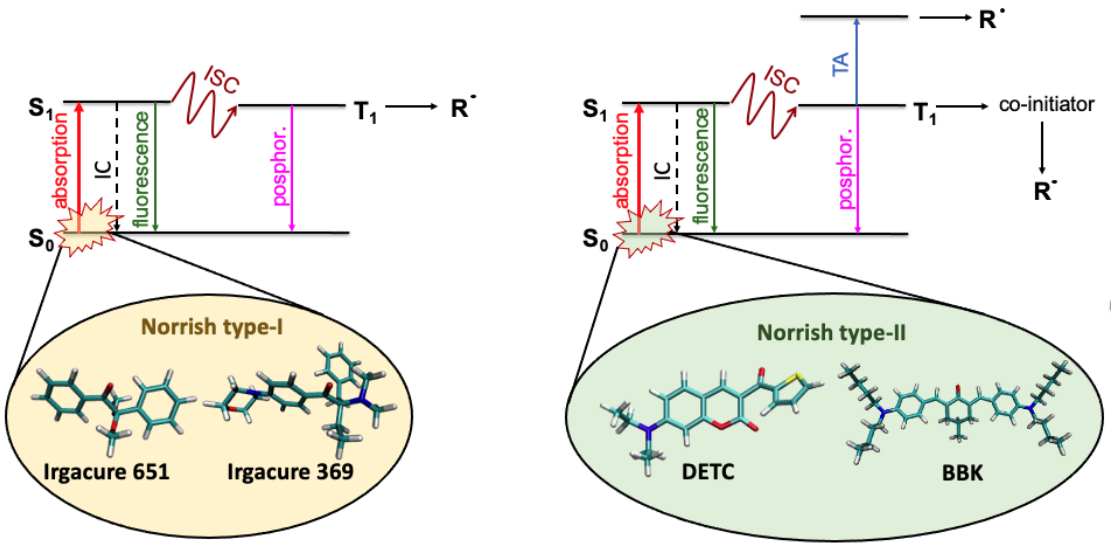

Figure 6.1: Radical formation mechanisms for Norrish type I e.g., Irgacure 651 and Irgacure 369 (left) and Norrish type II photoinitiators (PIs) e.g., DETC and BBK (right). The formation of radicals occurs through cleavage reaction (type I) and the interaction with a co-initiator (in most cases based on electron transfer process) (type II) as a result of the absorption from the ground state to the singlet excited state and subsequent ISC to the triplet state. For Norrish type II PIs, the additional triplet absorption (TA) channel contributing to the formation of high triplet excited states capable of generating radicals is also depicted.

The outcomes detailed in this Chapter are organized to offer the reader a comprehensive understanding of the processes guiding these PIs, upon multiphoton absorption, toward the creation of reactive radicals. This analysis encompasses the absorption and emission characteristics of PIs, initiating with the generation of excited states, followed by the computation of the photophysical rates that shine light on the probable pathways leading to radical formation. Various potential reactions are explored for the generation of these radicals, and the subsequent polymerization reaction with the monomer is thoroughly examined. Throughout the analysis, a focus is placed on comparing DETC and BBK individually and collectively as Norrish type II PIs, emphasizing their distinctions and similarities in relation to Norrish type I initiators (as discussed in Chapter 5) in order to provide a comprehensive overview of different classes of PIs used in the realm of 3D laser printing.

- Data presented in this Chapter on DETC are reported in the following paper - A. Mauri, P. Kiefer, P. Neidinger et al. Two- and three-photon processes during photopolymerization in 3D laser printing. Chem. Sci., 2024,15, 12695-12709
  DOI:10.1039/D4SC03527E

- Data presented in this Chapter on BBK will be reported in the following paper (planned submission before publication of the thesis): Planned submission before publication of the thesis, first author - **A. Mauri**, P. Kiefer, et al. Initiation of free radical polymerization in 3D laser printing

using Norrish type I and Norrish type II photoinitiators. Macromol. Rapid Commun. (2024-2025 planned).

6.1 Absorption and emission properties

Similar protocol to what was reported in Chapter 5 was applied in order to select the proper methodology for reproducing the properties of the investigated DETC and BBK.

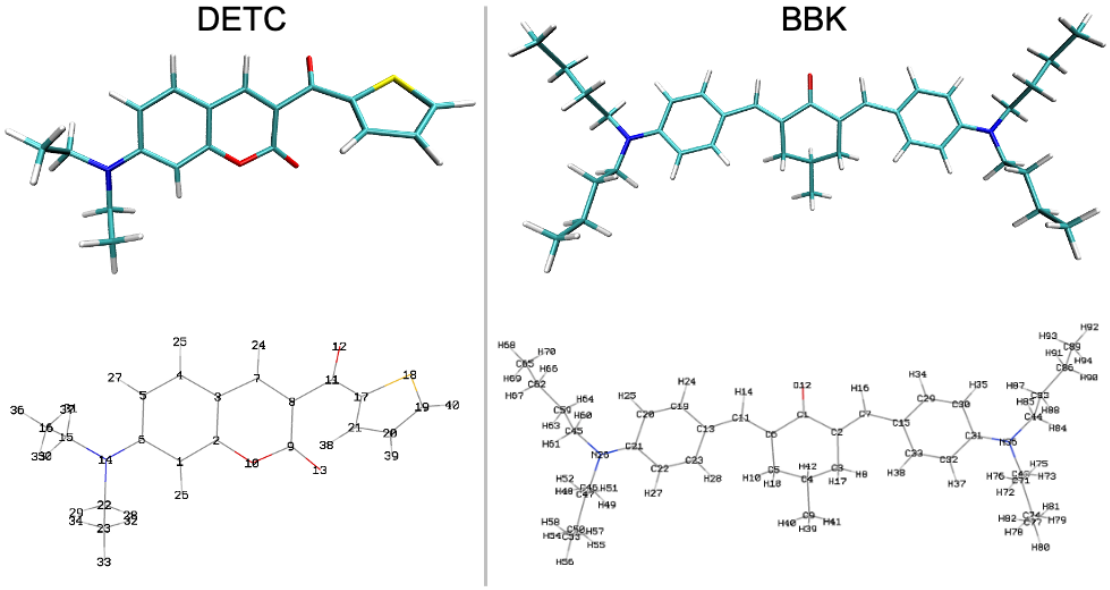

Figure 6.2: Ground state structure of DETC and BBK photoinitiators (PIs) optimized using CAM-B3LYP13-D3(BJ)/def2-TZVP in implicit ACN (PCM model).

6.1.1 One-photon absorption spectra

Initially, in order to reproduce the absorption properties of DETC and BBK in ACN and comparing to experimental available data, the 1PA spectra were performed. The 1PA spectra calculated in ACN using B3LYP (see Table B.2 and B.3) show ∼ 1 nm and ∼ 19 nm red-shift compared to the experimental value for DETC and BBK [208] reported in Table 6.1, B.6 and Figure B.1, B.2, respectively. Specifically, 422.64 nm and 467.67 nm in theory vs. 421 nm and 448 nm in experiment. Data reported employing CAM-B3LYP functional are blue-shifted with respect to experimental data by 61 nm and 70 nm (359.30 nm and 377.62 nm) for DETC and BBK, respectively (see Tables B.2, B.3 and Figure 6.3).

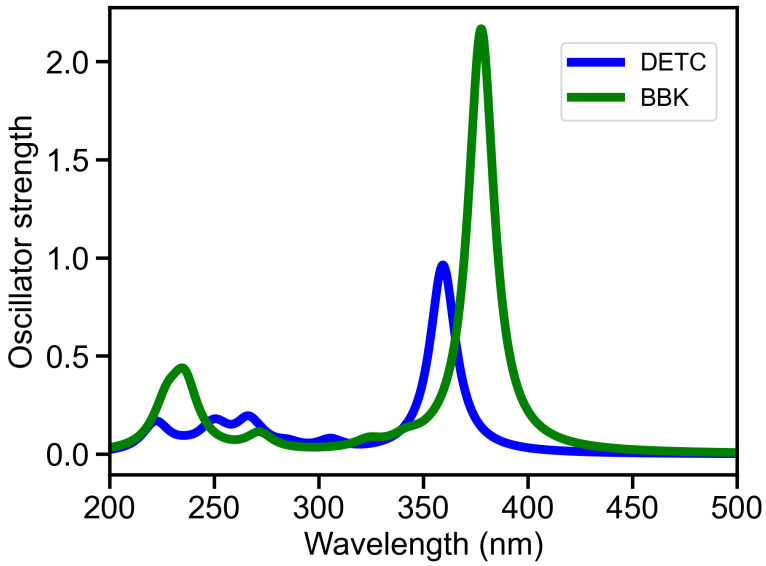

Figure 6.3: Theoretically calculated one-photon absorption (1PA) spectra of DETC and BBK using TD-CAM-B3LYP/def2-TZVP in ACN (PCM model). Spectra is plotted as described in Chapter 4.

As previously reported in Ref.[164, 165], a very precise comparison between computational data and experiment rely on the correlation between the computed 0–0 transition energy ν_{00} (i.e. between the ground vibrational states of the two electronic states) and the origin of the fluorescence spectrum, or the crossing point between absorption and emission spectra. The calculated energies and wavelengths reported in Table 6.2, corresponding to the transitions between the lowest vibrational state of the ground state and first singlet excited state (ν_{00}), agreed well with the $\frac{1}{2}$ Stoke shift calculated from experimental spectra, observed for DETC in both ACN and PETA (see Table 6.1 and Figure B.1).

Table 6.1: Values of absorption and emission peak maxima obtained experimentally and $\frac{1}{2}$ Stokes shift (St.s) of DETC in PETA and ACN.

	PETA			**ACN**		
	Absorption	Emission	$\frac{1}{2}$ St.s.	Absorption	Emission	$\frac{1}{2}$ St.s.
eV	2.90	2.52	2.71	2.94	2.48	2.69
nm	427	492	457.5	421	500	460.9

Specifically, a slightly larger blue-shift can be observed for DETC in the gas phase caused by the lack of the proper polarization environment induced by the solvent. 1PA and ν_{00} computed employing long-range corrected CAM-B3LYP [124], meta-hybrid M06-L [209] and hybrid PBE0 [210] functionals, show higher or equivalent deviation (i.e. for 1PA in ACN +0.43 eV, -0.37 eV and +0.06 eV, while for ν_{00} energies +0.34 eV, -0.57 eV, +0.11 eV using CAM-B3LYP, M06-L and PBE0, respectively) with respect to the experimental values than B3LYP (-0.01 and -0.09 eV for 1PA and ν_{00} energy).

Table 6.2: Values of E_{0-0} energies (ν_{00} i.e., between the ground vibrational states of the two electronic states considered) of DETC obtained using different DFT functionals and def2-TZVP basis set within linear response (LR) TD-DFT approach.

Energy	B3LYP	CAM-B3LYP	M06-L	PBE0
E_{0-0} gas (eV)	2.73	3.39	2.32	2.92
λ gas (nm)	454	366	534	425
E_{0-0} ACN (eV)	2.60	3.04	2.12	2.80
λ ACN (nm)	477	409	585	443

In the case of BBK, the experimental $\frac{1}{2}$Stokes shift is 2.51 eV (550 nm) (see Table B.6 and Figure B.3) and the calculated ν_{00} energy with CAM-B3LYP showed higher deviation than the one with B3LYP (2.35 eV and 2.87 eV, respectively) (see Table 6.4).

Table 6.3: Values of absorption and emission peak maxima obtained experimentally and $\frac{1}{2}$ Stokes shift (St.s) of BBK in ACN.

	Absorption	Emission	$\frac{1}{2}$ St.s.
eV	2.25	2.77	2.51
nm	448	550	494

Table 6.4: Values of E_{0-0} energies (ν_{00} i.e., between the ground vibrational states of the two electronic states considered) of BBK obtained using different DFT functionals and def2-TZVP basis set within linear response (LR) TD approach. E_{0-0} values in the gas phase and in ACN are marked in purple and green for clarity. B3LYP functional results in the E_{0-0} values similar to the experimental data reported, therefore, it was used for DFT and TD-DFT calculations. $\frac{1}{2}$Stokes shift from experiment was compared to E_{0-0} therefore only absorption values are listed.

Energy	B3LYP	CAM-B3LYP
E_{0-0} ACN (eV)	2.35	2.87
λ ACN (nm)	528	432

Although in such cases the performances of B3LYP functional seem to be higher than CAM-B3LYP, further validation is necessary, especially through the involvement of approaches that go beyond the LR method, to correctly reproduce the solvation effects thorough TD-DFT in the excited states as explained in Section 4.2.1.

6.1.2 Vibrationally resolved absorption and emission spectra

The first sign of the failure of the B3LYP functional in reproducing the properties of DETC lays in the vibronic absorption spectra of the PIs, computed in order to further investigate the absorption properties with the inclusion of the vibrations of the molecule upon absorption, which cannot be detected computing electronic absorption spectrum. Data reported in Figure 6.4 show that the vibrationally-resolved spectrum using CAM-B3LYP is in good agreement with respect to experimental data, presenting red-shift with respect to the electronic 1PA spectrum with absorption and emission peaks at 350 nm and

500 nm, respectively. On the other hand, the vibronic spectrum with B3LYP did not converge, probably due to the geometrical changes explained in Section 6.1.4 below.

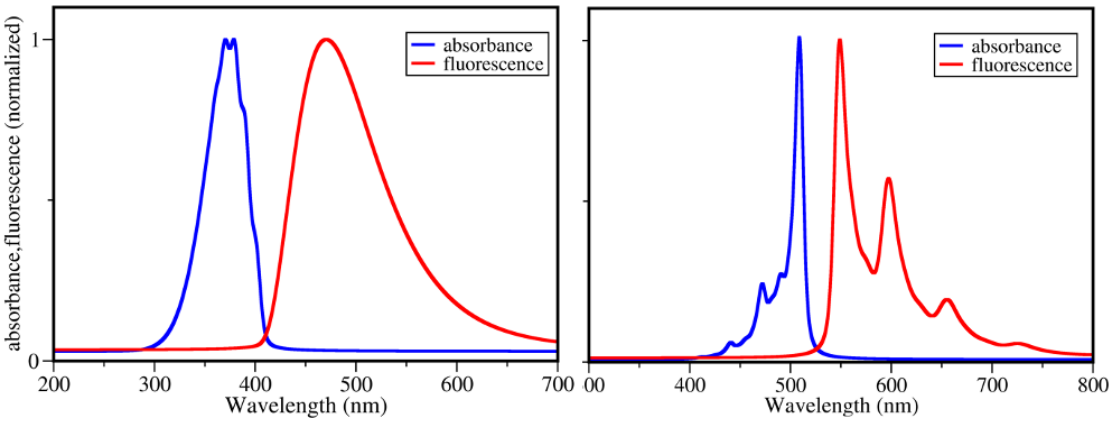

Figure 6.4: Calculated vibrationally-resolved absorption and emission (fluorescence) spectra of DETC (left) and BBK (right) in implicit ACN using TD-CAM-B3LYP-D3(BJ)/def2-TZVP for the former and TDA-B3LYP-D3(BJ)/def2-TZVP for the latter. Spectra were computed and plotted as reported in Chapter 4. Vibrationally-resolved spectrum using B3LYP for DETC and CAM-B3LYP for BBK did not converge.

6.1.3 Beyond the linear response approach

As reported in Section 4.2.1 and similarly to the approach adopted for Norrish type I PIs (see Chapter 5), to further validate the absorption and emission properties of DETC and BBK, the cLR [162] combined with the EI [167, 166] (SS corrections) approach was adopted for investigating the excited states energies and the solvent response. Data reported in Tables 6.5, 6.6 and 6.7 for DETC show that, despite the TD-DFT outcomes appearing more favorable with B3LYP in comparison to the experiment (emission at 553 nm with B3LYP vs. 418 nm in CAM-B3LYP), the effects of SS (cLR equilibrium (eq.), cLR non-equilibrium (noneq.), and EI noneq.) exert a significant influence on these results. This renders the data for B3LYP physically inconsistent, making it unsuitable for direct comparison with experimental values. Examining the non-equilibrium cLR data, it is evident that the energies obtained with B3LYP (i.e. 1.29 eV and 0.82 eV) are notably lower than the experimental emission of 2.48 eV. Data with CAM-B3LYP maintains physical consistency (2.82 eV vs. 2.69 eV in experiment). Similarly, the energy, obtained employing B3LYP, after the addition of SS effects (i.e. cLR) decreases (1.65 eV) and significantly deviates from the experimental Stoke shift of DETC in ACN (2.69 eV) while, on the contrary, the energy computed with CAM-B3LYP (2.82 eV) gets closer (see Table 6.6 and 6.1).

Table 6.5: Vertical excitation energies of DETC in implicit ACN employing linear response (LR), corrected LR (cLR) and external iteration (EI) state specific (SS) approach. Experimentally estimated absorption maximum at ACN is 421 nm (2.94 eV). Data with CAM-B3LYP were computed starting from the geometry obtained as a single point on the optimized B3LYP geometry (marked as SP CAM-B3LYP) and upon optimization with CAM-B3LYP (marked as CAM-B3LYP).

	LR		**cLR**		**EI**	
	eV	nm	eV	nm	eV	nm
B3LYP	2.93	422.64	2.86	433.22	2.27	544.70
SP CAM-B3LYP	3.38	367.04	3.42	362.33	3.20	387.94
CAM-B3LYP	3.45	359.30	3.49	356.27	3.25	381.96
PBE0	2.95	420.48	3.01	411.88	2.47	502.57
M06-L	2.57	482.08	2.43	510.22	1.82	681.23
M06-2X	3.25	381.12	3.39	366.15	3.14	394.60

Table 6.6: Adiabatic and E_{0-0} energy values for DETC computed with B3LYP and CAM-B3LYP with linear response (LR) and corrected LR (cLR) approach including zero-point energy correction (ZPVE).

	B3LYP		**CAM-B3LYP**	
	eV	nm	eV	nm
LR $E_{adiabatic}$	2.600	476.86	3.106	399.17
LR E_{0-0}	2.544	487.36	3.043	407.44
Δ ZPVE	-0.002	-	-0.063	-
cLR $E_{adiabatic}$	1.649	751.88	2.887	429.46
cLR E_{0-0}	1.647	752.79	2.824	439.04

Table 6.7: Comparison of the emission energy (fluorescence) of DETC computed with B3LYP and CAM-B3LYP using several approaches. The S_0 and S_1 geometry were optimized firstly with DFT and TD-DFT using the respective functional. The equilibrium corrected linear response (cLR eq.), non-equilibrium cLR (cLR noneq.) and noneq. external iteration (EI noneq.), were computed as a single point on the S_1 minimum geometry obtained with TD-DFT with both functionals. Vibronic emission could not be computed with B3LYP due to the fact that S_0 and S_1 are not harmonically related (see Figure 6.7).

	TD-DFT		TD-DFT vibr.		EI noneq*		cLR noneq**		cLR eq***	
	nm	ev	nm	eV	nm	eV	nm	eV	nm	eV
B3LYP	-	-	553	2.24	1878	0.66	1512	0.82	961	1.29
CAM-B3LYP	418	2.96	470	2.64	420	2.95	394	3.15	390	3.18

*Emission state-specific solvation external iteration approach (non-equilibrium solvation based)
**Emission corrected linear-response approach (non-equilibrium solvation based)
***Emission corrected linear-response approach (equilibrium solvation based: the corrected linear-response equilibrium solvation of the excited state S_1 at its equilibrium geometry)

Similarly to what was reported in Chapter 5, although B3LYP reproduces the absorption characteristics of DETC for the best (see Table 6.8), in agreement with the work published by Fang et al.[211], the employment of cLR and EI approaches drastically lowers the emission energies, reaching values below $\sim$ 1 eV, clearly not consistent with the experimental observations [20, 103].

Table 6.8: Values of vertical excitation energies for DETC in gas phase, ACN and PETA using B3LYP and CAM-B3LYP functionals. SP CAM-B3LYP refers to single point in CAM-B3LYP on optimized B3LYP geometry while CAM-B3LYP refers to optimized geometry in CAM-B3LYP.

	B3LYP	**SP CAM-B3LYP**	**CAM-B3LYP**
gas (eV)	3.23	3.62	3.69
gas (nm)	384	342	336
ACN (eV)	2.93	3.38	3.45
ACN (nm)	423	367	359
PETA (eV)	3.00	3.49	-
PETA (nm)	401	355	-

On the other hand, CAM-B3LYP is more consistent, reproducing experiments even better with the inclusion of cLR and EI in the analysis (see Table 6.6). The incorrect representation of the emission properties of DETC when employing B3LYP originates from the inadequate treatment of the CT character associated with the $S_0 \rightarrow S_1$ transition of the dye, as shown in Table 6.8 [128]. It might also be connected to the unexpected large difference between the vertical and ν_{00} in the gas phase (3.23-2.73=0.50 eV) with respect to ACN (2.93-2.54=0.39 eV), which seems to indicate that the relaxation of the dye is larger in the gas phase, counter intuitive for a CT system. The relaxation changes with CAM-B3LYP functional are captured correctly, i.e. the differences between the vertical and ν_{00} are: 3.62 - 3.39 = 0.23 eV in the gas phase and 3.38 - 3.04 = 0.34 eV in ACN (Tables 6.2 and 6.8). The mean absolute error of the transitions computed using TD-DFT in the present study is in the range of 0.19-0.27 eV based on comparison to experiments and high level wavefunction based methods e.g., CC2, which will be presented in Section 6.1.5 below. Additional comparisons between data generated by both functionals are provided in Tables 6.6 and 6.12.

Table 6.9: Vertical excitation energies of BBK in implicit ACN employing linear response (LR), corrected LR (cLR) and external iteration (EI) state specific (SS) approach. Experimentally estimated absorption maximum at ACN is 448 nm (2.76 eV). Data were computed starting from the optimized geometry with the respective functional.

	LR		**cLR**		**EI**	
	eV	nm	eV	nm	eV	nm
B3LYP	3.28	378.00	3.32	373.45	3.07	403.85
CAM-B3LYP	2.70	459.80	2.71	457.51	2.50	495.94

Table 6.10: Adiabatic and E_{0-0} energy values for BBK computed with B3LYP and CAM-B3LYP with linear response (LR) and corrected LR (cLR) approach including zero-point energy correction (ZPVE).

	B3LYP		**CAM-B3LYP**	
	eV	nm	eV	nm
LR $E_{adiabatic}$	2.43	510.22	2.93	422.64
LR E_{0-0}	2.35	527.59	2.87	432.00
Δ ZPVE	-0.003	-	-0.002	-
cLR $E_{adiabatic}$	3.13	396.12	2.63	471.42
cLR E_{0-0}	3.07	403.86	2.55	486.21

Table 6.11: Comparison of the emission energy (fluorescence) of BBK computed with B3LYP and CAM-B3LYP using several approaches. The S_0 and S_1 geometry were optimized firstly with DFT and TD-DFT using the respective functional. The equilibrium corrected linear response (cLR eq.), non-equilibrium cLR (cLR noneq.) and noneq. external iteration (EI noneq.), were computed as a single point on the S_1 minimum geometry obtained with TDA-DFT with both functionals.

	TD-DFT		EI noneq*		cLR noneq**		cLR eq***	
	nm	ev	nm	eV	nm	eV	nm	eV
B3LYP	529.85	2.34	-	-	426.07	2.91	432.00	2.87
CAM-B3LYP	457.51	2.71	467.86	2.65	486.21	2.55	493.96	2.51

*Emission state-specific solvation external iteration approach (non-equilibrium solvation based)
**Emission corrected linear-response approach (non-equilibrium solvation based)
***Emission corrected linear-response approach (equilibrium solvation based: the corrected linear-response equilibrium solvation of the excited state S_1 at its equilibrium geometry)

For BBK, the inclusion of cLR approach in the analysis lead to 2.87 eV and 3.07 eV for cLR emission in eq. (see Table 6.11) and corrected E_{00} (see Table 6.10) with the inclusion of ZPVE in B3LYP respectively, which show a deviation larger than 0.6 eV from the reported experimental emission of $\sim$ 2.25 eV (550 nm) (refer to Table B.6 and Figure B.3). Data with CAM-B3LYP i.e., 2.51 eV and 2.55 eV for cLR emission in eq. and corrected E_{00} with the inclusion of ZPVE, respectively, show significantly lower deviation (of approximately 0.25 eV) with respect to experiment (refer to Tables 6.11, 6.10 and Figure B.3). However, notably, B3LYP in this case does not produce entirely unrealistic data, as observed in the case of DETC. This observation prompted the adoption of the CAM-B3LYP functional for calculating DETC and, subsequently, all the PIs presented in the thesis.

The information presented in Table 6.13 indicates that BBK exhibits noteworthy fluorescence, particularly as observed from the computed values in ACN. Interestingly, experimental data on BBK suggested weaker fluorescence when compared to DETC. When the solvation model is excluded from consideration, the oscillator strength of the fluorescence emission of BBK diminishes to 0.15, falling below the 0.31 exhibited by DETC (see Table 6.12).

Table 6.12: Fluorescence peaks of DETC in ACN and gas phase. Note: emission in the experiment is reported to be at 492 nm in PETA and 500 nm in ACN.

Wavelength (nm)	Energy (eV)	Osc. str.	Method
418.17	2.96	1.2973	CAM-B3LYP ACN
386.97	3.20	0.3110	CAM-B3LYP gas
553.78	2.24	0.0093	B3LYP ACN
625.67	1.98	0.0008	B3LYP gas

Table 6.13: Fluorescence peaks of BBK in ACN and gas phase Note: emission in experiment is reported to be at 550 nm in ACN.

Wavelength (nm)	Energy (eV)	Osc.str.	Method
457.78	2.71	2.3272	CAM-B3LYP ACN
432.04	2.87	0.1539	CAM-B3LYP gas
528.96	2.34	2.1295	B3LYP ACN

6.1.4 Geometrical changes upon relaxation of excited states

The overlap of the optimized ground state and of excited state geometries of DETC reported in Figures 6.5, 6.7and 6.6 show that, while the ground state structure is similar, significant divergences are evident in the S_1 geometry computed employing B3LYP and CAM-B3LYP (Figure 6.7).

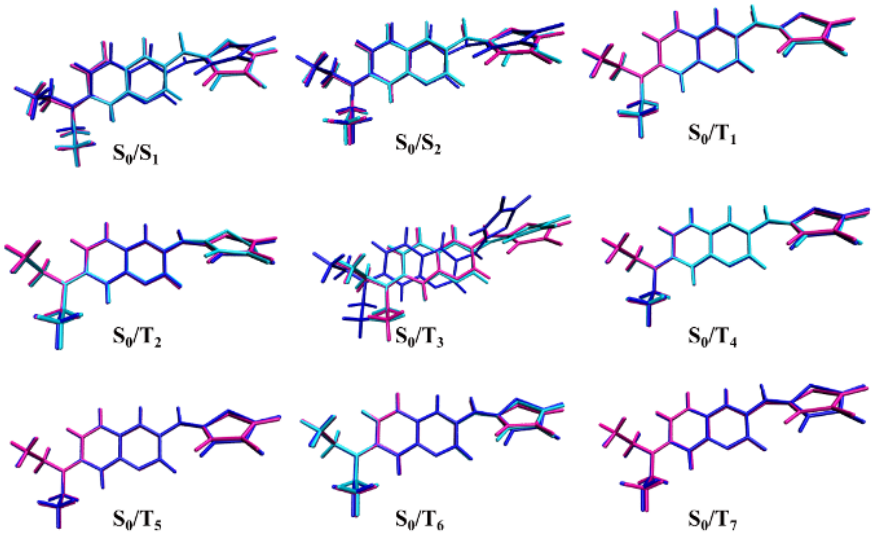

Figure 6.5: Graphical comparison of the ground state (S_0 in magenta) and different excited states structures of DETC (B3LYP in blue and CAM-B3LYP in cyan). No relevant changes have been observed for the S_0 in B3LYP and CAM-B3LYP and therefore only one geometry was reported. All structures were optimized in ACN and confirmed by vibrational analysis.

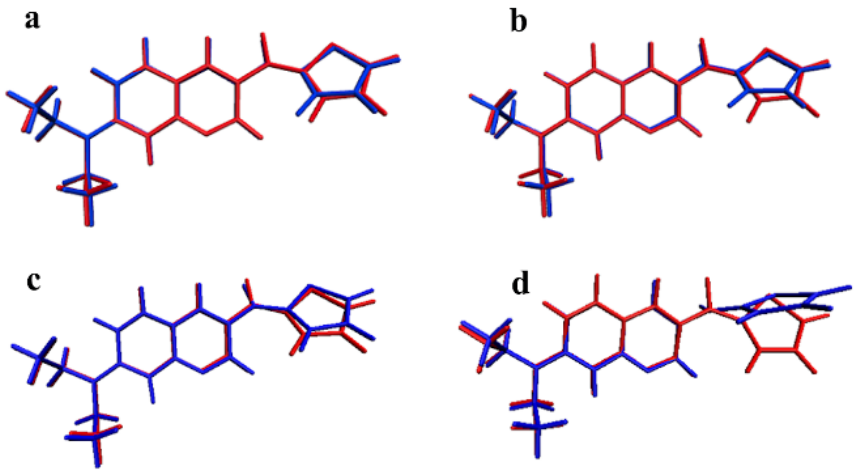

Figure 6.6: Graphical comparison of S_0, S_1 and T_3 optimized geometries of DETC with CAM-B3LYP: **a** ground state (in blue) to T_3 in gas-phase (in red) **b** ground state in ACN (in blue) to T_3 in gas-phase (in red) **c** S_1 in ACN (in blue) to S_1 in gas-phase (in red) and **d** T_3 in ACN (in blue) to T_3 in gas-phase (in red). Only slight changes have been observed for **a**, **b** and **c**, while the relevant deformation of the dihedral C9C8C11C17 is observed for T_3 in ACN (see **d** with respect to the T_3 in the gas-phase.

In the B3LYP-optimized S_1 geometry depicted in Figure 6.7**b** (cyan), a considerable relaxation is observed compared to the S_0 geometry (Figure 6.7**b** orange), resulting in a substantial side group twist of 97.7° with respect to the dye core (C9C8C11C17, Figures 6.2).

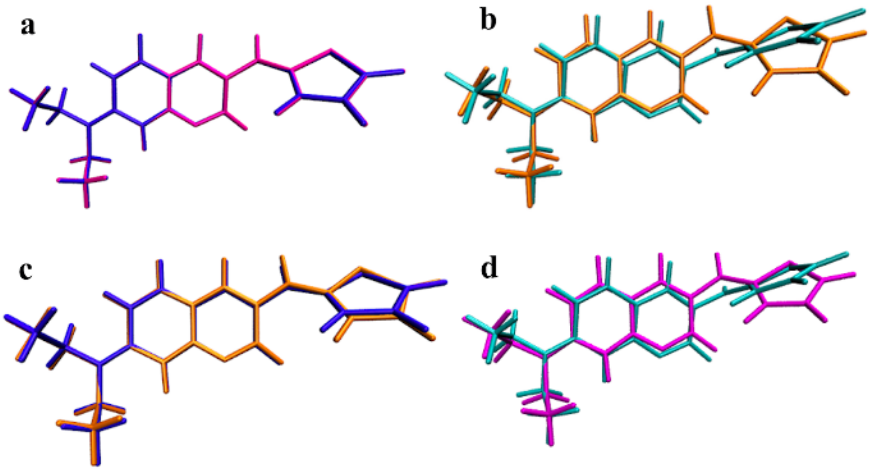

Figure 6.7: Overlap of the optimized DETC structures obtained with different functionals: **a** the optimized S_0 state with CAM-B3LYP (blue) and B3LYP (magenta), **b** the optimized S_1 state with CAM-B3LYP (orange) and B3LYP (cyan), **c** S_0 (blue) and S_1 (orange) geometries with CAM-B3LYP and **d** S_0 (magenta) and S_1 (cyan) geometries with B3LYP.

For comparison, the twist in the S_0 geometry is 45.9°. Conversely, the S_1 geometry optimized with CAM-B3LYP only slightly differs from the S_0 geometry, exhibiting a twist of 29.5° (47.3° in S_0), as depicted in Figure 6.7**c**. The significant relaxation observed in the B3LYP-optimized geometry, leading to a perpendicular orientation of the side group with respect to the core part of the molecule, is likely nonphysical, as previously shown by Wiggins et al. [212]. In this work the authors demonstrated that this effect is particularly notable in cases where a side group experiences a substantial twist ($\sim$ 90°), leading to the formation of an ICT state. Authors have shown that this breakdown is significant with PBE and B3LYP, while it is mitigated using a Coulomb-attenuated functional like CAM-B3LYP. Similar observation is found in the case of the DETC molecule studied here. The experimental Stoke shift of $\sim$ 3710.2 cm^{-1} (see Table 6.1) for DETC indicates CT character for S_1, accurately described by CAM-B3LYP, rather than twisted intramolecular charge transfer (TICT), which would yield to a much higher shift [202] as explained also in Section 5.2: the reported mega-Stokes shift typical of a TICT state is $\sim$ 200 nm [202] (in DMSO) while experimental Stokes shift for DETC in ACN is $\sim$ 80 nm (see Table 6.1). Therefore, DETC does not possess the TICT that B3LYP suggests, demonstrating that this functional fails to accurately describe the nature of the PI. In addition, similarly to S_1, also the T_3 state of DETC optimized in ACN shows a twist of -97.7° of the thiophenyl group with respect to the core (dihedral C9C8C11C17, see Figure 6.2 and Figure 6.7 and 6.6). For comparison, the dihedral angle in the ground state measures -45.9°. Such unnatural rotation of the dihedral angle is not present either in the case of T_3 computed in the gas phase, where the twist is only by -41.45° and between the ground state and S_1 geometries optimized in ACN and gas phase (see Figure 6.6). These observations emphasize the necessity of employing CAM-B3LYP instead of B3LYP, in order to correctly reproduce the properties of such PI where the CT is high and where B3LYP is known to fail [128]. The significance of the blue-shifted 1PA spectra calculated using CAM-B3LYP concerning the experimentally measured spectra (refer to Table **??**) is relatively minor in this context. It is more crucial to select a functional that accurately captures the CT nature of DETC, rather than focusing solely on closely reproducing the experimental spectra. Moreover, it has to be considered that the latter can be adequately represented only when accounting for the dynamic aspects of the molecule, that electronic calculations alone may not fully replicate, and which could not be simulated by B3LYP.

In the case of BBK, computational results obtained with B3LYP demonstrate proficiency in replicating the absorption and emission properties of the photosensitizer, in contrast to the challenges observed for DETC. The emission energy computed considering cLR and EI approaches could be reasonably compared with the experimental emission value with a deviation of $\sim$ 0.6 eV (see Table **??**). The comparison of S_1 and S_0 geometries computed using both B3LYP and CAM-B3LYP (refer to Figures 6.8 and 6.9) reveals no significant divergences, which could mean that no one of the functional suffers from incorrect representation of the CT character which leads to unphysical distortion of the structure in the excited states.

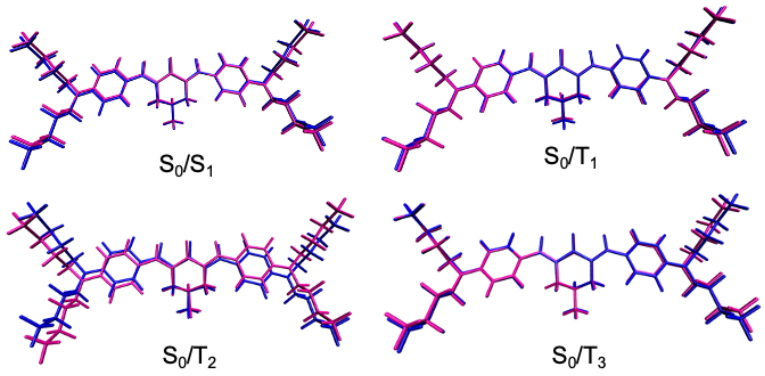

Figure 6.8: Graphical comparison of the ground state structure of BBK (in blue) and different excited states (in magenta). All structures were optimized with TDA-CAM-B3LYP-D3(BJ)-def2TZVP in implicit ACN and confirmed by vibrational analysis.

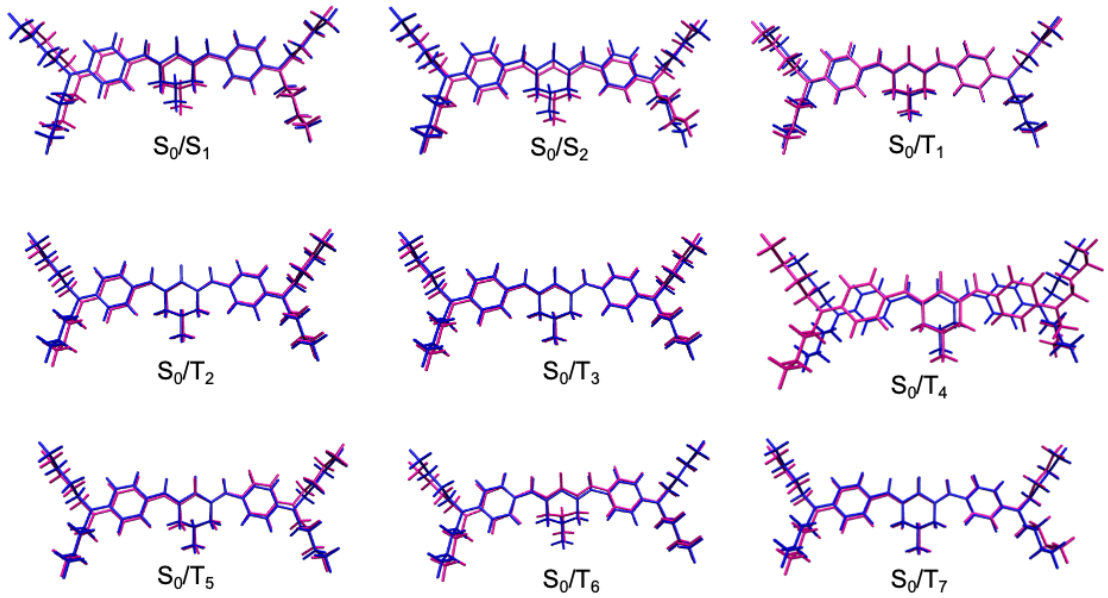

Figure 6.9: Graphical comparison of the ground state structure of BBK (in blue) and different excited states (in magenta). All structures were optimized with TDA-B3LYP-D3(BJ)-def2TZVP in implicit ACN and confirmed by vibrational analysis.

This discrepancy between the PIs regarding the CT representation operated by B3LYP and CAM-B3LYP might be attributed to the lower CT character of the excited states in BBK compared to DETC and Norrish type I PIs (see Table 6.15). B3LYP lacks indeed the correct asymptotic behavior for the electron-electron interaction, a critical aspect for precisely describing the long-range behavior of CT states. Consequently, functionals like CAM-B3LYP, characterized by range-separated and long-range corrected features, can correctly capture the electron-electron interaction, as observed for DETC (see

Tables 6.5 and 6.7) and Norrish type I PIs (see Table 5.9). Therefore, the reliability of B3LYP functional is system dependent and, whenever CT is not present or not significant, the functional is stable in reproducing the photophysical properties of the system under investigation, with better agreement between computed and experimental absorption spectra. On the contrary, CAM-B3LYP shows repetitively a significant blue-shift (see Table B.3). However, due to the inconsistency of B3LYP functional, not only for DETC but also for Irgacure 651 and Irgacure 369, CAM-B3LYP must be chosen for the study of the PIs in this thesis and data computed with B3LYP are included for comparative purposes, especially in the case of BBK, in order to provide a broader overview and comparison of the processes.

6.1.5 Time-dependent density functional theory versus higher level quantum-mechanical methods

The vertical excitation energies computed with TD-DFT approach (CAM-B3LYP) for DETC were further calibrated employing the comparison with both GW-BSE and higher level wavefunction-based methods like CC2 (see Chapter 4). The GW-BSE approach is known to reproduce the vertical excitation energies more accurately than TD-DFT when high separation between the excited electron and subsequent left behind hole is involved [128]. Results listed in Table B.18 show that the vertical excitation energies computed with TD-DFT (employing both B3LYP and CAM-B3LYP) and GW-BSE, taking into account the different solvation model employed (PCM and COSMO for TD-DFT and GW-BSE, respectively), agree with a maximum discrepancy of ~ 0.30 eV as reported in Figure 6.10.

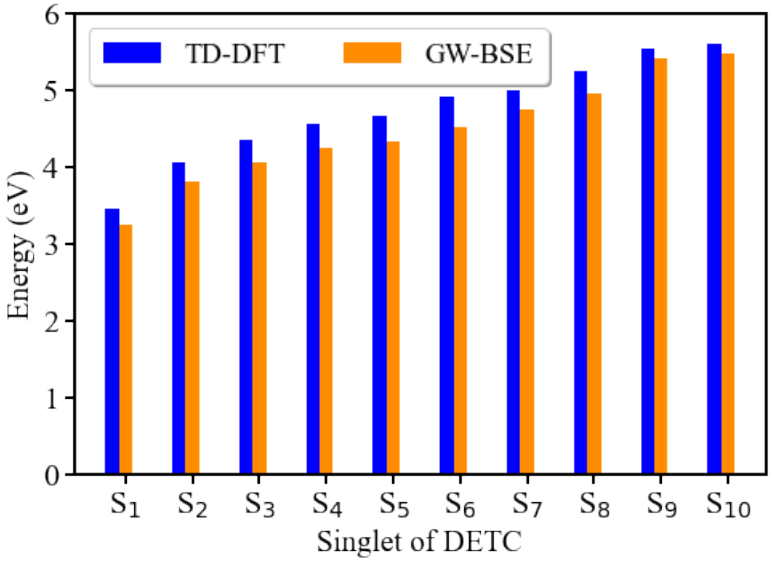

Figure 6.10: Graphical comparison of the vertical excitation energies for the first ten singlet of DETC obtained with TD-DFT (blue) and GW-BSE (orange) in CAM-B3LYP ACN (PCM for TD-DFT and COSMO for GW-BSE) starting from the optimized S_0 geometry. Data for the energies computed in TD-DFT and GW-BSE are reported in Tables B.2 and B.18 respectively.

Finally, the energy difference between the singlet and triplet states obtained in TD-DFT was compared with the following wavefunction-based methods (see Chapter 4 for more details): CC2, SCS-CC2, SCS-ADC2 and SOS-CC2. Data is reported in Table B.19 and B.20. The spin-component scaled (SCS) approach shows that the T_2 state is more aligned to S_1 ($\Delta E\ S_1$-T_2=-0.56 eV) than T_3 ($\Delta E\ S_1$-T_3=-0.80 eV). On the other hand, with CAM-B3LYP and with the addition of cLR correction: $\Delta E\ S_1$-T_2 and $\Delta E\ S_1$-T_3 in ACN become 0.48 eV and -0.11 eV, respectively. Here, the position of T_2 state is more far away than the T_3 state. On the contrary, TD-DFT data always indicate the T_3 state to be closer to S_1. However, vertical excitations in SCS-CC2 and all other wavefunction-based methods applied show that T_2 is closer to S_1 than T_3. However, the converged adiabatic T_2 state could not be obtained and therefore adiabatic energy differences are not provided. The presence of subtle dynamical effects or coupling between T_1 and T_2 states that TD-DFT cannot capture is possible, which should be further analyzed by high level molecular dynamics simulations in excited states. The inclusion of the cLR effects, which are important for DETC and has been performed by SCS-ADC2, shows a negligible difference of $\sim$ 0.01-0.03 eV with respect to COSMO. The spin-component scaled versions of CC2 as SOS-CC2 and SCS-CC2 show deviations that rise up with high triplets i.e. $\sim$ 0.39 eV as maximum deviation for T_7. The differences for SOS-CC2 and SCS-CC2 are slightly smaller than for unscaled CC2 and the accuracy is comparable[213], with the lowest deviations from the experimental values previously observed for SCS-CC2[158] for organic molecules. The ADC2 method with scaled-opposite-spin (SOS) variant showed results comparable to SOS-CC2 [158, 214].

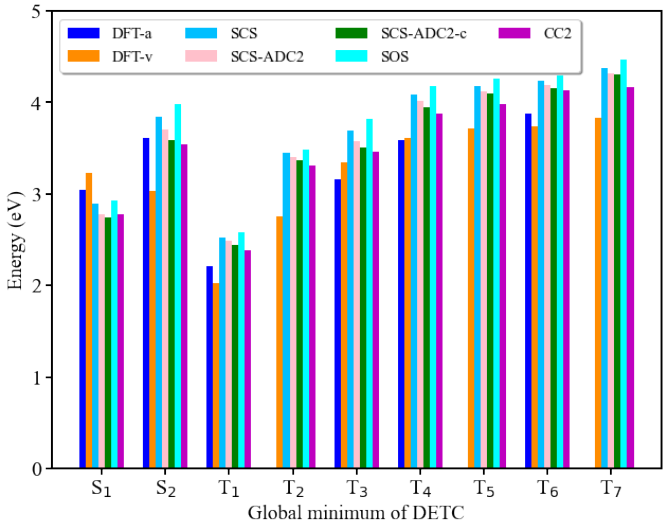

Figure 6.11: Graphical visualization of the excitation energies of Table B.19 obtained with DFT adiabatic (DFT-a), DFT vertical (DFT-v), SCS-CC2 (SCS), SCS-ADC2 (SCS-ADC2), SCS-ADC2 corrected linear response (cLR) (SCS-ADC2-c), SOS-CC2 (SOS) and CC2 (CC2)/def2-TZVP calculations in ACN (COSMO and cLR for SCS-ADC2, as reported in Chapter 4) on S_1 geometry obtained with TD-CAM-B3LYP in ACN. Results for TD-DFT were obtained with CAM-B3LYP-D3(BJ)/def2-TZVP in ACN.

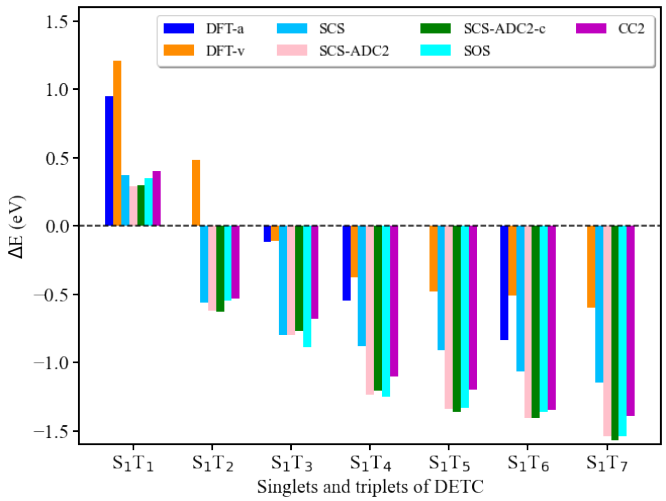

Figure 6.12: Graphical visualization of the energy difference (ΔE) between singlet S_1 and triplet T_1-T_7 excitations of DETC computed on S_1 geometry obtained with TD-CAM-B3LYP in ACN with the approaches reported in Figure 6.11 and Table B.20.

It is crucial to emphasize that, in the comparison, the structures representing global minima on PES of excited states were not optimized using the wavefunction-based methods but only vertical energies were utilized to compute differences in energy levels. The computational demands associated with the optimization of high excited states in systems featuring a large number of atoms made the application of wavefunction-based methods impractical for the analysis of DETC and BBK. Consequently, despite the acknowledged limitations, TD-DFT was employed as a more feasible alternative for the investigation of excited states in these PIs.

6.1.6 Molecular orbitals and charge transfer analysis

The MOs, CT analysis and the electron density localization over the π-conjugated system of DETC and BBK are reported in Figures 6.14, 6.13 and 6.16. The transitions to S_1 and to T_1-T_7 were extensively analyzed based on several indices as reported in Section 4.2.1 and 5.2. Data are reported in Tables 6.14 and 6.15 i.e. the average distribution of electron and hole (H index), the separation degree of electron and hole in the charge transfer direction (t index), the total magnitude of CT length (D index) and the overlap of electrons and holes (Sr index). In the case of DETC, all transitions exhibit relatively large H values. In the case of CAM-B3LYP, transitions $S_0 \rightarrow T_2$, $S_0 \rightarrow T_3$ and $S_0 \rightarrow T_5$ are characterized by lower H values (below 2.9 Å) with respect to the others, due to a localized distribution of holes and electrons in a specific region (refer to Figure 6.14). Conversely, for other transitions, the wider distribution of holes and electrons results in higher H indices. With B3LYP, transitions $S_0 \rightarrow T_2$, $S_0 \rightarrow T_5$ and $S_0 \rightarrow T_6$, which involve a localized distribution of holes and electrons, exhibit lower H values (Figure 6.13). Most other transitions display negative t values, except for $S_0 \rightarrow T_1$, which shows a slightly positive value, indicating a certain degree of separation between its hole and electron. The t indices calculated with CAM-B3LYP

are generally less positive than those with B3LYP. Transitions $S_0 \rightarrow S_1$, $S_0 \rightarrow T_1$ and $S_0 \rightarrow T_7$ exhibit less negative t parameters, suggesting higher CT. The remaining transitions have highly negative t values, indicating a mixed character of CT and LE transitions, as confirmed by Figure 6.14. The D parameter, indicating the distance between the main distribution regions of holes and electrons, shows high average values, exceeding 0.5 Å for all transitions. Specifically, $S_0 \rightarrow S_1$ and $S_0 \rightarrow T_3$ (B3LYP) and $S_0 \rightarrow S_1$, $S_0 \rightarrow T_1$ and $S_0 \rightarrow T_7$ (CAM-B3LYP) have the highest D values, confirming their higher CT character, while others exhibit a more mixed CT and LE character. Additionally, the overlap of electrons and holes (Sr) exceeds 0.5 a.u. in all cases, showing a certain degree of localized and CT, i.e. hybrid (mixed), character for most transitions.

Table 6.14: Charge transfer (CT) data of excited states of DETC computed in B3LYP-D3(BJ)/def2-TZVP and CAM-B3LYP-D3(BJ)/def2-TZVP in ACN. H is the average distribution of electron and hole, H_{CT} is the average degree of spatial extension of hole and electron distribution in CT direction, t is the separation degree of electron and hole in the charge transfer direction (t = D - H_{CT}), D is the total magnitude of CT length and Sr is the overlap of electrons and holes.

State	H (Å)	H_{CT} (Å)	t (Å)	D (Å)	Sr (a.u.)
		B3LYP			
S_1	3.294	2.751	1.160	3.911	0.548
T_1	3.094	2.464	0.040	2.504	0.620
T_2	2.664	1.803	-0.932	0.871	0.635
T_3	3.227	2.673	1.556	4.229	0.523
T_4	3.443	2.868	-1.728	1.139	0.596
T_5	2.886	2.163	-0.498	1.665	0.577
T_6	2.706	2.066	-0.692	1.374	0.590
T_7	3.307	2.692	-2.274	0.418	0.684
		CAM-B3LYP			
S_1	3.088	2.479	-0.262	2.216	0.600
T_1	2.969	2.309	-0.648	1.661	0.619
T_2	2.436	1.584	-0.795	0.789	0.652
T_3	2.888	2.092	-1.135	0.958	0.549
T_4	3.059	2.284	-1.411	0.874	0.673
T_5	2.690	2.084	-1.310	0.774	0.606
T_6	3.241	2.433	-1.753	0.680	0.649
T_7	3.318	2.761	-0.129	2.633	0.667

Concerning BBK, all transitions, except T_3, are characterized by very high H values, suggesting a wide distribution of the hole and electron with low CT character, as can be seen by the hole-electron density depicted in Figure 6.16. The T_3 transition, however, is characterized by a local distribution of the electron and hole. Further supporting the low CT character of BBK transitions, the D indices related to the CT lengths are lower than 0.6 Å for all transitions, with the S_1 transition showing a slightly higher mix of LE and CT character. The Sr values for BBK transitions are mostly higher than 0.5 a.u., indicating that more than half of the electron and hole overlap. An exception is T_3, which shows an Sr index of 0.4 a.u., related to its local distribution compared to the others, which are evidently wider. The t indices are all negative, indicating low CT character, with the least negative value for S_1, where a slightly higher

contribution of CT character is observed compared to the others. The same trends and observations apply to the indices computed with B3LYP related to S_1 and T_1 of BBK.

Table 6.15: Charge transfer (CT) data of the excited states of BBK. Data were calculated with B3LYP-D3(BJ)/def2-TZVP and CAM-B3LYP-D3(BJ)/def2-TZVP in ACN. H is the average distribution of electron and hole, t is the separation degree of electron and hole in the charge transfer direction (t = D - HCT), D is the total magnitude of CT length and Sr is the overlap of electrons and holes

	H (Å)	**t (Å)**	**D (Å)**	**Sr (a.u.)**
		B3LYP		
S_1	4.998	-0.314	0.741	0.570
T_1	4.747	-0.395	0.644	0.658
		CAM-B3LYP		
S_1	4.630	-0.395	0.637	0.634
T_1	4.556	-0.501	0.540	0.654
T_2	4.394	-0.770	0.342	0.712
T_3	2.605	-0.559	0.566	0.423
T_4	5.029	-0.959	0.209	0.722
T_5	5.898	-1.057	0.192	0.562
T_6	5.899	-1.053	0.197	0.563
T_7	5.193	-0.820	0.318	0.723

From holes and electrons analysis reported in Figure 6.13 and 6.14 for DETC can be seen that the HOMO → LUMO excitation for S_1 and T_1 (B3LYP and CAM-B3LYP) includes mostly CT from the nitrogen atom of the alkylamine chain (atom N14) to the carbonyl functionality (atoms C11-O12, see Figure 6.2). Similarly was shown by the density transition obtained in the SCS-CC2 method (see Figure 6.15). CT for triplet excited state T_3 (CAM-B3LYP) and T_4 (B3LYP) is mostly localized on carbonyl bond C11-O12 while CT for T_2 and high triplet excited states, i.e. T_5-T_7 involves mainly the thiophenyl ring and the alkylamine chain (N14, C15, C16, C22 and C23, see Figure 6.2). The T_3, T_4 and T_5, T_6 states in CAM-B3LYP are inverted in B3LYP. Note that in the case of the T_2 state, the distribution of hole and electron using both B3LYP and CAM-B3LYP differs from the SCS-CC2 transition, where the electron part is more delocalized within DETC (see Figure 6.14, 6.13 and 6.15. In addition, the hole-electron representation of S_1, T_1, T_2, T_3, T_4, T_7 in CAM-B3LYP is in perfect agreement with the one of SCS-CC2. T_5 and T_6 states show different distribution of hole and electron.

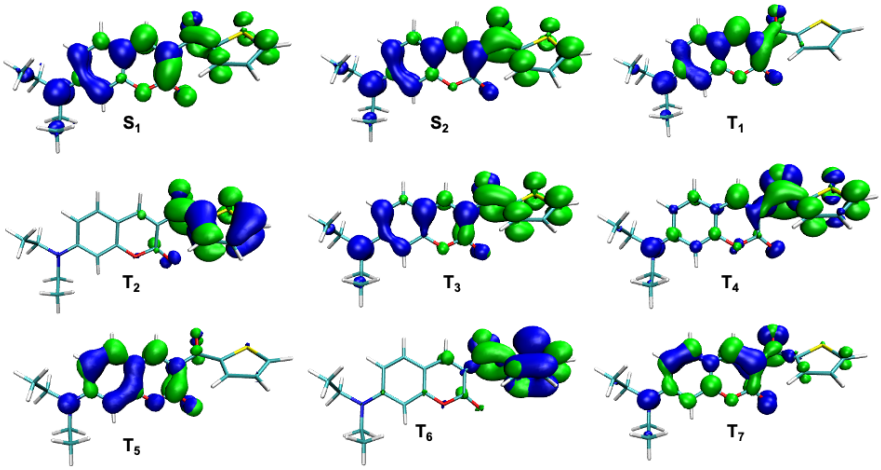

Figure 6.13: Visualization of electron donating (hole, in blue) and electron accepting (electron, in green) density transfer upon excitation of DETC from the ground state to the singlet and triplet states performed using B3LYP-D3(BJ)/def2TZVP in ACN. Isovalue 0.003 a.u. is used for visualization.

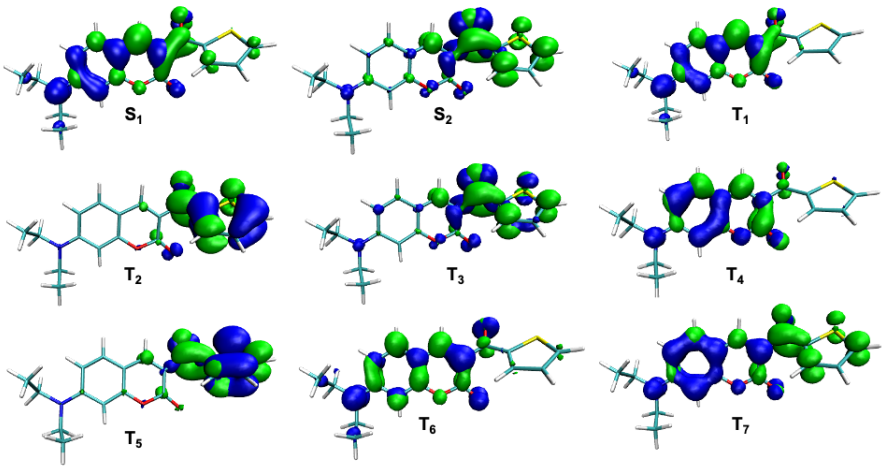

Figure 6.14: Visualization of electron donating (hole, in blue) and electron accepting (electron, in green) density transfer upon excitation of DETC from the ground state to the singlet and triplet states performed using CAM-B3LYP-D3(BJ)/def2TZVP in ACN. Isovalue 0.003 a.u. is used for visualization.

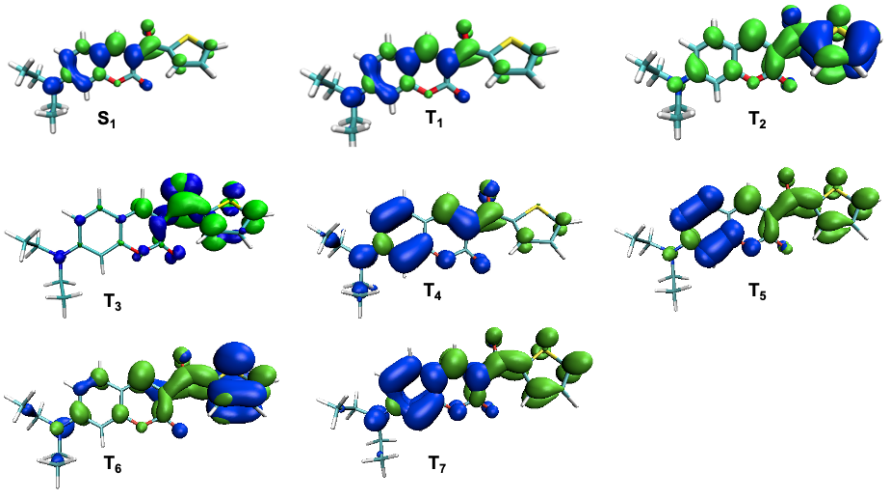

Figure 6.15: Visualization of electron donating (hole, in blue) and electron accepting (electron, in green) density transfer upon excitation of DETC from the ground state to the singlet and triplet states in ACN performed using spin-component scaled coupled cluster (SCS-CC2) in ACN (COSMO) with CAM-B3LYP. Isovalue 0.003 a.u. is used for visualization.

Figure 6.16 shows that for BBK the transitions to S_1 and T_1 is mostly HOMO → LUMO delocalized all over the π system while T_3 is HOMO-1 → LUMO localized on the carbonyl bond while the CT of T_2 and high triplet states i.e. T_4-T_7 are delocalized all over the π system with T_5 and T_6 showing more pronounced localization on the phenyl rings.

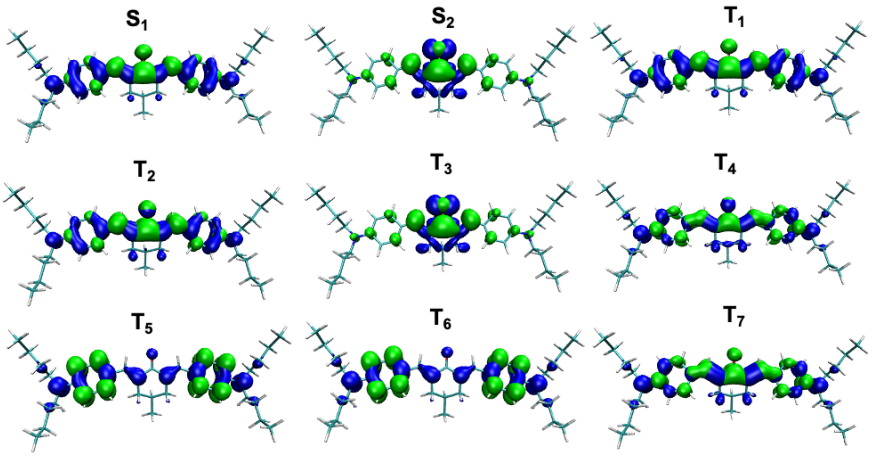

Figure 6.16: Visualization of electron donating (hole, in blue) and electron accepting (electron, in green) density transfer upon excitation of BBK from the ground state to singlet and triplet states in ACN. Electron-hole analysis and the visualization of the respective contributions were performed based on data obtained using TDA-CAM-B3LYP-D3(BJ)/def2-TZVP level of theory. Singlet excited and triplet excited states are labeled with S and T, respectively. Isovalue of 0.001 a.u. was used for visualization.

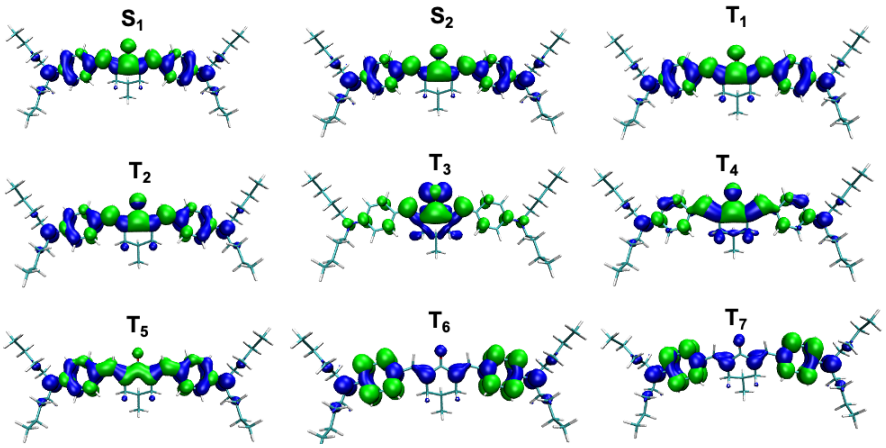

Figure 6.17: Visualization of electron donating (hole, in blue) and electron accepting (electron, in green) density transfer upon excitation of BBK from the ground state to singlet and triplet states in ACN. Electron-hole analysis and the visualization of the respective contributions were performed based on data obtained using TDA-B3LYP-D3(BJ)/def2-TZVP level of theory. Isovalue of 0.001 a.u. was used for visualization.

Overall, the character of the triplet transitions for both DETC and BBK are characterized by a more mixed LE and CT character, with $T_1 \rightarrow T_3$ being for both mostly localized on the carbonyl bond. The maximum CT character for both PIs is related to $S_0 \rightarrow S_1$ although for DETC it is much higher than for BBK (i.e. D index is 0.64 Åfor BBK vs. 2.22 Åfor DETC).

6.2 Two- and three-photon absorption spectra

Being both PIs extensively employed in two-photon FRP [5, 28, 20, 46, 6, 18, 26, 45, 208], the theoretical 2PA spectra were performed and reported in Tables B.11, 6.16, B.15, B.14 and Figure 6.18. DETC and BBK in ACN (CAM-B3LYP) display $S_0 \rightarrow S_1$ absorption peak at 720.84 nm and 760.64 nm respectively, with a corresponding cross-section of 119.00 GM and 40.50 GM at this wavelength (Table 6.16 and B.14). The red-shift observed in the 2PA spectrum compared to the 1PA spectrum can likely be attributed to solvation effects.

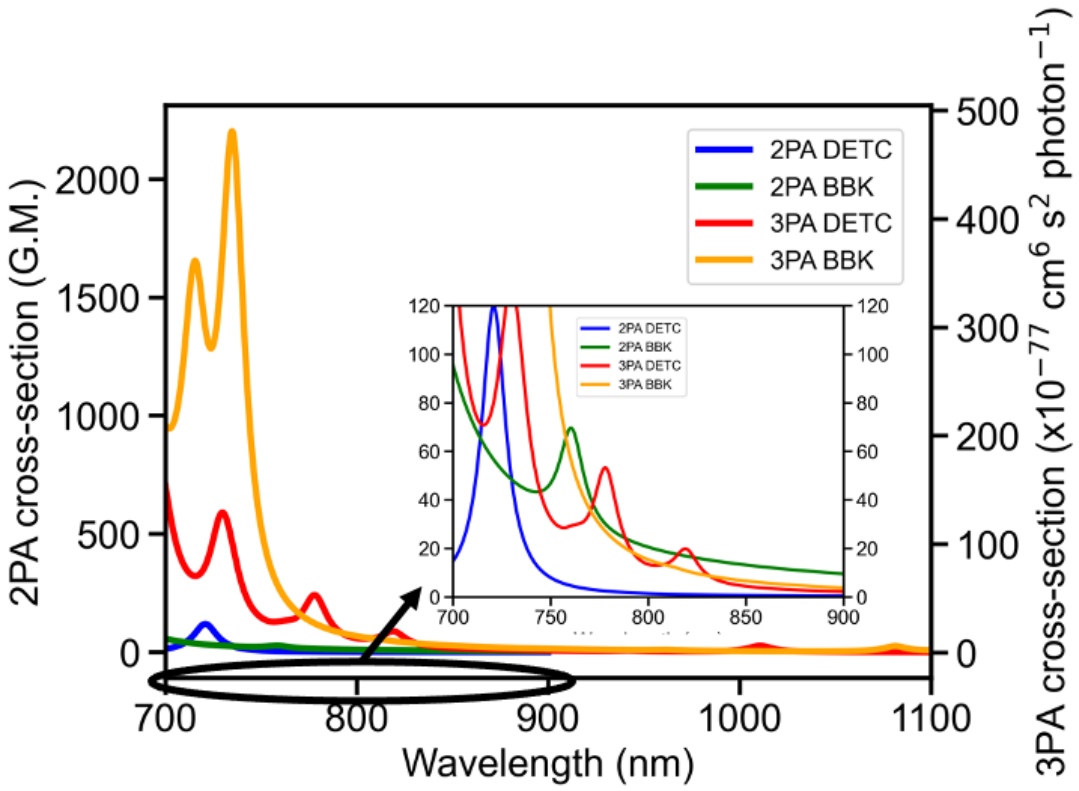

Figure 6.18: Theoretically calculated two-photon and three-photon absorption (2PA and 3PA) spectra of DETC and BBK using TD-CAM-B3LYP/def2-TZVP in ACN (PCM model) as described in Chapter 4.

Additionally, in order to enlarge the comparison between theory and experiment, 2PA spectra were calculated for DETC in PETA, gas phase, DCM and DMSO are reported in Figure B.6. Notably, the purely theoretical 2PA cross-sections obtained for DETC in DCM and DMSO exceed the experimentally reported values of 82 GM [201] and 40 GM [11], respectively, at wavelengths of 780 nm and 800 nm. However, the computed 2PA spectrum of DETC in PETA, exhibiting an absorption peak of 96 GM at 800 nm, aligns well with experimental observations [6, 18, 26, 215]. For benzylidene based initiators (slightly similar to BBK) the expected 2PA cross-sections are in the range of 190 GM at 800 nm in DCM [203, 204], higher than the computed 2PA spectrum of BBK. However the work of Li et al. [204] indicates that not only the size of the central ring but also the ring substitution of benzylidene ketone-based initiators can significantly affect the 2PA behavior. Considering the significant differences in the chemical structure of the benzylidene ketone-based initiators reported in the work and BBK, important differences in the 2PA cross sections can be expected. In addition, the blue shift of approximately 40 nm (computed absorption at 760 nm) of the spectrum with respect to experiment (800 nm is the printing wavelength) should be considered when employing the CAM-B3LYP functional; indeed, for comparison, the 2PA spectrum of BBK in B3LYP (see Table B.15) shows absorption at 808 nm, suggesting efficient 2PA during 3D laser nanoprinting utilizing this specific wavelength for both investigated PIs. It is essential to acknowledge

the challenges associated with directly comparing experimental and theoretical results in terms of 2PA spectra [137], as cross-sections are highly sensitive to various experimental parameters, referencing methods, and calculation parameters, including the consideration of environmental factors such as solvent effects. Several factors contribute to the discrepancy between experimental and theoretical values: the determination of 2PA absorption cross-sections using two-photon fluorescence has an accuracy limited to 8-10% [216] and it is known that z-scan data typically underestimates 2PA cross-section by up to a factor of 2.5-5 [217]. Finally, it is important to keep in mind that no one of the mentioned experimental studies of e.g. DETC considered the potential for higher-order absorption processes.

The multiphoton absorption character of DETC and BBK goes beyond the 2PA, as proved by the fact that, as reported in experiment [6, 20, 28, 46, 26, 45], three photons are necessary to start the FRP in absence of co-initiator. To explore this aspect, the corresponding 3PA spectrum was simulated and reported in Tables B.13, B.12, B.17, B.16and Figure 6.18. Since solvent implementation was not available in Dalton 2020.0, spectra were calculated solely in the gas phase. For the CAM-B3LYP spectra, while the presence of a peak related to the $S_0 \rightarrow S_1$ transition at 1010 nm and 1103 nm with 3PA cross-section value of $5.58\text{x}10^{-78}$ cm^6 s^2 $photon^{-1}$ and $1.13\text{x}10^{-77}$ cm^6 s^2 $photon^{-1}$ for DETC and BBK respectively, is evident (see Tables B.12 and B.16), the transitions between the $S_0 \rightarrow S_3$ and $S_0 \rightarrow S_4$ excited states when employing laser wavelengths of 819 nm and 807 nm, respectively for DETC and $S_0 \rightarrow S_4$, 5 excited states when employing laser wavelengths of 812 nm, respectively for BBK are the closest to experiment. 3PA spectra computed with B3LYP are red-shifted and involved higher excited states: $S_0 \rightarrow S_1$ transition at 1155 nm and 1252 nm with 3PA cross-section value of $9.53\text{x}10^{-78}$ cm^6 s^2 $photon^{-1}$ and $15.53\text{x}10^{-77}$ cm^6 s^2 $photon^{-1}$ for DETC and BBK respectively while the transitions $S_0 \rightarrow S_8$ and $S_0 \rightarrow S_9$ when employing laser wavelengths of 819-805 nm and 809-795 nm, respectively for DETC and BBK are the closest to experiment (see Tables B.13 and B.17). Consequently, theoretical calculations indicate that these PIs potentially possesses the ability to absorb three photons simultaneously, leading to highly excited singlet states. Nevertheless, such states are inherently unstable and exhibit rapid relaxation through conical intersections (typical vibrational frequencies of modes coupled to the electronic transition were calculated to be approximately 20 THz, i.e. 50 fs [218]), ultimately reaching the lowest singlet state. This relaxation process results in energy dissipation, thereby reducing the efficiency of the PI and leading to the conclusion that radical generation does not originate from subsequent ISC from these highly excited singlet states. This theory is further supported by the observation made by Fischer et al. [20] for which DETC fluorescence under 3D laser nanoprinting conditions, upon fs excitation, is primarily based on 2PA from the S_1 state, indicating that the S_1 state is accessed through the absorption of two photons at 775-800 nm. In summary, these findings align with the previously proposed hypothetical scenario concerning the non-linearities of the 3PA observed experimentally for these initiators [28, 45, 20, 46], with the direct responsibility for radical generation assigned to a separate third photon absorbed subsequent to 2PA initiation and ISC by the T_1 state.

Table 6.16: Values for two-photon absorption (2PA) as excitation energy (Energy, eV), wavelength (λ_{1PA}, nm), oscillator strength (Osc.str.), and 2PA wavelength (λ_{2PA}, nm), 2PA strength (δ_{2PA}, a.u.), cross section (σ_{2PA}, GM) of DETC in implicit ACN (PCM model). Data obtained using TD-CAM-B3LYP/def2-TZVP level of theory and optimized ground state geometry of DETC as reported in Chapter 4. No rescaling with regard to experimental data was applied. 1GM corresponds to 1×10^{-50} cm^4 s photon^{-1} molecule^{-1}. The spectra are depicted in Figures 6.3 and 6.18.

Excitation	Energy	λ_{1PA}	Osc.str.	λ_{2PA}	δ_{2PA}	σ_{2PA}
1	3.45	359.30	0.9611	720.84	13800	119.00
2	4.06	305.52	0.0505	615.31	325	3.96
3	4.35	285.10	0.0296	582.08	4480	61.60
4	4.56	272.09	0.0217	552.27	3090	46.90
5	4.66	266.19	0.1405	542.60	12500	198.00
6	4.92	251.90	0.0647	511.27	5520	97.60
7	4.99	248.36	0.0756	501.96	1110	20.30
8	5.25	236.06	0.0160	474.13	283	5.80
9	5.55	223.33	0.0613	451.67	644	14.60
10	5.61	221.01	0.0909	445.99	1110	25.60

Table 6.17: Values for two-photon absorption (2PA) as excitation energy (Energy, eV), wavelength (λ_{1PA}, nm), oscillator strength (Osc.str.), and 2PA wavelength (λ_{2PA}, nm), 2PA strength (δ_{2PA}, a.u.), cross section (σ_{2PA}, GM) of BBK in implicit ACN (PCM model). Data obtained using TD-CAM-B3LYP/def2-TZVP level of theory and optimized ground state geometry of DETC as reported in Chapter 4. No rescaling with regard to experimental data was applied. 1GM corresponds to 1×10^{-50} cm^4 s photon^{-1} molecule^{-1}. The spectra are depicted in Figures 6.3 and 6.18.

Excitation	Energy	λ_{1PA}	Osc.str.	λ_{2PA}	δ_{2PA}	σ_{2PA}
1	3.28	377.62	2.1643	760.64	5200	40.50
2	3.63	341.75	0.0370	677.51	195	1.91
3	3.83	323.62	0.0364	650.83	298000	3170.00
4	4.56	271.73	0.0127	543.79	1440	21.90
5	4.57	271.57	0.0701	543.79	3750	57.30
6	5.09	243.41	0.0086	487.17	250000	4740.00
7	5.26	235.75	0.3261	471.42	3690	74.60
8	5.40	229.46	0.0069	460.05	753000	16000.00
9	5.45	227.43	0.1916	456.66	12800	277.00
10	5.58	222.32	0.0140	445.99	38600	872.00

6.3 Formation of the T_1 state

Upon the 2PA of DETC, the excited state S_1 strongly couples to the T_3 excited state, which has a slightly higher adiabatic energy (by 0.12 eV), exhibiting SOC of 7.55 cm^{-1} (Table 6.18 and Figure 6.19). This coupling leads to a fast and efficient ISC rate of 1.72x10^8 s^{-1}. The transition is characterized by 60% allowed ISC ($\pi\pi^* \rightarrow n\pi^*$, in gas phase), consistent with the El-Sayed rule [74] for such processes. To note that, as reported in 4 the T_3 state employed for the computation of the rates mentioned was optimized in gas-phase due to the unphysical nature of T_3 in ACN (see Figure 6.6) and to the consequent poor

convergence of the correlation function in the computation of ISC rates between T_3 and S_1 both optimized in implicit ACN (refer to Chapter 4 for examples of correctly converged correlation functions). This suggests an influence of the polarization included by the implicit solvent and subtle (complex) electronic nature of higher excited states of DETC, which could not be resolved with the LR-TD-DFT. The coupling of higher level methods and non-adiabatic molecular dynamics beyond the adiabatic approximation would have been necessary, however it is beyond the present investigation. After the ISC $S_1 \rightarrow T_3$, the high $T_3 \rightarrow T_1$ internal conversion of 2.30x10^{11} s^{-1} suggests that T_1 can be rapidly formed.

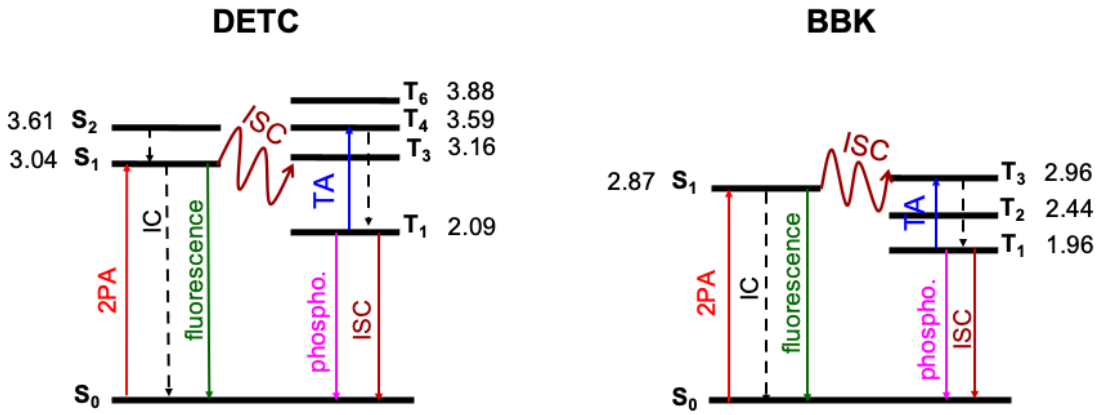

Figure 6.19: Jablonski diagram of DETC (left) and BBK (right). Excited states were optimized in ACN (PCM model) using TD-CAM-B3LYP-D3(BJ)/def2-TZVP and TDA-CAM-B3LYP-D3(BJ)/def2-TZVP for DETC and BBK respectively. Adiabatic energy values, including zero-point energy correction (ZPVE), are reported in eV. Rates of transitions between different states, calculated using electronic structure parameters, obtained with TD-DFT approach, are listed in Tables 6.18 and 6.19.

The ISC $S_1 \rightarrow T_3$ competes with the IC $S_1 \rightarrow S_0$ of 1.60x10^8 s^{-1} and fluorescence rate of 4.30x10^8 s^{-1} (lifetime 2.33 ns), comparable to the experimental values reported by Tang et al. [201], where the lifetime of DETC is $\sim$ 1 ns and the fluorescence rate is 2-4x10^9 s^{-1} (in toluene and methanol) [103] respectively. The long lifetime of $\sim$ 1.3 s of T_1 for DETC is associated to the slow phosphorescence rate of 7.69x10^{-1} s^{-1}; the ISC T_1-S_0 of 8.64x10^4 s^{-1} and lifetime of 11.6 μs, similar to the reported lifetime of 2.3-5 μs [20] allows other processes e.g. further TA to occur considering the fs laser pulse used in experiment. Charge density analysis, i.e. localization of electron-donating (hole) and electron-accepting (electron) parts of T_1 excited state demonstrates the activation of carbonyl moiety (atoms C11-O12 see areas in green in Figure 6.14) with higher local electron densities that should participate in ET and HAT.

Table 6.18: Photophysical non-radiative and radiative rates for DETC in implicit ACN (PCM model) computed using TD-CAM-B3LYP-D3(BJ)/def2-TZVP level of theory as reported in Section 4.5. The rates of IC and ISC processes involved the utilization of non-adiabatic coupling matrix elements (NACME in cm^{-1}), spin-orbit coupling (SOC in cm^{-1}), and reorganization energy (λ, in eV). For radiative rates the ΔE (in eV) and lifetime (in s) are reported. It has to be pointed out that all rates are calculated considering equilibrium states that are assumed to happen on the fs up to ps scale. NA refers to "not available" and in case of the rate signifies that the correlation function was not converged.

IC rates			
Transition	Rate	NACME	λ
$S_1 \rightarrow S_0$	$1.60x10^{8}$	0.009	0.205
$S_2 \rightarrow S_0$	NA	0.004	1.341
$T_6 \rightarrow T_1$	$1.25x10^{10}$	0.006	0.171
$T_4 \rightarrow T_1$	$4.50x10^{10}$	0.006	0.478
$^{*}T_3 \rightarrow T_1$	$2.30x10^{11}$	0.003	0.572
ISC rates			
Transition	Rate	SOC	λ
$S_1 \rightarrow T_1$	$8.84x10^{4}$	0.97	0.027
$^{*}S_1 \rightarrow T_3$	$1.72x10^{8}$	7.55	0.316
$S_1 \rightarrow T_4$	$3.94x10^{6}$	4.49	0.201
$S_1 \rightarrow T_6$	$6.56x10^{6}$	9.51	0.336
$S_2 \rightarrow T_1$	$6.33x10^{8}$	22.96	0.474
$^{*}S_2 \rightarrow T_3$	$1.57x10^{11}$	26.96	0.390
$S_2 \rightarrow T_4$	$1.12x10^{9}$	25.81	0.429
$S_2 \rightarrow T_6$	NA	9.43	0.960
$^{*}T_1 \rightarrow S_0$	$8.64x10^{4}$	2.16	0.181
RISC rates			
Transition	Rate	SOC	λ
$T_1 \rightarrow S_1$	$5.18x10^{4}$	0.80	0.021
$^{*}T_3 \rightarrow S_1$	$5.39x10^{9}$	5.47	0.284
$T_4 \rightarrow S_1$	$2.44x10^{9}$	7.68	0.600
$T_6 \rightarrow S_1$	$1.38x10^{8}$	2.09	0.362
$T_1 \rightarrow S_2$	$3.59x10^{6}$	15.52	0.351
$^{*}T_3 \rightarrow S_2$	$5.34x10^{6}$	6.41	0.384
$T_4 \rightarrow S_2$	$3.06x10^{7}$	1.49	1.974
$T_6 \rightarrow S_2$	NA	2.35	0.712
Radiative rates			
	Rate	ΔE	lifetime
Fluorescence	$4.30x10^{8}$	3.04	$2.33x10^{-9}$
Phosphorescence	$7.69x10^{-1}$	2.09	1.30

$^{*}T_3$ state is optimized in gas-phase
**lifetime of T_1 is $1.16x10^{-5}$ s

The photophysical rates computed for BBK indicate that, after reaching the first singlet excited state S_1, the most probable ISC rate 76% allowed is from S_1 ($\pi\pi^*$) to T_3 ($n\pi^*$) of $2.12x10^{6}$ s^{-1} with SOC of 3.63 cm^{-1} and ΔE S-T of -0.09 eV (Table 6.19). The state involved in the ISC with S_1 is T_3 which shows similar $n\pi^*$ character (see Figure B.5 and B.4) and similar ΔE S-T to DETC. However, the SOC associated to the

S_1-T_3 ISC rate of DETC (7.55 cm^{-1}) is higher than the one of BBK while the reorganization energies are similar (~ 0.3 eV). Important to note that the S_1-T_3 ISC rate of BBK is ~2 order of magnitude lower than fluorescence, which happens with the rate of 6.72x10^8 s^{-1} and IC $S_1 \rightarrow S_0$ of 1.38x10^8 s^{-1}. The fluorescence rate is in the same order as the one for DETC (4.30x10^8 s^{-1}). Interestingly, the fluorescence rates for Irgacure 651 and Irgacure 369 are significantly lower (~10^5 s^{-1} and ~10^2 s^{-1}, respectively, in Table 5.12) compared to Norrish type II PIs, as expected [26]. The rate of phosphorescence and non-radiative decay of the first triplet state of 9.41x10^{-1} s^{-1} and 3.64x10^5 s^{-1}, similar to DETC (7.69x10^{-1} s^{-1} and 8.64x10^4 s^{-1}) lead to a T_1 state lifetime of 1.06 s and 2.75 μs, respectively. Moreover, similarly to DETC, the charge density analysis, i.e. localization of electron-donating (hole) and electron-accepting (electron) parts of T_1 excited state demonstrates the activation of carbonyl moiety (atoms C1-O12 see areas in green in Figure 6.16) with higher local electron densities that should participate in ET and HAT.

Table 6.19: Photophysical non-radiative and radiative rates for BBK in implicit ACN (PCM model) computed using TDA-CAM-B3LYP-D3(BJ)/def2-TZVP level of theory as reported in Section 4.5. The rates of internal conversion (IC) and intersystem crossing (ISC) processes involved the utilization of non-adiabatic coupling matrix elements (NACME in cm^{-1}), spin-orbit coupling (SOC in cm^{-1}), and reorganization energy (λ in eV). For radiative rates the ΔE (in eV) and lifetime (in s) are reported. It has to be pointed out that all rates are calculated considering equilibrium states that are assumed to happen on the fs up to ps scale. NA refers to "not available" and in case of the rate signifies that the correlation function was not converged.

IC rates			
Transition	Rate	NACME	λ
$S_1 \rightarrow S_0$	1.38x10^8	0.009	0.237
$T_3 \rightarrow T_1$	NA	0.000	0.552
$T_2 \rightarrow T_1$	8.12x10^{10}	0.005	0.326
ISC and RISC rates			
Transition	Rate	SOC	λ
$S_1 \rightarrow T_1$	9.68x10^5	0.32	0.258
$S_1 \rightarrow T_2$	1.09x10^5	2.83	0.076
$S_1 \rightarrow T_3$	2.12x10^6	3.63	0.265
$T_1 \rightarrow S_1$	3.30x10^3	0.20	0.287
$T_2 \rightarrow S_1$	1.59x10^4	1.10	0.052
$T_3 \rightarrow S_1$	2.14x10^9	3.35	0.255
$T_1 \rightarrow S_0$	3.64x10^5	1.96	0.472
Radiative rates			
	Rate	ΔE	lifetime
Fluorescence	6.72x10^8	2.87	5.81x10^{-9}
Phosphorescence	9.41x10^{-1}	1.96	1.06

Due to the limited number of excited states that could be successfully optimized with CAM-B3LYP, because of their high instability during the optimization, as further explained in Chapter 4, data computed with B3LYP are also included to have a broader view of the processes (see Table 6.20 and Figure 6.20). In this scenario the highest ISC rate 40% allowed is from S_1 ($\pi\pi^*$, see Figure 6.17) to T_2 ($\pi\pi^*$,see Figure 6.17) of 3.70x10^8 s^{-1} with SOC of 3.35 cm^{-1} and ΔE S-T of 0.31 eV (Table 6.20 and Fig-

ure 6.20). To note that the S_1-T_3 rate for BBK in B3LYP is similar to the one computed with CAM-B3LYP but still too low to compete with the other decay processes. The IC rate from T_2 to T_1 is 8.12x10^{11} s^{-1}, resulting in the extremely fast formation of T_1 ($\pi\pi^*$). The RISC T_1-S_1 is 2.69x10^5 s^{-1} and therefore not particularly favored. The ISC from S_1 to T_2 competes with the IC from S_1 to S_0 (1.49x10^8 s^{-1}) and fluorescence emission of 4.15x10^8 s^{-1}), similarly to what was reported with CAM-B3LYP. The phosphorescence rate of 1.15x10^0 and T_1 state lifetime of $\sim$ 0.87 s are in agreement with data computed for BBK in CAM-B3LYP and DETC. Similarly to DETC, the non-radiative decay from the T_1 state is 8.94x10^4 s^{-1} (lifetime of 11 μs) which allows for further absorption to high triplets employing fs laser at 800 nm. The enhanced agreement with experimental data and the greater availability of B3LYP-computed data for BBK enable the depiction of a scenario that cannot be extrapolated from data obtained with CAM-B3LYP. Therefore, the comparison between the results obtained using these two functionals for this PI will be kept.

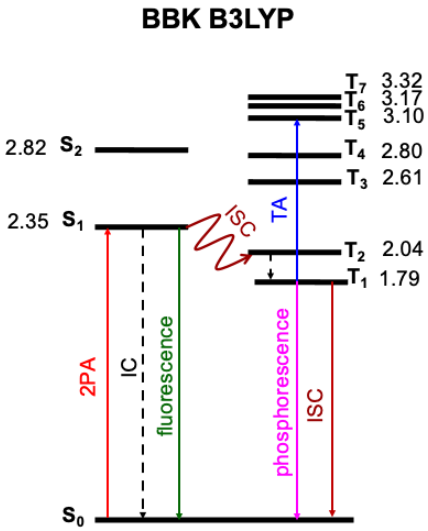

Figure 6.20: Jablonski diagram of BBK. Excited states in ACN (PCM model) were optimized using TDA-B3LYP-D3(BJ)/def2-TZVP and adiabatic energy values are expressed in eV and include the zero-point energy correction (ZPVE). Rates of transitions between different states, calculated using electronic structure parameters, obtained with TDA-DFT approach, are listed in Tables 6.20.

Table 6.20: Photophysical non-radiative and radiative rates for BBK in implicit ACN (PCM model) computed using TDA-B3LYP-D3(BJ)/def2-TZVP level of theory as reported in Section 4.5. The rates of IC and ISC processes involved the utilization of non-adiabatic coupling matrix elements (NACME in a.u.), spin-orbit coupling (SOC in cm^{-1}), and reorganization energy (λ in eV). For radiative rates the ΔE (in eV) and lifetime (in s) are reported. It has to be pointed out that all rates are calculated considering equilibrium states that are assumed to happen on the fs up to ps scale. NA refers to "not available" and in case of the rate signifies that the correlation function was not converged.

IC rates			
Transition	Rate	NACME	λ
$S_1 \rightarrow S_0$	$1.49x10^{8}$	0.007	0.114
$S_2 \rightarrow S_0$	$5.91x10^{7}$	0.005	0.089
$S_2 \rightarrow S_1$	$5.42x10^{11}$	0.005	0.034
$T_7 \rightarrow T_1$	$2.53x10^{10}$	0.002	0.632
$T_6 \rightarrow T_1$	$3.56x10^{11}$	0.004	0.999
$T_5 \rightarrow T_1$	NA	0.002	0.731
$T_4 \rightarrow T_1$	$1.19x10^{11}$	0.002	0.620
$T_3 \rightarrow T_1$	$1.12x10^{10}$	0.002	0.247
$T_2 \rightarrow T_1$	$8.12x10^{11}$	0.005	0.272
ISC rates			
Transition	Rate	SOC	λ
$S_1 \rightarrow T_1$	$5.11x10^{5}$	0.19	0.117
$S_1 \rightarrow T_2$	$3.70x10^{8}$	3.35	0.060
$S_1 \rightarrow T_3$	$5.14x10^{6}$	3.05	0.171
$^{*}T_1 \rightarrow S_0$	$8.94x10^{4}$	1.96	0.182
RISC rates			
Transition	Rate	SOC	λ
$T_1 \rightarrow S_1$	$2.69x10^{5}$	1.36	0.086
$T_2 \rightarrow S_1$	$7.87x10^{5}$	1.42	0.048
$T_3 \rightarrow S_1$	$2.10x10^{9}$	2.82	0.195
$T_4 \rightarrow S_1$	NA	0.75	NA
$T_5 \rightarrow S_1$	$4.72x10^{7}$	3.46	0.186
$T_6 \rightarrow S_1$	$1.65x10^{7}$	1.82	0.262
$T_7 \rightarrow S_1$	NA	0.22	0.263
$T_3 \rightarrow S_2$	$6.23x10^{4}$	0.36	0.214
$T_4 \rightarrow S_2$	NA	1.33	NA
$T_5 \rightarrow S_2$	$5.21x10^{8}$	1.38	0.356
$T_6 \rightarrow S_2$	$1.81x10^{6}$	0.10	0.579
$T_7 \rightarrow S_2$	$5.93x10^{7}$	1.40	0.133
Radiative rates			
	Rate	ΔE	lifetime
Fluorescence	$4.15x10^{8}$	2.35	$2.41x10^{-9}$
Phosphorescence	$1.15x10^{0}$	1.79	0.869

*lifetime of T_1 is $1.12x10^{-5}$ s

6.4 Reactivity of molecules in high triplet states

DETC and BBK possess the remarkable capability to trigger the polymerization of PETA by harnessing the energy of three photons[6, 20, 28, 46, 26, 45]. Upon undergoing 2PA to reach the excited state S_1, followed by ISC to T_3, and subsequent IC from T_3 to T_1, the system finally reaches the T_1 state. This state exhibits an enough long lifetime for both PIs, providing the possibility for the third photon to subsequently triggers the excitation of the system to high triplet states through the TA mechanism. In addition, as reported for Norrish type I and two-step absorption PIs, the energy of T_1 must be higher than the BDE in the ground state for a dissociation reaction to happen in the first triplet state. DETC and BBK, as expected being classified as Norrish type II PIs, exhibit the energy of T_1 lower than the bond energy (E_{BOND}), as reported in Table 6.21.

Table 6.21: Comparison of the bond dissociation energy (E_{BOND}) with the first triplet excited state optimized energy (E_{T1}) for BBK and DETC computed in CAM-B3LYP-D3(BJ)/def2-TZVP in ACN. For efficient bond scission from the triplet state, the triplet energy must be higher than the bond energy.

BOND	$\mathbf{E_{BOND}}$ eV	$\mathbf{E_{BOND}}$ kcal mol^{-1}	$\mathbf{E_{T1}}$ eV	$\mathbf{E_{T1}}$ kcal mol^{-1}	$\mathbf{E_{T1} < E_{BOND}}$ eV
		BBK			
C16-C17	5.08	117.23	2.34	53.93	2.34 <5.05
C35-C36	4.00	92.39			2.34 <4.00
C12-C15	3.70	85.23			2.34 <3.70
C34-C35	2.96	68.31			2.34 <2.96
C33-C34	3.24	74.70			2.34 <3.24
C45-N26	2.22	51.25			2.34 >2.22
		DETC			
C11-C17	3.47	80.03	2.09	50.96	2.09 <3.47
N14-C6	3.70	85.34			2.09 <3.70
C8-C11	3.54	81.72			2.09 <3.54

Due to the 3PA properties of the investigated PIs, in order to define which triplet excited state can be reached by the upcoming third photon, one-photon based TA in ACN was calculated for both DETC and BBK (Figures 6.21, 6.22, 6.23 and Tables B.21, B.22). The TA spectrum of DETC in CAM-B3LYP shows a peak located at 815 nm with oscillator strength of 0.18, reported in Figure 6.21 (see also Table B.21), demonstrating the presence of TA mechanism employing three photons at $\sim$ 800 nm. The GW-BSE excitations show similar results i.e. peak at 825 nm with lower oscillator strength of 0.02 (see Table B.23). In the case of BBK the maximum absorption is at 724 nm with oscillator strength of 0.07, blue shifted with respect to the wavelength of the laser used in experiment (i.e., $\sim$ 800 nm) (see Table B.22); however, the GW-BSE excitations show absorption at 782 nm with oscillator strength of 0.09 (see Table B.24).

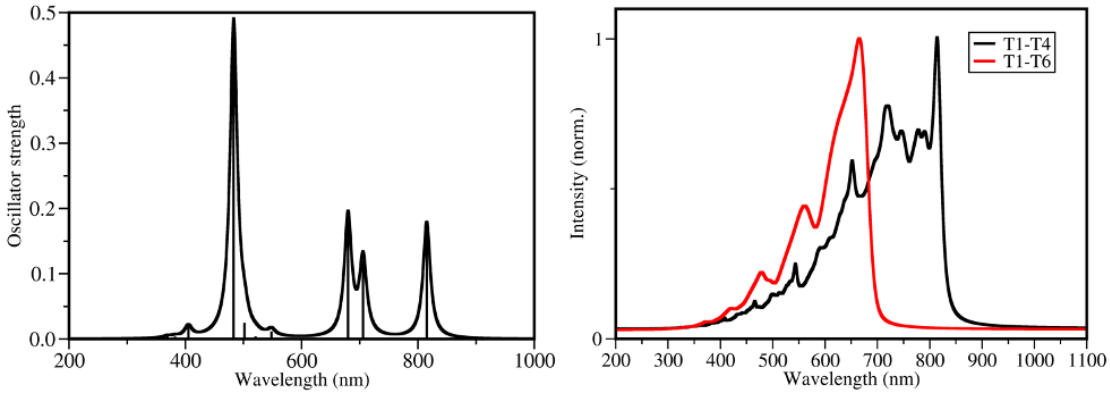

Figure 6.21: Triplet absorption (TA) spectrum of DETC computed starting from T_1 optimized geometry (left) and vibrationally resolved TA spectra in TD-DFT and plotted as reported in Chapter 4 (right). Spectra were computed in implicit ACN with (U)CAM-B3LYP-D3(BJ)/def2-TZVP level of theory. Due to significant geometry differences between T_1 and T_3 states in ACN (see Figure 6.6), the vibronically resolved spectrum for the transition $T_1 \rightarrow T_3$ was not generated. Spectra for $T_1 \rightarrow T_2$ and $T_1 \rightarrow T_5$ are not available due to TD-DFT convergence problems during the optimization of the related excited states.

The TA of DETC at $\sim$ 800 nm is reported to be higher than for other Norrish type II PIs i.e. isopropylthioxanthone (ITX) [215, 219, 220], index that fast TA may also favor the reactivity of the PI from higher triplet states. The comparison of TA strength between DETC and BBK is not yet reported experimentally; from the computed spectra with TD-DFT it can only be seen that the TA of DETC is stronger than for BBK, but not with GW-BSE. As expected, the oscillator strength of TA at the respective printing wavelength in GW-BSE is higher for DETC and BBK than for Irgacure 651 and Irgacure 369 (i.e. $\sim$ 0.002-0.009 see Table 5.14), which, being Norrish I Pis do not show TA from T_1 state [6, 18, 215]. However, the with the computation of the electronic TA spectra, that lack of the simulation of the dynamic of the system, the triplet state that can be formed upon the 3PA cannot be properly defined. Therefore, vibrational spectra[170] that consider the coupling of electronic and vibrational motion, related to the $T_1 \rightarrow T_n$ transitions were performed. Spectra for all possible transitions between $T_1 \rightarrow T_n$ (n=4,6 CAM-B3LYP and n=2-7 B3LYP) and $T_1 \rightarrow T_n$ (n=2,3 CAM-B3LYP and n=2,7 B3LYP) were computed for DETC and BBK respectively (see Figure 6.21, 6.22, 6.23). Considering data computed with CAM-B3LYP, among all spectra obtained, the transition $T_1 \rightarrow T_4$ overlaps with the experimentally used photon energy (see Figure 6.21) for DETC while $T_1 \rightarrow T_6$ is slightly blue-shifted in the $\sim$ 500-700 nm region. Data computed with B3LYP and depicted in Figure B.7 show that the $T_1 \rightarrow T_5$ and $T_1 \rightarrow T_6$ would be the most probable transitions. The hole and electron analysis of T_4 computed with CAM-B3LYP is the same as the one for T_5 computed with B3LYP (see Figure6.14,6.13), meaning that the triplet state that has higher probability to be reached is the same with both functional.

For BBK the transition $T_1 \rightarrow T_3$ shows absorption at 800 nm at the tail of the spectrum while $T_1 \rightarrow T_2$ is shift to higher wavelengths i.e. higher than 2000 nm. Since triplet states higher than T_3 could not be optimized for this PI employing CAM-B3LYP (see more details in Chapter 4), the respective vibronic transition from T_1 could not be performed. With the employment of B3LYP, more triplet excited states

could be optimized and therefore a more extensive analysis could be conducted on the vibronic transitions to high triplet states.

Similarly as for the CAM-B3LYP case reported in Figure 6.22, the vibronic spectra computed in Figure 6.23 show that the transition from T_1 would lead with high probability to T_3 or T_5 states, when using a laser beam at $\sim$ 800 nm, that would be responsible for the activation of the third photon at this energy. The hole and electron representation of T_3 state with both functional is similar (see Figure 6.16 and 6.17.)

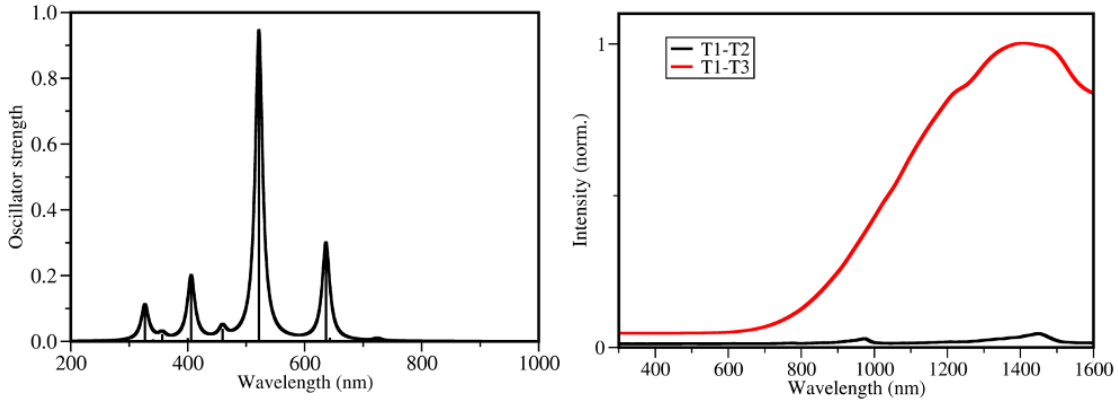

Figure 6.22: Triplet absorption (TA) spectrum of BBK computed starting from T_1 optimized geometry (left) and vibrationally resolved TA spectra in TDA-DFT and plotted as reported in Chapter 4. Spectra were computed in implicit ACN with (U)CAM-B3LYP-D3(BJ)/def2-TZVP level of theory. Vibronic spectra for triplet states higher than T_3 could not be performed due to TD-DFT convergence problems during the optimization.

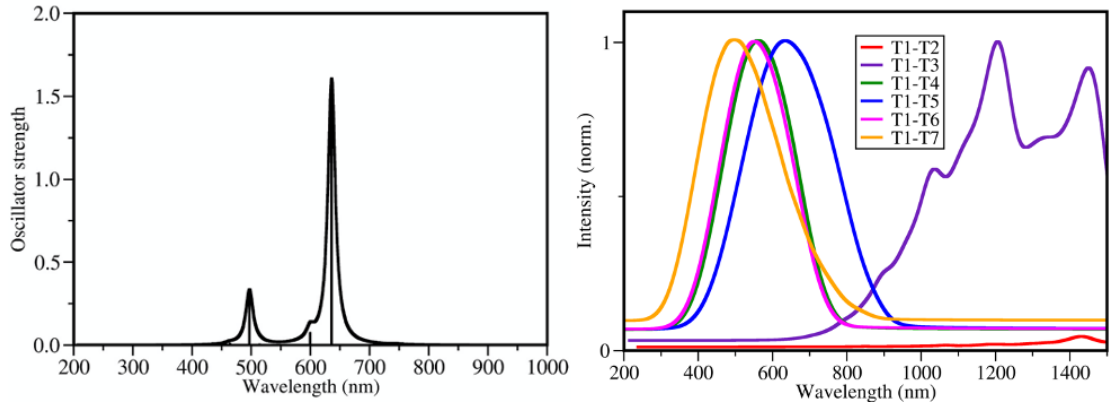

Figure 6.23: Triplet absorption (TA) spectrum of BBK computed starting from T_1 optimized geometry (left) and vibrationally resolved TA spectra in TDA-DFT and plotted as reported in Chapter 4. Spectra were computed in implicit ACN with (U)-B3LYP-D3(BJ)/def2-TZVP level of theory.

6.4.1 Depletion properties of DETC and BBK

DETC was reported to be excited by 2PA at 810 nm and efficiently depleted (via STED) using a second laser source at 532 nm while, when, using a second laser source at 800 nm (fs) [20] or 808 nm (cw) [40], in addition to printing, also inhibition of printing was observed. This process is not yet fully understood and STED mechanism of DETC was not further investigated in this work. From the computation of the T_1-T_n vibronic spectra, the possible mechanism of RISC from high triplets can be observed. Once reached high triplet states upon TA, DETC may also decay to the lowest triplet state (calculated IC $T_4 \rightarrow T_1$ is 4.50x10^{10} s^{-1} see Table 6.18) or return to singlet states via RISC. RISC rates from T_4 to the singlet states of DETC (e.g., rate of 2.44x10^{9} s^{-1} for $T_4 \rightarrow S_1$, 3.06x10^{7} s^{-1} for $T_4 \rightarrow S_2$) might cause a possible deactivation of DETC. However, since the mechanism of the process is not clarified, this is only, up to now, an assumption.

Similarly, BBK showed depletion mechanism (no STED) in addition to printing when using a cw 800 nm laser beam as second laser source. Depletion mechanism was also observed employing cw 400 nm laser beam for the first excitation combined with cw laser beam at 640 nm. On the other hand, when a cw 532 nm laser beam is employed instead of the cw 640 nm beam, the polymerization is observed to be improved rather than depleted. However experiments made are not yet published and more investigation is necessary in this direction to further clarify the scenario, which was not made in the present dissertation.

6.5 Possible radical generation mechanisms in high triplet states

The activation of triplet states in DETC is a crucial requirement for initiating polymerization, either in combination with DBA [28] or in the absence of any co-initiator. Initially, the HAT reaction between DETC and DBA was explored by considering DETC in the T_1 state and the amine in the S_0 state, resembling a standard Norrish type II initiator scenario (see Figure 6.24).

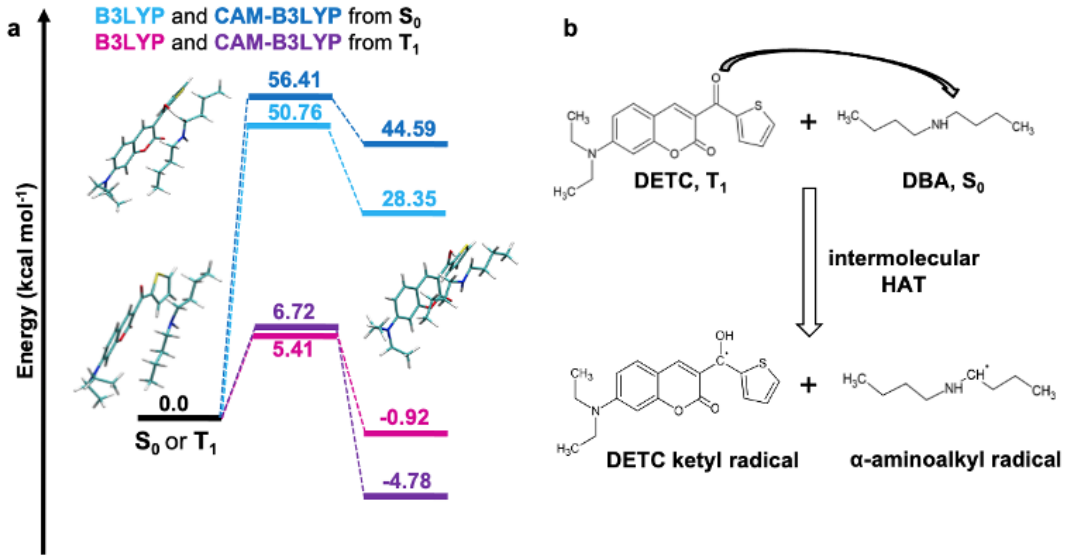

Figure 6.24: The activation energy barrier for the formation of radicals according to the Norrish type II mechanism calculated using B3LYP and CAM-B3LYP. **a** The energy barrier of HAT reaction between the carbonyl moiety of DETC and the C15-H19 bond of DBA co-initiator forming a ketyl and an α-aminoalkyl radical, respectively. The reaction energy barrier was obtained performing intrinsic reaction coordinate (IRC) calculation in implicit ACN starting from S_0 and T_1 state of DETC and S_0 state of DBA. **b** The mechanism of HAT reaction between the photoinitiator (PI) and the amine co-initiator.

In this scenario, in the first step, the carbonyl group of DETC attacks the ethyl group of DBA closest to the N atom, upon previous analysis of the breakable bonds of DBA (reported in Table B.25 and Figure 6.25), through an inter-HAT reaction, forming the ketyl and α-aminoalkyl radical on the PI and co-initiator, respectively. The presence of N atom, with higher electronegativity than C, weakens the adjacent C-H bonds favouring the cleavage. Specifically, the BDE for R_1 depicted in Figure 6.25 is 81.21 kcal mol^{-1}, in agreement with the reported experimental value [221], index that the C-H cleavage in DBA cannot occur without the presence of the PI.

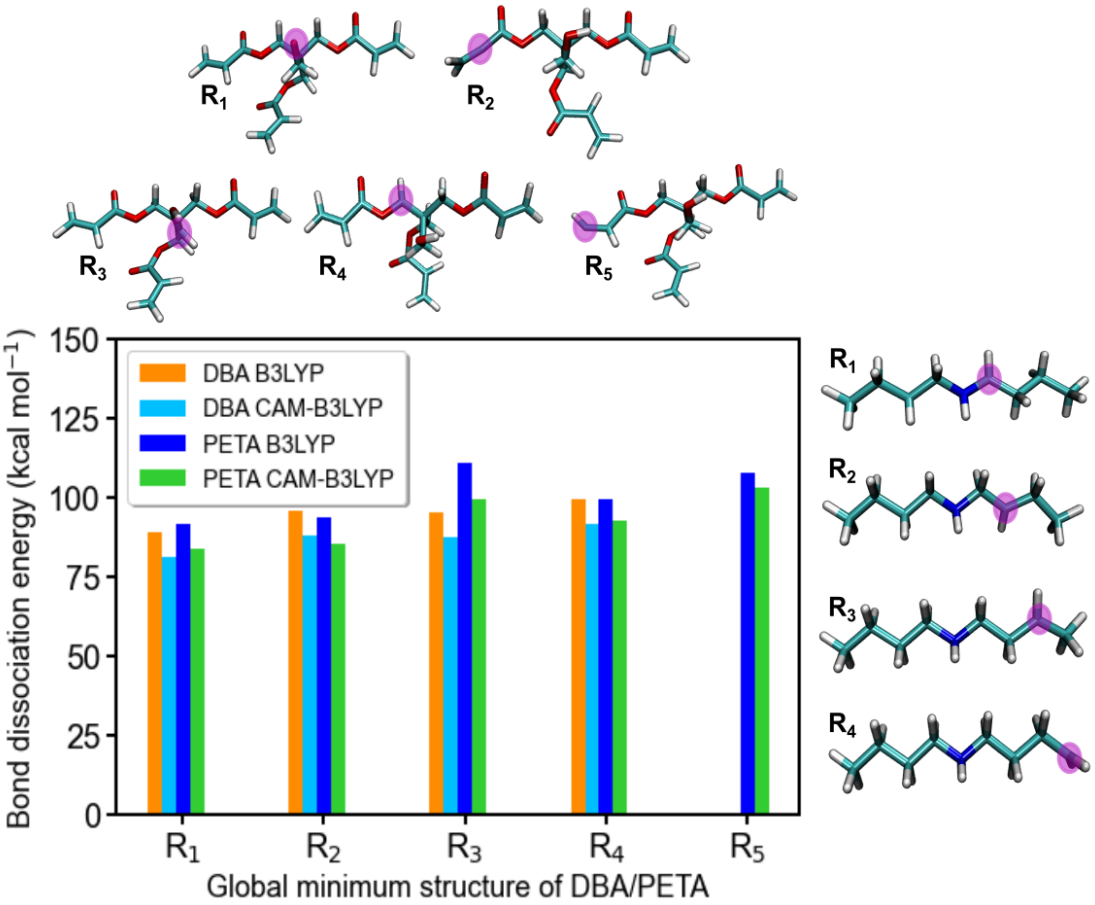

Figure 6.25: Possible types of DBA and PETA radicals in order to detect which C-H bond is the most probable to be broken during the first step of the inter-hydrogen atom transfer (HAT) reaction with DETC are visualized (R_1-R_5). Data are reported in Table B.25.

The calculated (CAM-B3LYP) energy barrier for the inter-HAT between DETC and DBA is 6.72 kcal mol^{-1} in ACN (see Table 6.22) which suggest rapid formation ($7.33x10^7$ s^{-1}) of reactive radicals, overcoming the non-radiative decay of the triplet state but several orders of magnitude. Notably, when DETC is in the S_0 state instead of T_1, the computed energy barrier for the same reaction is significantly higher, at 48.19 kcal mol^{-1}, indicating the impossibility from a thermodinamically and kinetically point of view for the reaction to occur in this condition.

Table 6.22: Comparison of Gibbs free energies and rates related to the Norrish type II radical formation reactions (inter-hydrogen atom transfer (HAT) mechanism) between DETC (either in S_0 or in different excited states) with DBA and PETA. The change in the Gibbs free energy of reaction (in kcal mol^{-1}) was computed as reported in Chapter 4 considering the formation of the R_1 type radical. E_a refers to the computation of the reaction energy barrier with the transition state and intrinsic reaction coordinate (IRC). Rates (in s^{-1}) were computed only when the energy barrier was known as reported in Chapter 4. All calculations were performed in implicit ACN with (U)B3LYP-D3BJ/def2-TZVP and (U)CAM-B3LYP-D3BJ/def2-TZVP level of theory.

	DBA				**PETA**	
	B3LYP		CAM-B3LYP		B3LYP	CAM-B3LYP
State	ΔG	Rate	ΔG	Rate	ΔG	ΔG
S_0	48.03	-	48.19	-	51.78	52.77
	(E_a:50.76)	$3.84x10^{-25}$	(E_a:56.41)	$2.76x10^{-29}$	-	-
S_1	-10.56*	-	-21.91*	-	-6.81*	-17.33*
T_1	1.86	-	0.44	-	5.61	5.47
	(E_a:5.41)	$6.77x10^{8}$	(E_a:6.72)	$7.33x10^{7}$	-	-
T_2	-7.09	-	-	-	-3.34	-
T_3	-12.27	-	-24.72	-	-8.52	-20.14
T_4	-23.58	-	-34.05	-	-19.83	-29.47
T_5	-30.56	-	-	-	-26.82	-
T_6	-32.58	-	-40.20	-	-28.83	-35.62
T_7	-38.55	-	-	-	-34.80	-

*:due to geometrical changes between the optimized first singlet excited states with both functional differences of energies are high

This reaction is ∼ 3-4 orders of magnitude slower than the computed cleavage reaction for Irgacure 651 and Irgacure 369, reported to be in the order of 10^{10}-10^{11} s^{-1} (see Section 5.5), in agreement with the fact that the former requires the interaction of two molecules (bimolecular) with subsequent HAT, while the latter is a unimolecular reaction involving bond cleavage. The absence in the experimental observations of the reaction between DETC and DBA (see Figure 1.3) shares similarities with the findings reported by Xue et al. [222] regarding the reaction between benzylidene ketone PIs and amine-based co-initiators. In that study, it was reported that the reaction was predominantly influenced by material diffusion rather than the activation process. This phenomenon could provide an explanation for the lack of changes in three-photon scaling during the 3D printing of PETA when photoresists containing DBA and DETC are used (see Figure 1.3). For these reasons, it seems that the primary pathway for the generation of reactive radicals is through TA upon previous 2PA, resulting in the formation of highly reactive triplet states. Due to the absence of experimental measurements on the combination of DBA and BBK, calculations involving these molecules were not performed.

Since the photoresists contains also PETA monomers, the impact of DETC and BBK on the radical formation directly by PETA was investigated. The mechanism is similar to the HAT reaction with DBA, involving the attack of the carbonyl bond of DETC or BBK to the C-H bond of PETA with the formation of a ketly radical on the PI and an alkyl radical on the monomer (see Figure 6.26). Activation energies upon formation of transition state, as for DBA, were not computed due to the large number of atoms and

complexity of the reactions involved, that lead to convergence problems on the transition state search. Similarly to DBA, the breakable C-H bonds of PETA were investigated via BDEs reported in Table B.25. Data show that the easiest radicals to be formed are R_1 and R_2. The Gibbs free energy of the reaction involving DETC and BBK in T_1 with R_1 is 5.47 kcal mol^{-1} and 2.34 kcal mol^{-1} while in S_0 is 52.77 kcal mol^{-1} and 47.25 kcal mol^{-1} (see Tables 6.22 and B.27, meaning that the reaction can not happen if the PI is not excited. Similarly the reaction is not spontaneous when the PI is in T_1 state. The formation of radicals with the participation of the T_1 state of PIs (for photoresists without co-initiator) was previously reported[20, 201, 45, 220], however, up to now, there is lack of experimental evidence on the formation of such radicals or reaction mechanisms. Therefore, since the inter-HAT reaction between DETC (in T_1) and DBA is more spontaneous than the reaction with PETA (0.44 kcal mol^{-1} vs 5.47 kcal mol^{-1}, see Table 6.22) and the former could not be observed in the printing conditions (see Figure 1.3), the HAT reaction between PETA and DETC should not occur, when DETC is in T_1. The Gibbs free energy for this reaction when DETC or BBK are in higher triplet states is highly spontaneous, i.e. -29.47 kcal mol^{-1} and -35.62 kcal mol^{-1} for DETC in T_4 and T_6, respectively (Figure 6.26 and Table 6.22).

The inter-HAT reaction between BBK and PETA exhibits spontaneity when BBK is in T_1, with Gibbs free energies approximately around -6 kcal mol^{-1} (R_1 and R_2). However, when BBK is in higher triplet states (e.g., T_3), a significantly higher degree of spontaneity is observed (approximately -21 kcal mol^{-1}). However, due to the absence of experimental data on the interaction between BBK and DBA is not possible to compare and therefore further validation from experiment and theory would be necessary to establish if the reaction can effectively take place from T_1. In addition, the ΔG computed in Table B.27 consider only to the thermodynamics of the reaction and the extension to the analysis of the kinetics through the computation of the TS should be performed to be able to determine if the reaction takes place.

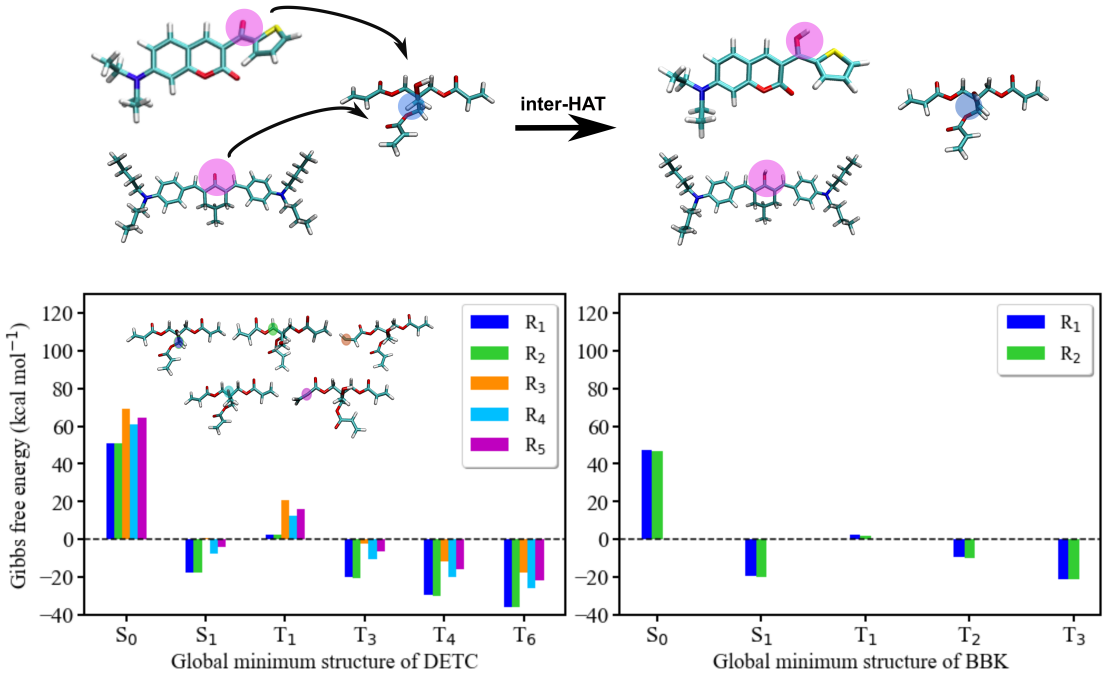

Figure 6.26: Radical reaction mechanism between DETC and PETA (left) and between BBK and PETA (right). These are two distinct reactions of each photoinitiator (PI) with the monomer. The hydrogen atom transfer (HAT) reaction between DETC (or BBK) in a high triplet state and PETA in the ground state leads to the formation of a ketyl radical on DETC (or BBK) and an alkyl radical on PETA (R_1 or R_2, R_1 depicted in the Figure 6.25) that consequently initiates the polymerization (R_1 is reported in the figure). It is important to note that all carbon atoms in the α position with respect to the central carbon atom in the pentaerythritol fragment of PETA are equally susceptible to form radicals (upper part of the Figure). Gibbs free energy of the reaction involving different PETA radicals (R1-R5, see Figure 6.25) as a function of the electronic state of DETC or BBK (see Table B.26 ans B.27) (down). Energies were computed employing (U)CAM-B3LYP-D3(BJ)/def2-TZVP approach in implicit ACN.

Beyond the reaction between the PIs and the monomer or co-initiator, the analysis of several other possible radical formation mechanisms such as photoactivated H-abstraction, photolysis, and biradical formation is necessary. Similar to the formation of alkyl radicals upon the reaction with PETA (see Figure 6.26), the photoactivated H-abstraction, photolysis and biradical formation reaction were evaluated through BDEs and Gibbs free energies, as explained in Chapter 4.

The photoactivated H-abstraction investigates the possibility for the third photon to abstract H atom from the PIs, leading to the formation of radicals upon cleavage of the respective C-H bond, as reported in [223]. Results are illustrated in Table B.28, B.29 and B.30 where several possible C-H cleavage were investigated for DETC and BBK. Data shows that the H-atom abstraction of H_5 of DETC and H_4 of BBK are characterized by the lowest Gibbs free energy, specifically 7.66 kcal mol^{-1} in T_4 and 29.82 kcal mol^{-1} in T_3 for DETC and BBK, respectively. These results are in agreement with the reactivity induction observed in molecules containing heteroatoms, such as N-atoms, with higher electronegativity than C,

which influence the reactivity of neighboring C-H bonds facilitating the cleavage[223]. The abstraction of H_5 and H_4 cannot occur either from these states and from T_1, due to the high Gibbs free energies (39.83 kcal mol^{-1} and 44.55 kcal mol^{-1} for DETC and BBK in T_1, respectively). The process is therefore not spontaneous and competes with IC (Table 6.18). Consequently, the radical formation via C-H bond breaking, as depicted in Figure 6.27 is disabled for both PIs.

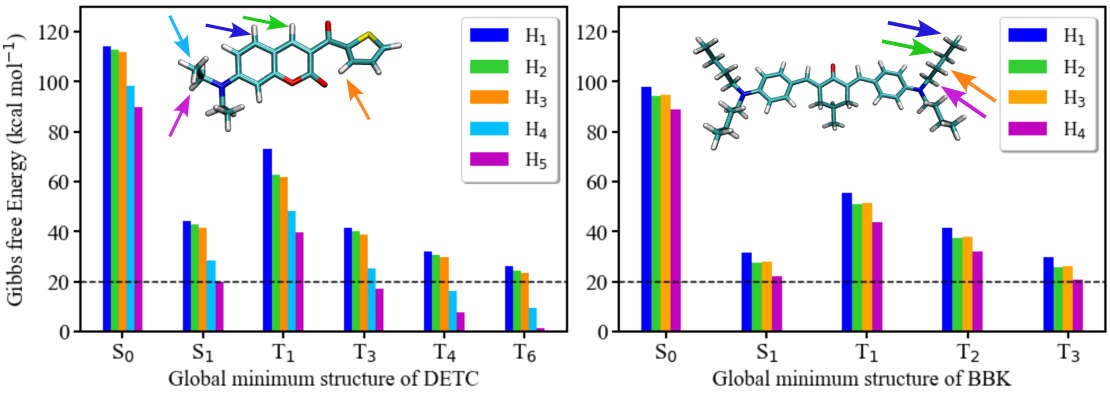

Figure 6.27: Gibbs free energy for different hypothetical C-H bond breaking for DETC (H_1-H_5) (left) and for BBK (H_1-H_4) (right). Energies were computed employing (U)CAM-B3LYP-D3(BJ)/def2-TZVP in implicit ACN.

The investigation of the radical generation mechanism involving the cleavage of several C-C and C-N bonds of the PIs upon the absorption of the third-photon, specifically through photolysis following a typical Norrish type I mechanism, was conducted. Results for DETC and BBK are assessed in Table B.31 and Table B.32) for DETC and Table B.33 for BBK, respectively. The cleavage of C8-C11, N4-C6 and C11-C17 of DETC (see Figure 6.28 demonstrates a higher likelihood of being broken, as evidenced by the lowest Gibbs free energies, particularly in high triplet states, such as -0.52 kcal mol^{-1}, 3.10 kcal mol^{-1} and -2.21 kcal mol^{-1} in T_4 respectively and -6.67 kcal mol^{-1}, -3.06 kcal mol^{-1} and -8.35 kcal mol^{-1} in T_6 respectively (see Table B.31 and B.32). However, the reaction is still less probable than the reaction with PETA (i.e. -30 kcal mol^{-1} from T_4, see Table B.26) and therefore, in order to effectively generate radicals, it must overcome the IC or RISC processes, which happen with the rate of 4.50x10^{10} s^{-1} and 2.44x10^{9} s^{-1}/3.06x10^{7} s^{-1} (see Table 6.18) from T_4 excited state, respectively. Similarly to DETC, the Gibbs free energy associated to the cleavage of the C33-C34 and C45-N26 bonds of BBK (see Figure 6.28**b**) is -9.33 kcal mol^{-1} and -17.02 kcal mol^{-1} from T_3, again less spontaneous than the $\sim$ -21 kcal mol^{-1} for the Gibbs free energy of the reaction with the monomer from the same state (see Table B.27. The RISC T_3-S_1 happens with the rate of 2.14x10^{9} s^{-1}.

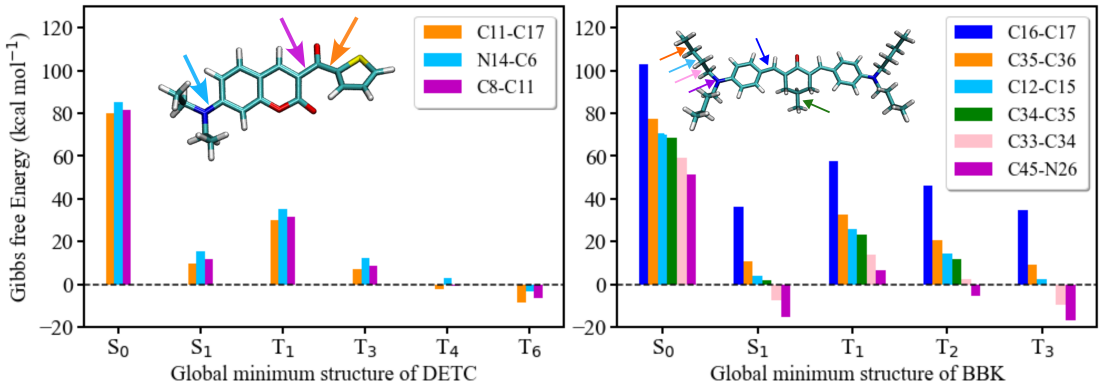

Figure 6.28: Gibbs free energy for hypothetical DETC (left) and BBK (right) radical formations through the photolysis of several possible CH and C-N bonds:C11-C17, N14-C6 and C8-C11 for DETC (left) and C16-C17, C35-C36, C12-C15, C34-C35, C33-C34, C45-N26 for BBK (right) as a function of the respective electronic state. Energies were computed employing (U)CAM-B3LYP-D3(BJ)/def2-TZVP in implicit ACN.

This study indicates that DETC and BBK should not spontaneously form any reactive radical on their own for FRP in 3D printing upon H-abstraction while the generation of radicals upon cleavage of C-C or C-N bonds would be theoretically possible from high triplet states when it overcomes IC and ISC processes but, as previously mentioned, less probable than the reaction between the PIs and PETA. The Gibbs free energy associated to the cleavage reaction from the T_1 state is in the order of $\sim$ 30 kcal mol^{-1} and 6-60 kcal mol^{-1} for all possible investigated bonds of DETC and BBK, respectively, indicating non spontaneous process to form radical from the T_1. To note that the results computed with B3LYP shows a similar scenario. In order to further validate the result from the kinetic point of view considering CAM-B3LYP, the activation energy would be needed. For comparison, the computed Gibbs free energy for the cleavage of Irgacure 651 and Irgacure 369 in T_1 is -19.56 kcal mol^{-1} and -16.20 kcal mol^{-1}, respectively. In addition the comparison of the BDEs associated to the cleavage of the investigated bonds with the energy of the T_1 state for DETC and BBK, as reported in Table 5.17 for Norrish type I PIs, is reported in Table 6.21. Data shows that for DETC and BBK the T_1 energy is always lower than the bond energy while, on the contrary, for Irgacure 651 and Irgacure 369 the energy of T_1 is always higher than the bond energy (see Table 5.17), meaning that the cleavage of DETC and BBK cannot occur in T_1 while it does for Norrish type I PIs.

The process of biradical formation, previously observed in other photosensitizers [224, 225, 226, 227], entails intra-HAT between the same functional groups involved in inter-HAT transfer with DBA or PETA. Both DETC and BBK, being Norrish type II PIs, possess these functionalities in their chemical structure. The transfer originates from the C-H bond adjacent to the N atom of the initiator's chain to its carbonyl functionality, resulting in the generation of a biradical specie where the alkyl radical may initiate polymerization, given the higher steric hindrance of the ketyl radical (refer to Section 6.6). However, due to the combination of the inherent rigidity of the chemical structure common to Norrish type II PIs and the long-range HAT required for this process (approximately 8.85 Å for DETC and 8.95

Å for BBK measured on T_1 geometry), the actual occurrence of this reaction is considered unlikely. For thoroughness, the computation of Gibbs free energies related to H-abstraction and attachment, using global minima structures of DETC at various potential energy surfaces, is presented in Figure B.8. The ten biradicals are divided into two main groups labeled as "**a**" and "**b**", differentiated by the involved carbonyl group. Specifically, biradicals 1-5Bi-**a** are associated with the C11-O12 carbonyl group (see Figure 6.2), while biradicals 1-5Bi-**b** involve the C9-O13 carbonyl group (refer to Figure B.8). The BDEs for the Bi-**a** type of radicals are presented in Table B.34 and B.35. Among these, the formation of biradical 5Bi-**a** exhibits the lowest Gibbs free energies and BDEs, ranging from -28 to -30 kcal mol^{-1}, associated with high triplet excited states. Due to the extremely low probability and lack of experimental confirmation of intramolecular hydrogen atom transfer (intra-HAT) on rather long distances for rigid-like molecules, it was not considered as a possible radical formation mechanism for the initiators, and therefore, calculations for BBK were not performed. The inter-HAT between DETC molecules has not been investigated due to the low concentration of the photoinitiator (0.25 and 0.50 wt%), limited by its low solubility into the monomer, during the printing condition.

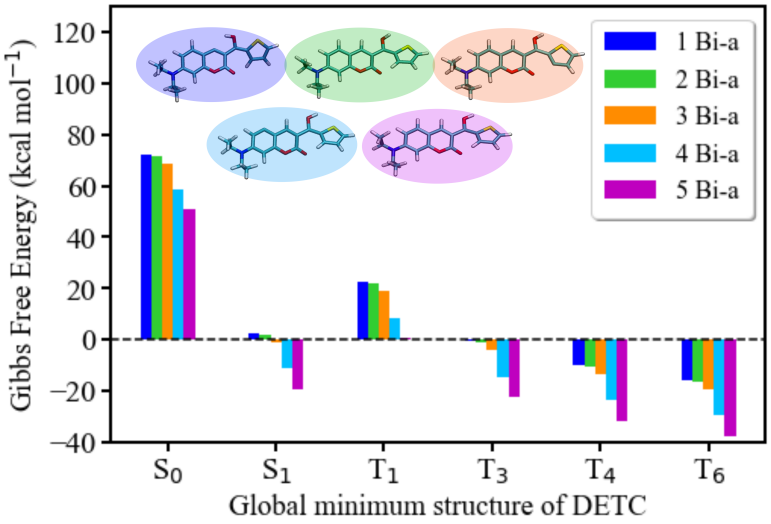

Figure 6.29: Gibbs free energy for hypothetical DETC biradicals (1Bi-**aa** to 5Bi-**a**)formation upon intra-HAT reaction. Energies were computed employing (U)CAM-B3LYP-D3(BJ)/def2-TZVP in implicit ACN.

6.6 Free radical polymerization with the monomer

The FRP of PETA monomer involves the conversion of the α,β-unsaturated double bond of the monomer into a single C-C bond through the attack of the reactive radicals discussed above [99], as illustrated in Figure 6.30. However, since the specific radicals that initiate the reaction remain unknown experimentally, calculations of the Gibbs free energies associated with the polymerization reaction were conducted. This analysis aimed to determine the spontaneity of the reaction and identify the most reactive radical species. The investigated radicals include:α-aminoalkyl radical of DETC formed either via a) intramolec-

ular HAT, i.e. DETC biradical (**step 1a** in Figure 6.30) or **b** intermolecular HAT (**step 1b** in Figure 6.30), DETC ketyl radical (**step 1c** in Figure 6.30), as well as the α-aminoalkyl radical of DBA (**step 1d** in Figure 6.30) generated by intermolecular HAT with DETC in (probably) high triplet states (Table 6.22), alkyl radical of PETA (**step 1e** in Figure 6.30) generated by intermolecular HAT with DETC in (probably) high triplet states (Table 6.22), alkyl radicals (**step 1f** and **step 1g** in Figure 6.30) formed on DETC fragments upon photolysis of bond C8-C11 (Table B.32). Upon initiation of the radical formed (**step 2a-g**), it should react with the next PETA monomer to form another alkyl radical, which subsequently forms a radical chain (**step 3**) or crosslinks until the termination step occurs. Important to mention that the propagation step might be characterized by many transfer processes since polymerization mechanisms are usually complex and characterized by many different processes e.g disproportion or radical coupling reactions that can terminate the growing polymer chain. In Figure 6.30, we report hypothetical radical polymerization mechanisms during the FRP initiation. In Table 6.30, we summarized the key findings of the FRP of PETA monomers in the case of the DETC usage. Data reported show that the reaction between the α-aminoalkyl DETC radical (step 1a, 1b) or alkyl DETC radical (**step 1f**,**step 1g**) with PETA may be spontaneous, therefore if these radicals could be formed they could possibly initiate FRP. However, the formation of these radicals is hindered due to faster intersystem crossing to T_1. Therefore, most probably such FRP is not possible. Ketyl radical of DETC does not allow spontaneous FRP, so it is less reactive than all the others, which was also reported experimentally [228, 107]. FRP is spontaneous, when the α-aminoalkyl radical generated on DBA and the alkyl radical of PETA (**step 1d**,**step 1e**) are present. The formation of these radicals was shown to be permitted due to the DETC excitation to higher triplet states (see Table B.25). Since the nonlinearity of 3D printing with DETC+DBA+PETA has not changed from N $\sim$ 3 to N $\sim$ 2, we tend to believe that the formation of these two radicals is hindered in the presence of DETC in T_1, therefore, TA to higher triplets states is necessary to excite DETC towards DBA and PETA radical activation.

Similarly as for DETC, the ketyl radical on BBK, generated through inter-HAT with PETA, possesses a high steric hindrance and exhibits no reactivity towards polymerization [228, 107]. This is indicated by its Gibbs free energy value > 100 kcal mol^{-1}. On the other hand, the alkyl radicals on the BBK core and arm, generated through photolysis (Table B.33), display much higher reactivity with Gibbs free energy values of -3.59 kcal mol^{-1} and -14.07 kcal mol^{-1}, respectively. However, similar to what has been previously reported for DETC, the alkyl radical on the PETA monomer, generated through inter-HAT with BBK, demonstrates the lowest Gibbs free energy (-22.80 kcal mol^{-1}) for activating the polymerization reaction, as shown in Table B.33.

Table 6.23: Gibbs free energies of hypothetical radical generation mechanisms for the conversion of the α,β-unsaturated double C=C bond of PETA into a single C-C bond (**step 1a-g**). Calculations performed using (U)CAM-B3LYP-D3(BJ)/def2-TZVP level of theory in ACN.

Step	**Components**	ΔG **(kcal mol^{-1})**
1a	biradical DETC + PETA	-5.46
1b	aminoalkyl radical DETC + PETA	-12.00
1c	ketyl radical DETC + PETA	-0.37
1d	aminoalkyl radical DBA + PETA	-14.90
1e	alkyl radical PETA + PETA	-25.10
1f	photolysis DETC + PETA	-45.06
1g	photolysis DETC + PETA	-25.64

Table 6.24: Gibbs free energies of hypothetical radical generation mechanisms for the conversion of the α,β-unsaturated double C=C bond of PETA into a single C-C bond through the reaction with BBK. Calculations performed using (U)CAM-B3LYP-D3(BJ)/def2-TZVP level of theory in ACN. The polymerization mechanisms are not shown. ∞ is used when the ΔG of the reaction is higher than 100 kcal mol-1.

Components	ΔG **(kcal mol^{-1})**
ketyl radical BBK	∞
alkyl radical PETA	-22.80
alkyl radical on BBK (core)	-3.59
alkyl radical on BBK (arm)	-14.07

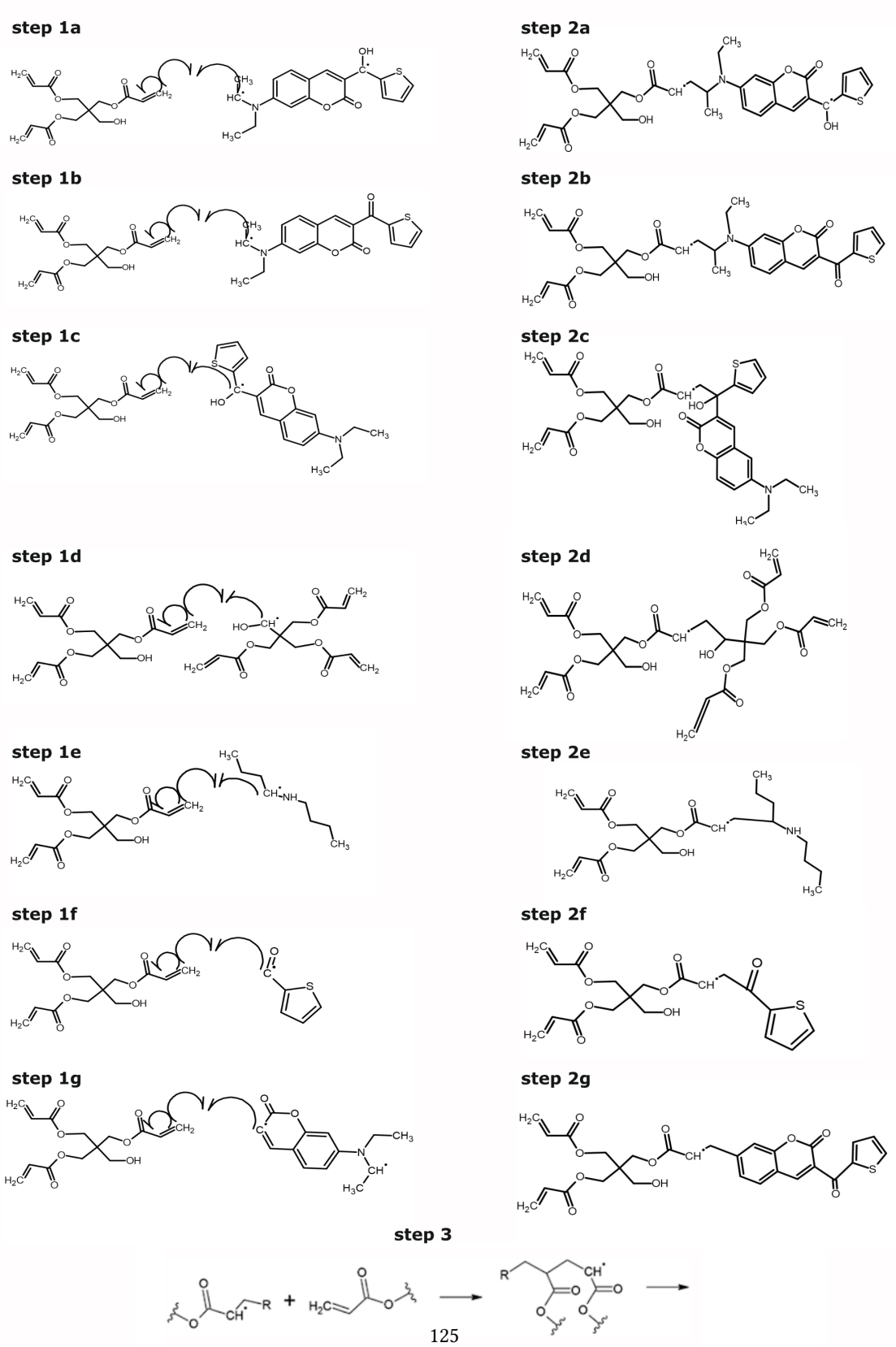

Figure 6.30: Hypothetical photopolymerization reaction mechanisms that may activate PETA monomer through the FRP that should lead to the conversion of the α,β-unsaturated double C=C bond of PETA into a single C-C bond (**step 1a**-**g**). Propagation radical that could be formed (**step 2a**-**g**) with the general polymerization propagation scheme (**step 3**).

7

Two-step absorption photoinitiators

This chapter extensively explores the photochemical and photophysical properties exhibited by PIs involved in two-step absorption, specifically benzil, biacetyl, and tetramethylbenzil. These PIs were selected from the candidates listed in Ref. [51], representing one-color two-step, two-color two-step, and two-color two-step with depletion mechanism, as elucidated in Chapter 1. The 2D and 3D chemical structures are presented in Figure 7.1. The primary objective is to discern the differences and similarities in the mechanisms leading to FRP, aiming to gain a deeper understanding of their properties and explore the possibility of designing even more sensitive PIs for this recently discovered technique that surpasses conventional 2PA. Utilizing the two-step two-photon absorption mechanism illustrated in Figure 1.6, the analysis encompasses simulating the first-step absorption leading to the singlet excited state, followed by ISC and the formation of the first triplet state. From T_1, TA spectra are generated, and subsequent investigations into radical formation reactions are conducted using QM calculations, as detailed in Chapter 4.

Data presented in this Chapter are as of yet unpublished and more validation from an experimental and theoretical view is needed.

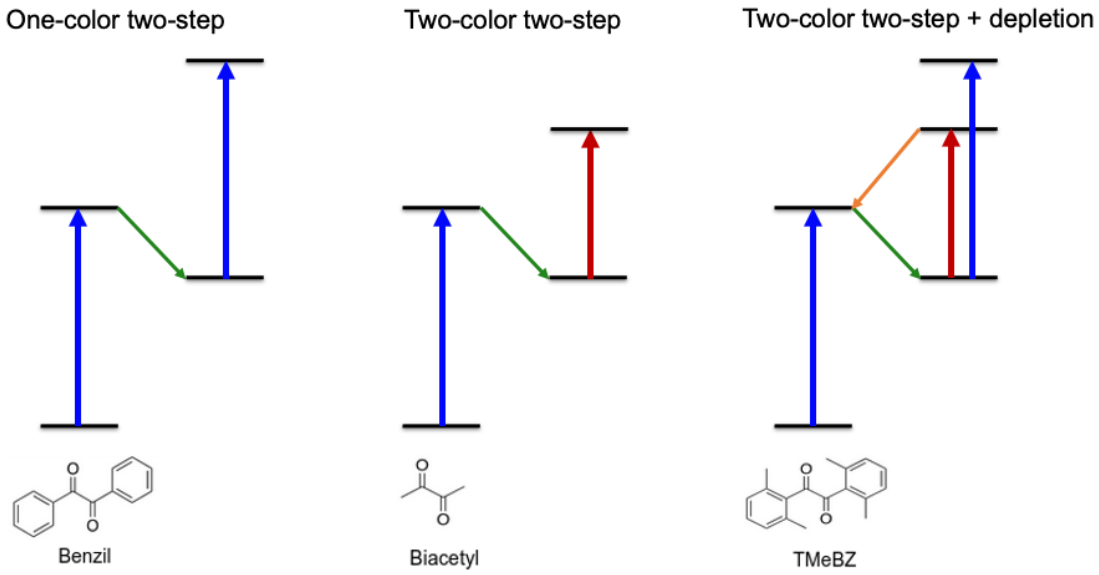

Figure 7.1: Photoinitiators for different investigated two-step two-photon absorption processes. The photoinitiators belong to three classes: one-color two-step absorption (e.g. benzil), two-color two-step absorption (e.g. biacetyl), and two-color two-step absorption with depletion (e.g. tetramethylbenzil (TMeBZ)).

7.1 Benzil

The singlet ground state and triplet excited state of benzil can be optically excited by employing laser wavelengths at 405 nm (blue), as reported in Ref. [51], classifying this PI as one-color two-step absorption active. Benzil is an α-diketone and consists of two phenyl groups attached to a central ethanedione unit.

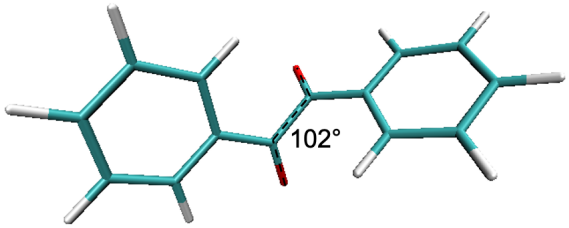

Figure 7.2: Optimized ground state geometry of benzil calculated with CAM-B3LYP-D3(BJ)/def2-TZVP in ACN with the measured dihedral angle between the carbonyl groups.

The optimization of the ground state geometry of benzil, as depicted in Figure 7.2, reveals a twist in the carbonyl bond with a dihedral angle of 102°, consistent with prior findings [229].

7.1.1 Absorption properties

The computed 1PA from S_0 to the singlet manifold is presented in Table 7.1 and Figure 7.4. The data indicate that the maximum absorption occurs around ∼ 351 nm, exhibiting a blue-shift of approximately 40 nm compared to the experimental data in ACN (see Figure 7.4 [31]). As discussed in Chapter 5 and 6, the utilization of CAM-B3LYP is primarily responsible for this blue-shift. However, it is crucial to prioritize a methodology that accurately describes the photophysical properties of molecules rather than aiming for a perfect reproduction of experimental spectra. The oscillator strength associated with the $S_0 \rightarrow S_1$ transition is remarkably low (i.e., 0.0009), aligning with the experimental requirement for material transparency, crucial for achieving high-quality printing.

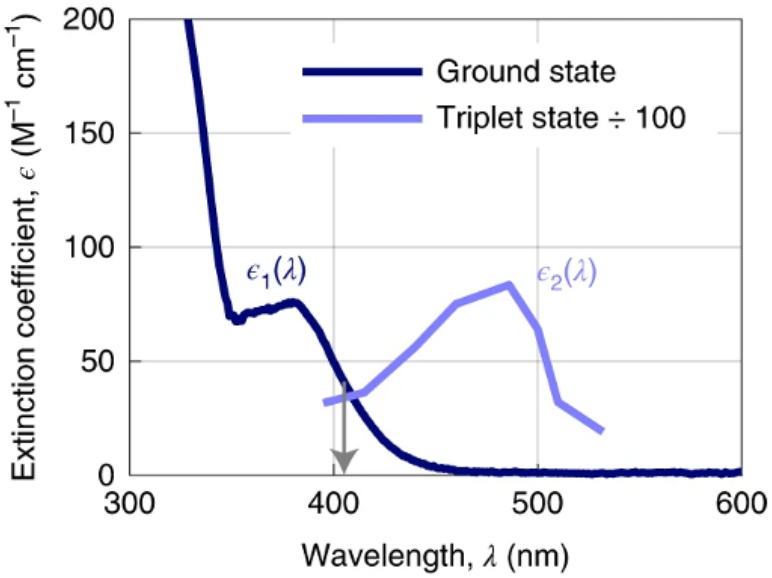

Figure 7.3: Experimental ground-state extinction (dark blue) and flash-photolysis triplet excitation spectra (light blue) of benzil in ACN and benzene, respectively. Readapted with permission from Ref. [31]. Copyright 2022 Springer Nature.

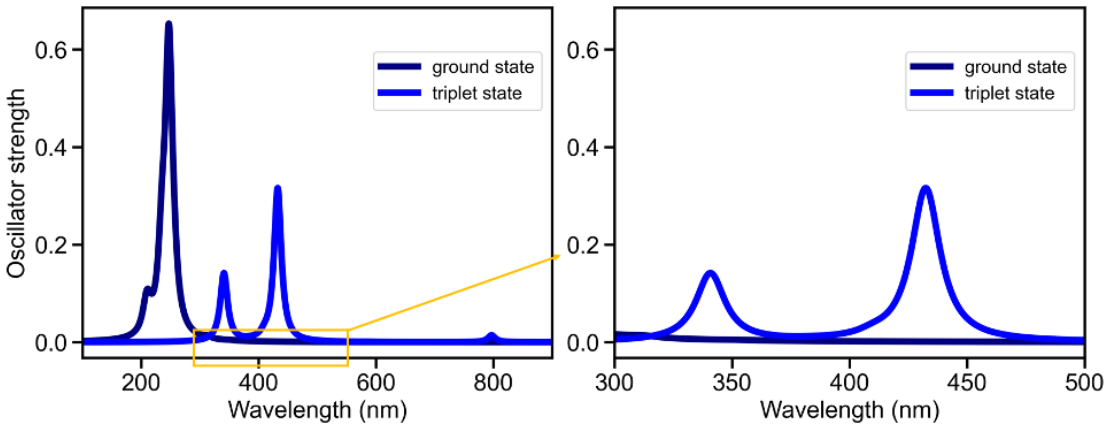

Figure 7.4: Theoretical one-photon absorption (1PA) and triplet absorption (TA) spectra of benzil in ACN computed from S_0 and T_1 optimized geometry, respectively using CAM-B3LYP/def2-TZVP (right).

Table 7.1: Vertical excitation energies for the first ten singlet of benzil in ACN calculated using TD-CAM-B3LYP-D3(BJ)/def2-TZVP (PCM model) and eigenvalue-only self-consistent GW (evGW) (COSMO model), starting from the optimized S_0 geometry.

Excited State	Energy (eV)	Wavelength (nm)	Osc.str.
	TD-DFT		
1	3.53	351.49	0.0009
2	3.97	312.13	0.0039
3	4.86	255.18	0.0481
4	4.87	254.34	0.0061
5	5.02	246.90	0.5809
6	5.27	235.26	0.1519
7	5.76	215.35	0.0050
8	5.87	211.07	0.0341
9	5.92	209.21	0.0122
10	5.98	207.49	0.0258
	GW-BSE		
1	3.46	358.14	0.0008
2	3.90	318.11	0.0030
3	4.64	267.25	0.0479
4	4.65	266.70	0.0070
5	4.93	251.38	0.5968
6	5.14	241.06	0.1536
7	5.98	207.37	0.02111
8	6.01	206.44	0.02832
9	6.07	204.26	0.02487
10	6.13	202.21	0.09820

Moreover, to refine the vertical excitation energies calculated through TD-DFT the GW-BSE approach was employed and reported in Table 7.1. The corresponding data reveal minimal deviation from

the TD-DFT energies e.g. for the first excitation, the deviation is approximately 8 nm, with both TD-DFT and GW-BSE displaying very low oscillator strengths, specifically 0.0009 and 0.0008, respectively.

The MOs contributions to the ten singlet transitions computed from the ground state are detailed in Table 7.2 and depicted in Figure 7.12. The primary transition is predominantly characterized by HOMO → LUMO (82.8%). Upon excitation, the hole and electron representation exhibit nπ^* character, with the hole localized on the nonbonding orbital (n) and the electrons occupying the anti-bonding π^* orbital associated with the carbonyl functional group , as illustrated in Figure 7.6. This electronic transition signifies alterations in the electron density within the carbonyl moiety, indicating the interaction of nonbonding electrons with the π^* antibonding orbital, consistent with previous observations [51]).

Table 7.2: Transition orbitals of benzil in ACN with CAM-B3LYP-D3(BJ)/def2-TZVP with respective contributions.

Transition	Molecular Orbital	Contribution (%)
$S_0 \rightarrow S_1$	HOMO → LUMO	82.8
$S_0 \rightarrow S_2$	HOMO → LUMO +1	78.6
$S_0 \rightarrow T_1$	HOMO → LUMO	82.1
$S_0 \rightarrow T_2$	HOMO -1 → LUMO	36.0
	HOMO -4 → LUMO+1	17.0
$S_0 \rightarrow T_3$	HOMO -1 → LUMO +1	33.5
	HOMO-4 → LUMO	26.1
$S_0 \rightarrow T_4$	HOMO → LUMO+1	64.8
$S_0 \rightarrow T_5$	HOMO -3 → LUMO	43.6
$S_0 \rightarrow T_6$	HOMO -3 → LUMO+1	38.4
	HOMO -2 → LUMO	34.6
$S_0 \rightarrow T_7$	HOMO -3 → LUMO +2	35.1
	HOMO-2 → LUMO +3	29.31
$S_0 \rightarrow T_8$	HOMO -3 → LUMO +4	33.4
	HOMO -2 → LUMO +3	33.0
$S_0 \rightarrow T_9$	HOMO -1 → LUMO +2	38.3
	HOMO -4 → LUMO +4	21.7
$S_0 \rightarrow T_{10}$	HOMO -1 → LUMO +3	40.5

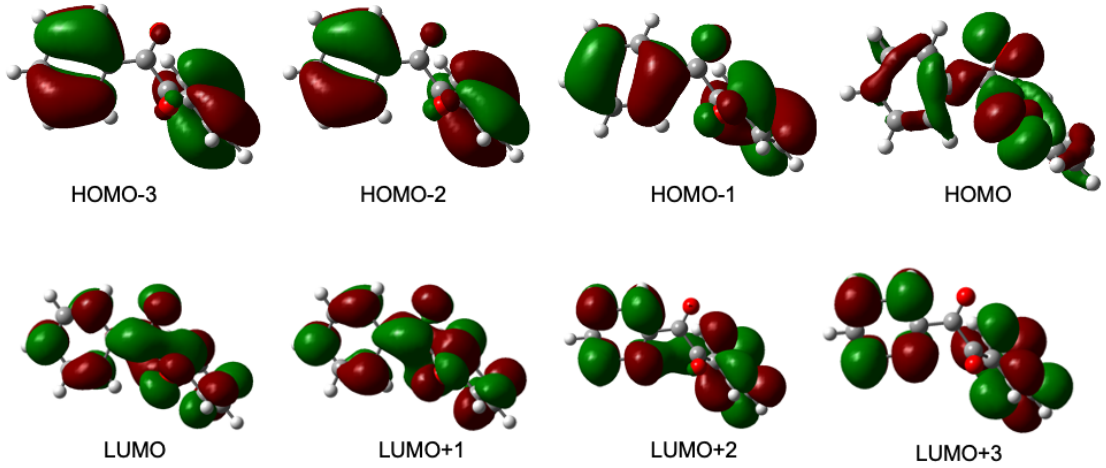

Figure 7.5: Visualization of molecular orbitals (MOs) of benzil in ACN obtained using CAM-B3LYP-D3(BJ)/def2-TZVP level of theory. HOMO and LUMO correspond to the Highest Occupied Molecular Orbital and Lowest Unoccupied Molecular Orbital, respectively. Isovalue of 0.03 a.u. was used for visualization.

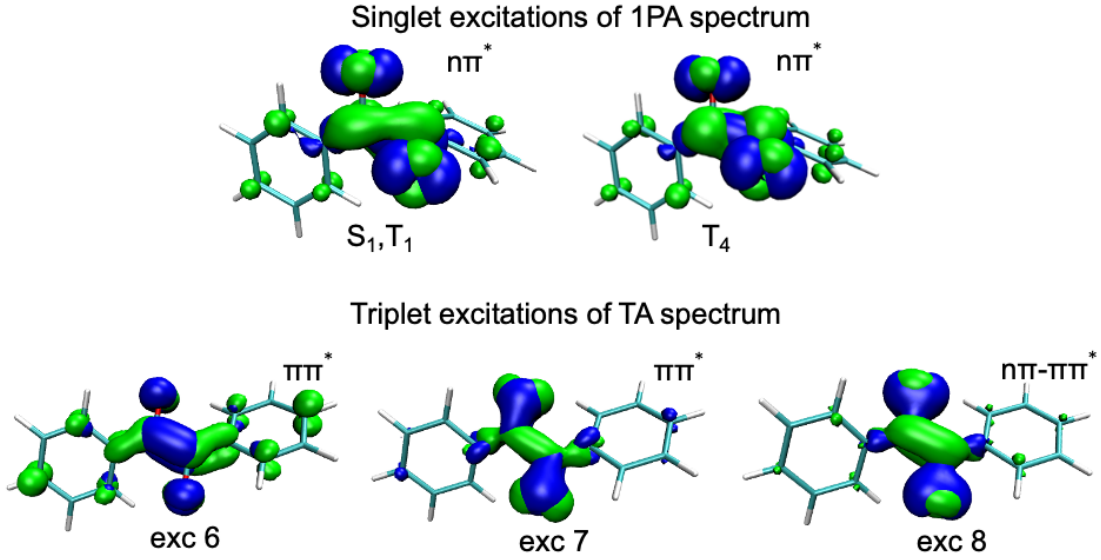

Figure 7.6: Hole and electron representation of the singlet and triplet excitations of benzil computed with CAM-B3LYP-D3(BJ)/def2-TZVP in ACN. Isovalue of 0.003 is used for visualization.

7.1.2 Photophysical properties

Upon absorption at 405 nm, the initial singlet state S_1 is accessed, paving the way for subsequent ISC to the triplet manifold [51]. Figure 7.7 presents the optimized singlet and triplet states, complete with their respective energies and geometries. Conformational alterations, primarily involving the C-C and C=O

bonds of benzil, are outlined in Table 7.3, upon absorption. While the lengths of these bonds exhibit small changes during the optimization of excited states, a noticeable variation in the dihedral angle between the carbonyl bonds is observed for T_4 (see Table 7.3 and Figure 7.7). Here, the optimization results in a cis conformation of benzil, featuring a dihedral angle of 23.82° compared to the 102.01° in the ground state (S_0) and approximately 170° in S_1 and T_1. This transition from trans to cis might enhance the likelihood of radical formation, as the trans conformation allows for a more favorable alignment of the carbonyl groups, minimizing steric hindrance and favoring stability due to resonance effects. In contrast, the cis conformation introduces additional steric hindrance between adjacent carbonyl groups, potentially leading to higher energy and reduced stability compared to the trans conformation (see Figure 7.7).

Table 7.3: Bond lengths (in Å) of C-C and carbonyl bonds along with the dihedral angle (°) between the two carbonyl groups of benzil upon optimization of various excited states. Data are computed with CAM-B3LYP-D3(BJ)/def2-TZVP in ACN.

Excited State	C=O	C-C	dihedral
S_0	1.21	1.53	102.01
S_1	1.23	1.49	173.81
T_1	1.23	1.49	171.94
T_2	1.23	1.50	23.82

The energy difference between S_1 and T_1 amounts to 0.57 eV (see Figure 7.7). When coupled with a SOC of 0.70 cm^{-1}, this results in an ISC rate of 4.86x10^3 s^{-1} (see Table 7.4). In the case of S_1-T_4, the ISC rate is determined by a SOC of 9.75 cm^{-1} and an S-T energy gap of 0.32 eV (see Figure 7.7). However, the process is hindered by an exceptionally high reorganization energy exceeding 3 eV due to the conformational change from trans (S_1) to cis (T_4), indicating that the transition is unlikely to occur. According to El-Sayed's rule, ISC transitions between states with identical electronic configurations are prohibited, but spin-orbit coupling, along with a small singlet-triplet energy gap, can facilitate the process. For benzil, the allowed percentage of ISC in S_1-T_1 is around 5%. Experimental data, however, reports an ISC in benzil with a quantum yield of 92% [48], contradicting the significantly lower efficiency mentioned earlier. In addition the ISC S_1-T_1 is not competitive with IC and therefore, the ISC is likely to occur between S_1 and T_2 or T_3, characterized by $\pi\pi^*$ character (see Figure 7.6) and energy levels close to S_1 as depicted in the Jablonski diagram in Figure 7.7. These S_1 - T_2 or S_1 - T_3 ISC rates are expected to exhibit high ISC efficiency, consistent with experimental observations, taking into account the computed SOC of S_1-T_2 and S_1-T_3 at 3.96 cm^{-1} and 31.64 cm^{-1}. However, due to the non-convergence of the optimization for the T_2 and T_3 excited states, the corresponding photophysical rates could not be determined. The rate of RISC from the triplet state T_1 to the singlet state S_1 is 1.92x10^3 s^{-1}, indicating a lack of preference for the transition back to the singlet manifold. The calculated IC rate from S_1 to S_0 is 2.56x10^7 s^{-1}, while, in agreement with previous reports [47], the fluorescence is very weak with a computed rate of 1.58x10^2 s^{-1} and S_1 state lifetime of 0.002 s, much longer than for Norrish type II initiators (in the order of ns). Similarly, the T_1 state is characterized by an $n\pi^*$ transition, as indicated by Ref. [51]. The phosphorescence rate of 9.58x10^1 s^{-1} and ISC from T_1 to S_0, result in a triplet state lifetime of 0.010 s and 0.30 μs, slightly shorter than the Norrish type II initiators. However it must be

consider that in this case a cw laser (instead of a fs laser pulsed, as it was for Norrish type II PIs) is used.

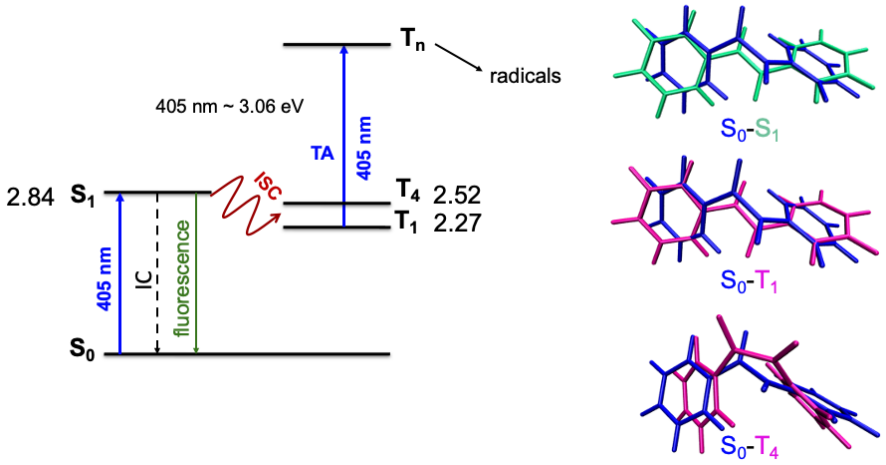

Figure 7.7: Jablonski diagram of benzil computed with CAM-B3LYP-D3(BJ)/def2-TZVP in ACN. Adiabatic energies are reported with the inclusion of zero-point energy correction (ZPVE). The overlap of the optimized geometries is also reported. The printing wavelength from experiment is 405 nm.

Table 7.4: Photophysical rates of benzil: internal conversion (IC), intersystem crossing (ISC) and reverse ISC (RISC) were computed as reported in Section 4.5 in implicit ACN with TD-CAM-B3LYP-D3(BJ)/def2-TZVP level of theory. For the IC and ISC rates (in s^{-1}) the non-adiabatic coupling matrix elements (NACME, in a.u.), spin-orbit coupling (SOC, in cm^{-1}) and reorganization energy (λ, in eV) were also calculating as described in Section 4.5. For the radiative rates such as fluorescence and phosphorescence, the level of theory reported in Section 4.5 was employed.

Non-radiative rates			
	Rate	NACME	λ
IC $S_1 \rightarrow S_0$	$1.56x10^{7}$	0.004	0.739
	Rate	SOC	λ
ISC $S_1 \rightarrow T_1$	$4.86x10^{3}$	0.70	0.013
RISC $T_1 \rightarrow S_1$	$1.92x10^{3}$	0.72	0.014
*ISC $T_1 \rightarrow S_0$	$3.35x10^{6}$	4.55	0.848
Radiative rates			
	Rate	ΔE (eV)	lifetime (s)
Fluorescence	$4.58x10^{2}$	2.84	0.002
Phosphorescence	$9.58x10^{1}$	2.27	0.010

* T_1 state lifetime is $2.99x10^{-6}$ s.

7.1.3 "Reluctant" Norrish type I character

Caceres et al. [53] reported the T_1 state of benzil to lye at 2.3 eV, well below the bond-cleavage energy of ≈ 3 eV and therefore in T_1 not sufficient energy is provided to overcome this energy barrier and to fragment benzil into two benzoyl radicals [54, 55], in agreement with the "reluctant" Norrish type I

character of the PIs used in two-step absorption. The dissociation mechanism is reported in Figure 7.8.

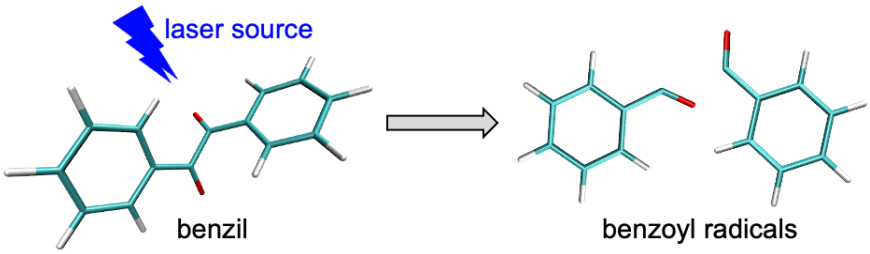

Figure 7.8: Reaction cleavage of benzil leading to the formation of benzoyl radicals

The computed T_1 energy of the PI is 2.27 eV (see Table 7.5), lower than the bond energy (E_{BOND}) of 2.96 eV, in agreement with reported values [53].

Table 7.5: Comparison of bond dissociation energies (E_{BOND}) and first triplet excited state energies (E_{T_1}) for benzil, biacetyl and tetrametylbenzil.

	E_{BOND}		E_{T_1}		$E_{T_1} < E_{BOND}$
	eV	kcal mol^{-1}	eV	kcal mol^{-1}	eV
benzil	2.96	68.36	2.27	52.29	2.27 < 2.96
biacetyl	3.07	70.86	2.21	50.96	2.21 < 3.07
tetrametylbenzil	2.52	58.04	1.93	44.59	1.93 < 2.52

The BDEs, calculated using the formula in equation 4.5 [178], are presented in Table 7.6. The data indicates that cleavage from S_0 and T_1 states is improbable, given the high BDE values of 68.36 kcal mol^{-1} and 16.13 kcal mol^{-1}, respectively, considering that it must overcome the rate of non-radiate decay of the T_1 state which is in the order of μs. The BDE from T_2 experiences a slight decrease to 10.26 kcal mol^{-1}, suggesting that the reaction may not occur; however, a notable trend is observed — higher triplet excited states tend to exhibit lower BDEs. As reported above, convergence issues prevented the optimization of triplet excited states of benzil and consequently, energies could not be computed for these states.

Table 7.6: Bond dissociation energies (BDEs) of benzil in ACN calculated using TD-(U)CAM-B3LYP-D3(BJ)/def2-TZVP method.

Excited State	**BDE (eV)**	**BDE (kcal mol^{-1})**
S_0	2.96	68.36
S_1	0.13	2.93
T_1	0.70	16.13
T_2	0.46	10.26

7.1.4 Triplet absorption spectrum

The critical attribute of an efficient two-step absorption PI lies in the TA spectrum originating from the T_1 state. In the case of benzil, this spectrum displays absorption at 405 nm, situated in the tail region [31]. Hence, scrutinizing the TA spectrum is essential for validating experimental findings. Figure 7.4 illustrates the TA spectrum from the T_1 state, revealing peaks at $\sim$ 400 nm wavelength for transitions excitation 6 to excitation 8 (exc.6-exc.8) within the tail of the spectrum. Hole and electron analyses in Figure 7.6 show that electrons are localized on the C-C bond between the two carbonyl groups for excitation 7 and excitation 8 with a bonding character while excitation 6 exhibits hole localized on this bond and the carbonyl bond. Remarkably, the oscillator strength for T_6 transitions is approximately 350 times higher than that for singlets 1PA, aligning with experimental data where the triplet spectrum is reduced by a factor of 100 compared to the singlet one (see Figure 7.4). While this analysis offers insights into the accessible triplet states, challenges in optimizing high triplet states hinder further exploration of these triplets and making definitive statements about the triplet state from which radicals are formed.

Table 7.7: Triplet vertical excitation energies for benzil in ACN calculated using TD-CAM-B3LYP-D3(BJ)/def2-TZVP method, starting from the optimized T_1 geometry.

Excited State	Energy (eV)	Wavelength (nm)	Osc.str.
1	0.81	1529.24	0.0200
2	1.46	847.30	0.0000
3	1.56	796.84	0.0143
4	2.08	596.37	0.0000
5	2.12	584.41	0.0003
6	2.87	432.36	0.3146
7	3.03	409.78	0.0074
8	3.22	384.84	0.0009
9	3.44	360.07	0.0000
10	3.64	340.74	0.1397

7.2 Biacetyl

Biacetyl is identified as a two-color two-step absorption candidate, capable of being excited by an initial laser source at 405 nm (blue) to high singlet excited states. Following the ISC to the triplets and the formation of T_1, a subsequent absorption with a second laser source at 640 nm (red) induces the cleavage reaction in high triplet states. As a dichetone, biacetyl exhibits a cis-planar geometry in its ground state, as delineated by a plane, consistent with calculations (dihedral angle of 180° degrees, see Figure 7.9), as reported in Ref. [230]).

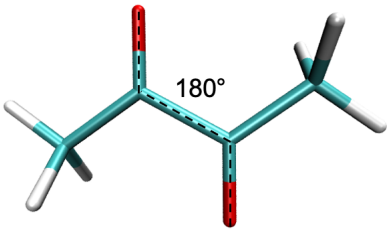

Figure 7.9: Optimized ground state geometry of biacetyl calculated with CAM-B3LYP-D3(BJ)/def2-TZVP in ACN with the measured dihedral angle between the carbonyl groups.

7.2.1 Absorption properties

The 1PA spectrum, outlined in Table 7.8 and depicted in Figure 7.11, exhibits its maximum absorption at 417.12 nm, aligning with experimental findings around ~ 440 nm [27]. The associated oscillator strength for the $S_0 \rightarrow S_1$ transition, akin to benzil, maintains a low value of 0.0001, as anticipated for a transparent material. Calibration of the 1PA spectrum using TD-DFT involved a comparison with GW-BSE-based 1PA. The data presented in Table 7.8 reveals a negligible shift of less than approximately 10 nm between the two datasets, affirming the validity of the employed TD-DFT approach.

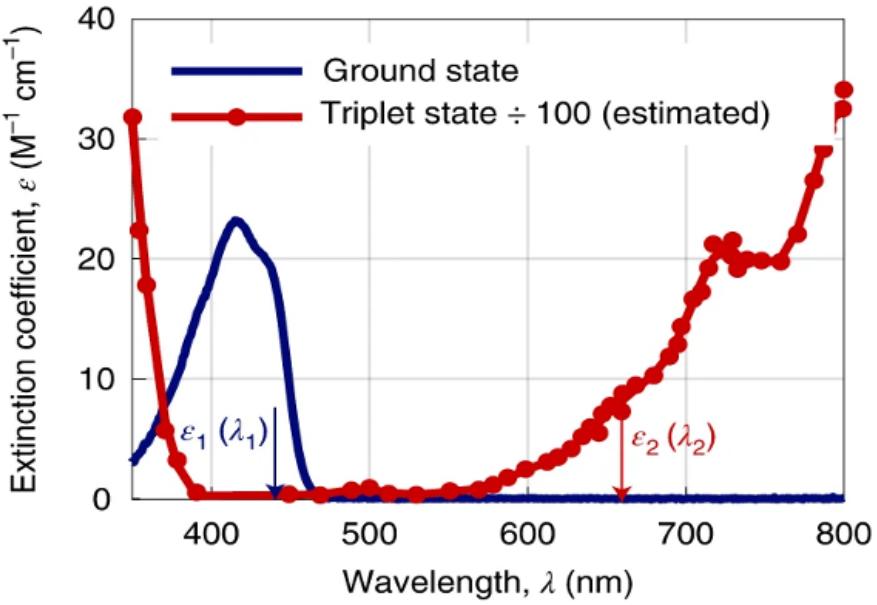

Figure 7.10: Ground-state (blue) and excited-state (red) molar decadic ex- tinction coefficient of biacetyl in ACN and benzene, respectively. The absolute value of the triplet- state molar decadic extinction coefficient ϵ_2 is estimated from Refs. [49, 231]. The red arrows indicate the wavelengths at 405 nm and 640 nm used in the light-sheet 3D printing experiments. Adapted from Ref. [27] with permission from Springer Nature.

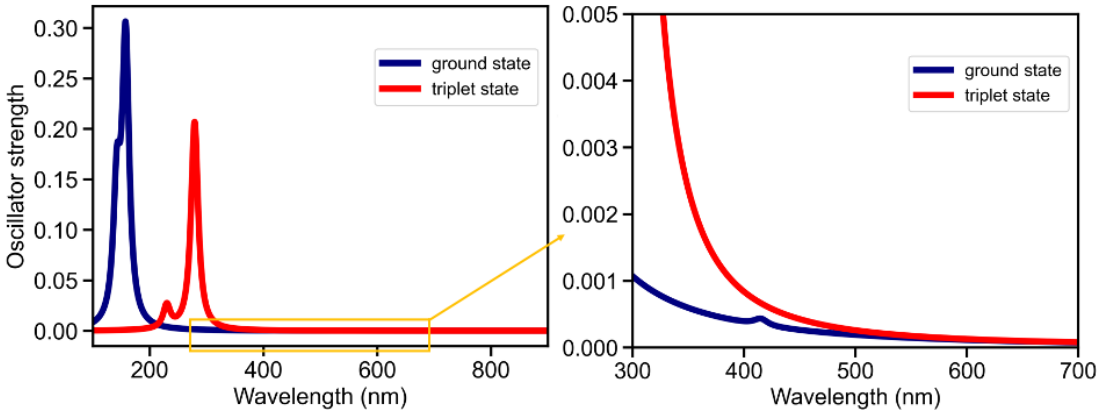

Figure 7.11: Theoretical one-photon absorption (1PA) and triplet-absorption (TA) spectra of biacetyl in ACN computed from S_0 and T_1 optimized geometry, respectively using CAM-B3LYP/def2-TZVP (right).

Table 7.8: Vertical excitation energies for the first ten singlet of biacetyl in ACN calculated using TD-CAM-B3LYP-D3(BJ)/def2-TZVP (PCM model) and eigenvalue-only self-consistent GW (evGW) (COSMO model), starting from the optimized S_0 geometry.

Excited State	Energy (eV)	Wavelength (nm)	Osc.str.
	TD-DFT		
1	2.99	414.98	0.0001
2	4.83	256.82	0.0000
3	6.92	179.23	0.0000
4	7.41	167.29	0.0004
5	7.61	162.88	0.0000
6	7.72	160.62	0.0000
7	7.87	157.61	0.2811
8	8.19	151.31	0.0000
9	8.54	145.16	0.0000
10	8.71	142.30	0.1286
	GW-BSE		
1	2.98	415.61	0.0001
2	4.70	263.95	0.0000
3	7.24	171.34	0.00000
4	7.55	164.25	0.00022
5	7.89	157.08	0.00000
6	7.96	155.82	0.32876
7	8.20	151.22	0.00015
8	8.34	148.72	0.00000
9	8.73	141.99	0.00000
10	9.09	136.45	0.00013

The first transition, in agreement to what was reported for benzil has $n\pi*$ character characterized by HOMO $\rightarrow$ LUMO with contribution of 98% (see Figure 7.13 and Table 7.9); similarly to benzil, the

representation of hole and electron depicted shows transition, upon excitation, from the non bonding to the antibonding orbital of the carbonyl bonds. The MOs related to the singlet and triplet transitions are reported in Figure 7.12 and Table 7.9.

Table 7.9: Transition orbitals of biacetyl in ACN with CAM-B3LYP-D3(BJ)/def2-TZVP with respective contributions.

Transition	Molecular Orbital	Contribution (%)
$S_0 \rightarrow S_1$	HOMO → LUMO	97.7
$S_0 \rightarrow S_2$	HOMO -1 → LUMO	83.2
$S_0 \rightarrow T_1$	HOMO → LUMO	96.9
$S_0 \rightarrow T_2$	HOMO -1 → LUMO	80.3
$S_0 \rightarrow T_3$	HOMO -2 → LUMO	82.4
$S_0 \rightarrow T_4$	HOMO -3 → LUMO	70.8
$S_0 \rightarrow T_5$	HOMO → LUMO +2	77.9
$S_0 \rightarrow T_6$	HOMO -4 → LUMO	73.9
$S_0 \rightarrow T_7$	HOMO → LUMO +1	95.0
$S_0 \rightarrow T_8$	HOMO -7 → LUMO	84.5
$S_0 \rightarrow T_9$	HOMO -5 → LUMO	45.1
$S_0 \rightarrow T_9$	HOMO -5 → LUMO	45.1
$S_0 \rightarrow T_{10}$	HOMO -6 → LUMO	85.9

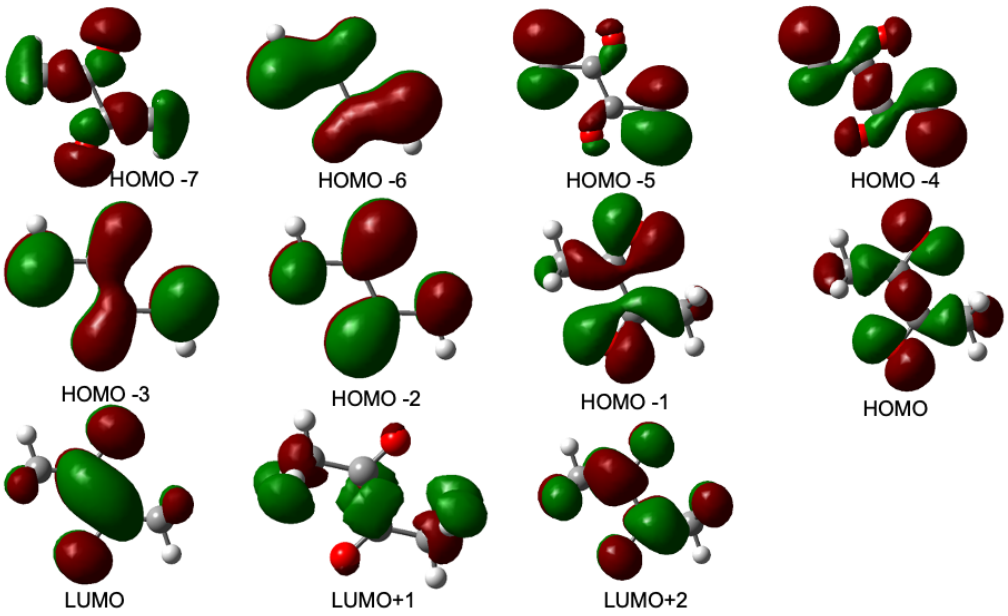

Figure 7.12: Visualization of molecular orbitals (MOs) of biacetyl in ACN obtained using CAM-B3LYP-D3(BJ)/def2-TZVP level of theory. HOMO and LUMO correspond to the Highest Occupied Molecular Orbital and Lowest Unoccupied Molecular Orbital, respectively. Isovalue of 0.03 a.u. was used for visualization.

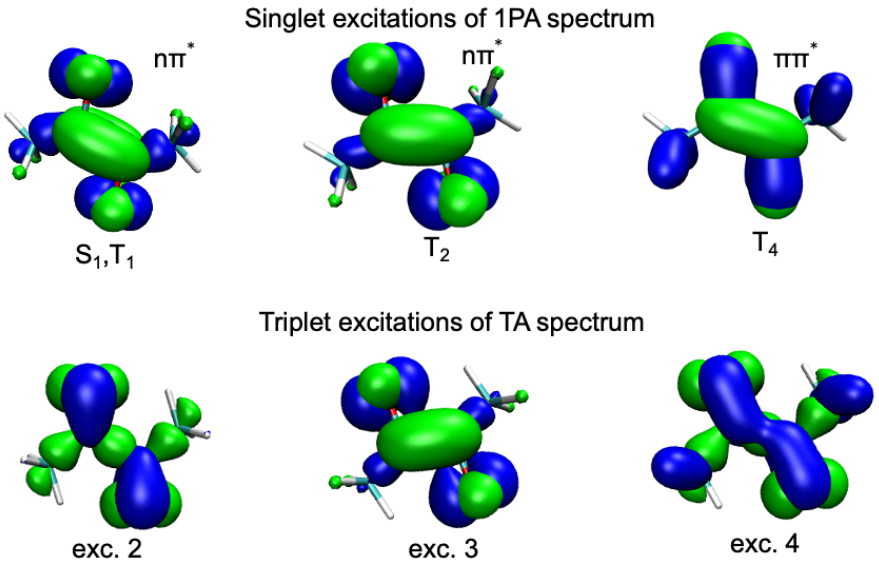

Figure 7.13: Visualization of electron donating (hole, in blue) and electron accepting (electron, in green) density upon excitation of biacetyl from the ground state to the singlet and triplet states in ACN. Electron-hole analysis and the visualization of the respective contributions were performed as reported in Chapter 4. Isovalue of 0.03 a.u. was used for visualization.

7.2.2 Photophysical properties

The optimized excited states, along with their respective hole-electron representations, are elaborated in Figure 7.14 and Figure 7.13. A closer examination of the structural dynamics of biacetyl, inferred from changes in bond lengths during electronic transitions, suggests a propensity for acetyl radical formation. The initial absorption event (S_0 to S_1) triggers a significant reduction in the C-C bond length, while the length of the carbonyl bond remains relatively stable (refer to Table 7.10). In the T_1 state, the C-C bond retains its characteristics from the S_1 state. T_2 exhibits further alterations, characterized by a notable decrease in the length of the C-C bond and an increase in the length of the carbonyl bond by 0.05 ÅṪhe T_3 state displays similar C-C bond length as T_1 while the length of carbonyl bond significantly increase. The important variations in the T_3 state might be indication of significant electronic rearrangement inside the molecule that could lead to the generation of radicals. However, further analysis is necessary to establish with certainty which triplet can generate radical species.

Table 7.10: Bond lengths (in Å) of C-C and carbonyl bonds C=O of biacetyl upon optimization of various excited states. Data are computed with CAM-B3LYP-D3(BJ)/def2-TZVP in ACN.

Excited State	C=O	C-C
S_0	1.21	1.54
S_1	1.23	1.48
T_1	1.23	1.48
T_2	1.28	1.40
T_3	1.32	1.47

Due to the higher energy of T_2 and T_3 with respect to S_1 by 0.68 eV and 1.84 eV (see Figure 7.14) respectively, the ISC involves directly the T_1 state (S-T energy gap of 0.57 eV) with SOC of 1.46 cm^{-1} and rates of 2.54x10^5 s^{-1} (see Table 7.11). According to El-Sayed's rule the process is allowed for 3% but experimentally is reported that the ISC process happens with nearly unity quantum yield [27], and therefore TD-DFT MOs analysis might be not enough for underlying the properties of this PI but higher level methods, which are out of the scope of this thesis, would be necessary. The fluorescence rate of 2.54x10^5 s^{-1} is competitive with the ISC rate and lower than the IC of 8.13x10^6 s^{-1}, in agreement to the reported weak fluorescence emission for the two-step two-photon PIs. The computed phosphorescence rate and lifetime are 6.75x10^1 s^{-1} and 0.015 s, similarly to benzil.

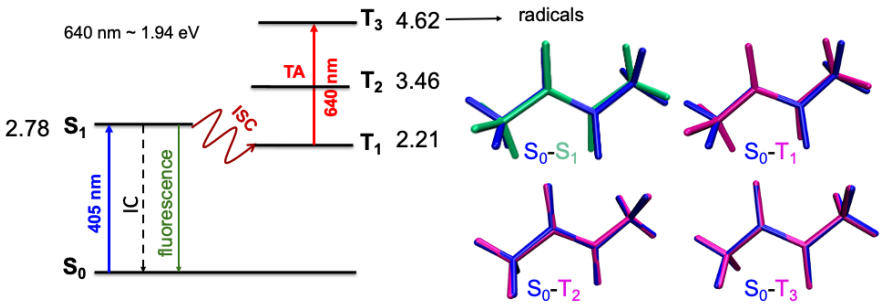

Figure 7.14: Jablonski diagram of biacetyl computed with CAM-B3LYP-D3(BJ)/def2-TZVP in ACN. Overlap of optimized geometries is also reported.

Table 7.11: Photophysical rates of biacetyl: internal conversion (IC), intersystem crossing (ISC) and reverse ISC (RISC) were computed as reported in Section 4.5 in implicit ACN with TD-CAM-B3LYP-D3(BJ)/def2-TZVP level of theory. For the IC and ISC rates (in s^{-1}) the non-adiabatic coupling matrix elements (NACME, in a.u.), spin-orbit coupling (SOC, in cm^{-1}) and reorganization energy (λ, in eV) were also calculating as described in Section 4.5. For the radiative rates such as fluorescence and phosphorescence, the level of theory reported in Section 4.5 was employed.

Non-radiative rates			
	Rate	NACME	λ
IC $S_1 \rightarrow S_0$	$8.13x10^{6}$	0.005	0.264
	Rate	SOC	λ
ISC $S_1 \rightarrow T_1$	$2.54x10^{5}$	1.46	0.003
RISC $T_1 \rightarrow S_1$	-	1.13	0.003
*ISC $T_1 \rightarrow S_0$	NA	0.00	-
Radiative rates			
	Rate	ΔE (eV)	lifetime (s)
Fluorescence	$3.41x10^{4}$	2.78	$2.93x10^{-5}$
Phosphorescence	$6.75x10^{1}$	2.21	0.015

7.2.3 "Reluctant" Norrish type I character

Biacetyl, employed as a two-step two-photon PI, exhibits an experimental T_1 energy positioned 2.4 eV below the computed bond dissociation energy of 3.2 eV [232, 233] (refer to Table 7.5). Consequently, the bond cleavage reaction leading to the generation of two acetyl radicals, as illustrated in Figure 7.15, does not take place from T_1 but rather from high triplet states. The calculated energy for T_1 is 2.21 eV, below the computed bond dissociation energy of 3.07 eV and aligns with reported data. BDEs associated with the cleavage reaction are presented in Table 7.12. The data indicates a significantly more favorable bond cleavage from high triplet states, such as T_2 and T_3, compared to T_1, where the BDE is 20.76 kcal mol^{-1} too high for the reaction to occur. It is noteworthy to highlight the similarity between biacetyl and benzil, where the BDE related to T_1 is 13.82 kcal mol^{-1}. The BDE from T_2 and T_3 measures -9.09 kcal mol^{-1} and -35.68 kcal mol^{-1}, respectively.

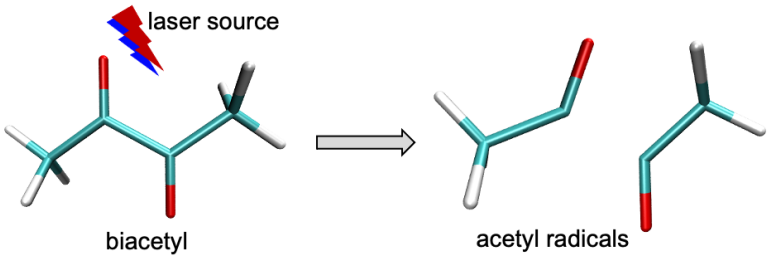

Figure 7.15: Reaction cleavage of biacetyl

The investigation into the PI cleavage was extended using the IRC and transition state methods, as described in Chapter 4. The computed energy barrier for the cleavage reaction from the T_1 state, leading

to the formation of two acetyl radicals, is 18.47 kcal mol^{-1} (refer to Figure 7.16), consistent with the reported BDE for this state (20.76 kcal mol^{-1}, see Table 7.12). The determined activation energy indicates that the reaction is unlikely to occur, with an expected rate of 1.79x10^{-1} s^{-1} (for detailed computational information, see Chapter 4). The MOs associated to the formed radicals (P in Figure 7.16) show the antibonding character over the C-C bond, as expected. This supports the conclusion that the cleavage reaction is more likely initiated in higher triplet states. Unfortunately, due to convergence issues, transition states for T_2 and T_3 could not be obtained, limiting the available data to BDEs. However, the agreement between the BDE and activation energy for T_1 reinforces the validity of the obtained results.

Table 7.12: Bond dissociation energies (BDEs) of biacetyl in ACN calculated using TD-CAM-B3LYP-D3(BJ)/def2-TZVP method.

Excited State	BDE (eV)	BDE (kcal mol^{-1})
S_0	3.07	70.86
S_1	0.29	6.76
T_1	0.90	20.76
T_2	-0.39	-9.09
T_3	-1.55	-35.68

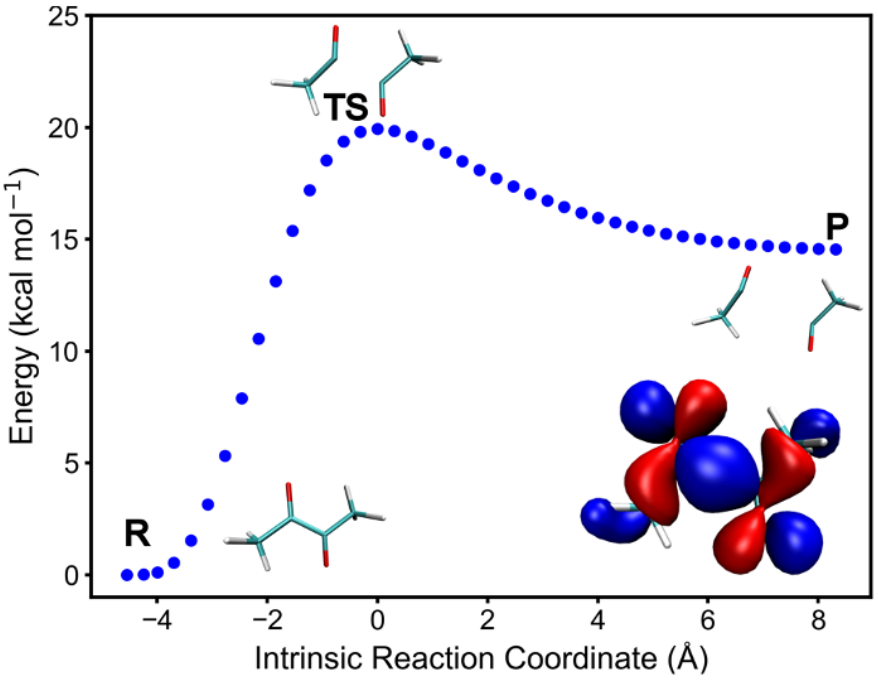

Figure 7.16: Profile of the fragmentation reaction mechanism of biacetyl. Intrinsic reaction coordinates (IRC) were calculated at the ACN (PCM) level of theory using (U)CAM-B3LYP/def2-TZVP. The IRC profile was computed starting from the T_1 optimized geometry (R, reagent) and moving through the transition state (TS) where the actual cleavage occurs, for finally reaching the formation of the products (P) upon relaxation and rearrangement.

7.2.4 Triplet absorption spectra

Upon the formation of the T_1 state, biacetyl can undergo further excitation to higher triplets using a second laser source [31, 51]. In the triplet state, biacetyl exhibits weak absorbance in the wavelength range of 400–550 nm. However, stronger absorption peaks are observed at longer wavelengths, allowing the use of laser wavelengths at 640 nm [51]. The calculated TA spectrum of biacetyl is presented in Table 7.13 and Figure 7.11. The data reveal that the closest transition to 640 nm is the one peaked at 493.54 nm (exc.2). According to the hole and electron representation shown in Figure 7.13, this transition leads to a triplet state where the hole is localized on the carbonyl bond and the electron is on the lone pair of the oxygen atoms of the same carbonyl bond. Similarly is the case of excitation 4 (exc.4) at 364.40 nm. In contrast, excitation 3 (exc.3), peaked at 365.64 nm, is associated with a state presenting bonding electrons on the bond that is supposed to be cleaved. The significant blue-shift of approximately 100 nm for the second transition at 493.54 nm, compared to the experimental spectrum, can be attributed to the functional used. However, the oscillator strength is 0, indicating that the PI would not absorb at that wavelength. Energies computed with the GW-BSE approach and reported in Table 7.14 show a similar scenario, with only a slight blue-shift of the transition at $\sim$ 490 nm.

Table 7.13: Vertical excitation energies for the first ten triplet of biacetyl in ACN calculated using TD-CAM-B3LYP-D3(BJ)/def2-TZVP method, starting from the optimized T_1 geometry.

Excited State	Energy (eV)	Wavelength (nm)	Osc.str.
1	1.07	1161.12	0.0403
2	2.51	493.54	0.0000
3	3.39	365.64	0.0000
4	3.58	346.40	0.0000
5	4.36	284.15	0.0000
6	4.45	278.91	0.2065
7	4.89	253.37	0.0000
8	5.39	229.94	0.0228
9	5.79	214.19	0.0000
10	5.97	207.74	0.0000

Table 7.14: Vertical excitation energies of biacetyl for the first ten triplet excitations in ACN (COSMO implicit solvation) starting from optimized triplet state geometry (T_1). Excitations were computed in CAM-B3LYP-D3(BJ)/def2-TZVP using using eigenvalue-only self-consistent GW (evGW).

Excited State	Energy (eV)	Wavelength (nm)	Osc.str.
1	1.09	1137.15	0.0210
2	2.46	504.41	0.0000
3	3.37	367.69	0.0000
4	3.45	359.48	0.0000
5	4.25	291.93	0.1727
6	4.25	291.69	0.0000
7	4.74	261.55	0.0000
8	5.33	232.77	0.0208
9	5.95	208.50	0.0000
10	6.00	206.72	0.0673

The observed experimental absorption at 640 nm ($\sim$ 1.96 eV) from T_1 (2.21 eV) could potentially lead directly to T_2 or T_3, which requires 1.25 eV and 2.41 eV. The vibronic spectrum, computed from T_1 and T_3 to incorporate the vibrational motion of the PI upon absorption, is illustrated in Figure 7.17. This spectrum reveals significant absorption at approximately 500 nm, which is blue-shifted compared to the experimental wavelength at 640 nm but in contrast to the 0 oscillator strength observed for the electronic spectrum. Therefore, the computation of the vibronic spectrum is fundamental in this case, where the high flexibility of the molecule (e.g. of the methyl groups) can deeply influence the results. This suggests that T_3 could be reached with printing laser used in experiment (640 nm), where the cleavage reaction might occur with a BDE of -35.7 kcal mol^{-1}, as reported in Table 7.12.

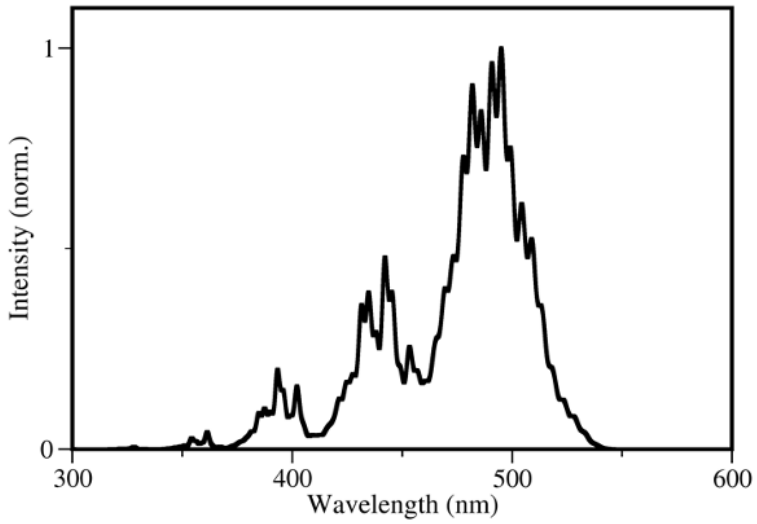

Figure 7.17: Computed triplet vibronic absorption spectrum between T_1 and T_3 states of biacetyl using CAM-B3LYP/def2-TZVP. For the details see Chapter 4.

Important note The comparison of the reported theoretical and experimental data of biacetyl must be taken with careful consideration since the molecule is significantly small and very flexible, and therefore the relation of experimental data should include data computed, in addition to TD-DFT, with higher level methods.

7.3 Tetramethylbenzil

Tetramethylbenzil is a two-step two-photon absorption PI reported to undergo absorption at 405 nm from both ground state and T_1 and depletion at 640 nm [51]. Specifically, the second absorption step from T_1 geometry can happen with both laser wavelength i.e. 405 nm and 640 nm but the latter leads to depletion of the PI and RISC back to singlet manifold while the former leads to the radical formation and bond dissociation reaction. The compound has the same carbonyl core of benzil with four methyl groups. The optimized ground state geometry of the glsPI is reported in Figure 7.18, showing dihedral angle between the carbonyl bonds at 120°.

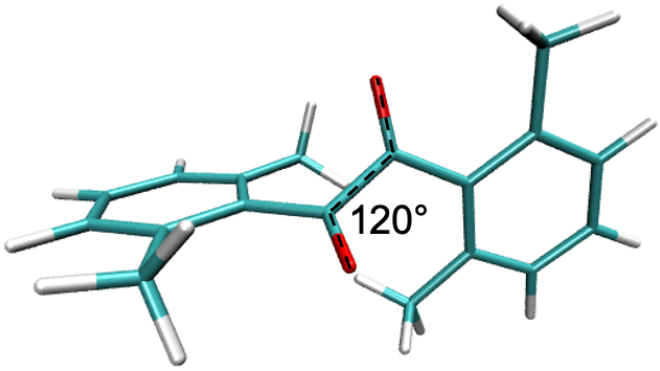

Figure 7.18: Optimized ground state geometry of biacetyl calculated with CAM-B3LYP-D3(BJ)/def2-TZVP in ACN with the measured dihedral angle between the carbonyl groups.

7.3.1 Absorption properties

The computed 1PA spectrum is reported in Figure 7.19 and Table 7.15 and it shows $S_0 \rightarrow S_1$ absorption at 386.42 nm with oscillator strength of 0.0006, similarly to what was observed for benzil (i.e. 0.0001) and biacetyl (0.0009). No transient spectra is available for tetramethylbenzil specifically, but a similar compound i.e. mesistil can be used for comparison. The experimental absorption spectrum of mesistil is reported to be at approximately 300 nm, in agreement to the computed 1PA [234].

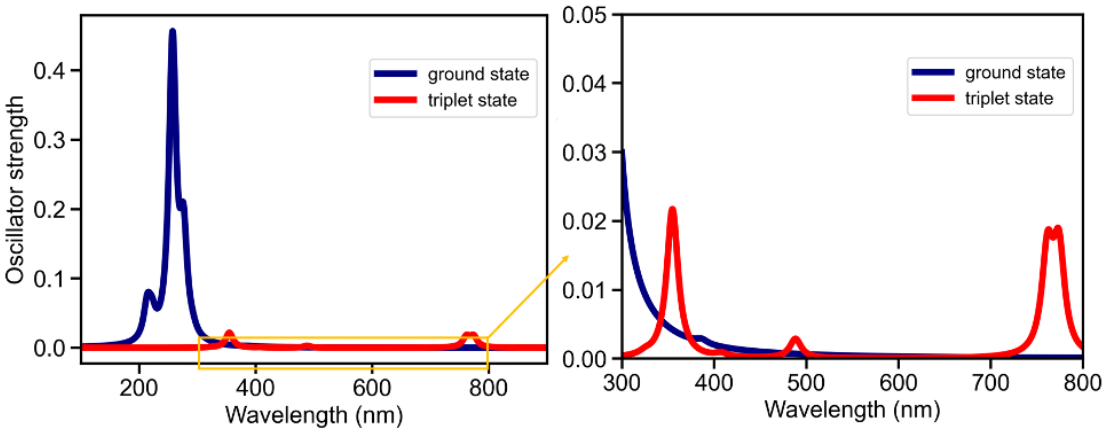

Figure 7.19: Theoretical one-photon absorption (1PA) (blue) and triplet absorption (TA) (red) spectra of tetrametylbenzil in ACN computed from S_0 and T_1 optimized geometry, respectively using CAM-B3LYP/def2-TZVP.

Table 7.15: Singlet vertical excitation energies for tetrametylbenzil in ACN calculated using TD-CAM-B3LYP-D3(BJ)/def2-TZVP method, starting from the optimized ground state geometry.

Excited State	Energy (eV)	Wavelength (nm)	Osc.str.
1	3.21	386.42	0.0006
2	4.25	291.42	0.0069
3	4.49	276.18	0.0474
4	4.49	276.03	0.0997
5	4.81	257.57	0.0179
6	4.82	257.26	0.4157
7	5.57	222.65	0.0156
8	5.59	221.80	0.0064
9	5.63	220.33	0.0079
10	5.79	213.96	0.0490

The MOs analysis associated to the first singlet and triplet transitions is reported in Table 7.16. The excitation $S_0 \rightarrow S_1$ is a HOMO-2 $\rightarrow$ LUMO transition with contribution of 90% and nπ^* character, as depicted in Figure 7.21. The hole are mainly localized on the non orbital bond and the electron on the π^* bond of the carbonyl groups, similarly to the previously investigate transitions of benzil and biacetyl. The hole-electron representation of T_1 state is similar to S_1 and depicted in Figure 7.21.

Table 7.16: Transition orbitals of tetramethylbenzil in ACN with CAM-B3LYP-D3(BJ)/def2-TZVP with respective contributions.

Transition	Molecular Orbitals	Contribution (%)
$S_0 \rightarrow S_1$	HOMO -2→ LUMO	72.3
$S_0 \rightarrow S_2$	HOMO -2 → LUMO +1	58.7
$S_0 \rightarrow T_1$	HOMO -2 → LUMO	73.2
$S_0 \rightarrow T_2$	HOMO -4 → LUMO	39.2
	HOMO -3 LUMO +1	21.8
$S_0 \rightarrow T_3$	HOMO -3 → LUMO	40.4
$S_0 \rightarrow T_4$	HOMO -2 → LUMO +1	40.4
$S_0 \rightarrow T_5$	HOMO → LUMO	52.5
$S_0 \rightarrow T_6$	HOMO -1 → LUMO	44.4
$S_0 \rightarrow T_7$	HOMO -1 → LUMO +3	33.1
	HOMO → LUMO +3	32.5
$S_0 \rightarrow T_8$	HOMO -1 → LUMO +2	36.2
	HOMO → LUMO +3	31.9
$S_0 \rightarrow T_9$	HOMO -2 → LUMO +1	15.5
	HOMO -8 LUMO	14.8
$S_0 \rightarrow T_{10}$	HOMO -4 → LUMO	31.0

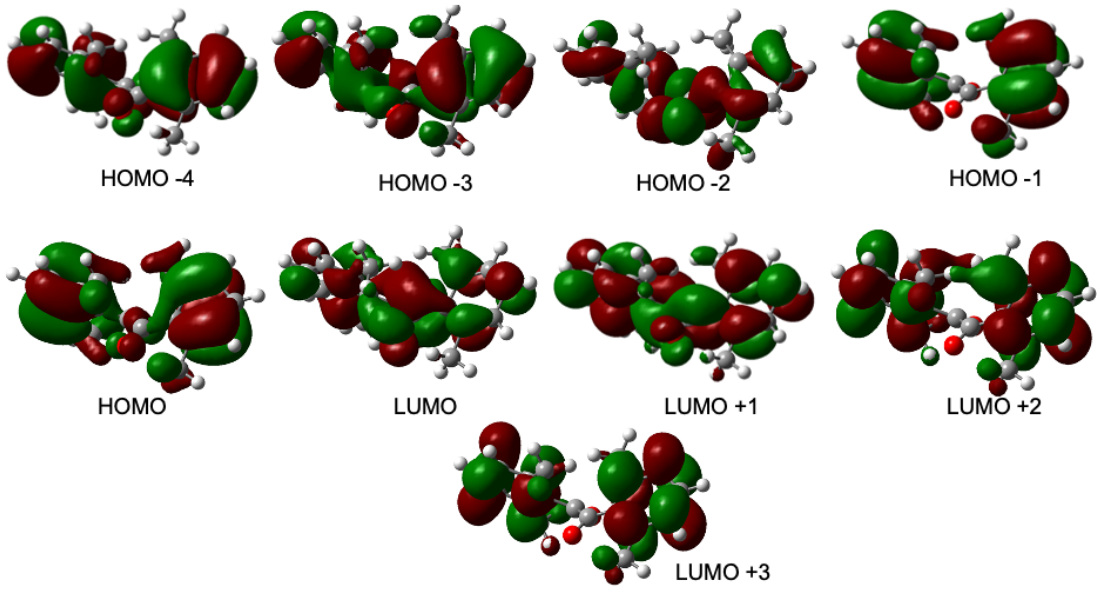

Figure 7.20: Visualization of molecular orbitals (MOs) of tetramethylbenzil in ACN obtained using CAM-B3LYP-D3(BJ)/def2-TZVP level of theory. HOMO and LUMO correspond to the Highest Occupied Molecular Orbital and Lowest Unoccupied Molecular Orbital, respectively. Isovalue of 0.03 a.u. was used for visualization.

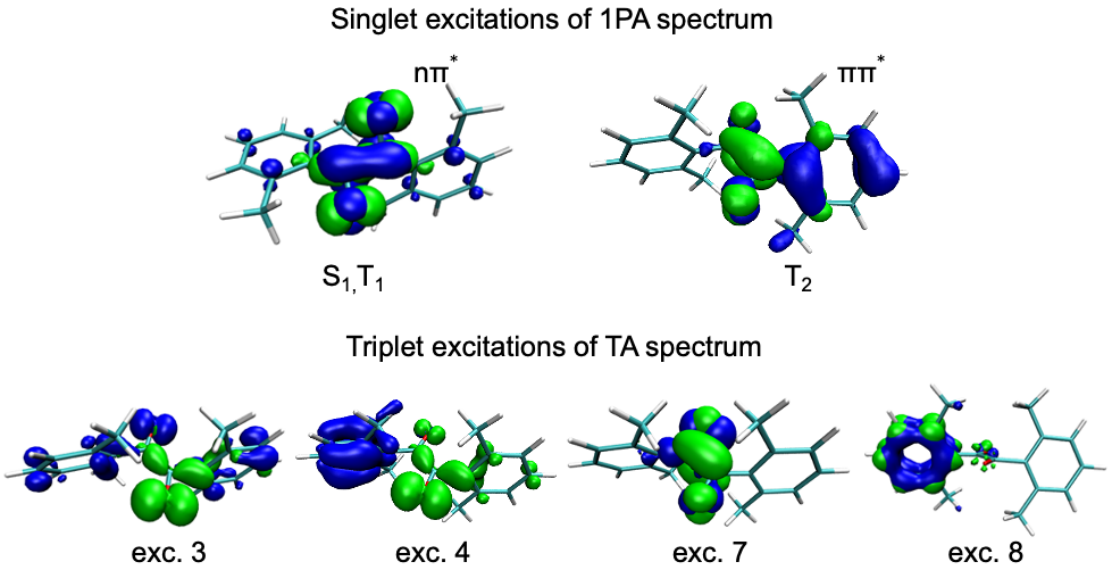

Figure 7.21: Visualization of electron donating (hole, in blue) and electron accepting (electron, in green) density upon excitation of tetramethylbenzil from the ground state to the singlet and triplet states in ACN. Electron-hole analysis and the visualization of the respective contributions were performed as reported in Chapter 4. Isovalue of 0.03 a.u. was used for visualization.

7.3.2 Photophysical properties

The optimization of the excited states is reported in Figure 7.22. Interestingly, upon optimization, the C=O bond stays more or less constant (i.e. 1.21 Å and 1.23 Å) while the C-C bond undergoes significant shortening i.e. from 1.53 Å in S_0 to 1.46 Å in S_1, 1.47 in T_1 and 1.23 Å in T_2. Also, the dihedral angle between the two carbonyl groups change from 120° to 180° in S_1 and T_1, revealing a planar conformation, and goes back to 168° in T_2. The shortening of the C-C bond with the elongation of the C=O bond is a sign of easier radical formation.

Table 7.17: Bond lengths of C-C and C=O bonds (Å) and dihedral angle (°) between the carbonyl bonds

Excited State	C=O	C-C	dihedral
S_0	1.21	1.53	120
S_1	1.23	1.46	180
T_1	1.23	1.47	180
T_2	1.23	1.48	168

The 5% El-Sayed allowed ISC S_1-T_1 happens with a rate of 1.12×10^8 s^{-1} and is chracterized by 0.57 eV (see Figure 7.22 and Table 7.18). IC S_1-S_0 of 2.72×10^{11} s^{-1} is larger than the ISC S_1-T_1 but the two processes might be still competitive. The ISC S_1-T_2 was not computed due to the high (>3 eV) reorganization energies between the two states. The fluorescence rate was not determined due to the non convergence of the correlation function in MOMAP (as explained in Section 4). The phosphorescence

rate is 4.71x10^{1} s^{-1} related to the T_1 state lifetime of 0.021 s, similarly to benzil and biacetyl. The non-radiative decay of the first triplet state is 9.14x10^{6} s^{-1} with T_1 state lifetime in the order of 0.10 μs, in agreement with benzil and slightly shorter than Norrish type II initiators.

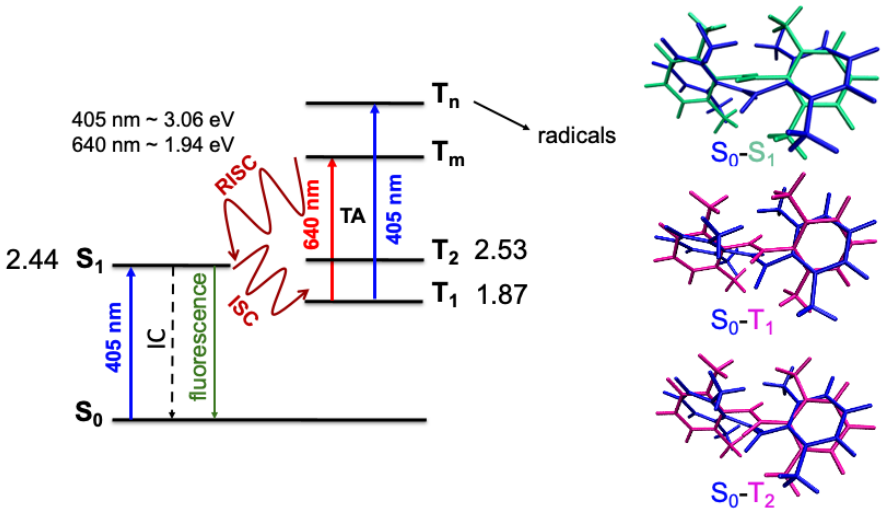

Figure 7.22: Jablonski diagram of biacetyl computed with CAM-B3LYP-D3(BJ)/def2-TZVP in ACN. The adibatic energies were computed including the zero-point energy correction (ZPVE). Overlap of optimized geometries is also reported.

Table 7.18: Photophysical rates of tetramethylbenzil: internal conversion (IC), intersystem crossing (ISC) and reverse ISC (RISC) were computed as reported in Section 4.5 in implicit ACN with TD-CAM-B3LYP-D3(BJ)/def2-TZVP level of theory. For the IC and ISC rates (in s^{-1}) the non-adiabatic coupling matrix elements (NACME, in a.u.), spin-orbit coupling (SOC, in cm^{-1}) and reorganization energy (λ, in eV) were also calculating as described in Section 4.5. For the radiative rates such as fluorescence and phosphorescence, the level of theory reported in Section 4.5 was employed.

Non-radiative rates			
	Rate	NACME	λ
IC $S_1 \rightarrow S_0$	2.72x10^{11}	0.004	1.853
	Rate	SOC	λ
ISC $S_1 \rightarrow T_1$	1.12x10^{8}	2.75	0.006
RISC $T_1 \rightarrow S_1$	2.93x10^{5}	2.57	0.006
*ISC $T_1 \rightarrow S_0$	9.14x10^{6}	0.27	1.789
Radiative rates			
	Rate	ΔE (eV)	lifetime (s)
Fluorescence	NA	2.44	-
Phosphorescence	4.71x10^{1}	1.87	0.021

* T_1 state lifetime is 1.09x10^{-7} s.

7.3.3 "Reluctant" Norrish type I character

The computed BDEs associated with the cleavage of the C-C bond in various states of the PI are presented in Table 7.19. The data reveals a significant increase in energy in T_1, reaching 14.19 kcal mol^{-1}. However, in T_2, the energy drops considerably to -0.92 kcal mol^{-1}, indicating that radicals are more easily formed from this state. Further analysis using the computational expensive IRC and transition state approach was not conducted for this PI. Nevertheless, given the reliability of the BDEs, as demonstrated in biacetyl case where the data align with IRC values with a maximum divergence of approximately 2 kcal mol^{-1}, we can consider BDEs as a clear indication of the presence of the same mechanism as observed in other two-step absorption PIs.

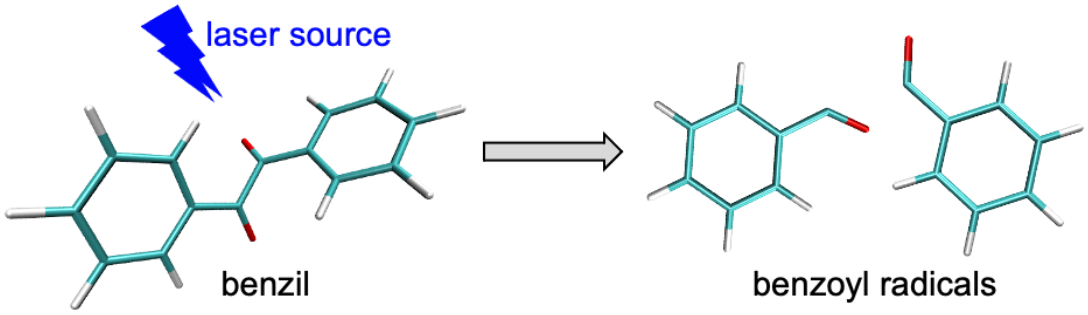

Figure 7.23: Reaction cleavage of tetramethylbenzil

Table 7.19: Bond dissociation energies (BDE)s of tetramethylbenzil in ACN calculated using TD-CAM-B3LYP-D3(BJ)/def2-TZVP method.

Excited State	BDE (eV)	BDE (kcal mol-1)
S_0	2.52	58.04
S_1	0.04	0.87
T_1	0.62	14.19
T_2	-0.04	-0.92

7.3.4 Triplet absorption spectra

The TA spectrum of tetramethylbenzil computed starting from the T_1 geometry in order to simulate the second absorption step is reported in Table 7.20, 7.21 and Figure 7.19. The presence of peak at 407.53 nm (exc.7) for the second step that would lead to the formation of radicals is red-shifted with respect to the experimental wavelength of 405 nm. The hole and electron representation is reported in Figure 7.21 and shows bonding electron localized on the C-C bond, where radicals are expected to be formed, similarly to the hole and electron distribution observed for Irgacure 651. The oscillator strength is low (0.0005) but, as reported in [31] for benzil, it is enough that the absorption is present even at the tail of the spectrum. For the second peak expected to be at 640 nm there is no actual transition reported in the spectrum and exc.5, exc.4 and exc.3 are significantly red shifted. The hole and electron representation

reported in Figure 7.21 shows antibonding character of the electron localized on the C-C bond where radicals are supposed to be formed. According to experimental data, the transition at 640 nm would lead to inhibition of the PIs and not radical formation. The TA spectrum computed with GW gives similar values considering a certain shift i.e. 384.36 nm (exc.7), 457.91 nm (exc.6) and 676.68 nm (exc.5).

Table 7.20: Vertical excitation energies for the first ten triplet of tetramethylbenzil in ACN calculated using TD-CAM-B3LYP-D3(BJ)/def2-TZVP method, starting from the optimized T_1 geometry.

Excited State	Energy (eV)	Wavelength (nm)	Osc.str.
1	0.72	1733.17	0.0327
2	1.22	1016.04	0.0000
3	1.60	774.01	0.0146
4	1.61	769.21	0.0004
5	1.63	761.58	0.0144
6	2.54	488.18	0.0028
7	3.04	407.53	0.0005
8	3.50	354.71	0.0216
9	3.53	351.35	0.0001
10	3.81	325.20	0.0004

Table 7.21: Vertical excitation energies of tetramethylbenzil for the first ten triplet excitations in ACN (COSMO implicit solvation) starting from optimized triplet state geometry (T_1). Excitations were computed in CAM-B3LYP-D3(BJ)/def2-TZVP using using eigenvalue-only self-consistent GW (evGW).

Excited State	Energy (eV)	Wavelength (nm)	Osc.str.
1	1.01	1233.58	0.0192
2	1.42	871.45	0.0000
3	1.71	725.10	0.0041
4	1.71	723.73	0.0005
5	1.83	676.68	0.0325
6	2.71	457.91	0.0031
7	3.23	384.36	0.0011
8	3.49	354.85	0.0911
9	3.65	339.80	0.0000
10	3.79	327.09	0.0882

The assessment of tetramethylbenzil proves more challenging than for benzil and biacetyl in drawing conclusions about the triplet state reachable with both laser sources. In addition, the difference in the depletion reached at 640 nm with respect to the radical formation employing laser wavelength at 405 nm should be clarified.

The analysis of two-step absorption PIs presented in this chapter aims to offer foundational insights for comprehending the mechanism of radical formation upon absorption. Nevertheless, various challenges persist, particularly in optimizing high triplet excited states using the TD-DFT method and in computing the activation energies from different triplet excited states. To enhance understanding, fur-

ther comparison between experimental data and calculations is necessary. It is crucial to develop a more efficient approach for optimizing excited states, investigated absorption spectra and analyzed cleavage reactions from several triplet states reducing computational time and effort, in order to provide a better understanding of the most efficient two-step absorption PIs that can be employed in 3D printing.

8

Summary and conclusions

8.1 Summary

In this PhD thesis, an extensive and highly detailed exploration of the molecular and electronic properties of various PIs utilized in 3D printing was conducted through QM calculations, primarily employing DFT and TD-DFT. The aim was to unravel the intricate mechanisms governing radical generation in the PIs employed in FRP. The selected PIs belonged to different categories, namely Norrish type I, "reluctant" Norrish type I and Norrish type II PIs, each leading to the formation of distinct radicals and characterized by diverse polymerization reaction mechanisms. Distinguishing between Norrish type I and Norrish type II PIs, the former initiates radicals through the unimolecular cleavage of a bond, while the latter involves a bimolecular reaction with a co-initiator molecule. "Reluctant" Norrish type I initiates the radical formation upon cleavage but not in T_1, as for common Norrish type I PIs, but rather in high triplet states.

The central focus of the thesis is the analysis of DETC and BBK, for their unique and mysterious mechanism based on three-photon instead of the common two-photon in absence of co-initiator. The 1PA spectra obtained with CAM-B3LYP exhibit a blue shift of 61 nm and 70 nm for DETC and BBK, respectively, in comparison to the experimental values (refer to Figures B.1, B.2, 6.3 and Tables B.2 and B.3). It is important to note that the functional selection prioritized the accurate reproduction of the photophysical characteristics of the PIs over achieving a smaller deviation from the experimental spectra, which is of secondary importance. Similarly, the computed 2PA spectra for DETC and BBK

show a blue shift of 80 nm and 40 nm, respectively, considering the experimental fs laser wavelength of $\sim$ 800 nm (refer to Figures 6.18 and Tables 6.16,B.14). Both PIs demonstrate significant 2PA cross-sections at this wavelength, approximately 119 GM at 721 nm for DETC and 40.50 GM at 761 nm for BBK. DETC exhibits a higher tendency for 3PA (1-42x10^{-78} cm^6 s^2 $photon^{-1}$, Figure 6.18 and Table B.12) at the printing wavelengths compared to BBK (0.08-0.59x10^{-77} cm^6 s^2 $photon^{-1}$, see Figure 6.18 and Table B.16). Although the simultaneous absorption of three photons for DETC and BBK has not been reported to date, such a process may occur in addition to 2PA, as reported for other chromophores. This 3PA with a range of 775-800 nm may excite DETC and BBK to S_3-S_5 states, which, being highly unstable, will rapidly decay to the S_1 state. Consequently, higher singlet states do not play a role in radical formation. Upon absorption from the ground state to the first singlet state, ISC occurs to the T_3 state (with ΔE S_1-T_3 of -0.12 and -0.09 eV) with rates of 1.72x10^8 s^{-1} and 2.12x10^6 s^{-1} and SOC of 7.55 cm^{-1} and 3.63 cm^{-1} for DETC and BBK, respectively (see Tables 6.18 and 6.19). Notably, there is a significant allowed ISC for both PIs, with $\pi\pi^*$ $n\pi^*$ contributing to more than 60%. The rapid IC at rate of 2.33x10^{11} s^{-1} (for DETC) then guides the system to the long-lived T_1 state (approximately 11 μs, see Tables 6.18). However, due to the fact that the the ISC S_1-T_3 for BBK is lower than IC S_1-S_0 and fluorescence (1.38x10^8 s^{-1} and 6.72x10^8 s^{-1}), data computed with B3LYP were added and explained. In this scenario the ISC S_1-T_2 of 3.70x10^8 s^{-1} and IC T_2-T_1 of 8.12x10^{11} s^{-1} bring the system to T_1, whose lifetime is 11 μs (Table 6.20). This observation aligns with the distinctive three-photon dependence exhibited by this PI upon excitation at around 800 nm using an experimental fs laser. The vibronic TA spectra computed show that absorption of this printing wavelength could indeed lead to T_4 and T_3/T_5 in the case of DETC and BBK (CAM-B3LYP) respectively (see Figures 6.21 and 6.22). With the employee of the B3LYP functional for BBK, the vibronic spectra computed show that the transition from T_1 would lead with high probability to T_3 or T_5 states, using a cw laser beam at 800 nm, that would be responsible for the activation of the third photon at this energy.

The investigated Norrish type II mechanism, typically characterized by a bimolecular reaction between the PI and an amine synergist or onium salt, was explored through the inter-HAT reaction of DETC with DBA (refer to Figure 6.24). Experimental observations revealed that when combined with DBA, DETC exhibits N = 3 photon dependency, while with salt, it displays N = 2. This deviation from the expected nonlinearities of 2, typical for Norrish type II PIs, is illustrated in Figure 1.3. This reaction requires light activation, as indicated by the activation energy values reported in Table 6.22 of 6.72 kcal mol^{-1} (0.44 kcal mol^{-1} Gibbs free energy) in T_1 compared to 56.41 kcal mol^{-1} (48.19 kcal mol^{-1} Gibbs free energy) in S_0. However, the absence of experimental observation suggests that diffusion in the printing conditions may hinder the reaction, and the formation of reactive radicals might occur when DETC is excited to higher triplet states. A similar scenario is observed for the reaction between DETC and PETA, where the activation energy is even higher than that for DBA (5.47 from T_1 and 52.77 from S_0) (see Table 6.22). On the contrary, calculations indicate that H-atom transfer with PETA in high triplets should be spontaneous (see Table 6.22). Interestingly, S_1 appears to be reactive with DBA and PETA, with Gibbs free energies of -21.91 kcal mol^{-1} and -17.33 kcal mol^{-1}, respectively (see Table 6.22). However, the observed N = 3 in polymerization, both with and without the co-initiator (see Figure 1.3), implies ad-

ditional processes beyond singlet-singlet absorption. As a result, a two-step absorption process unfolds, involving a subsequent TA of DETC from the T_1 triplet state, which exhibits strong absorption at the printing wavelength (computed oscillator strength of 0.18 at 815 nm, see Table B.21). This leads to the nonlinearities observed in 3D printing, ranging from 3.0 to 3.2 reported in Figure 1.3. In the case of BBK, no experimental measurements regarding the reaction with DBA or DPIHFP are available, and thus no calculations were performed. The investigation of the reaction between BBK and PETA is reported in Table B.27. Calculations show results similar to DETC with Gibbs free energy of 2.34 kcal mol^{-1} in T_1, while 47.25 kcal mol^{-1} in S_0, and -9 kcal mol^{-1} to -21 kcal mol^{-1} in high triplet states.

In addition to the inter-HAT reaction other possible radical formation processes were investigated: photolysis, photoactivated H-transfer and biradical formation. The Gibbs free energies required for C-H, C-C, or C-N bond cleavage proved to be excessively high in T_1 ($\sim$ 30-35 kcal mol^{-1} for DETC and $\sim$ 6-60 kcal mol^{-1} for BBK), thus hindering photoinitiation in a second-order scenario (see Figure 6.28 and Tables B.32 and B.33). However, the affinity for bond breaking of the PIs changes significantly upon absorbing the third photon at approximately 800 nm, reaching spontaneity. Despite this, these processes are still less spontaneous than the reaction with PETA and must contend with fast internal conversion to T_1 of 4.50x10^{10} s^{-1} (T_4-T_1 DETC), 1.12x10^{10} s^{-1} (T_3-T_1 BBK B3LYP) that impede the formation of active DETC radicals. The photoactivated H abstraction show extremely high Gibbs free energies in T_1 and remain positive in high triplets (see Figure 6.27.Additionally, for DETC, the biradical formation mechanism led to its classification as not possible to occur and was therefore not investigated for BBK. In conclusion, the radicals that should initiate FRP, especially in the absence of a co-initiator, are alkyl-based radicals of PETA (R_1 or R_2, see Figure 6.25 and Table B.25), formed upon H-atom abstraction reactions from PETA to DETC or PETA to BBK (Figure 6.26). These reactions, if capable of competing with photophysical processes such as IC and RISC from high triplets occurring with the order of 10^7-10^{10} s^{-1} will initiate FRP.

The exploration of Norrish type I PIs involved the use of well-known commercial initiators, Irgacure 651 and Irgacure 369. A similar validation process for the choice of the functional, as conducted for DETC and BBK, led to the selection of CAM-B3LYP. Irgacure 369, in particular, exhibits characteristics similar to DETC, for which the B3LYP functional fails to provide accurate characterization (see Chapter 5). The data indicate that, despite a modest energy difference of approximately 0.80 eV between S_1 and T_1 upon 2PA for both Irgacure 651 and Irgacure 369, the ISC process is feasible (see Figure 5.9 and Table 5.12). The ISC rates are on the order of approximately 10^7 s^{-1} for both Norrish type I initiators, with SOC of around 1 cm^{-1} (refer to Table 5.12). This rate competes with the singlet-to-ground state IC of 1.35-1.37x10^7, and the weak fluorescence reported in experiments is corroborated by the calculations (with a rate of 4.53x10^5 and 4.21x10^2 for Irgacure 651 and Irgacure 369, respectively). Radicals are formed from both Irgacure 651 and Irgacure 369 in the lowest triplet state following bond cleavage. Interestingly, the T_1 lifetime is slightly shorter (1-8 μs) compared to the ones observed for DETC and BBK (see Tables 6.18 and 6.19). The simulation of the α- cleavage reaction mechanism yielded activation energies of $\sim$ 4 kcal mol^{-1} and $\sim$ 2 kcal mol^{-1} for Irgacure 651 and Irgacure 369, respectively, with rates

of 10^9 and 10^{11} (see Figure 5.12), much faster than the non-radiative decay from the first triplet state. In addition, interesting is the comparison to the activation energy of the reaction between DETC and DBA from T_1, which was in the order of 10^7 s^{-1} (see Figure 6.24 and table 6.22).

The reluctant Norrish type I PIs, which participate in the recently uncovered two-step absorption polymerization involving cw lasers at 405 nm and 640 nm as an alternative to two-photon FRP, have been noted for their ability to generate radicals through a bond-cleavage reaction occurring from high triplet states. They exhibit a hybrid radical generation mechanism that combines aspects of Norrish type I and Norrish type II. Among the PIs investigated by Bojanowski et al.[51] three candidates were selected and reported in this thesis i.e., benzil (one-color two-step), biacetyl (two-color two-step), and tetramethylbenzil (two-color two-step with depletion) and their absorption properties, excited state energies, and cleavage mechanisms were explored. The investigation encompassed 1PA from the ground state and TA from the T_1 state. The initiators demonstrated minimal oscillator strengths related to singlet transitions, such as 0.0009 at 351 nm for benzil, 0.0001 at 415 nm for biacetyl, and 0.0006 at 386 nm for tetramethylbenzil (see Tables 7.1, 7.8 and 7.15). This aligns with the requirement for these initiators to be transparent to light for an high performance 3D printing. The initiators presented $n\pi^*$ singlet (S_1) and triplet (T_1) states (see Figures 7.13, 7.6 and 7.21) characterized by ISC rates of $4.86x10^3$ s^{-1}, $9.84x10^6$ s^{-1}, and $1.12x10^8$ s^{-1} not always competitive with other decay processes such as fluorescence and IC. These indicates that other triplet states might be involved in the ISC process. The energy difference (ΔE S-T) between singlet and triplet states is 0.57 eV, smaller than the 0.80 eV for Norrish type I. In the computed TA spectra, benzil showed significant oscillator strength in the range of 410-432 nm (i.e., 0.0074-0.3146). The TA spectrum of biacetyl in the 500 nm range exhibited a null value for the oscillator strength, indicating no absorption at that wavelength, contrary to experimental expectations (see Table 7.13). Nevertheless, the vibronic absorption spectrum from T_1 to T_3 revealed non-negligible absorption in the 500 nm range, albeit blue-shifted by more than 100 nm compared to the 640 nm wavelength (see Figure 7.17). The TA spectrum of tetramethylbenzil displayed weak absorption at 407 nm (0.0005) and at 670 nm (i.e., 0.0325 only with GW-BSE) (see Tables 7.20 and 7.21). The difficulties encountered in attaining convergence for high triplet states and in performing coherent absorption spectra in these initiators introduce uncertainties into the conclusions of the analysis, prompting the need for further exploration through both theoretical and experimental investigations.

In Figure 8.1 a summary of all radical formation channels discussed in the thesis is depicted.

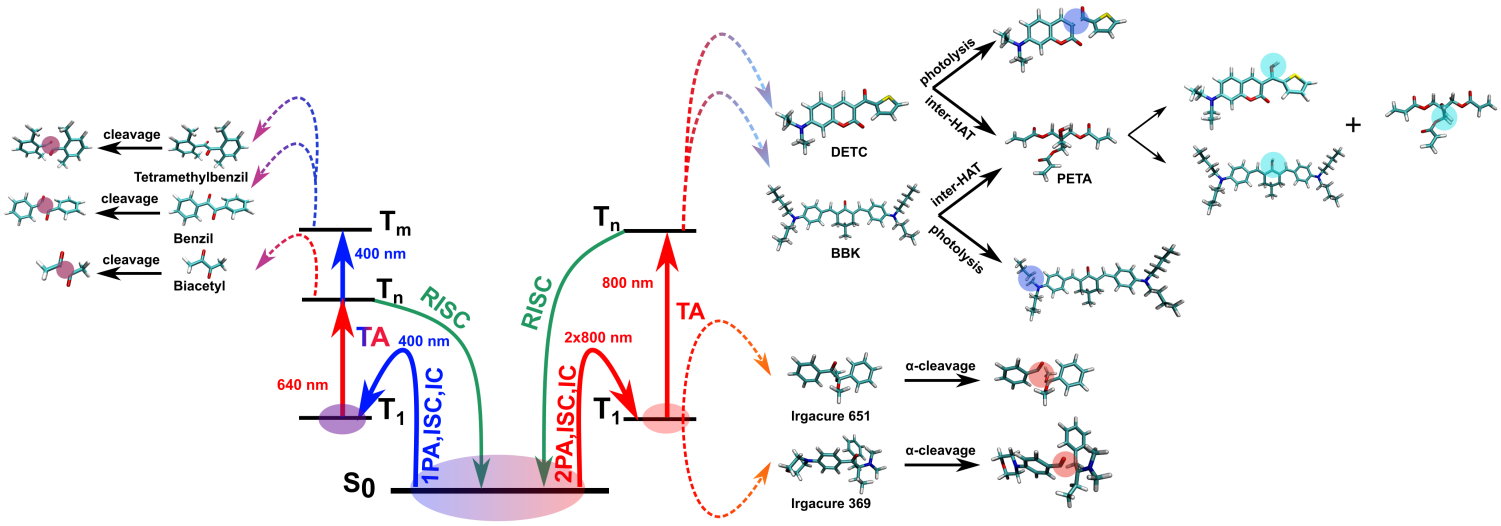

Figure 8.1: Multiple pathways of radical formation for DETC, BBK, Irgacure 651, Irgacure 369, benzil, biacetyl and tetramethylbenzil are depicted. When Norrish type I compounds are excited by multiple photons to their first singlet excited states (S_1), they become reactive and undergo intersystem crossing (ISC) and internal conversion (IC), which lead to the formation of T_1. Polymerization is then initiated through the a-cleavage of Irgacure 651 and Irgacure 369. In the case of DETC and BBK, radical formation pathways involve high triplet excited states (T_n), which can trigger radical formation reactions such as photolysis and/or inter-HAT with PETA monomer. Moreover, from high triplet states the reverse intersystem crossing (RISC) process can bring the system back to the ground state. For "reluctant" Norrish type I photoinitiators (PIs) the radical formation mechanism involves high triplet states and a cleaveg reaction.

8.2 Conclusions and outlook

The efficiency and properties of multiphoton absorption PIs play a crucial role in determining the resolution and speed of 3D laser nanoprinting. The intricate nature of competing excited states and complex photochemical reactions contributes to the generation of reactive species, which, in turn, activate FRP upon absorption of high-energy light, such as laser irradiation. The rationalization of these phenomena is challenging due to the multitude of concurrent processes occurring during a 3D printing operation and the inherent limitations of available computational tools in accurately simulating all aspects of the PI properties. The characterization of the multiphoton absorption and emission properties of the PIs involved was conducted computing 1PA, 2PA, and 3PA spectra, as well as optimizing high singlet and triplet states. The initial verification of the chosen functional relied on a comparison between experimental absorption and emission spectra and the corresponding computed spectra with the chosen functional. Subsequently, the analysis extended to a comparison with the E_{00}, focusing on the opti-

mization of the first singlet state instead of the maximum absorption peaks. The cLR and EI approaches were then employed to ensure accurate simulation of solvent dynamics. Concurrently, investigations into the CT properties associated with the transition from the ground state to singlet and triplet states were carried out. The overall findings favored the utilization of CAM-B3LYP as the most suitable functional for the analysis. Notably, B3LYP, commonly effective in reproducing the properties of organic compounds [211], exhibited limitations in characterizing the CT of excited states, especially for DETC. While this limitation was less pronounced for the other investigated PIs, for consistency, CAM-B3LYP was adopted in all cases and results computed with B3LYP, especially in the case of BBK, were used for comparison.

The core of the analysis focused on DETC and BBK, the most sensitive and efficient PIs used in two-photon 3D printing. Their mechanism, involving a unique and mysterious 3PA dependency in the absence of co-initiators and supposed to involve high triplet states in a so called two-step process characterized by an initial 2PA at 800 nm (printing wavelength) to S_1 followed by an additional 1PA from T_1, at the printing wavelength, to high triplets, was poorly understood for many years. The breakthroughs made in comprehending the radical formation mechanisms of these PIs laid the foundation for investigating other classes of PIs used in 3D printing, such as Norrish type I and, as a branch and extension of this class, the two-step absorption characterized by "reluctant" Norrish type I PIs.

The second-order scaling reactivity of DETC with the DPIHFP salt and the generation of radicals in the bimolecular system, encompassing DETC and the DBA co-initiator, as well as DETC or BBK and the PETA monomer, was explored. The findings reported in the thesis revealed that, in the absence of a co-initiator, DETC and BBK function as efficient photosensitizers, preferentially activating the alkyl radicals on PETA and ketyl radical on the PI from high triplet states. Other radical formation process might be possible i.e. photolysis although characterized by lower spontaneity with respect to the reaction with PETA monomer. Subsequently, a comparison was drawn with the more established class of Norrish type I PIs, whose mechanism is well-known for generating radicals from the first triplet state upon bond cleavage. In this case, Irgacure 651 and Irgacure 369 show high tendency of bond cleavage in T_1 characterized by fast dissociation reaction. Lastly, the analysis was extended to the class of PIs, recently utilized in the discovered two-step absorption mechanism, combining aspects from both Norrish type I and Norrish type II PIs. However, due to the challenges associated to the optimization of high triplet states combined with the difficulties in computing singlet and triplet absorption spectra that match experiments, further analysis for these PIs is necessary from a theoretical and experimental point of view.

Experimental observations aimed at understanding the underlying principles for designing new PIs to enhance 3D printing speed have remained challenging and less comprehensible for several years. While further validation and refinement of proposed models through additional computational and experimental studies are essential, a key aspect requiring attention is the reactivity of PIs in the first triplet state (T_1) in comparison to higher triplet states. Experimental studies will play a crucial role in providing additional insights and validating the theoretical findings. This thesis plays a role in elucidating the

current limitation and challenges associated to the investigation of PIs in 3D printing. Throughout this work, especially the optimization of high triplet excited states and the subsequent analysis of radical formation mechanisms have posed substantial obstacles. A critical need exists to develop a more efficient approach for optimizing high excited states, especially triplets, while addressing issues such as computational time constraints, convergence challenges in TD-DFT, and the limited accuracy in predicting energies and geometries that requires continuous calibration and comparison of various functionals. While employing high-level QM wavefunction-based methods like CC2 may provide reliable data upon optimization of high excited states for smaller systems like biacetyl, its feasibility wanes for larger systems, such as DETC and BBK, characterized by a large number of atoms. Efficiently bench-marking the properties of numerous PIs and classifying them based on specific characteristics, predicting their usability in experiments beforehand, is imperative. The automation of scrutinizing hundreds of PIs in parallel necessitates the use of more efficient, reliable, and faster methods. The future challenge lies in providing experimentalists with efficient PIs before blind testing, thereby reversing the traditional sequence of simulating and rationalizing properties of PIs post-experimental tests during 3D printing. This shift is crucial in shaping the trajectory of 3D printing research and development.

A Appendix

A.1 Supplementary Information for Chapter 5

A.1.1 Absorption properties

Table A.1: Vertical excitation energies (energy in eV and wavelength in nm) for triplet excitations of Irgacure 651 in ACN calculated using TD-CAM-B3LYP-D3(BJ)/def2-TZVP method, starting from the optimized ground state geometry (S_0). The oscillator strength (Osc.str.) values for triplet excitations are zero and therefore not reported.

Excited State	Energy	Wavelength
1	3.18	389.92
2	3.37	368.08
3	3.62	342.71
4	4.17	297.37
5	4.54	273.30
6	4.76	260.64
7	4.79	259.02
8	5.13	241.90
9	5.23	237.20
10	5.49	225.74

Table A.2: Vertical excitation energies (energy in eV and wavelength in nm) for triplet excitations of Irgacure 369 in ACN calculated using TD-CAM-B3LYP-D3(BJ)/def2-TZVP method, starting from the optimized ground state geometry (S_0). The oscillator strength (Osc.str.))values for triplet excitations are zero and therefore not reported.

Excited State	Energy	Wavelength
1	2.98	415.51
2	3.59	345.85
3	3.60	344.57
4	4.05	306.21
5	4.15	298.44
6	4.34	285.72
7	4.66	266.07
8	4.70	264.06
9	4.71	263.50
10	5.09	243.60

Table A.3: Values for one-photon absorption (1PA) as excitation energy (Energy, in eV), wavelength (λ1PA, in nm), oscillator strength (Osc.str.), and 2PA as wavelength (λ2PA, in nm), 2PA strength (δ2PA, in a.u.), cross section (σ2PA, in G.M.) of Irgacure 651 in ACN (COSMO) computed as reported in Chapter 4. Data obtained using TD-B3LYP-D3(BJ)/def2-TZVP level of theory starting from the optimized ground state geometry. No rescaling with regard to experimental data was applied. 1GM corresponds to 1×10^{-50} cm^4 s photon^{-1} molecule^{-1}.

Excitation	Energy	$\lambda_{\mathbf{1PA}}$	Osc.str.	$\lambda_{\mathbf{2PA}}$	$\delta_{\mathbf{2PA}}$	$\sigma_{\mathbf{2PA}}$
1	3.48	356.68	0.00	713.36	6.80	0.06
2	4.32	286.83	0.03	573.67	102.93	1.41
3	4.41	281.03	0.04	562.06	131.09	1.87
4	4.49	276.33	0.02	552.65	14.10	0.21
5	4.76	260.28	0.25	520.56	740.23	12.31
6	5.15	240.80	0.00	481.59	3.58	0.07
7	5.19	238.87	0.05	477.73	332.10	6.56
8	5.28	234.79	0.00	469.57	7.59	0.16
9	5.34	232.08	0.01	464.16	11.25	0.24
10	5.50	225.49	0.00	450.99	46.47	1.03

Table A.4: Values for one-photon absorption (1PA) as excitation energy (Energy, in eV), wavelength (λ1PA, in nm), oscillator strength (Osc.str.), and 2PA as wavelength (λ2PA, in nm), 2PA strength (δ2PA, in a.u.) and 2PA cross section (σ2PA, in G.M.) of Irgacure 369 in ACN (COSMO) computed as reported in chapter 4. Data obtained using TD-B3LYP-D3(BJ)/def2-TZVP level of theory starting from the optimized ground state geometry. No rescaling with regard to experimental data was applied. 1GM corresponds to $1{\times}10^{-50}$ cm^4 s photon^{-1} molecule^{-1}.

Excitation	**Energy**	$\lambda_{\mathbf{1PA}}$	**Osc.str.**	$\lambda_{\mathbf{2PA}}$	$\delta_{\mathbf{2PA}}$	$\sigma_{\mathbf{2PA}}$
1	3.17	391.07	0.02	782.13	416.44	3.07
2	3.83	323.99	0.40	647.98	3842.49	41.23
3	3.93	315.47	0.11	630.95	1293.68	14.64
4	4.34	285.93	0.02	571.86	176.28	2.43
5	4.42	280.20	0.01	560.40	64.90	0.93
6	4.47	277.13	0.01	554.26	41.65	0.61
7	4.57	271.07	0.01	542.14	206.11	3.16
8	4.68	265.12	0.00	530.24	101.22	1.62
9	4.88	254.16	0.01	508.33	455.57	7.94
10	4.93	251.70	0.02	503.40	112.61	2.00

B

Appendix

B.1 Supplementary Information for Chapter 6

B.1.1 Absorption and emission spectra

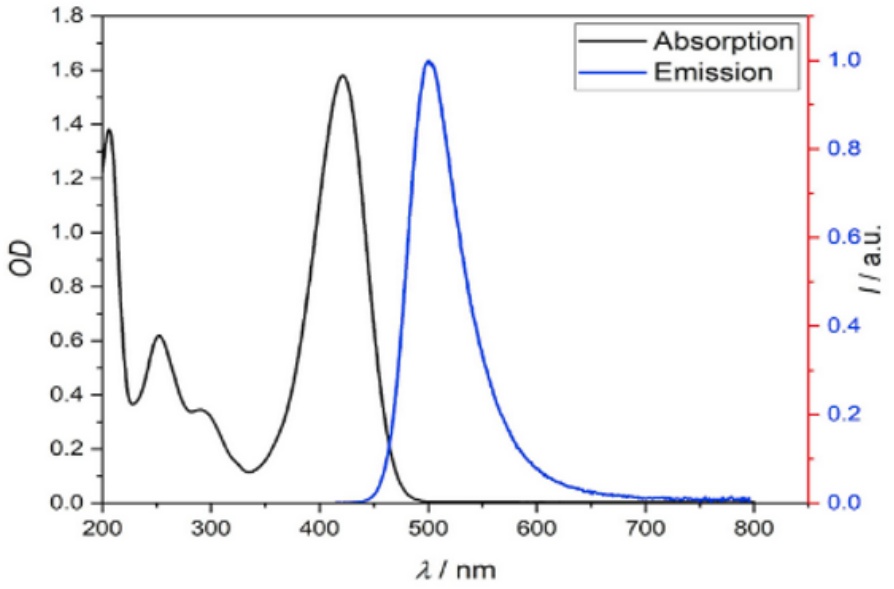

Figure B.1: Experimental absorption and emission (fluorescence) spectra of DETC in ACN. Maxima of absorption and emission are at 421 nm and 500 nm, respectively.

Table B.1: Vertical excitation energies (energy in eV and wavelength in nm) for the first ten triplet excitations of DETC in ACN calculated using TD-B3LYP-D3(BJ)/def2-TZVP method, starting from the optimized ground state geometry (S_0). The oscillator strength (Osc.str.) values for triplet excitations are zero and therefore not reported.

Excited State	**Energy**	**Wavelength**
1	2.18	568.52
2	2.80	442.54
3	3.07	404.25
4	3.33	372.74
5	3.51	353.39
6	3.59	345.36
7	3.73	332.05
8	3.91	317.10
9	4.06	305.42
10	4.11	301.48

Table B.2: Vertical excitation energies (energy in eV and wavelength in nm) for the first ten singlet excitations of DETC in ACN calculated using TD-B3LYP-D3(BJ)/def2-TZVP method, starting from the optimized ground state geometry (S_0). The oscillator strength (Osc.str.) values for triplet excitations are zero and therefore not reported.

	B3LYP			**CAM-B3LYP**		
State	Energy	Wavelength	Osc. str.	Energy	Wavelength	Osc. str.
1	2.93	422.64	0.65	3.45	359.30	0.96
2	3.51	352.44	0.25	4.06	305.52	0.05
3	3.73	332.30	0.01	4.35	285.10	0.03
4	3.93	314.70	0.02	4.56	272.09	0.02
5	4.02	307.71	0.05	4.66	266.19	0.14
6	4.27	290.23	0.02	4.92	251.90	0.06
7	4.43	279.57	0.03	4.99	248.36	0.08
8	4.57	270.80	0.14	5.25	236.06	0.02
9	4.61	268.61	0.01	5.55	223.33	0.06
10	4.73	262.09	0.09	5.61	221.01	0.09

Table B.3: Vertical excitation energies (energy in eV and wavelength in nm) for the first ten singlet excitations of BBK in ACN calculated using TDA-B3LYP-D3(BJ)/def2-TZVP method, starting from the optimized ground state geometry (S_0). The oscillator strength (Osc.str.) values for triplet excitations are zero and therefore not reported.

	B3LYP			**CAM-B3LYP**		
State	Energy	Wavelength	Osc. str.	Energy	Wavelength	Osc. str.
1	2.65	467.67	1.97	3.28	377.62	2.16
2	3.09	401.77	0.03	3.63	341.75	0.04
3	3.25	381.45	0.01	3.83	323.62	0.04
4	4.15	298.97	0.02	4.56	271.73	0.01
5	4.15	298.86	0.05	4.57	271.57	0.07
6	4.27	290.34	0.76	5.09	243.41	0.01
7	4.29	289.14	0.02	5.26	235.75	0.33
8	4.45	278.38	0.00	5.40	229.46	0.01
9	4.47	277.22	0.01	5.45	227.43	0.19
10	4.51	274.87	0.00	5.58	222.32	0.01

Table B.4: Vertical excitation energies (energy in eV and wavelength in nm) for the first ten triplet excitations of DETC in ACN calculated using TD-CAM-B3LYP-D3(BJ)/def2-TZVP method, starting from the optimized ground state geometry (S_0). The oscillator strength (Osc.str.) values for triplet excitations are zero and therefore not reported.

Excited State	**Energy**	**Wavelength**
1	2.36	525.77
2	2.84	436.56
3	3.52	352.61
4	3.77	328.77
5	3.80	326.27
6	3.96	312.81
7	4.04	306.70
8	4.25	291.61
9	4.31	287.87
10	4.87	254.44

Table B.5: Vertical excitation energies for first ten singlet and triplet excitations in the gas phase starting from optimized ground state geometry (S_0) using TD-B3LYP-D3(BJ)/def2-TZVP. Oscillator strength values for triplet excitations are zero and therefore not reported in the table.

	Singlet Excitation			**Triplet Excitation**	
Excited State	Energy (eV)	Wavelength (nm)	Osc. str.	Energy (eV)	Wavelength (nm)
1	3.23	384.39	0.60	2.32	533.79
2	3.57	347.10	0.10	2.78	446.19
3	3.86	321.59	0.04	3.13	395.99
4	3.89	318.76	0.06	3.47	357.82
5	4.05	305.90	0.01	3.52	351.82
6	4.12	301.30	0.02	3.61	343.21
7	4.47	277.63	0.00	3.78	328.03
8	4.52	274.48	0.02	3.94	314.75
9	4.64	267.46	0.09	3.98	311.49
10	4.66	265.98	0.07	4.09	302.85

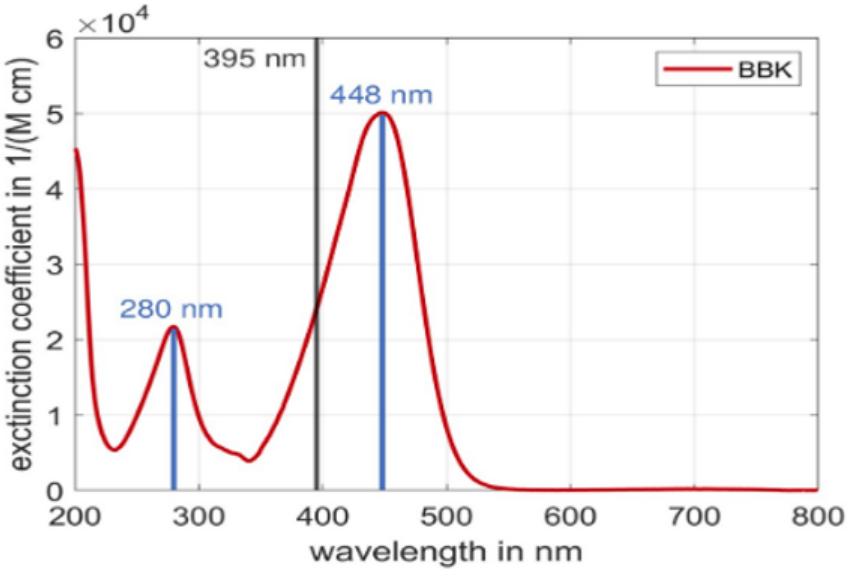

Figure B.2: Experimental absorption spectrum of BBK in ACN. Maximum of absorption is located at 448 nm.

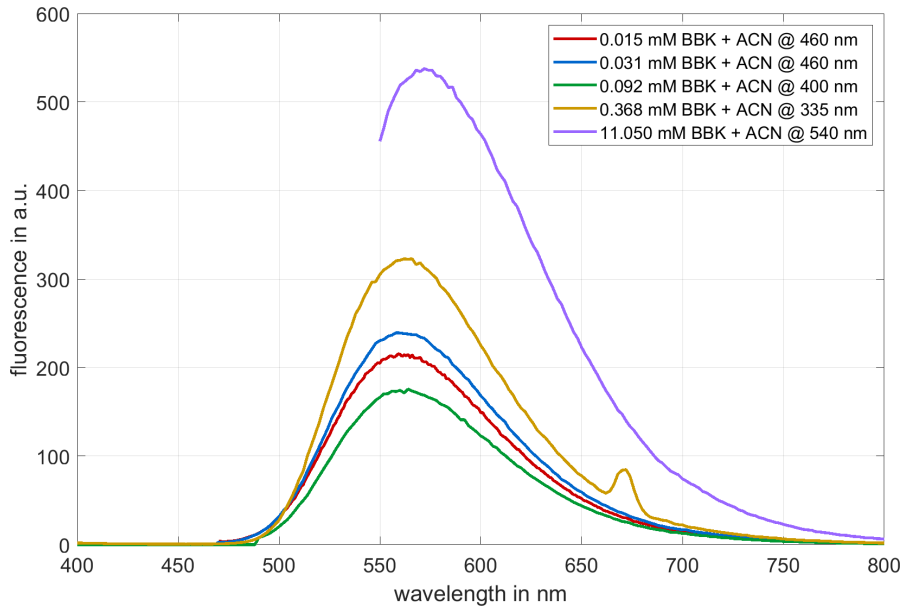

Figure B.3: Experimental emission spectrum of BBK in ACN.

Table B.6: Experimental absorption of BBK in ACN and Toluene [208]

	ACN	**Toluene**
eV	2.76	2.85
nm	448	435

Table B.7: Vertical excitation energies (energy in eV and wavelength in nm) for the first ten triplet excitations of BBK in ACN calculated using TDA-B3LYP-D3(BJ)/def2-TZVP method, starting from the optimized ground state geometry (S_0). The oscillator strength (Osc.str.) values for triplet excitations are zero and therefore not reported.

Excited State	**Energy**	**Wavelength**
1	2.11	589.07
2	2.22	558.55
3	3.00	413.25
4	3.47	357.65
5	3.51	353.33
6	3.57	347.79
7	3.58	346.77
8	3.62	342.56
9	3.74	331.23
10	4.15	298.69

Table B.8: Vertical excitation energies (energy in eV and wavelength in nm) for the first ten triplet excitations of BBK in ACN calculated using TDA-CAM-B3LYP-D3(BJ)/def2-TZVP method, starting from the optimized ground state geometry (S_0). The oscillator strength (Osc.str.) values for triplet excitations are zero and therefore not reported.

Excited State	Energy	Wavelength
1	2.44	508.23
2	2.49	497.26
3	3.26	380.44
4	3.73	332.13
5	3.78	328.18
6	3.78	328.04
7	3.87	320.75
8	4.39	282.56
9	4.50	275.81
10	4.70	263.65

B.1.2 Molecular orbitals and charge transfer analysis

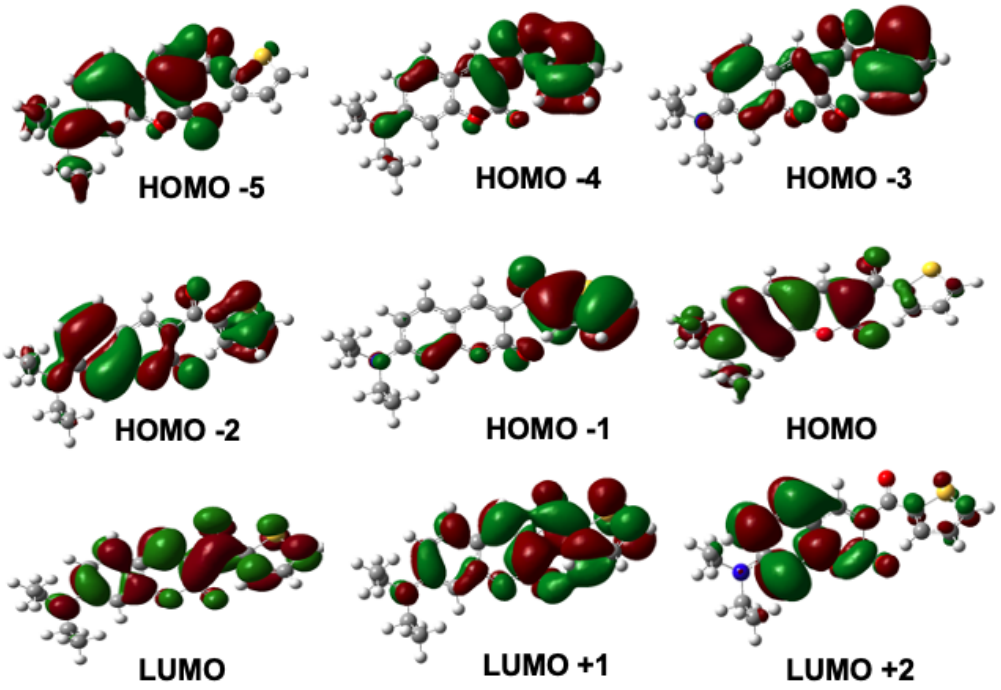

Figure B.4: Visualization of molecular orbitals (MOs) of DETC in ACN obtained using CAM-B3LYP-D3(BJ)/def2-TZVP level of theory. HOMO and LUMO correspond to the Highest Occupied Molecular Orbital and Lowest Unoccupied Molecular Orbital, respectively. Isovalue of 0.002 a.u. was used for visualization. Molecular orbitals obtained for the optimized DETC using B3LYP-D3(BJ)/def2-TZVP are similar.

Table B.9: Transition orbitals of DETC in ACN with CAM-B3LYP-D3(BJ)/def2-TZVP and B3LYP-D3(BJ)/def2-TZVP with respective contributions.

B3LYP		
Transition	Molecular Orbitals	Contribution (%)
$S_0 \rightarrow S_1$	HOMO → LUMO	97
$S_0 \rightarrow S_2$	HOMO → LUMO+1	95
$S_0 \rightarrow T_1$	HOMO → LUMO	86
$S_0 \rightarrow T_2$	HOMO-1 → LUMO	60
	HOMO-1 → LUMO+1	27
$S_0 \rightarrow T_3$	HOMO → LUMO+1	70
	HOMO → LUMO	8
	HOMO-1 → LUMO	7
	HOMO-2 → LUMO+1	4
	HOMO-3 → LUMO	10
	HOMO-4 → LUMO	4
$S_0 \rightarrow T_4$	HOMO-3 → LUMO	32
	HOMO-4 → LUMO	27
	HOMO-2 → LUMO	11
	HOMO → LUMO+1	8
$S_0 \rightarrow T_5$	HOMO-3 → LUMO	61
	HOMO-2 → LUMO+1	11
	HOMO-3 → LUMO	5
$S_0 \rightarrow T_6$	HOMO-4 → LUMO	39
	HOMO-3 → LUMO	27
	HOMO-3 → LUMO+1	11
$S_0 \rightarrow T_7$	HOMO-5 → LUMO	40
	HOMO → LUMO+2	23
	HOMO-3 → LUMO+1	6
CAM-B3LYP		
Transition	Molecular Orbitals	Contribution (%)
$S_0 \rightarrow S_1$	HOMO → LUMO	97
$S_0 \rightarrow S_2$	HOMO → LUMO+1	94
$S_0 \rightarrow T_1$	HOMO → LUMO	72
$S_0 \rightarrow T_2$	HOMO-1 → LUMO	45
	HOMO-1 → LUMO+1	40
$S_0 \rightarrow T_3$	HOMO-4 → LUMO	21
	HOMO-3 → LUMO	20
	HOMO-5 → LUMO	18
	HOMO → LUMO+1	19
$S_0 \rightarrow T_4$	HOMO-2 → LUMO	32
	HOMO → LUMO+2	19
	HOMO-2 → LUMO+1	11
$S_0 \rightarrow T_5$	HOMO-3 → LUMO+1	22
	HOMO-3 → LUMO	20
	HOMO-2 → LUMO	20
$S_0 \rightarrow T_6$	HOMO-5 → LUMO	17
	HOMO → LUMO+3	17
	HOMO → LUMO+2	15
	HOMO-4 → LUMO+1	15
$S_0 \rightarrow T_7$	HOMO-2 → LUMO	12
	HOMO → LUMO+1	33
	HOMO → LUMO	10

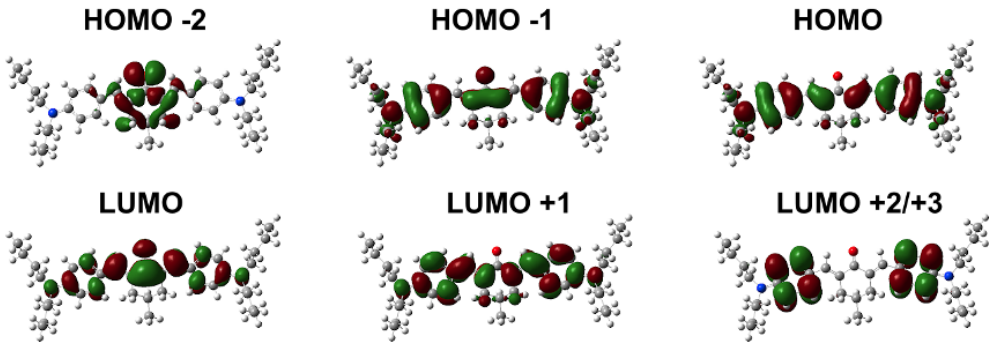

Figure B.5: Visualization of molecular orbitals (MOs) of BBK in ACN obtained using CAM-B3LYP-D3(BJ)/def2-TZVP level of theory. HOMO and LUMO correspond to the Highest Occupied Molecular Orbital and Lowest Unoccupied Molecular Orbital, respectively. Isovalue of 0.002 a.u. was used for visualization. Molecular orbitals obtained for the optimized using B3LYP-D3(BJ)/def2-TZVP are similar.

Table B.10: Transition orbitals of BBK in ACN with CAM-B3LYP-D3(BJ)/def2-TZVP and B3LYP-D3(BJ)/def2-TZVP with respective contributions.

CAM-B3LYP		
Transition	Molecular Orbitals	Contribution (%)
$S_0 \rightarrow S_1$	HOMO → LUMO	88.3
$S_0 \rightarrow S_2$	HOMO -2 → LUMO	76.9
$S_0 \rightarrow T_1$	HOMO → LUMO	71.5
$S_0 \rightarrow T_2$	HOMO -1 → LUMO	62.1
$S_0 \rightarrow T_3$	HOMO -3 → LUMO	76.2
$S_0 \rightarrow T_4$	HOMO -4 → LUMO	36.3
	HOMO → LUMO +1	22.7
$S_0 \rightarrow T_5$	HOMO → LUMO +2	52.1
$S_0 \rightarrow T_6$	HOMO → LUMO +3	51.1
$S_0 \rightarrow T_7$	HOMO -4 → LUMO	28.9
	HOMO -1 → LUMO+1	21.0
B3LYP		
Transition	Molecular Orbitals	Contribution (%)
$S_0 \rightarrow S_1$	HOMO → LUMO	98.4
$0_0 \rightarrow S_2$	HOMO -1 → LUMO	93.4
$S_0 \rightarrow T_1$	HOMO → LUMO	71.5
$S_0 \rightarrow T_2$	HOMO → LUMO +1	62.1
$S_0 \rightarrow T_3$	HOMO -1 → LUMO	76.2
$S_0 \rightarrow T_4$	HOMO -2 → LUMO	36.3
	HOMO → LUMO +1	22.7
$S_0 \rightarrow T_5$	HOMO → LUMO +2	52.1
$S_0 \rightarrow T_6$	HOMO → LUMO +2	60.3
$S_0 \rightarrow T_7$	HOMO → LUMO +3	58.2

B.1.3 Multiphoton absorption spectra

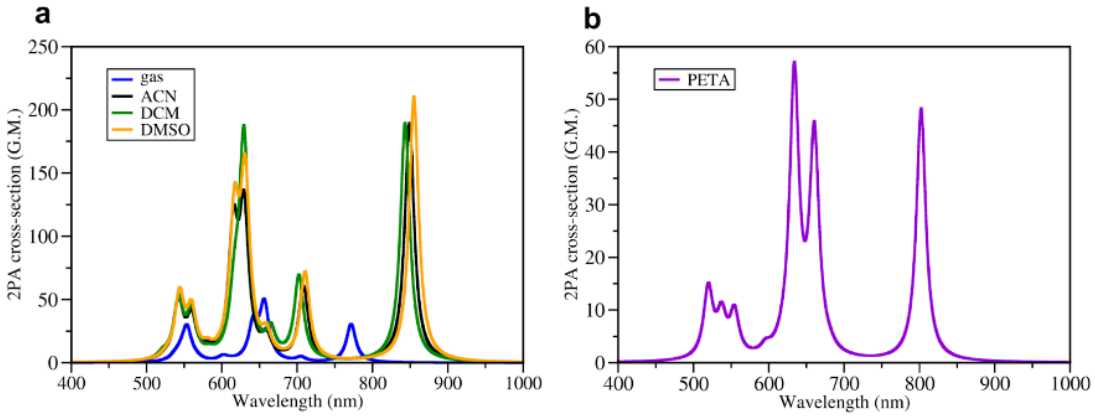

Figure B.6: **a** Two-photon absorption (2PA) spectra of DETC obtained using TD-B3LYP/def2-TZVP level of theory in the gas phase, implicit ACN, DCM and DMSO (PCM model). **b** 2PA spectra of DETC obtained using TD-B3LYP/def2-TZVP level of theory in PETA. Spectra were plotted as reported in chapter 4.

Table B.11: Values for one-photon absorption (1PA) as excitation energy (Energy, eV), wavelength (λ_{1PA} nm), oscillator strength (Osc.str.), and two-photon absorption (2PA) as wavelength (λ_{2PA}, nm), 2PA strength (δ_{2PA}, a.u.), cross section (σ_{2PA}, GM) of DETC in implicit ACN (PCM model). Data obtained using TD-B3LYP/def2-TZVP level of theory and optimized ground state geometry of DETC as reported in Chapter 4. No rescaling with regard to experimental data was applied. 1GM corresponds to $1{\times}10^{-50}$ cm^4 s $photon^{-1}$ $molecule^{-1}$.

Excitation	Energy	λ_{1PA}	Osc.str.	λ_{2PA}	δ_{2PA}	σ_{2PA}
1	2.65	467.67	1.97	942.84	14600	74.00
2	3.09	401.77	0.03	807.71	1280000	8820.00
3	3.25	381.45	0.01	756.00	79.60	0.63
4	4.15	298.97	0.02	598.96	5740	72.10
5	4.15	298.86	0.05	598.96	25700	324.00
6	4.27	290.34	0.76	582.08	2320	30.90
7	4.29	289.14	0.02	579.36	107000	1430.00
8	4.45	278.38	0.00	558.49	1090000	15700.00
9	4.47	277.22	0.01	555.98	3200	46.50
10	4.51	274.87	0.00	551.04	32000	475.00

Table B.12: Values for three-photon absorption (3PA) as excitation energy (Energy, eV), wavelength (λ_{1PA}, nm), oscillator strength (Osc.str.), and 3PA as wavelength (λ_{3PA}, nm), strength (δ_{3PA}, a.u.), cross section (σ_{3PA}, cm^6 s^2 $photon^{-1}$) of DETC in the gas phase. Data obtained using TD-CAM-B3LYP/def2-TZVP level of theory and optimized ground state geometry of DETC as reported in Chapter 4. Spectrum is depicted in Figure 6.18.

Excitation	**Energy**	$\lambda_{\mathbf{1PA}}$	**Osc.str.**	$\lambda_{\mathbf{3PA}}$	$\delta_{\mathbf{3PA}} x 10^6$	$\sigma_{\mathbf{3PA}} x 10^{-78}$
1	3.68	336.91	0.76	1010.74	100	5.58
2	3.95	313.88	0.13	941.65	8.85	0.63
3	4.54	273.09	0.07	819.28	64.3	13.38
4	4.61	268.95	0.03	806.84	63.7	1.10
5	4.78	259.38	0.04	778.14	143	41.51
6	4.88	254.07	0.03	762.20	100	5.771
7	5.07	244.54	0.06	733.63	8.85	26.41
8	5.10	243.11	0.02	729.32	64.3	81.69
9	5.34	232.18	0.01	696.54	63.7	86.11
10	5.57	222.59	0.02	667.78	143	1490.00

Table B.13: Values for one-photon absorption (1PA) as excitation energy (Energy, eV), wavelength (λ_{1PA}, nm), oscillator strength (Osc.str.), and three-photon absorption (3PA) as wavelength (λ_{3PA}, nm), 3PA strength (δ_{3PA}, a.u.), cross section (σ_{3PA}, cm^6 s^2 $photon^{-1}$) of DETC in gas phase. Data obtained using TD-B3LYP/def2-TZVP level of theory and optimized ground state geometry of DETC as reported in Chapter 4. No rescaling with regard to experimental data was applied.

Excitation	**Energy**	$\lambda_{\mathbf{1PA}}$	**Osc.str.**	$\lambda_{\mathbf{3PA}}$	$\delta_{\mathbf{3PA}} x 10^6$	$\sigma_{\mathbf{3PA}} x 10^{-78}$
1	3.23	384.39	0.59	1155.20	431	9.528
2	3.57	347.10	0.10	1053.70	72.3	2.106
3	3.86	321.59	0.03	978.81	24.8	0.901
4	3.89	318.76	0.06	944.07	1290	52.244
5	4.05	305.90	0.01	925.26	35.1	1.510
6	4.12	301.30	0.00	913.87	23.7	1.058
7	4.47	277.63	0.00	830.27	60.7	3.614
8	4.52	274.48	0.02	819.30	1770	109.673
9	4.64	267.46	0.08	805.09	397	25.922
10	4.66	265.98	0.07	796.46	1430	96.437

Table B.14: Values for two-photon absorption (2PA) as excitation energy (Energy, eV), wavelength (λ_{1PA}, nm), oscillator strength (Osc.str.), and 2PA wavelength (λ_{2PA}, nm), 2PA strength (δ_{2PA}, a.u.), cross section (σ_{2PA}, GM) of BBK in implicit ACN (PCM model). Data obtained using TDA-CAM-B3LYP/def2-TZVP level of theory and optimized ground state geometry of DETC as reported in Chapter 4. No rescaling with regard to experimental data was applied. 1GM corresponds to $1{\times}10^{-50}$ cm^4 s $photon^{-1}$ $molecule^{-1}$. The spectra are depicted in Figures 6.3 and 6.18.

Excitation	**Energy**	$\lambda_{\mathbf{1PA}}$	**Osc.str.**	$\lambda_{\mathbf{2PA}}$	$\delta_{\mathbf{2PA}}$	$\sigma_{\mathbf{2PA}}$
1	3.28	377.62	2.16	782.23	2190	16.10
2	3.63	341.75	0.04	683.11	217000	2090.00
3	3.83	323.62	0.04	683.11	61.10	0.59
4	4.56	271.73	0.01	555.98	356	5.19
5	4.57	271.57	0.07	555.98	3710	54.10
6	5.09	243.41	0.01	501.96	162000	2890.00
7	5.26	235.75	0.32	486.21	687	13.10
8	5.40	229.46	0.01	473.22	753000	15100.00
9	5.45	227.43	0.19	464.36	5210	109.00
10	5.58	222.32	0.01	455.82	748	16.20

Table B.15: Values for one-photon absorption (1PA) as excitation energy (Energy, eV), wavelength (λ_{1PA} nm), oscillator strength (Osc.str.), and two-photon absorption (2PA) as wavelength (λ_{2PA}, nm), 2PA strength (δ_{2PA}, a.u.), cross section (σ_{2PA}, GM) of BBK in implicit ACN (PCM model). Data obtained using TDA-B3LYP/def2-TZVP level of theory and optimized ground state geometry of DETC as reported in Chapter 4. No rescaling with regard to experimental data was applied. 1GM corresponds to $1{\times}10^{-50}$ cm^4 s $photon^{-1}$ $molecule^{-1}$.

Excitation	**Energy**	$\lambda_{\mathbf{1PA}}$	**Osc.str.**	$\lambda_{\mathbf{2PA}}$	$\delta_{\mathbf{2PA}}$	$\sigma_{\mathbf{2PA}}$
1	2.65	467.67	1.97	942.84	14600	74.00
2	3.09	401.77	0.03	807.71	1280000	8820.00
3	3.25	381.45	0.01	756.00	79.60	0.63
4	4.15	298.97	0.02	598.96	5740	72.10
5	4.15	298.86	0.05	598.96	25700	324.00
6	4.27	290.34	0.76	582.08	2320	30.90
7	4.29	289.14	0.02	579.36	107000	1430.00
8	4.45	278.38	0.00	558.49	1090000	15700.00
9	4.47	277.22	0.01	555.98	3200	46.50
10	4.51	274.87	0.00	551.04	32000	475.00

Table B.16: Values for three-photon absorption (3PA) as excitation energy (Energy, eV), wavelength (λ_{1PA}, nm), and 3PA as wavelength (λ_{3PA}, nm), 3PA strength (δ_{3PA}, a.u.), cross section (σ_{3PA}, cm^6 s^2 photon^{-1}) of BBK in the gas phase. Data obtained using TD-CAM-B3LYP/def2-SVP level of theory and optimized ground state geometry of BBK as reported in Chapter 4. Spectrum is depicted in Figure 6.18.

Excitation	**Energy**	$\lambda_{\mathbf{1PA}}$	$\lambda_{\mathbf{3PA}}$	$\delta_{\mathbf{3PA}} x10^{8}$	$\sigma_{\mathbf{3PA}} x10^{-77}$
1	3.37	367.91	1103.72	4.47	1.13
2	3.44	360.42	1081.26	18.50	4.99
3	3.87	320.37	961.12	1.42	0.54
4	4.58	270.71	812.12	0.92	0.59
5	4.58	270.71	812.12	0.12	0.08
6	5.06	245.03	735.08	488	418.63
7	5.20	238.43	715.29	263	244.86
8	5.41	229.18	687.53	7.98	8.37
9	5.54	223.80	671.39	1900	2139.15
10	5.69	217.90	653.69	144	175.65

Table B.17: Values for one-photon absorption (1PA) as excitation energy (Energy, eV), wavelength (λ_{1PA} nm), and three-photon absorption (3PA) as wavelength (λ_{3PA}, nm), 3PA strength (δ_{3PA}, a.u.), cross section (σ_{3PA}, cm^6 s^2 photon^{-1}) of BBK in gas phase. Data obtained using TD-B3LYP/def2-SVP level of theory and optimized ground state geometry of BBK as reported in Chapter 4. No rescaling with regard to experimental data was applied.

Excitation	**Energy**	$\lambda_{\mathbf{1PA}}$	$\lambda_{\mathbf{3PA}}$	$\delta_{\mathbf{3PA}} x10^{8}$	$\sigma_{\mathbf{3PA}} x10^{-77}$
1	2.97	417.45	1252.36	89.5	15.53
2	3.13	396.12	1188.35	5.11	1.04
3	3.31	374.57	1123.72	3.02	0.73
4	4.27	290.36	871.08	50.90	26.24
5	4.27	290.36	871.08	1.24	0.64
6	4.41	281.14	843.43	151.00	857.53
7	4.42	280.15	841.52	226.00	129.22
8	4.60	269.53	808.59	6.48	4.18
9	4.68	264.92	794.77	2.13	1.45
10	4.68	264.92	794.77	123.00	83.48

B.1.4 Time-dependent density functional theory versus high level quantum-mechanical methods

Table B.18: GW-BSE singlet vertical excitation energies (in eV and nm) of DETC in ACN (COSMO model) starting from optimized S_0 geometry. Excitations were computed using evGW calculations, employing CD variant with B3LYP and CAM-B3LYP functional, def2-TZVP basis set and def2-TZVP auxiliary basis set. RI approximation for the Coulomb term in molecular and periodic systems was also included.

	B3LYP			**CAM-B3LYP**		
Excited State	Energy	Wavelength	Osc. str.	Energy	Wavelength	Osc. str.
1	3.04	407.30	0.55	3.25	381.91	0.87
2	3.18	390.28	0.47	3.82	324.44	0.04
3	3.66	338.77	0.05	4.07	304.51	0.08
4	3.83	323.61	0.02	4.26	290.87	0.03
5	3.91	316.72	0.01	4.34	285.53	0.02
6	4.09	303.13	0.10	4.52	274.16	0.12
7	4.21	294.30	0.01	4.76	260.74	0.03
8	4.36	284.08	0.01	4.96	249.75	0.00
9	4.80	258.46	0.02	5.41	229.07	0.11
10	4.94	250.98	0.03	5.47	226.64	0.02

Table B.19: Vertical excitation energies obtained with SCS-CC2, SCS-ADC2, SOS-CC2, CC2 and CCS/def2-TZVP calculations in ACN (COSMO and corrected LR for SCS-ADC2, as reported in Chapter 4) on S_1 geometry obtained with TD-CAM-B3LYP in ACN. Results for TD-DFT were obtained with CAM-B3LYP-D3(BJ)/def2-TZVP in ACN. Results are reported in eV.

	$\mathbf{S_1}$	$\mathbf{S_2}$	$\mathbf{T_1}$	$\mathbf{T_2}$	$\mathbf{T_3}$	$\mathbf{T_4}$	$\mathbf{T_5}$	$\mathbf{T_6}$	$\mathbf{T_7}$
DFT adiab.*	3.04	3.61	2.09	-	3.16	3.59	-	3.88	-
DFT vert. from S1 cLR	3.23	3.03	2.02	2.75	3.34	3.61	3.71	3.74	3.83
SCS	2.89	3.84	2.52	3.45	3.69	4.09	4.18	4.24	4.37
SCS-ADC2	2.78	3.70	2.49	3.40	3.58	4.02	4.12	4.19	4.32
SCS-ADC2 cLR	2.74	3.59	2.44	3.37	3.51	3.95	4.10	4.15	4.31
SOS	2.93	3.98	2.58	3.48	3.82	4.18	4.26	4.29	4.47
CC2	2.78	3.54	2.38	3.31	3.46	3.88	3.98	4.13	4.17

Table B.20: Energy difference (ΔE) between singlet S_1 and triplet T_1-T_7 excitations of DETC computed on S_1 geometry obtained with TD-CAM-B3LYP in ACN with the approaches reported in Table B.19. Results are reported in eV.

	ΔE S_1-T_1	**ΔE S_1-T_2**	**ΔE S_1-T_3**	**ΔE S_1-T_4**	**ΔE S_1-T_5**	**ΔE S_1-T_6**	**ΔE S_1-T_7**
DFT adiab.*	095	-	-0.12	-0.55	-	-0.84	-
DFT vert. from S_1 cLR	1.21	0.48	-0.11	-0.38	-0.48	-0.51	-0.60
SCS	0.37	-0.56	-0.80	-0.88	-0.91	-1.07	-1.15
SCS-ADC2	0.29	-0.62	-0.80	-1.24	-1.34	-1.41	-1.54
SCS-ADC2 cLR	0.30	-0.63	-0.77	-1.21	-1.36	-1.41	-1.57
SOS	0.35	-0.55	-0.89	-1.25	-1.33	-1.36	-1.54
CC2	0.40	-0.53	-0.68	-1.10	-1.20	-1.35	-1.39

B.1.5 Triplet absorption properties

Table B.21: Triplet vertical excitation energies (in eV and nm) of DETC in ACN starting from optimized T_1 geometry. Triplet absorption (TA) excitations were computed using (U)B3LYP-D3(BJ)/def2-TZVP and (U)CAM-B3LYP-D3(BJ)/def2-TZVP levels of theory. Transitions labeled "1" to "10" are not directly related to triplet excited states numbering used in Table B.2. They are described with the mixed molecular orbitals contributions, therefore can be assigned to the specific triplet state after additional analysis. Reported spin contamination is negligible, i.e. lower than 10% [235] of the value of S^2, i.e. s(s+1), generally accepted for organic molecules. TD-DFT results are qualitatively comparable to evGW-BSE+CD data in Table B.23.

	B3LYP			**CAM-B3LYP**		
Excitation	Energy	Wavelength	Osc.str	Energy	Wavelength	Osc.str.
1	1.27	979.45	0.0154	1.52	815.20	0.1778
2	1.34	924.26	0.0003	1.75	705.75	0.1182
3	1.42	873.49	0.1352	1.82	679.83	0.1858
4	1.50	825.64	0.1211	2.26	548.21	0.0098
5	1.75	708.41	0.1720	2.38	520.97	0.0023
6	1.94	640.71	0.0004	2.47	501.85	0.0231
7	2.01	616.58	0.0049	2.56	483.20	0.4869
8	2.46	503.81	0.4373	3.06	405.21	0.0172
9	2.51	494.81	0.0128	3.24	382.50	0.0022
10	2.98	416.05	0.0659	3.35	369.22	0.0026

Table B.22: Triplet vertical excitation energies (in eV and nm) of BBK computed using (U)B3LYP-D3(BJ)/def2-TZVP and (U)CAM-B3LYP-D3(BJ)/def2-TZVP in ACN starting from the optimized first triplet state. To note that the transitions reported in the Table are not directly related to triplet excited states numbering used in Table B.3 but further analysis is necessary to identify the nature of the triplet states.

		B3LYP			**CAM-B3LYP**	
Excitation	Energy	Wavelength	Osc.str.	Energy	Wavelength	Osc.str.
1	0.70	1777.83	0.0679	1.71	724.17	0.0068
2	1.20	1033.81	0.0007	1.93	642.98	0.0074
3	1.67	743.34	0.0037	1.95	636.25	0.2921
4	1.95	635.82	1.6025	2.38	521.72	0.9421
5	2.07	599.67	0.0717	2.70	459.61	0.0344
6	2.11	587.3	0.0017	3.05	406.04	0.1910
7	2.41	514.09	0.0029	3.10	400.03	0.0066
8	2.49	497.01	0.3286	3.48	356.51	0.0186
9	2.63	471.98	0.0003	3.64	340.77	0.0024
10	2.67	463.95	0.0085	3.79	326.91	0.1075

Table B.23: GW-BSE triplet vertical excitation energies (in eV and nm) of DETC in ACN starting from optimized T_1 geometry. Excitations were computed using evGW calculations, employing CD variant with CAM-B3LYP functional, def2-TZVP basis set and def2-TZVP auxiliary basis set. RI approximation for the Coulomb term in molecular and periodic systems was also included. Transitions labeled "1" to "10" are not directly related to triplet excited states numbering used in Table B.4.

Excitation	**Energy**	**Wavelength**	**Osc.str.**
1	1.39	888.04	0.0575
2	1.50	825.79	0.0200
3	1.63	758.11	0.2898
4	2.07	598.73	0.0122
5	2.22	556.71	0.0016
6	2.33	530.44	0.0283
7	2.41	512.96	0.4108
8	2.85	434.22	0.0267
9	3.04	407.75	0.0005
10	3.17	390.34	0.0019

Table B.24: GW-BSE triplet vertical excitation energies (in eV and nm) of BBK in ACN starting from optimized T_1 geometry. Excitations were computed using evGW calculations, employing CD variant with CAM-B3LYP functional, def2-TZVP basis set and def2-TZVP auxiliary basis set. RI approximation for the Coulomb term in molecular and periodic systems was also included. Transitions labeled "1" to "10" are not directly related to triplet excited states numbering used in Table B.8

Excitation	Energy	Wavelength	Osc.str.
1	1.58	782.48	0.0929
2	1.62	764.64	0.0881
3	1.72	722.81	0.0594
4	2.16	574.62	0.8894
5	2.30	539.98	0.0840
6	2.66	466.17	0.0048
7	2.81	441.82	0.1795
8	3.21	385.70	0.0060
9	3.24	382.65	0.0017
10	3.50	354.75	0.0589

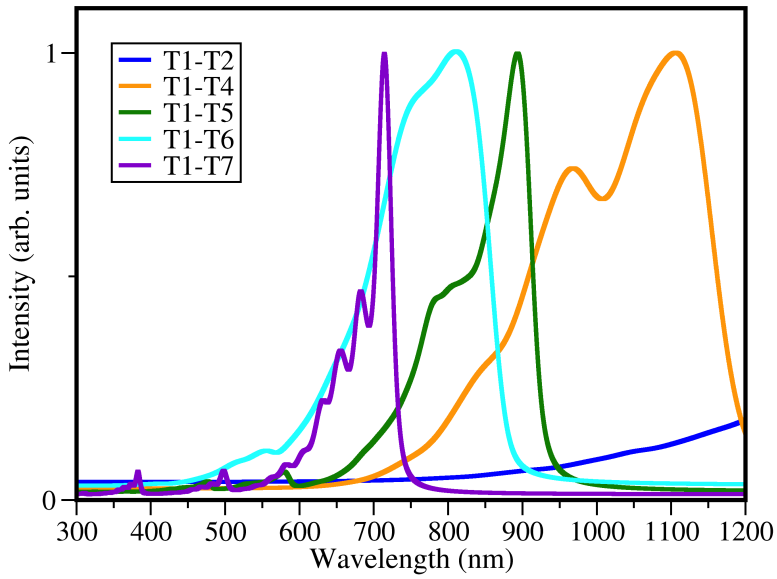

Figure B.7: Vibrationally resolved TA spectra of DETC in ACN with B3LYP-D3(BJ)/def2-TZVP. Spectra were plotted with HWHM of 80 cm-1 (i.e. 0.01 eV), convergence factor of $1.0x10^{-4}$ and Lorentzian type broadening function and computed as reported in Chapter 4. Due to significant geometry differences between T_1 and T_3 states, optimized using B3LYP, which go beyond the harmonic vibrational potentials within Franck-Condon approximation and due to the consequent failure of several different models employed for the computation of the PES: i.e. Time-independent and -dependent Franck-Condon and non-Condon simulation including Duschinsky effect and Franck-Condon and non-Condon simulations based on LCM, the vibronically resolved spectrum for the transition $T_1 \rightarrow S_3$ was not generated.

B.1.6 Investigation of possible radical formation mechanisms

Reaction with DBA and PETA

Table B.25: Bond dissociation energies (BDEs) computed for the H-atom abstraction reaction in PETA and DBA. Different types of possible PETA and DBA radicals were investigated in order to detect which C-H bond is the most probable to be broken during the first step of the inter-HAT reaction with DETC (see Figure 6.25). Values reported are in kcal mol^{-1}.

	PETA		**DBA**	
Radical	B3LYP	CAM-B3LYP	B3LYP	CAM-B3LYP
R_1	91.679	84.047	88.889	81.208
R_2	93.606	85.251	95.921	88.198
R_3	110.993	99.576	95.385	87.622
R_4	99.410	92.642	99.430	91.642
R_5	107.864	103.263	-	-

The data presented in Table B.25, along with the information depicted in Figure 6.25, reveal that the more probable radical to be formed on DBA and PETA upon reaction with DETC is radical R_1. It is crucial to note that all computed BDEs values for molecules in their ground state come with a mean absolute error of approximately 2.4 kcal mol^{-1}. This error has been reported for BDEs calculated using both B3LYP and CAM-B3LYP, combined with the def2-TZVP basis set, in comparison to experimental data [178, 179]. Specifically, the computed BDEs value for R_1 in DBA (as shown in Figure 6.25) aligns remarkably well with the experimentally reported BDEs for the same α(C–H) bond in ACN, recorded at 88.9 kcal mol^{-1} [221] (presenting values of 88.9 kcal mol^{-1} and 81.2 kcal mol^{-1} with B3LYP and CAM-B3LYP, respectively, as per Table B.25).

Table B.26: Gibbs free energy related to the Norrish type II radical formation reactions (inter-HAT mechanism) between DETC, either in S_0 and in different excited states, with PETA. Different types of possible PETA radicals were investigated (R_1-R_5) and reported in Figure 6.25 in order to detect which C-H bond is the most probable to be broken in the first step of the reaction with the photoinitiator. The change in the Gibbs free energy of reaction was computed as reported in Chapter 4. All calculations were performed in implicit ACN with (U)CAM-B3LYP-D3BJ/def2-TZVP level of theory.

State	R_1	R_2	R_3	R_4	R_5
			CAM-B3LYP		
S_0	52.77	52.47	62.42	66.40	70.75
S_1	-17.33	-17.62	-7.68	-3.70	0.65
T_1	5.47	5.18	15.11	19.10	23.45
T_3	-20.14	-20.43	-10.49	-6.51	-2.16
T_4	-29.47	-29.76	-19.82	-15.84	-11.49
T_6	-35.62	-35.92	-25.98	-21.99	-17.64
			B3LYP		
S_0	51.79	52.82	60.81	66.51	70.27
S_1	-6.81	-5.77	2.22	7.92	11.68
T_1	5.61	6.65	14.64	20.33	9.97
T_2	-3.34	-2.30	5.69	11.38	15.15
T_3	-8.52	-7.48	0.51	6.20	9.97
T_4	-19.83	-18.79	-10.80	-5.12	-1.35
T_5	-26.82	-25.77	-17.78	-12.09	-8.33
T_6	-28.83	-27.79	-19.80	-14.11	-10.34
T_7	-34.80	-33.75	-25.77	-20.07	-16.31

Table B.27: Gibbs free energies (in kcal mol^{-1}) related to the Norrish type II radical formation reactions through the inter-HAT mechanism between BBK, in both the S_0 state and different excited states, with PETA. All calculations were performed at the (U)CAM-B3LYP-D3BJ/def2-TZVP and (U)B3LYP-D3BJ/def2-TZVP level of theory in implicit ACN.

State	**PETA** R_1	**PETA** R_2
	CAM-B3LYP	
S_0	47.25	46.96
S_1	-19.42	-19.71
T_1	2.34	2.05
T_2	-9.33	-9.63
T_3	-21.02	-21.31
	B3LYP	
S_0	48.83	-
S_1	-3.46	-
T_1	7.64	-
T_2	1.59	-
T_3	-11.56	-
T_4	-16.73	-
T_5	-22.02	-
T_6	-23.37	-
T_7	-26.99	-

Photoactivated H abstraction

Table B.28: Bond dissociation energies (BDEs) related to the cleavage of C-H bond involving atom H_5 of DETC in the ground state (S_0), singlet (S_1) and triplet (T_1-T_7) excited state structures. All ΔG were calculated with CAM-B3LYP-D3(BJ)/def2-TZVP level of theory in implicit ACN. Results are reported in kcal mol^{-1}. The representation of the H bonds is reported in Figure 6.27.

State	H1	H2	H3	H4	H5
S_0	105.57	104.34	106.36	91.34	81.97
S_1	35.21	33.98	36.00	20.98	11.62
T_1	57.59	56.36	58.38	43.36	33.99
T_3	32.40	31.18	33.20	18.17	8.81
T_4	22.54	21.32	23.33	8.31	-1.06
T_6	15.71	14.49	16.51	1.49	-7.88

Table B.29: Gibbs free energies related to the cleavage of C-H bond involving atom H_5 of DETC in the ground state (S_0), singlet (S_1) and triplet (T_1-T_7) excited state structures. All ΔG were calculated with CAM-B3LYP-D3(BJ)/def2-TZVP level of theory in implicit ACN. Results are reported in kcal mol^{-1}.

State	Gibbs free energy (ΔG)
S_0	89.89
S_1	19.80
T_1	42.15
T_3	16.99
T_4	7.66
T_6	1.50

Calculated energies reveal a substantial influence of DETC photoactivation on the dynamic propensity of hydrogen atoms toward radical formation. The process of H-atom abstraction from H_5 is linked to the lowest Gibbs free energy, aligning with the recognized reactivity induction in molecules containing heteroatoms. Polar functionalities, such as N-atoms, are known to impact the reactivity of adjacent C-H bonds through polarity matching and the hyperconjugation effect, enhancing the likelihood of bond cleavage by the H-abstractor and stabilization of the radical intermediate for subsequent HAT. This process remains unfeasible from the S_0 or T_1 state of DETC due to the elevated Gibbs free energies and BDEs associated with the abstraction of H_5: 82.00 kcal mol^{-1} and 30.8 kcal mol^{-1}, respectively.

Table B.30: Gibbs free energies (in kcal mol^{-1}) related to the Norrish type II radical formation reaction (inter-hydrogen atom transfer (HAT) mechanism) for BBK either in S_0 and in different excited states. The change in the Gibbs free energies of reaction were computed as reported in Chapter 4. All calculations were performed in implicit ACN with (U)CAM-B3LYP-D3BJ/def2-TZVP and (U)B3LYP-D3BJ/def2-TZVP level of theory. The representation of the H bonds is reported in Figure 6.27.

State	H3	H4	H2	H1
		CAM-B3LYP		
S_0	94.60	88.81	94.14	98.09
S_1	27.93	22.15	27.48	31.42
T_1	49.69	43.91	49.24	53.18
T_2	38.02	32.24	37.56	41.51
T_3	26.33	20.55	25.88	29.82
		B3LYP		
S_0	92.18	85.18	92.49	96.68
S_1	39.90	32.89	40.20	44.39
T_1	50.99	43.98	51.30	55.48
T_2	44.95	37.94	45.25	49.44
T_3	31.79	24.78	32.10	36.29
T_4	26.62	19.61	26.93	31.12
T_5	21.33	14.32	21.64	25.83
T_6	19.98	12.97	20.29	24.48

Photolysis

Table B.31: Bond dissociation energies (BDEs) for different bonds of DETC in the ground state (S_0), singlet (S_1) and triplet (T_1-T_7) excited state structures. Bonds are depicted in Figure 6.28. All BDEs were calculated with CAM-B3LYP-D3(BJ)/def2-TZVP level of theory in implicit ACN. Results are reported in kcal mol^{-1}.

State	C11-C17	N4-C6	C8-C11
S_0	95.22	99.23	95.72
S_1	24.86	28.88	25.36
T_1	47.24	51.25	47.73
T_3	22.06	26.07	22.55
T_4	22.19	16.20	12.68
T_6	5.37	9.38	5.86

Table B.32: Gibbs free energies for different bonds of DETC in the ground state (S_0), singlet (S_1) and triplet (T_1-T_7) excited state structures. onds are depicted in Figure 6.28. All energies were calculated with UCAM-B3LYP-D3(BJ)/def2-TZVP level of theory in implicit ACN. Results are reported in kcal mol^{-1}.

State	C11-C17	N4-C6	C8-C11
S_0	80.03	85.34	81.72
S_1	9.93	15.24	11.62
T_1	32.28	37.59	33.97
T_3	7.13	12.43	8.82
T_4	-2.21	3.10	-0.52
T_6	-8.35	-3.06	-6.67

Table B.33: Gibbs free energies for different bonds of BBK in the ground state (S_0), singlet (S_1) and triplet (T_1-T_7) excited state structures. onds are depicted in Figure 6.28. All energies were calculated with (U)CAM-B3LYP-D3(BJ)/def2-TZVP and (U)B3LYP-D3(BJ)/def2-TZVP level of theory in implicit ACN. Results are reported in kcal mol^{-1}.

State	C16-C17	C35-C36	C12-C15	C34-C35	C33-C34	C45-N26
			CAM-B3LYP			
S_0	102.73	77.29	70.78	68.31	58.94	51.25
S_1	36.06	10.62	4.11	1.64	-7.73	-15.42
T_1	57.82	32.38	25.87	23.40	14.02	6.34
T_2	46.15	20.71	14.20	11.74	2.35	-5.34
T_3	34.46	9.02	2.51	0.04	-9.33	-17.02
			B3LYP			
S_0	102.83	76.63	69.63	66.90	57.69	49.75
S_1	50.54	24.34	17.34	14.61	5.41	-2.53
T_1	61.64	35.44	28.43	25.71	16.50	8.56
T_2	55.59	29.39	22.39	19.66	10.45	2.51
T_3	42.44	16.23	9.24	6.51	-2.70	-10.64
T_4	37.27	11.06	4.06	1.33	-7.87	-15.81
T_5	31.98	5.78	-1.22	-3.95	-13.16	-21.10
T_6	30.63	4.43	-2.57	-5.30	-14.50	-22.45
T_7	27.01	0.80	-6.20	-8.92	-18.13	-26.07

Biradical formation

Intriguingly, intramolecular hydrogen atom transfer (HAT) has been proposed for other chromophore molecules in prior studies [224, 225, 226, 227]; however, the confirmation of distance criteria for such HAT processes remains unverified. If this mechanism is feasible, DETC has the potential to generate biradicals following the photoactivated H-abstraction and intra-HAT. The investigation of the Gibbs free energies for hydrogen abstraction and attachment of DETC biradicals was evaluated. Ten biradicals were categorized into two main groups denoted as “a” and “b,” distinguished by the carbonyl group under consideration, i.e., C11-O12 for biradicals 1-5Bi-a and C9-O13 for biradicals 1-5Bi-b. The products in equation 4.5 correspond to the biradicals formed (1Bi-a to 5Bi-a and 1Bi-b to 5Bi-b), while the reagents

pertain to each optimized state considered, including the ground state, singlet, or triplet configurations.

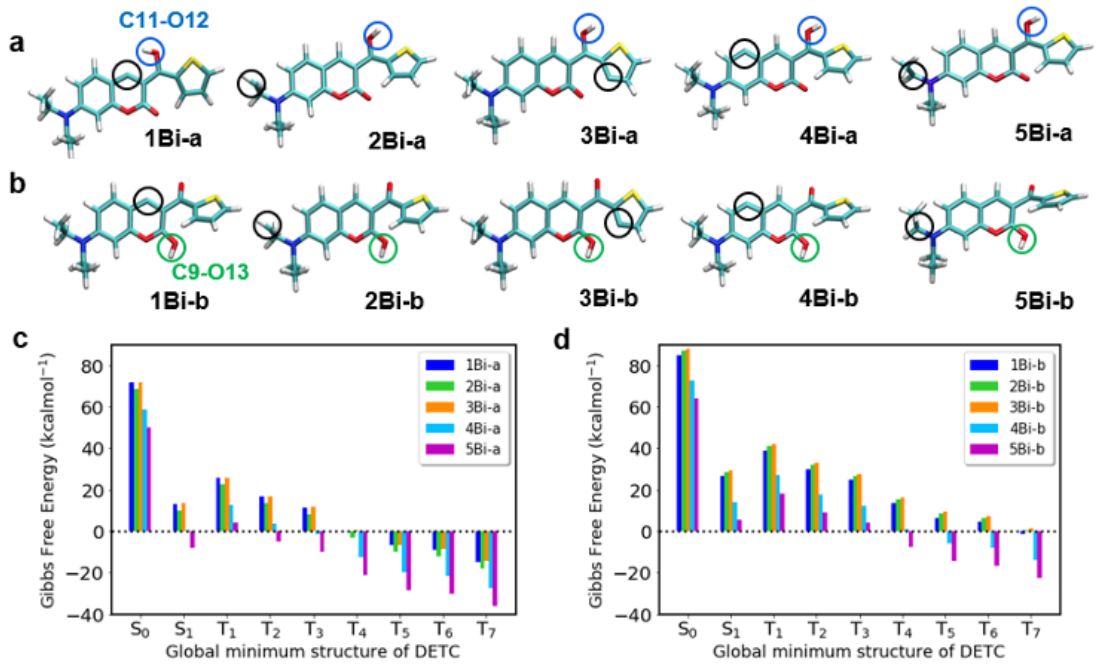

Figure B.8: a DETC biradicals calculated: 1Bi-a to 5Bi-a formed via ketyl radical on C11 (C11-O12 carbonyl bond, marked in blue) and aminoalkyl radical on C-atom in $H_1 - H_5$ positions (marked in black) with the corresponding Gibbs free energies. **b** Biradicals 1Bi-b to 5Bi-b formed via C9-O13 carbonyl (marked in green) and aminoalkyl moiety (marked in black) with the corresponding Gibbs free energies. All calculations were performed using the unrestricted B3LYP-D3(BJ)/def2-TZVP level of theory including implicit ACN.

Table B.34: Bond dissociation energies (BDEs) of DETC biradicals formation from the ground state (S_0), singlet (S_1) and triplet (T_1-T_7) excited state structures. Formation of biradicals, considering ketyl radical generation on C11-O12 carbonyl bond, labeled from 1Bi-a to 5Bi-a is depicted in Fig.B.8. Energies obtained with CAM-B3LYP-D3(BJ)/def2-TZVP level of theory in implicit ACN. Results are reported in kcal mol^{-1}.

State	1Bi-a	2Bi-a	3Bi-a	4Bi-a	5Bi-a
S_0	69.95	60.22	73.38	72.70	52.28
S_1	-0.40	-10.13	3.02	2.35	-18.08
T_1	21.97	12.24	25.39	24.72	4.30
T_3	-3.21	-12.94	0.21	-0.46	-20.88
T_4	-1308	-22.81	-9.65	-10.33	-30.75
T_6	-19.90	-29.63	-16.47	-17.15	-35.58

Table B.35: Gibbs free energy of DETC biradicals formation from the ground state (S_0), singlet (S_1) and triplet (T_1-T_7) excited state structures. Formation of biradicals, considering ketyl radical generation on C11-O12 carbonyl bond, labeled from 1Bi-a to 5Bi-a is depicted in Fig.B.8. Energies obtained with CAM-B3LYP-D3(BJ)/def2-TZVP level of theory in implicit ACN. Results are reported in kcal mol^{-1}.

State	1Bi-a	2Bi-a	3Bi-a	4Bi-a	5Bi-a
S_0	68.89	58.75	72.41	71.78	50.77
S_1	-1.20	-11.35	2.32	1.69	-19.32
T_1	21.59	11.45	25.11	24.48	3.47
T_3	-4.01	-14.15	-0.49	-1.12	-22.13
T_4	-13.34	-23.49	-9.82	-10.45	-31.46
T_6	-19.50	-29.64	-15.98	-16.61	-37.62

Results obtained demonstrate that the formation of biradicals should be spontaneous from triplet states higher than T_1. The formation of biradical 5Bi-a is associated with the lowest Gibbs free energies, i.e. in the range -31 to -37 kcal mol^{-1}, related to high triplet excited states. However, the presence of the long intra-HAT combined with the rigidity of the DETC molecule has been never confirmed experimentally and therefore the process is not likely to occur.

The biradicals formation of BBK was not investigated due to the low probability of this process to occur already reported for DETC.

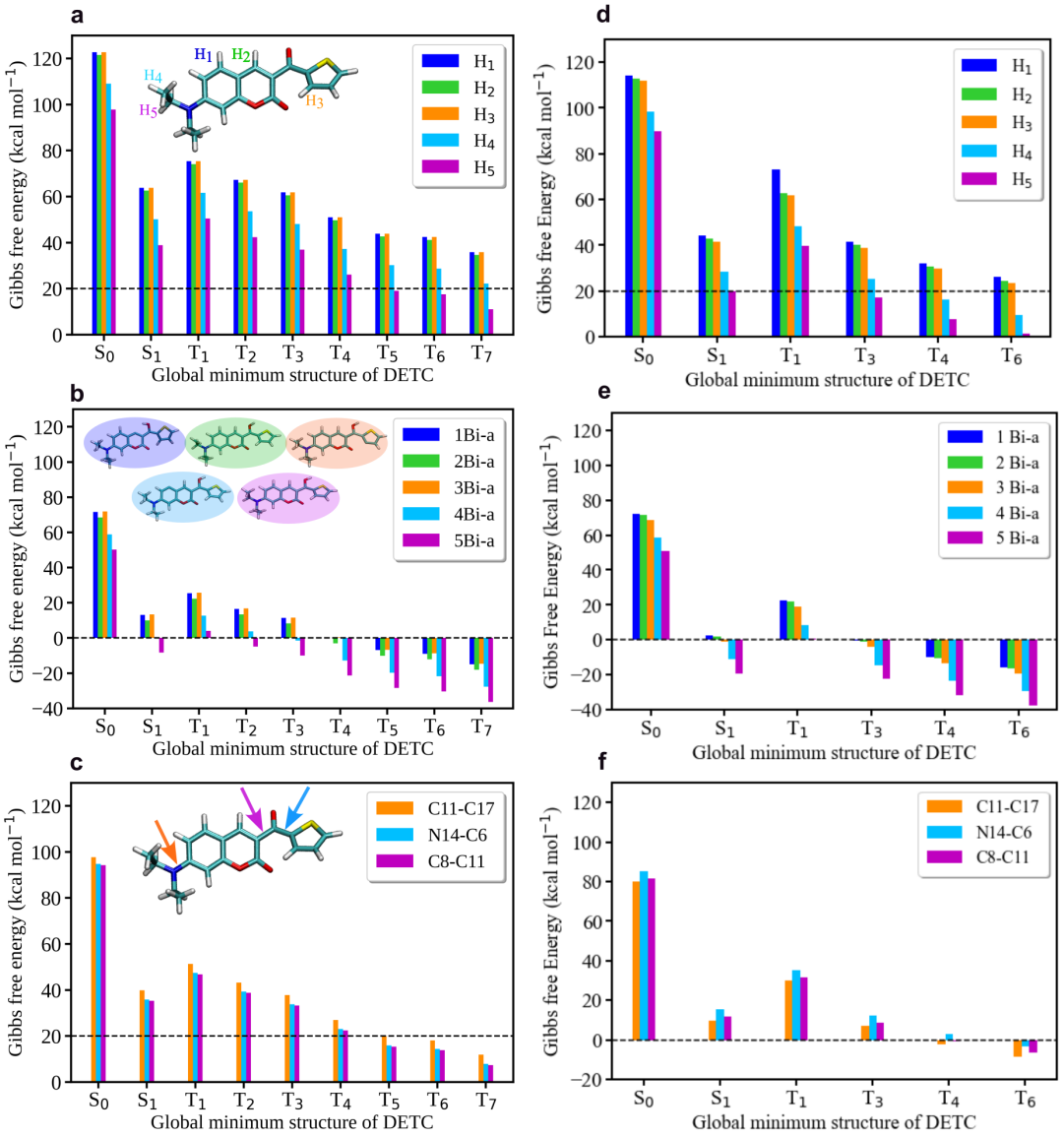

Figure B.9: Gibbs free energy for different hypothetical DETC radical formations: C-H bond breaking (H_1-H_5) calculated using **a** B3LYP and **d** CAM-B3LYP functional; biradical formation using **b** B3LYP and **e** CAM-B3LYP; photolysis using **c** B3LYP and **f** CAM-B3LYP as a function of the DETC electronic state. Energies were computed employing (U)B3LYP-D3(BJ)/def2-TZVP and (U)CAM-B3LYP-D3(BJ)/def2-TZVP approach in implicit ACN.

Bibliography

[1] Ian Gibson, David Rosen, Brent Stucker, and Mahyar Khorasani. *Additive Manufacturing Technologies*. Springer International Publishing, 2021.

[2] Andreas Gebhardt. *Understanding additive manufacturing: rapid prototyping, rapid tooling, rapid manufacturing*. Hanser.

[3] Shoji Maruo, Osamu Nakamura, and Satoshi Kawata. Three-dimensional microfabrication with two-photon-absorbed photopolymerization. *Optics Letters*, 22(2):132, 1997.

[4] Satoshi Kawata, Hong-Bo Sun, Tomokazu Tanaka, and Kenji Takada. Finer features for functional microdevices. *Nature*, 412(6848):697–698, 2001.

[5] Christopher Barner-Kowollik, Martin Bastmeyer, Eva Blasco, Guillaume Delaittre, Patrick Müller, Benjamin Richter, and Martin Wegener. 3d laser micro- and nanoprinting: Challenges for chemistry. *Angewandte Chemie International Edition*, 56(50):15828–15845, 2017.

[6] Joachim Fischer, Jonathan B. Mueller, Johannes Kaschke, Thomas J. A. Wolf, Andreas-Neil Unterreiner, and Martin Wegener. Three-dimensional multi-photon direct laser writing with variable repetition rate. *Optics Express*, 21(22):26244–26260, 2013.

[7] Kwang-Sup Lee, Ran Hee Kim, Dong-Yol Yang, and Sang Hu Park. Advances in 3d nano/microfabrication using two-photon initiated polymerization. *Progress in Polymer Science*, 33(6):631–681, 2008.

[8] Chengteh Lee, Weitao Yang, and Robert G. Parr. Development of the colle-salvetti correlation-energy formula into a functional of the electron density. *Physical Review B*, 37(2):785–789, 1988.

[9] S.-H. Park, D.-Y. Yang, and K.-S. Lee. Two-photon stereolithography for realizing ultraprecise three-dimensional nano/microdevices. *Laser & Photonics Reviews*, 3(1):1–11, 2009.

[10] Maria Farsari and Boris N. Chichkov. Two-photon fabrication. *Nature Photonics*, 3(8):450–452, 2009.

[11] Yusheng Zhang, Yuming Su, Yi Zhao, Zhiye Wang, and Cheng Wang. Two-photon 3d printing in metal–organic framework single crystals. *Small*, 18(18):2200514, 2022.

[12] Zouheir Sekkat and Satoshi Kawata. Laser nanofabrication in photoresists and azopolymers: Laser nanofabrication in photoresists and azopolymers. *Laser & Photonics Reviews*, 8(1):1–26, 2014.

[13] Hyunwoo Yuk, Baoyang Lu, Shen Lin, Kai Qu, Jingkun Xu, Jianhong Luo, and Xuanhe Zhao. 3d printing of conducting polymers. *Nature Communications*, 11(1):1604, 2020.

[14] Marc Hippler, Enrico Domenico Lemma, Sarah Bertels, Eva Blasco, Christopher Barner-Kowollik, Martin Wegener, and Martin Bastmeyer. 3d scaffolds to study basic cell biology. *Advanced Materials*, 31(26):1808110, 2019.

[15] Zhen Bai, Jingsong Wei, Xin Liang, Kui Zhang, Tao Wei, and Rui Wang. High-speed laser writing of arbitrary patterns in polar coordinate system. *Review of Scientific Instruments*, 87(12):125118, 2016.

[16] Shi-Jie Zhang, Yan Li, Yang-Kai Wang, Li-Pu Liu, Hong-Da Wang, Yun-Feng Xiao, Hong Yang, and Qihuang Gong. Controlling young's modulus of polymerized structures fabricated by direct laser writing. *Applied Physics A*, 118(2):437–441, 2015.

[17] Elaheh Sedghamiz, Modan Liu, and Wolfgang Wenzel. Challenges and limits of mechanical stability in 3d direct laser writing, 2021.

[18] Joachim Fischer and Martin Wegener. Three-dimensional optical laser lithography beyond the diffraction limit. *Laser & Photonics Reviews*, 7(1):22–44, 2013.

[19] Xiaolong He, Tianlong Li, Jia Zhang, and Zhenlong Wang. STED direct laser writing of 45 nm width nanowire. *Micromachines*, 10(11):726, 2019.

[20] Joachim Fischer, Jonathan B. Mueller, Alexander S. Quick, Johannes Kaschke, Christopher Barner-Kowollik, and Martin Wegener. Exploring the mechanisms in STED-enhanced direct laser writing. *Advanced Optical Materials*, 3(2):221–232, 2015.

[21] Joachim Fischer, Georg von Freymann, and Martin Wegener. The materials challenge in diffraction-unlimited direct-laser-writing optical lithography. *Advanced Materials*, 22(32):3578–3582, 2010.

[22] Stefan W. Hell and Jan Wichmann. Breaking the diffraction resolution limit by stimulated emission: stimulated-emission-depletion fluorescence microscopy. *Optics Letters*, 19(11):780, 1994.

[23] Stefan W Hell. Microscopy and its focal switch. *Nature Methods*, 6(1):24–32, 2009.

[24] Stefan W. Hell. Strategy for far-field optical imaging and writing without diffraction limit. *Physics Letters A*, 326(1):140–145, 2004.

[25] Joachim Fischer and Martin Wegener. Ultrafast polymerization inhibition by stimulated emission depletion for three-dimensional nanolithography. *Advanced Materials*, 24(10):OP65–OP69, 2012.

[26] Joachim Fischer and Martin Wegener. Three-dimensional direct laser writing inspired by stimulated-emission-depletion microscopy [invited]. *Optical Materials Express*, 1(4):614–624, 2011.

[27] Vincent Hahn, Pascal Rietz, Frank Hermann, Patrick Müller, Christopher Barner-Kowollik, Tobias Schlöder, Wolfgang Wenzel, Eva Blasco, and Martin Wegener. Light-sheet 3d microprinting via two-colour two-step absorption. *Nature Photonics*, 16(11):784–791, 2022.

[28] Pascal Kiefer, Vincent Hahn, Martina Nardi, Liang Yang, Eva Blasco, Christopher Barner-Kowollik, and Martin Wegener. Sensitive photoresists for rapid multiphoton 3d laser micro- and nanoprinting. *Advanced Optical Materials*, 8(19):2000895, 2020.

[29] Anna Mauri, Pascal Kiefer, Philipp Neidinger, Tobias Messer, N. Maximilian Bojanowski, Liang Yang, Sarah Walden, Andreas-Neil Unterreiner, Christopher Barner-Kowollik, Martin Wegener, Wolfgang Wenzel, and Mariana Kozlowska. Two- and three-photon processes in photoinitiators for 3d laser printing, 2022.

[30] Jonathan B. Mueller, Joachim Fischer, Yatin J. Mange, Thomas Nann, and Martin Wegener. *In-situ* local temperature measurement during three-dimensional direct laser writing. *Applied Physics Letters*, 103(12):123107, 2013.

[31] Vincent Hahn, Tobias Messer, N. Maximilian Bojanowski, Ernest Ronald Curticean, Irene Wacker, Rasmus R. Schröder, Eva Blasco, and Martin Wegener. Two-step absorption instead of two-photon absorption in 3d nanoprinting. *Nature Photonics*, 15(12):932–938, 2021.

[32] Nicholas J. Turro. *Modern molecular photochemistry*. Univ. Science Books, 2. print edition, 1991.

[33] R. G. W. Norrish and C. H. Bamford. Photodecomposition of aldehydes and ketones. *Nature*, 138(3502):1016–1016, 1936.

[34] R. G. W. Norrish and C. H. Bamford. Photo-decomposition of aldehydes and ketones. *Nature*, 140(3535):195–196, 1937.

[35] Joachim Fischer and Martin Wegener. Ultrafast polymerization inhibition by stimulated emission depletion for three-dimensional nanolithography. *Advanced Materials*, 24(10):OP65–OP69, 2012.

[36] Jean Pierre Fouassier and Jacques Lalevée. *Photoinitiators for Polymer Synthesis: Scope, Reactivity and Efficiency*. Wiley, 1 edition, 2012.

[37] G. Rist, A. Borer, K. Dietliker, V. Desobry, J. P. Fouassier, and D. Ruhlmann. Sensitization of α-aminoketone photoinitiators: a time-resolved CIDNP and laser spectroscopy investigation. *Macromolecules*, 25(16):4182–4193, 1992.

[38] H.F. Gruber. Photoinitiators for free radical polymerization. *Progress in Polymer Science*, 17(6):953–1044, 1992.

[39] Sajjad Dadashi-Silab, Sean Doran, and Yusuf Yagci. Photoinduced electron transfer reactions for macromolecular syntheses. *Chemical Reviews*, 116(17):10212–10275, 2016.

[40] Sumon Sarkar, Kelvin Pak Shing Cheung, and Vladimir Gevorgyan. C–h functionalization reactions enabled by hydrogen atom transfer to carbon-centered radicals. *Chemical Science*, 11(48):12974–12993, 2020.

[41] Janina Kabatc, Joanna Ortyl, and Katarzyna Kostrzewska. New kinetic and mechanistic aspects of photosensitization of iodonium salts in photopolymerization of acrylates. *RSC Advances*, 7(66):41619–41629, 2017.

[42] Shalin J. Jhaveri, Jesse D. McMullen, Rint Sijbesma, Loon-Seng Tan, Warren Zipfel, and Christopher K. Ober. Direct three-dimensional microfabrication of hydrogels via two-photon lithography in aqueous solution. *Chemistry of Materials*, 21(10):2003–2006, 2009.

[43] Angelo Alberti, Massimo Benaglia, Dante Macciantelli, Stefano Rossetti, and Marco Scoponi. Further EPR-spin trapping studies of the photoinitiating activity of irgacure 369. *European Polymer Journal*, 44(9):3022–3027, 2008.

[44] Halina Kaczmarek and Piotr Galka. Effect of irgacure 651 initiator on poly(methyl methacrylate)photostability studied by UV-vis spectroscopy#. *The Open Process Chemistry Journal*, 1(1):8–11, 2008.

[45] Paul Somers, Zihao Liang, Teng Chi, Jason E. Johnson, Liang Pan, Bryan W. Boudouris, and Xianfan Xu. Photo-activated polymerization inhibition process in photoinitiator systems for high-throughput 3d nanoprinting. *Nanophotonics*, 0(0), 2023.

[46] Liang Yang, Alexander Münchinger, Muamer Kadic, Vincent Hahn, Frederik Mayer, Eva Blasco, Christopher Barner-Kowollik, and Martin Wegener. On the schwarzschild effect in 3d two-photon laser lithography. *Advanced Optical Materials*, 7(22):1901040, 2019.

[47] Lucia Flamigni, Francesco Barigelletti, Sergio Dellonte, and Giorgio Orlandi. Photophysical properties of benzil in solution: triplet state deactivation pathways. *Journal of Photochemistry*, 21(2):237–244, 1983.

[48] Angelo A. Lamola and George S. Hammond. Mechanisms of photochemical reactions in solution. XXXIII. intersystem crossing efficiencies. *The Journal of Chemical Physics*, 43(6):2129–2135, 1965.

[49] Ajit Singh, Arthur Reginald Scott, and F. Sopchyshyn. Flash photolysis of camphorquinone and biacetyl. *The Journal of Physical Chemistry*, 73(8):2633–2643, 1969.

[50] Hans L. J. Bäckström, Kjell Sandros, Haakon Haraldsen, A. Grönvall, B. Zaar, and E. Diczfalusy. The quenching of the long-lived fluorescence of biacetyl in solution. *Acta Chemica Scandinavica*, 12:823–832, 1958.

[51] N. Maximilian Bojanowski, Aleksandra Vranic, Vincent Hahn, Pascal Rietz, Tobias Messer, Julian Brückel, Christopher Barner-Kowollik, Eva Blasco, Stefan Bräse, and Martin Wegener. Search for alternative two-step-absorption photoinitiators for 3d laser nanoprinting. *Advanced Functional Materials*, page 2212482, 2022.

[52] Peter J. Wagner, Allen E. Kemppainen, and Herbert N. Schott. Effects of ring substituents on the type II photoreactions of phenyl ketones. how interactions between nearby excited triplets affect chemical reactivity. *Journal of the American Chemical Society*, 95(17):5604–5614, 1973.

[53] T. Cáceres, M.V. Encinas, and E.A. Lissi. Photocleavage of benzil. *Journal of Photochemistry*, 27(1):109–114, 1984.

[54] W. G. McGimpsey and J. C. Scaiano. A two-photon study of the "reluctant" norrish type i reaction of benzil. *Journal of the American Chemical Society*, 109(7):2179–2181, 1987.

[55] Masahiro Mukai, Seigo Yamauchi, and Noboru Hirota. A time-resolved EPR study of one- and two-photon processes in the photochemical reactions of benzil. *The Journal of Physical Chemistry*, 93(11):4411–4413, 1989.

[56] A. S. Tatikolov, P. P. Levin, T. A. Kokrashvili, and V. A. Kuz'min. Quenching of the triplet states of carbonyl compounds by nitroxyl radicals. *Bulletin of the Academy of Sciences of the USSR Division of Chemical Science*, 32(3):465–468, 1983.

[57] Linda J. Johnston, Michal Tencer, and J. C. Scaiano. Evidence for hydrogen transfer in the photochemistry of 2,2,6,6-tetramethylpiperidine n-oxyl. *The Journal of Organic Chemistry*, 51(14):2806–2808, 1986.

[58] Linda J Johnston, Michal Tencer, and JC Scaiano. Evidence for hydrogen transfer in the photochemistry of 2, 2, 6, 6-tetramethylpiperidine n-oxyl. *The Journal of Organic Chemistry*, 51(14):2806–2808, 1986.

[59] A.S. Tatikolov, V.A. Kuzmin, and L.A. Singer. Quenching of triplet states by nitroxyl radicals in the presence of surfactants. *Chemical Physics Letters*, 124(5):451–455, 1986.

[60] Vincenzo Balzani, Paola Ceroni, and Alberto Juris. *Photochemistry and photophysics: concepts, research, applications*. Wiley-VCH, 2014.

[61] Rodney Loudon. *The quantum theory of light*. Oxford science publications. Oxford University Press, 3rd ed edition, 2000.

[62] Gerd Wedler and Hans-Joachim Freund. *Lehrbuch der physikalischen Chemie*. Wiley-VCH, 6., vollst. überarb. und aktualisierte aufl edition, 2012.

[63] Gerd Wedler and Hans-Joachim Freund. *Lehr- und Arbeitsbuch physikalische Chemie*. Wiley-VCH Verlag GmbH & Co. KGaA, siebte, wesentlich überarbeitete und erweiterte auflage edition, 2018.

[64] H. H. Jaffe and Albert L. Miller. The fates of electronic excitation energy. *Journal of Chemical Education*, 43(9):469, 1966.

[65] E. B. Priestley and A. Haug. Phosphorescence spectrum of pure crystalline naphthalene. *The Journal of Chemical Physics*, 49(2):622–629, 1968.

[66] J. Franck and E. G. Dymond. Elementary processes of photochemical reactions. *Transactions of the Faraday Society*, 21:536, 1926.

[67] İlker Özkan. Franck-condon principle for polyatomic molecules: Axis-switching effects and transformation of normal coordinates. *Journal of Molecular Spectroscopy*, 139(1):147–162, 1990.

[68] Michael Kasha. Characterization of electronic transitions in complex molecules. *Discussions of the Faraday Society*, 9:14, 1950.

[69] Juan Carlos Del Valle and Javier Catalán. Kasha's rule: a reappraisal. *Physical Chemistry Chemical Physics*, 21(19):10061–10069, 2019.

[70] F. Albert Cotton. *Chemical applications of group theory*. Wiley, 3rd ed edition, 1990.

[71] Daniel C. Harris and Michael D. Bertolucci. *Symmetry and spectroscopy: An introduction to vibrational and electronic spectroscopy*. Oxford Univ. Pr, 1978.

[72] Alan Corney. *Atomic and Laser Spectroscopy*. Oxford University Press, 2006.

[73] Wenhao Shao, Hanjie Jiang, Ramin Ansari, Paul M. Zimmerman, and Jinsang Kim. Heavy atom oriented orbital angular momentum manipulation in metal-free organic phosphors. *Chemical Science*, 13(3):789–797, 2022.

[74] M. A. El-Sayed. Spin—orbit coupling and the radiationless processes in nitrogen heterocyclics. *The Journal of Chemical Physics*, 38(12):2834–2838, 1963.

[75] S. K. Lower and M. A. El-Sayed. The triplet state and molecular electronic processes in organic molecules. *Chemical Reviews*, 66(2):199–241, 1966.

[76] Masaaki Baba. Intersystem crossing in the ^{1} nπ* and ^{1} ππ* states. *The Journal of Physical Chemistry A*, 115(34):9514–9519, 2011.

[77] Edward Condon. A theory of intensity distribution in band systems. *Physical Review*, 28(6):1182–1201, 1926.

[78] Edward U. Condon. Nuclear motions associated with electron transitions in diatomic molecules. *Physical Review*, 32(6):858–872, 1928.

[79] J. W. Verhoeven. Glossary of terms used in photochemistry (IUPAC recommendations 1996). *Pure and Applied Chemistry*, 68(12):2223–2286, 1996.

[80] P. W. Atkins and Julio De Paula. *Physical chemistry for the life sciences*. W.H. Freeman and Co. ; Oxford University Press, 2nd ed edition, 2011. OCLC: ocn695528594.

[81] Maria Göppert-Mayer. Über elementarakte mit zwei quantensprüngen. *Annalen der Physik*, 401(3):273–294, 1931.

[82] Christof Hättig, Ove Christiansen, and Poul Jo/rgensen. Multiphoton transition moments and absorption cross sections in coupled cluster response theory employing variational transition moment functionals. *The Journal of Chemical Physics*, 108(20):8331–8354, 1998.

[83] Miłosz Pawlicki, Hazel A. Collins, Robert G. Denning, and Harry L. Anderson. Two-photon absorption and the design of two-photon dyes. *Angewandte Chemie International Edition*, 48(18):3244–3266, 2009.

[84] W. Kaiser and C. G. B. Garrett. Two-photon excitation in ca f 2 : Eu 2 +. *Physical Review Letters*, 7(6):229–231, 1961.

[85] Handbook of radical polymerization, 2002.

[86] Matthew P. Tonge, Atsushi Kajiwara, Mikiharu Kamachi, and Robert G. Gilbert. E.s.r. measurements of the propagation rate coefficient for styrene free radical polymerisation. *Polymer*, 39(11):2305–2313, 1998.

[87] Max S. Matheson, E. E. Auer, Ellen B. Bevilacqua, and E. J. Hart. Rate constants in free radical polymerization. III. styrene [1]. *Journal of the American Chemical Society*, 73(4):1700–1706, 1951.

[88] P. E. M. Allen and C. R. Patrick. Diffusion-controlled reactions in free radical polymerisation. *Die Makromolekulare Chemie*, 47(1):154–167, 1961.

[89] Ali Bagheri and Jianyong Jin. Photopolymerization in 3d printing. *ACS Applied Polymer Materials*, 1(4):593–611, 2019.

[90] Xiaoyu Zheng, William Smith, Julie Jackson, Bryan Moran, Huachen Cui, Da Chen, Jianchao Ye, Nicholas Fang, Nicholas Rodriguez, Todd Weisgraber, and Christopher M. Spadaccini. Multiscale metallic metamaterials. *Nature Materials*, 15(10):1100–1106, 2016.

[91] Napolabel B. Palaganas, Joey Dacula Mangadlao, Al Christopher C. De Leon, Jerome O. Palaganas, Katrina D. Pangilinan, Yan Jie Lee, and Rigoberto C. Advincula. 3d printing of photocurable cellulose nanocrystal composite for fabrication of complex architectures via stereolithography. *ACS Applied Materials & Interfaces*, 9(39):34314–34324, 2017.

[92] R. Liska, M. Schuster, R. Inführ, C. Turecek, C. Fritscher, B. Seidl, V. Schmidt, L. Kuna, A. Haase, F. Varga, H. Lichtenegger, and J. Stampfl. Photopolymers for rapid prototyping. *Journal of Coatings Technology and Research*, 4(4):505–510, 2007.

[93] Assi Al Mousawi, Patxi Garra, Xavier Sallenave, Frederic Dumur, Joumana Toufaily, Tayssir Hamieh, Bernadette Graff, Didier Gigmes, Jean Pierre Fouassier, and Jacques Lalevée. π-conjugated dithienophosphole derivatives as high performance photoinitiators for 3d printing resins. *Macromolecules*, 51(5):1811–1821, 2018.

[94] Rima Janusziewicz, John R. Tumbleston, Adam L. Quintanilla, Sue J. Mecham, and Joseph M. DeSimone. Layerless fabrication with continuous liquid interface production. *Proceedings of the National Academy of Sciences*, 113(42):11703–11708, 2016.

[95] Caterina Credi, Alessandro Fiorese, Marco Tironi, Roberto Bernasconi, Luca Magagnin, Marinella Levi, and Stefano Turri. 3d printing of cantilever-type microstructures by stereolithography of ferromagnetic photopolymers. *ACS Applied Materials & Interfaces*, 8(39):26332–26342, 2016.

[96] Christopher S. Colley, David C. Grills, Nicholas A. Besley, Steffen Jockusch, Pavel Matousek, Anthony W. Parker, Michael Towrie, Nicholas J. Turro, Peter M. W. Gill, and Michael W. George. Probing the reactivity of photoinitiators for free radical polymerization: time-resolved infrared spectroscopic study of benzoyl radicals. *Journal of the American Chemical Society*, 124(50):14952–14958, 2002.

[97] Yusuf Yagci, Steffen Jockusch, and Nicholas J. Turro. Photoinitiated polymerization: Advances, challenges, and opportunities. *Macromolecules*, 43(15):6245–6260, 2010.

[98] Jonathan B. Mueller, Joachim Fischer, Frederik Mayer, Muamer Kadic, and Martin Wegener. Polymerization kinetics in three-dimensional direct laser writing. *Advanced Materials*, 26(38):6566–6571, 2014.

[99] Ermias Girma Leggesse, Wan-Rou Tong, Santhanamoorthi Nachimuthu, Tai-Yu Chen, and Jyh-Chiang Jiang. Theoretical study on photochemistry of irgacure 907. *Journal of Photochemistry and Photobiology A: Chemistry*, 347:78–85, 2017.

[100] W. Arthur Green. *Industrial photoinitiators: a technical guide.* CRC Press, 2010. OCLC: ocn435419206.

[101] Juan Segurola, Norman S Allen, Michele Edge, Adam McMahon, and Stephen Wilson. Photoyellowing and discolouration of UV cured acrylated clear coatings systems: influence of photoinitiator type. *Polymer Degradation and Stability*, 64(1):39–48, 1999.

[102] Zuleykhan Tomova, Nikolaos Liaros, Sandra A. Gutierrez Razo, Steven M. Wolf, and John T. Fourkas. In situ measurement of the effective nonlinear absorption order in multiphoton photoresists. *Laser & Photonics Reviews*, 10(5):849–854, 2016.

[103] Basavaraja Jana, S.R. Inamdar, and Suresh Kumar H.M. Effect of quencher and temperature on fluorescence intensity of laser dyes: DETC and c504t. *Spectrochimica Acta Part A: Molecular and Biomolecular Spectroscopy*, 170:124–130, 2017.

[104] J. L. R. Williams, D. P. Specht, and S. Farid. Ketocoumarins as photosensitizers and photoinitiators. *Polymer Engineering and Science*, 23(18):1022–1024, 1983.

[105] Jingjing Xie, Pan Xu, Yiling Zhu, Jingyi Wang, Wan-Chen Cindy Lee, and X. Peter Zhang. New catalytic radical process involving 1,4-hydrogen atom abstraction: Asymmetric construction of cyclobutanones. *Journal of the American Chemical Society*, 143(30):11670–11678, 2021.

[106] J.P. Fouassier, D. Ruhlmann, B. Graff, F. Morlet-Savary, and F. Wieder. Excited state processes in polymerization photoinitiators. *Progress in Organic Coatings*, 25(3):235–271, 1995.

[107] Jean-Pierre Fouassier, Denis Ruhlmann, Yasuyuki Takimoto, Masahiko Harada, and Masami Kawabata. New three-component initiation systems in UV curing: A time-resolved laser-spectroscopy investigation. *Journal of Polymer Science Part A: Polymer Chemistry*, 31(9):2245–2248, 1993.

[108] J. C. Scaiano, L. J. Johnston, W. G. McGimpsey, and D. Weir. Photochemistry of organic reaction intermediates: novel reaction paths induced by two-photon laser excitation. *Accounts of Chemical Research*, 21(1):22–29, 1988.

[109] Vincent Hahn, Frederik Mayer, Michael Thiel, and Martin Wegener. 3-d laser nanoprinting. *Optics and Photonics News*, 30(10):28–35, 2019.

[110] Wolfram Koch and Max C. Holthausen. *A chemist's guide to density functional theory*. Wiley-VCH, 2nd ed., 5. reprint edition.

[111] Frank Jensen. *Introduction to computational chemistry*. John Wiley & Sons, third edition edition, 2017.

[112] W. Kohn, A. D. Becke, and R. G. Parr. Density functional theory of electronic structure. *The Journal of Physical Chemistry*, 100(31):12974–12980, 1996.

[113] M. Born and R. Oppenheimer. Zur quantentheorie der molekeln. *Annalen der Physik*, 389(20):457–484, 1927.

[114] David P. Tew, Wim Klopper, and Trygve Helgaker. Electron correlation: The many-body problem at the heart of chemistry. *Journal of Computational Chemistry*, 28(8):1307–1320, 2007.

[115] István Mayer. *The Hartree-Fock Method*, pages 165–225. Springer US, 2003. Series Title: Mathematical and Computational Chemistry.

[116] Errol G. Lewars. *Computational Chemistry*. Springer Netherlands, 2011.

[117] P. Hohenberg and W. Kohn. Inhomogeneous electron gas. *Physical Review*, 136(3):B864–B871, 1964.

[118] Viraht Sahni. *The Hohenberg-Kohn Theorems and Kohn-Sham Density Functional Theory*, pages 99–123. Springer Berlin Heidelberg, 2004.

[119] Stefan Grimme, Stephan Ehrlich, and Lars Goerigk. Effect of the damping function in dispersion corrected density functional theory. *Journal of Computational Chemistry*, 32(7):1456–1465, 2011.

[120] Erich Runge and E. K. U. Gross. Density-functional theory for time-dependent systems. *Physical Review Letters*, 52(12):997–1000, 1984.

[121] Carsten Ullrich. *Time-dependent density-functional theory: concepts and applications*. Oxford graduate texts. Oxford University Press, 2012. OCLC: ocn751833811.

[122] Annual reports in computational chemistry. volume 15, 2019. OCLC: 1124925941.

[123] Stephan Kümmel. Charge-transfer excitations: A challenge for time-dependent density functional theory that has been met. *Advanced Energy Materials*, 7(16):1700440, 2017.

[124] Takeshi Yanai, David P Tew, and Nicholas C Handy. A new hybrid exchange–correlation functional using the coulomb-attenuating method (CAM-b3lyp). *Chemical Physics Letters*, 393(1):51–57, 2004.

[125] Andreas Dreuw, Jennifer L. Weisman, and Martin Head-Gordon. Long-range charge-transfer excited states in time-dependent density functional theory require non-local exchange. *The Journal of Chemical Physics*, 119(6):2943–2946, 2003.

[126] X. Blase and C. Attaccalite. Charge-transfer excitations in molecular donor-acceptor complexes within the many-body bethe-salpeter approach. *Applied Physics Letters*, 99(17):171909, 2011.

[127] I. Duchemin, T. Deutsch, and X. Blase. Short-range to long-range charge-transfer excitations in the zincbacteriochlorin-bacteriochlorin complex: A bethe-salpeter study. *Physical Review Letters*, 109(16):167801, 2012.

[128] C. Faber, P. Boulanger, C. Attaccalite, I. Duchemin, and X. Blase. Excited states properties of organic molecules: from density functional theory to the *GW* and bethe–salpeter green's function formalisms. *Philosophical Transactions of the Royal Society A: Mathematical, Physical and Engineering Sciences*, 372(2011):20130271, 2014.

[129] Katharina Krause and Wim Klopper. Implementation of the bethe–salpeter equation in the TURBOMOLE program. *Journal of Computational Chemistry*, 38(6):383–388, 2017.

[130] Denis Jacquemin, Eric A. Perpète, Ilaria Ciofini, Carlo Adamo, Rosendo Valero, Yan Zhao, and Donald G. Truhlar. On the performances of the m06 family of density functionals for electronic excitation energies. *Journal of Chemical Theory and Computation*, 6(7):2071–2085, 2010.

[131] Pierre-François Loos, Anthony Scemama, and Denis Jacquemin. The quest for highly accurate excitation energies: A computational perspective. *The Journal of Physical Chemistry Letters*, 11(6):2374–2383, 2020.

[132] Giovanni Onida, Lucia Reining, and Angel Rubio. Electronic excitations: density-functional versus many-body green's-function approaches. *Reviews of Modern Physics*, 74(2):601–659, 2002.

[133] F Aryasetiawan and O Gunnarsson. The ***GW*** method. *Reports on Progress in Physics*, 61(3):237–312, 2024.

[134] Dorothea Golze, Marc Dvorak, and Patrick Rinke. The GW compendium: A practical guide to theoretical photoemission spectroscopy. *Frontiers in Chemistry*, 7:377, 2019.

[135] Xavier Blase, Ivan Duchemin, Denis Jacquemin, and Pierre-François Loos. The bethe–salpeter equation formalism: From physics to chemistry. *The Journal of Physical Chemistry Letters*, 11(17):7371–7382, 2020.

[136] Poul Jo/rgensen, Hans Jo/rgen Aagaard Jensen, and Jeppe Olsen. Linear response calculations for large scale multiconfiguration self-consistent field wave functions. *The Journal of Chemical Physics*, 89(6):3654–3661, 1988.

[137] Maarten T. P. Beerepoot, Daniel H. Friese, Nanna H. List, Jacob Kongsted, and Kenneth Ruud. Benchmarking two-photon absorption cross sections: performance of CC2 and CAM-b3lyp. *Physical Chemistry Chemical Physics*, 17(29):19306–19314, 2015.

[138] Peter Cronstrand, Patrick Norman, Yi Luo, and Hans Ågren. Few-states models for three-photon absorption. *The Journal of Chemical Physics*, 121(5):2020–2029, 2004.

[139] Giovanni Scalmani and Michael J. Frisch. Continuous surface charge polarizable continuum models of solvation. i. general formalism. *The Journal of Chemical Physics*, 132(11):114110, 2010.

[140] A. Klamt and G. Schüürmann. COSMO: a new approach to dielectric screening in solvents with explicit expressions for the screening energy and its gradient. *J. Chem. Soc., Perkin Trans. 2*, (5):799–805, 1993.

[141] Ansgar Schäfer, Hans Horn, and Reinhart Ahlrichs. Fully optimized contracted gaussian basis sets for atoms li to kr. *The Journal of Chemical Physics*, 97(4):2571–2577, 1992.

[142] Florian Weigend and Reinhart Ahlrichs. Balanced basis sets of split valence, triple zeta valence and quadruple zeta valence quality for h to rn: Design and assessment of accuracy. *Physical Chemistry Chemical Physics*, 7(18):3297, 2005.

[143] Florian Weigend. Accurate coulomb-fitting basis sets for h to rn. *Physical Chemistry Chemical Physics*, 8(9):1057, 2006.

[144] Axel D. Becke. Density-functional thermochemistry. III. the role of exact exchange. *The Journal of Chemical Physics*, 98(7):5648–5652, 1993.

[145] Thibaud Etienne, Xavier Assfeld, and Antonio Monari. Toward a quantitative assessment of electronic transitions' charge-transfer character. *Journal of Chemical Theory and Computation*, 10(9):3896–3905, 2014.

[146] M. J. Frisch, G. W. Trucks, H. B. Schlegel, G. E. Scuseria, M. A. Robb, J. R. Cheeseman, G. Scalmani, V. Barone, G. A. Petersson, and Hiroshi Nakatsuji. *Gaussian 16*. Gaussian, Inc. Wallingford, CT.

[147] Kestutis Aidas, Celestino Angeli, Keld L. Bak, Vebjørn Bakken, Radovan Bast, Linus Boman, Ove Christiansen, Renzo Cimiraglia, Sonia Coriani, Pål Dahle, Erik K. Dalskov, Ulf Ekström, Thomas Enevoldsen, Janus J. Eriksen, Patrick Ettenhuber, Berta Fernández, Lara Ferrighi, Heike Fliegl, Luca Frediani, Kasper Hald, Asger Halkier, Christof Hättig, Hanne Heiberg, Trygve Helgaker, Alf Christian Hennum, Hinne Hettema, Eirik Hjertenaes, Stinne Høst, Ida-Marie Høyvik, Maria Francesca Iozzi, Branislav Jansík, Hans Jørgen Aa. Jensen, Dan Jonsson, Poul Jørgensen, Joanna Kauczor, Sheela Kirpekar, Thomas Kjaergaard, Wim Klopper, Stefan Knecht, Rika Kobayashi, Henrik Koch, Jacob Kongsted, Andreas Krapp, Kasper Kristensen, Andrea Ligabue, Ola B. Lutnaes, Juan I. Melo, Kurt V. Mikkelsen, Rolf H. Myhre, Christian Neiss, Christian B. Nielsen, Patrick Norman, Jeppe Olsen, Jógvan Magnus H. Olsen, Anders Osted, Martin J. Packer, Filip Pawlowski, Thomas B. Pedersen, Patricio F. Provasi, Simen Reine, Zilvinas Rinkevicius, Torgeir A. Ruden, Kenneth Ruud, Vladimir V. Rybkin, Pawel Sałek, Claire C. M. Samson, Alfredo Sánchez de Merás, Trond Saue, Stephan P. A. Sauer, Bernd Schimmelpfennig, Kristian Sneskov, Arnfinn H. Steindal, Kristian O. Sylvester-Hvid, Peter R. Taylor, Andrew M. Teale, Erik I. Tellgren, David P. Tew, Andreas J. Thorvaldsen, Lea Thøgersen, Olav Vahtras, Mark A. Watson, David J. D. Wilson, Marcin Ziolkowski, and Hans Ågren. The dalton quantum chemistry program system: The dalton program. *Wiley Interdisciplinary Reviews: Computational Molecular Science*, 4(3):269–284, 2014.

[148] P. R. Monson and W. M. McClain. Polarization dependence of the two-photon absorption of tumbling molecules with application to liquid 1-chloronaphthalene and benzene. *The Journal of Chemical Physics*, 53(1):29–37, 1970.

[149] D. L. Andrews and T. Thirunamachandran. On three-dimensional rotational averages. *The Journal of Chemical Physics*, 67(11):5026–5033, 1977.

[150] Daniel H. Friese, Maarten T. P. Beerepoot, and Kenneth Ruud. Rotational averaging of multiphoton absorption cross sections. *The Journal of Chemical Physics*, 141(20):204103, 2014.

[151] M. J. van Setten, F. Weigend, and F. Evers. The *GW* -method for quantum chemistry applications: Theory and implementation. *Journal of Chemical Theory and Computation*, 9(1):232–246, 2013.

[152] Christof Holzer and Wim Klopper. Ionized, electron-attached, and excited states of molecular systems with spin–orbit coupling: Two-component *GW* and bethe–salpeter implementations. *The Journal of Chemical Physics*, 150(20):204116, 2019.

[153] Rodrigo Cortés-Mejía, Sebastian Höfener, and Wim Klopper. Effects of rotational conformation on electronic properties of 4,4′-bis(carbazol-9-yl)biphenyl (CBP): the single-molecule picture and beyond. *Molecular Physics*, 119(8):e1876936, 2021.

[154] Michael Rohlfing and Steven G. Louie. Excitonic effects and the optical absorption spectrum of hydrogenated si clusters. *Physical Review Letters*, 80(15):3320–3323, 1998.

[155] K Eichkorn, O Treutler, H Öhm, M Häser, and R Ahlrichs. Auxiliary basis sets to approximate coulomb potentials (chem. phys. letters 240 (1995) 283-290). *Chemical Physics Letters*, 242(6):652–660, 1995.

[156] Marek Sierka, Annika Hogekamp, and Reinhart Ahlrichs. Fast evaluation of the coulomb potential for electron densities using multipole accelerated resolution of identity approximation. *The Journal of Chemical Physics*, 118(20):9136–9148, 2003.

[157] Reinhart Ahlrichs. Efficient evaluation of three-center two-electron integrals over gaussian functions. *Physical Chemistry Chemical Physics*, 6(22):5119, 2004.

[158] Nina O. C. Winter, Nora K. Graf, Samuel Leutwyler, and Christof Hättig. Benchmarks for 0–0 transitions of aromatic organic molecules: DFT/b3lyp, ADC(2), CC2, SOS-CC2 and SCS-CC2 compared to high-resolution gas-phase data. *Phys. Chem. Chem. Phys.*, 15(18):6623–6630, 2013.

[159] Jochen Autschbach and Monika Srebro. Delocalization error and "functional tuning" in kohn–sham calculations of molecular properties. *Accounts of Chemical Research*, 47(8):2592–2602, 2014.

[160] Carlo Adamo and Denis Jacquemin. The calculations of excited-state properties with time-dependent density functional theory. *Chem. Soc. Rev.*, 42(3):845–856, 2013.

[161] Kamal Batra, Stefan Zahn, and Thomas Heine. Benchmark of simplified time-dependent density functional theory for UV–vis spectral properties of porphyrinoids. *Advanced Theory and Simulations*, 3(1):1900192, 2020.

[162] Marco Caricato, Benedetta Mennucci, Jacopo Tomasi, Francesca Ingrosso, Roberto Cammi, Stefano Corni, and Giovanni Scalmani. Formation and relaxation of excited states in solution: A new time dependent polarizable continuum model based on time dependent density functional theory. *The Journal of Chemical Physics*, 124(12):124520, 2006.

[163] TURBOMOLE v7.5 2020, a development of university of karlsruhe and forschungszentrum karlsruhe GmbH, 1989-2007, TURBOMOLE GmbH, since 2007; available from https://www.turbomole.org.

[164] Francisco J. Avila Ferrer, Javier Cerezo, Emiliano Stendardo, Roberto Improta, and Fabrizio Santoro. Insights for an accurate comparison of computational data to experimental absorption and emission spectra: Beyond the vertical transition approximation. *Journal of Chemical Theory and Computation*, 9(4):2072–2082, 2013.

[165] Denis Jacquemin, Aurélien Planchat, Carlo Adamo, and Benedetta Mennucci. TD-DFT assessment of functionals for optical 0–0 transitions in solvated dyes. *Journal of Chemical Theory and Computation*, 8(7):2359–2372, 2012.

[166] Roberto Improta, Vincenzo Barone, Giovanni Scalmani, and Michael J. Frisch. A state-specific polarizable continuum model time dependent density functional theory method for excited state calculations in solution. *The Journal of Chemical Physics*, 125(5):054103, 2006.

[167] Roberto Improta, Giovanni Scalmani, Michael J. Frisch, and Vincenzo Barone. Toward effective and reliable fluorescence energies in solution by a new state specific polarizable continuum model time dependent density functional theory approach. *The Journal of Chemical Physics*, 127(7):074504, 2007.

[168] Tangui Le Bahers, Carlo Adamo, and Ilaria Ciofini. A qualitative index of spatial extent in charge-transfer excitations. *Journal of Chemical Theory and Computation*, 7(8):2498–2506, 2011.

[169] Tian Lu and Feiwu Chen. Multiwfn: A multifunctional wavefunction analyzer. *Journal of Computational Chemistry*, 33(5):580–592, 2012.

[170] Fabrizio Santoro, Roberto Improta, Alessandro Lami, Julien Bloino, and Vincenzo Barone. Effective method to compute franck-condon integrals for optical spectra of large molecules in solution. *The Journal of Chemical Physics*, 126(8):084509, 2007.

[171] Fabrizio Santoro, Alessandro Lami, Roberto Improta, Julien Bloino, and Vincenzo Barone. Effective method for the computation of optical spectra of large molecules at finite temperature including the duschinsky and herzberg–teller effect: The qx band of porphyrin as a case study. *The Journal of Chemical Physics*, 128(22):224311, 2008.

[172] G. Herzberg and E. Teller. Schwingungsstruktur der elektronenübergänge bei mehratomigen molekülen. *Zeitschrift für Physikalische Chemie*, 21B(1):410–446, 1933.

[173] Guangjun Tian and Yi Luo. Isomer-dependent franck–condon blockade in weakly coupled bipyridine molecular junctions. *The Journal of Physical Chemistry C*, 118(27):14853–14859, 2014.

[174] Guangjun Tian and Yi Luo. Fluorescence and phosphorescence of single c $_{60}$ molecules as stimulated by a scanning tunneling microscope. *Angewandte Chemie International Edition*, 52(18):4814–4817, 2013.

[175] E. van Lenthe, E. J. Baerends, and J. G. Snijders. Relativistic regular two-component hamiltonians. *The Journal of Chemical Physics*, 99(6):4597–4610, 1993.

[176] G. Tian, S. Duan, W. Hua, and Y. Luo. DynaVib version 1.0. *Royal Institute of Technology, Sweden*, 2012.

[177] Yafu Pan, Li Li, Feifei Qiu, Yong Wei, Weijie Hua, and Guangjun Tian. On the spectral profile change in the q band absorption spectra of metalloporphyrins (mg, zn, and pd): A first-principles study. *The Journal of Chemical Physics*, 150(16):164308, 2019.

[178] Peter C. St. John, Yanfei Guan, Yeonjoon Kim, Seonah Kim, and Robert S. Paton. Prediction of organic homolytic bond dissociation enthalpies at near chemical accuracy with sub-second computational cost. *Nature Communications*, 11(1):2328, 2020.

[179] Li-Juan Yu, Stephen G. Dale, Bun Chan, and Amir Karton. Benchmark study of DFT and composite methods for bond dissociation energies in argon compounds. *Chemical Physics*, 531:110676, 2020.

[180] Carlos. Gonzalez and H. Bernhard. Schlegel. Reaction path following in mass-weighted internal coordinates. *The Journal of Physical Chemistry*, 94(14):5523–5527, 1990.

[181] Henry Eyring. The activated complex in chemical reactions. *The Journal of Chemical Physics*, 3(2):107–115, 1935.

[182] Zhigang Shuai and Qian Peng. Organic light-emitting diodes: theoretical understanding of highly efficient materials and development of computational methodology. *National Science Review*, 4(2):224–239, 2017.

[183] Yingli Niu, Wenqiang Li, Qian Peng, Hua Geng, Yuanping Yi, Linjun Wang, Guangjun Nan, Dong Wang, and Zhigang Shuai. MOlecular MAterials property prediction package (MOMAP) 1.0: a software package for predicting the luminescent properties and mobility of organic functional materials. *Molecular Physics*, 116(7):1078–1090, 2018.

[184] Qian Peng, Yuanping Yi, Zhigang Shuai, and Jiushu Shao. Excited state radiationless decay process with duschinsky rotation effect: Formalism and implementation. *The Journal of Chemical Physics*, 126(11):114302, 2007.

[185] Qian Peng, Yingli Niu, Qinghua Shi, Xing Gao, and Zhigang Shuai. Correlation function formalism for triplet excited state decay: Combined spin–orbit and nonadiabatic couplings. *Journal of Chemical Theory and Computation*, 9(2):1132–1143, 2013.

[186] YingLi Niu, Qian Peng, and ZhiGang Shuai. Promoting-mode free formalism for excited state radiationless decay process with duschinsky rotation effect. *Science in China Series B: Chemistry*, 51(12):1153–1158, 2008.

[187] Yingli Niu, Qian Peng, Chunmei Deng, Xing Gao, and Zhigang Shuai. Theory of excited state decays and optical spectra: Application to polyatomic molecules. *The Journal of Physical Chemistry A*, 114(30):7817–7831, 2010.

[188] A. M. Mebel, M. Hayashi, K. K. Liang, and S. H. Lin. Ab initio calculations of vibronic spectra and dynamics for small polyatomic molecules: Role of duschinsky effect. *The Journal of Physical Chemistry A*, 103(50):10674–10690, 1999.

[189] Feiyan Li, Guanyu Jiang, Muzhen Li, Jianzhong Fan, Yuzhi Song, Chuan-Kui Wang, and Lili Lin. Thermally activated delayed fluorescence emitters with dual conformations for white organic light-emitting diodes: mechanism and molecular design. *Physical Chemistry Chemical Physics*, 22(3):1313–1323.

[190] Robert Send and Filipp Furche. First-order nonadiabatic couplings from time-dependent hybrid density functional response theory: Consistent formalism, implementation, and performance. *The Journal of Chemical Physics*, 132(4):044107, 2010.

[191] Zhendong Li and Wenjian Liu. First-order nonadiabatic coupling matrix elements between excited states: A lagrangian formulation at the CIS, RPA, TD-HF, and TD-DFT levels. *The Journal of Chemical Physics*, 141(1):014110, 2014.

[192] Zhendong Li, Bingbing Suo, and Wenjian Liu. First order nonadiabatic coupling matrix elements between excited states: Implementation and application at the TD-DFT and pp-TDA levels. *The Journal of Chemical Physics*, 141(24):244105, 2014.

[193] G. te Velde, F. M. Bickelhaupt, E. J. Baerends, C. Fonseca Guerra, S. J. A. van Gisbergen, J. G. Snijders, and T. Ziegler. Chemistry with ADF. *Journal of Computational Chemistry*, 22(9):931–967, 2001.

[194] Erik van Lenthe, Andreas Ehlers, and Evert-Jan Baerends. Geometry optimizations in the zero order regular approximation for relativistic effects. *The Journal of Chemical Physics*, 110(18):8943–8953, 1999.

[195] E. van Lenthe, E. J. Baerends, and J. G. Snijders. Relativistic total energy using regular approximations. *The Journal of Chemical Physics*, 101(11):9783–9792, 1994.

[196] D. Maryenko, M. Kawamura, A. Ernst, V. K. Dugaev, E. Ya. Sherman, M. Kriener, M. S. Bahramy, Y. Kozuka, and M. Kawasaki. Interplay of spin–orbit coupling and coulomb interaction in ZnO-based electron system. *Nature Communications*, 12(1):3180, 2021.

[197] Frank Neese, Frank Wennmohs, Ute Becker, and Christoph Riplinger. The ORCA quantum chemistry program package. *The Journal of Chemical Physics*, 152(22):224108, 2020.

[198] Bernardo De Souza, Giliandro Farias, Frank Neese, and Róbert Izsák. Predicting phosphorescence rates of light organic molecules using time-dependent density functional theory and the path integral approach to dynamics. *Journal of Chemical Theory and Computation*, 15(3):1896–1904, 2019.

[199] Vincenzo Barone and Maurizio Cossi. Quantum calculation of molecular energies and energy gradients in solution by a conductor solvent model. *The Journal of Physical Chemistry A*, 102(11):1995–2001, 1998.

[200] Shiyun Lin, Qi Ou, and Zhigang Shuai. Computational selection of thermally activated delayed fluorescence (TADF) molecules with promising electrically pumped lasing property. *ACS Materials Letters*, 4(3):487–496, 2022.

[201] Jin Tang, Xiaoyi Xu, Xiaoming Shen, Cuifang Kuang, Hongzheng Chen, Minmin Shi, and Ning Huang. Ketocoumarin-based photoinitiators for high-sensitivity two-photon lithography. *ACS Applied Polymer Materials*, 5(4):2956–2963, 2023.

[202] Cheng Cao, Xiaogang Liu, Qinglong Qiao, Miao Zhao, Wenting Yin, Deqi Mao, Hui Zhang, and Zhaochao Xu. A twisted-intramolecular-charge-transfer (TICT) based ratiometric fluorescent thermometer with a mega-stokes shift and a positive temperature coefficient. *Chem. Commun.*, 50(99):15811–15814, 2014.

[203] Thomas Wloka, Michael Gottschaldt, and Ulrich S. Schubert. From light to structure: Photo initiators for radical two-photon polymerization. *Chemistry – A European Journal*, 28(32), 2022.

[204] Zhiquan Li, Niklas Pucher, Klaus Cicha, Jan Torgersen, Samuel C. Ligon, Aliasghar Ajami, Wolfgang Husinsky, Arnulf Rosspeintner, Eric Vauthey, Sergej Naumov, Tom Scherzer, Jürgen Stampfl, and Robert Liska. A straightforward synthesis and structure–activity relationship of highly efficient initiators for two-photon polymerization. *Macromolecules*, 46(2):352–361, 2013.

[205] Christel M. Marian. Spin-orbit coupling and intersystem crossing in molecules: Spin-orbit coupling. *Wiley Interdisciplinary Reviews: Computational Molecular Science*, 2(2):187–203, 2012.

[206] Benjamin Harke, William Dallari, Giulia Grancini, Daniele Fazzi, Fernando Brandi, Annamaria Petrozza, and Alberto Diaspro. Polymerization inhibition by triplet state absorption for nanoscale lithography. *Advanced Materials*, 25(6):904–909, 2013.

[207] Veronica Mucci and Claudia Vallo. Efficiency of 2,2-dimethoxy-2-phenylacetophenone for the photopolymerization of methacrylate monomers in thick sections. *Journal of Applied Polymer Science*, 123(1):418–425, 2012.

[208] Paul Somers, Zihao Liang, Jason E. Johnson, Bryan W. Boudouris, Liang Pan, and Xianfan Xu. Rapid, continuous projection multi-photon 3d printing enabled by spatiotemporal focusing of femtosecond pulses. *Light: Science & Applications*, 10(1):199, 2021.

[209] Yan Zhao and Donald G. Truhlar. Density functional for spectroscopy: No long-range self-interaction error, good performance for rydberg and charge-transfer states, and better performance on average than b3lyp for ground states. *The Journal of Physical Chemistry A*, 110(49):13126–13130, 2006.

[210] Carlo Adamo and Vincenzo Barone. Toward reliable density functional methods without adjustable parameters: The PBE0 model. *The Journal of Chemical Physics*, 110(13):6158–6170, 1999.

[211] Changfeng Fang, Baswanth Oruganti, and Bo Durbeej. How method-dependent are calculated differences between vertical, adiabatic, and 0–0 excitation energies? *The Journal of Physical Chemistry A*, 118(23):4157–4171, 2014.

[212] Paul Wiggins, J. A. Gareth Williams, and David J. Tozer. Excited state surfaces in density functional theory: A new twist on an old problem. *The Journal of Chemical Physics*, 131(9):091101, 2009.

[213] Cinthia Suellen, Renato Garcia Freitas, Pierre-François Loos, and Denis Jacquemin. Cross-comparisons between experiment, TD-DFT, CC, and ADC for transition energies. *Journal of Chemical Theory and Computation*, 15(8):4581–4590, 2019.

[214] Attila Tajti, Levente Tulipán, and Péter G. Szalay. Accuracy of spin-component scaled ADC(2) excitation energies and potential energy surfaces. *Journal of Chemical Theory and Computation*, 16(1):468–474, 2020.

[215] Benjamin Harke, William Dallari, Giulia Grancini, Daniele Fazzi, Fernando Brandi, Annamaria Petrozza, and Alberto Diaspro. Polymerization inhibition by triplet state absorption for nanoscale lithography. *Advanced Materials*, 25(6):904–909, 2013.

[216] Sophie De Reguardati, Juri Pahapill, Alexander Mikhailov, Yuriy Stepanenko, and Aleksander Rebane. High-accuracy reference standards for two-photon absorption in the 680–1050 nm wavelength range. *Optics Express*, 24(8):9053, 2016.

[217] Nikolay S. Makarov, Mikhail Drobizhev, and Aleksander Rebane. Two-photon absorption standards in the 550-1600 nm excitation wavelength range. *Optics Express*, 16(6):4029, 2008.

[218] Camille A. Farfan and Daniel B. Turner. A systematic model study quantifying how conical intersection topography modulates photochemical reactions. *Physical Chemistry Chemical Physics*, 22(36):20265–20283, 2020.

[219] Nikolaos Liaros, Sandra A. Gutierrez Razo, Matthew D. Thum, Hannah M. Ogden, Andrea N. Zeppuhar, Steven Wolf, Tommaso Baldacchini, Matthew J. Kelley, John S. Petersen, Daniel E. Falvey, Amy S. Mullin, and John T. Fourkas. Elucidating complex triplet-state dynamics in the model system isopropylthioxanthone. *iScience*, 25(1):103600, 2022.

[220] Jason E. Johnson, Yijie Chen, and Xianfan Xu. Model for polymerization and self-deactivation in two-photon nanolithography. *Optics Express*, 30(15):26824, 2022.

[221] Jacques Lalevée, Xavier Allonas, and Jean-Pierre Fouassier. N–h and α(c–h) bond dissociation enthalpies of aliphatic amines. *Journal of the American Chemical Society*, 124(32):9613–9621, 2002.

[222] Tanlong Xue, Yang Li, Xin Li, Boyuan Huang, Qiuyan Song, Jun Nie, and Xiaoqun Zhu. Benzylidene ketones as visible light radical photoinitiator: The effects of electron-donating group and co-initiator. *Journal of Photochemistry and Photobiology A: Chemistry*, 418:113395, 2021.

[223] Luca Capaldo, Davide Ravelli, and Maurizio Fagnoni. Direct photocatalyzed hydrogen atom transfer (HAT) for aliphatic c–h bonds elaboration. *Chemical Reviews*, 122(2):1875–1924, 2022.

[224] Sevnur Keskin Dogruyol, Zekeriya Dogruyol, and Nergis Arsu. A thioxanthone-based visible photoinitiator: Thioxanthone-based visible photoinitiator. *Journal of Polymer Science Part A: Polymer Chemistry*, 49(18):4037–4043, 2011.

[225] Gokhan Temel, Burak Enginol, Meral Aydin, Demet Karaca Balta, and Nergis Arsu. Photopolymerization and photophysical properties of amine linked benzophenone photoinitiator for free radical polymerization. *Journal of Photochemistry and Photobiology A: Chemistry*, 219(1):26–31, 2011.

[226] Gokhan Temel, Duygu Sevinc Esen, and Nergis Arsu. One-component benzoxazine type photoinitiator for free radical polymerization. *Polymer Engineering & Science*, 52(1):133–138, 2012.

[227] Ge Ding, Chuan Jing, Xiaozhuan Qin, Yulong Gong, Xueping Zhang, Shengtao Zhang, Ziping Luo, Hongru Li, and Fang Gao. Conjugated dyes carrying n, n-dialkylamino and ketone groups: One-component visible light norrish type II photoinitiators. *Dyes and Pigments*, 137:456–467, 2017.

[228] Xiangcheng Pan, Mehmet Atilla Tasdelen, Joachim Laun, Thomas Junkers, Yusuf Yagci, and Krzysztof Matyjaszewski. Photomediated controlled radical polymerization. *Progress in Polymer Science*, 62:73–125, 2016.

[229] Quang. Shen and Kolbjoern. Hagen. Gas-phase molecular structure and conformation of benzil as determined by electron diffraction. *The Journal of Physical Chemistry*, 91(6):1357–1360, 1987.

[230] K. Eriks, T. D. Hayden, S. Hsi Yang, and I. Y. Chan. Crystal and molecular structure of biacetyl (2,3-butanedione), (h3cco)2, at -12 and -100.degree.c. *Journal of the American Chemical Society*, 105(12):3940–3942, 1983.

[231] R. Bensasson and E. J. Land. Triplet-triplet extinction coefficients via energy transfer. *Transactions of the Faraday Society*, 67:1904, 1971.

[232] Gilbert N. Lewis and M. Kasha. Phosphorescence and the triplet state. 66(12):2100–2116, 1944.

[233] Fujio Tanaka, Shoji Ogura, and Shigeru Yamashita. Energy transfer from the triplet state of 2-acetylnaphthalene to eu3+ in micellar solutions. 54(2):213–217, 1990.

[234] Sen Patric McGlynn, T Azumi, and M Kinoshita. *Molecular spectroscopy of the triplet state*. Prentice-Hall, 1969. OCLC: 925961844.

[235] David Young. *Computational chemistry: a practical guide for applying techniques to real world problems*. John Wiley & Sons, 2004.